Vibrational Energy Transfer Between CO Molecules on a NaCl(100) Surface Studied by Infrared Fluorescence Spectroscopy

Dissertation
zur Erlangung des mathematisch-naturwissenschaftlichen Doktorgrades
„Doctor rerum naturalium"
der Georg-August-Universität Göttingen

im Promotionsstudiengang Chemie
der Georg-August University School of Science (GAUSS)

vorgelegt von

Jascha Alexander Lau

aus Gronau (Leine)

Göttingen, 2021

Betreuungsausschuss

Prof. Dr. Alec M. Wodtke
Institut für Physikalische Chemie, Georg-August-Universität Göttingen

Prof. Dr. Martin A. Suhm
Institut für Physikalische Chemie, Georg-August-Universität Göttingen

Mitglieder der Prüfungskommission

Referent: Prof. Dr. Alec M. Wodtke
Institut für Physikalische Chemie, Georg-August-Universität Göttingen

Korreferent: Prof. Dr. Martin A. Suhm
Institut für Physikalische Chemie, Georg-August-Universität Göttingen

Weitere Mitglieder der Prüfungskommission:

Prof. Dr. Dirk Schwarzer
Max-Planck-Institut für Biophysikalische Chemie, Göttingen

Prof. Dr. Claus Ropers
IV. Physikalisches Institut, Georg-August-Universität Göttingen

Prof. Dr. Jörg Behler
Institut für Physikalische Chemie, Georg-August-Universität Göttingen

Prof. Dr. Ricardo A. Mata
Institut für Physikalische Chemie, Georg-August-Universität Göttingen

Tag der mündlichen Prüfung: 02. März 2021

The following peer-reviewed publications are related to this thesis:

1. J. A. Lau, L. Chen, A. Choudhury, D. Schwarzer, V. B. Verma, A. M. Wodtke, Transporting and concentrating vibrational energy to promote isomerization, *Nature* **589**, 391–395 (2021).

2. J. A. Lau, A.-M. Schönemann, D. Schwarzer, A. M. Wodtke, The coverage dependence of the infrared absorption of CO adsorbed to NaCl(100), *J. Chem. Phys.* **153**, 154703 (2020).

3. J. A. Lau, A. Choudhury, L. Chen, D. Schwarzer, V. B. Verma, A. M. Wodtke, Observation of an isomerizing double-well quantum system in the condensed phase, *Science* **367**, 175–178 (2020).

4. L. Chen*, J. A. Lau*, D. Schwarzer, J. Meyer, V. B. Verma, A. M. Wodtke, The Sommerfeld ground-wave limit for a molecule adsorbed at a surface, *Science* **363**, 158–161 (2019). * Both authors contributed equally to this work.

5. L. Chen, D. Schwarzer, J. A. Lau, V. B. Verma, M. J. Stevens, F. Marsili, R. P. Mirin, S. W. Nam, A. M. Wodtke, Ultra-sensitive mid-infrared emission spectrometer with sub-ns temporal resolution, *Opt. Express* **26**, 14859–14868 (2018).

Abstract

The breaking of chemical bonds in surface reactions is inherently connected to highly excited molecular vibrations. Therefore, understanding the vibrational energy transfer dynamics of adsorbed molecules, which effectively determine the lifetime of vibrational excitation, is of great importance. CO adsorbed on NaCl(100) is possibly the best studied physisorbed molecule. Despite that, most previous experiments have focused on the vibrational ground state and the $v = 0 \rightarrow 1$ transition of CO—mainly because dispersed fluorescence from high vibrational states could not be observed with conventional infrared detectors. In this thesis, I thus investigate the vibrational energy transfer dynamics of CO on NaCl(100) in highly vibrationally excited states up to $v = 30$.

Dispersed and time-resolved laser-induced fluorescence (LIF) is used to observe the vibrational dynamics. For this, an improved version of a recently developed mid-infrared emission spectrometer based on superconducting nanowire single-photon detectors (SNSPDs) is used. The current setup is capable of detecting infrared fluorescence from a single adsorbate layer with spectral and temporal resolution of 7 nm and ~1 µs, respectively. High vibrational states, CO(v), are prepared by pulsed infrared laser excitation of CO to $v = 1$ at cryogenic temperatures around 7 K. Subsequent vibrational energy pooling (VEP), driven by the anharmonicity of the CO oscillators, concentrates many vibrational quanta in single molecules via vibration-to-vibration (V-V) energy transfer from the surrounding molecules: $CO(n) + CO(m) \rightarrow CO(n+1) + CO(m-1)$.

Kinetic Monte Carlo simulations of the vibrational dynamics in a $^{13}C^{18}O$ monolayer show that VEP proceeds via a sequential mechanism, in which adsorbates in high vibrational states are further excited by collecting vibrational quanta from molecules in lower vibrational states over increasingly large distances and timescales, up to 100 µs. The shape of the phonon spectrum, to which the excess energy in the V-V transfer processes is dissipated, causes a distinct peak structure in the vibrational state distribution. Furthermore, dissipation to transverse phonons that involve Na atom motion in the surface plane is found to be most effective. Vibrational relaxation to the NaCl substrate is slower than VEP and occurs on the millisecond time scale for $v \leq 23$. The v-dependent relaxation rates can be explained by a classical electrodynamic mechanism, whereby energy is transferred non-radiatively to the absorbing NaCl medium via the near-field of the oscillating CO dipole. This finding is in strong contrast to the dominating mechanism for more strongly bound adsorbates, where energy is dissipated via anharmonic couplings between the CO vibration and the surface phonons.

The improved resolution of the emission spectrometer revealed a previously unknown metastable O-down orientation ($Na^+ - OC$), which is formed from the stable C-down

orientation ($Na^+ - CO$) in the highest vibrational states. The well-resolved emission spectra of the two orientational isomers show characteristic vibrational blue- and red-shifts relative to the frequency of gas phase CO ($+7.6\,cm^{-1}$ and $-9.3\,cm^{-1}$ for the fundamental frequencies of the C-down and O-down isomer, respectively). The dinstinct frequency shifts are explained and modeled based on the orientation-dependent electrostatic interactions of the CO molecule with its environment. The O-down isomer has a comparatively long lifetime for back-conversion to the C-down isomer, which is estimated between 0.1 and 100 s at 7 K. By adsorption of additional CO overlayers on top of the monolayer, this lifetime can be made indefinitely long.

For the $^{13}C^{18}O$ monolayer covered by 100 $^{12}C^{16}O$ overlayers, it is found that the O-down isomer is most efficiently formed when the overlayer, which can absorb 100 times more photons, is excited. The resulting vibrational excitation transferred from multilayer to monolayer is found to be 30 times higher than the excitation achieved with direct excitation of the monolayer. Furthermore, the preferred direction of energy transfer across the CO monolayer/multilayer interface is investigated for several different isotopic combinations of $^{13}C^{18}O$ and $^{12}C^{16}O$. Vibrational energy can be efficiently transferred from the $^{12}C^{16}O$ to the $^{13}C^{18}O$ layer, rationalized by the energetic preference that results from the $100\,cm^{-1}$ difference in the fundamental vibrational frequencies. Reverse energy flow from $^{13}C^{18}O$ to $^{12}C^{16}O$ is not observed.

In addition, coverage-dependent infrared absorption measurements of CO on NaCl(100) are used to determine the infrared absorption cross section of the $v = 0 \rightarrow 1$ transition of an isolated CO molecule on the NaCl surface without assumptions about its polarizability. The determined integrated cross section of $(2.51 \pm 0.08) \times 10^{-17}\,cm\,molecule^{-1}$ is 18 % lower than that of the gas phase molecule but significantly larger than the effective cross section in the monolayer. The 18 % reduction for the isolated adsorbate is consistent with previous theoretical work that considered the interaction of CO and the surface electric field.

The well-resolved vibrational spectra of both orientational isomers make CO on NaCl(100) an interesting system for future studies on quantum state-resolved isomerization dynamics. In addition, the mechanism for controlled vibrational energy transport suggests that large amounts of vibrational energy could be transferred from CO to infrared-active vibrations of more reactive acceptor molecules. It is worth noting that the phenomena observed in this thesis can mostly be explained by electrostatic interactions of CO with its environment and they should therefore apply to other vibrationally excited physisorbed molecules as well. In conclusion, the presented results not only provide a deeper understanding of the vibrational dynamics in the CO/NaCl(100) system but of physisorbed molecules in general.

Acknowledgments

First and foremost, I would like to express my deepest gratitude to my supervisor Alec Wodtke for getting the chance to work on this exciting project. I really appreciate that he found my work just as interesting as I did and introduced me to so many researchers from around the world. In addition, he always found the right balance between guiding me in the right direction and letting me pursue my own ideas. I am also extremely grateful to my second supervisor Martin Suhm. A large part of the interpretation in this work originated from concepts I learned in his outstanding lectures.

From all members of the IR-LIF team, I am deeply indebted to Dirk Schwarzer. He really is a brilliant scientist who is well-versed in both experimentation and theory. I am very grateful for all the valuable discussions I had with him about the experiment and the results. He really taught me a lot. Special thanks also go to my predecessor Li Chen. He not only built the IR-LIF apparatus and measured the first CO monolayer data on which my simulations in Chapter 4 were based; he also introduced me to the machine and showed me all the "tricks"! Furthermore, I would like to acknowledge Dirk Schwarzer and Tim Diedrichs for their beautiful design of the molecular beam source chamber and the 40 K monochromator. Installing these components together with Tim was probably one of the most enjoyable parts of my doctoral project and taught me so much. I really could not think of a better technician to learn from than him. Many thanks also go to Arnab Choudhury and Jessalyn DeVine who joined the IR-LIF team more recently and supported me in my final experiments. It was great to finally get some company in the lab after Li had left!

In addition, I want to thank all the people outside the Wodtke group that I had the opportunity to work with. Without them, this thesis would look different. Many thanks go to Varun Verma for always sending us state-of-the-art SNSPDs for our infrared applications. I also want to thank Jörg Meyer who provided the NaCl phonon spectrum in Chapter 4, which was the missing piece of the puzzle. Many thanks also go to Steven Corcelli who sent me his kinetic Monte Carlo code. In addition, I would like to acknowledge Joel Bowman, Hua Guo, Jörg Meyer, Peter Saalfrank and Claus Ropers for their great enthusiasm for the flipped CO molecules, which has already led to new results and insights into this fascinating phenomenon.

Next, I would like to thank all my colleagues in the Wodtke group for the enjoyable working atmosphere. Special thanks go to my office neighbors in the "fun office", Sven Kaufmann and Nils Hertl. I really enjoyed the frequent chats in between work. Besides Sven and Nils, I would also like to thank Arthur Fast, Marvin Kammler and Tim Diedrichs for the relaxing table soccer breaks and all the time we spent together outside

of work. Special thanks go to Sascha Kandratsenka who always helped me out when I had computer- or theory-related problems. I am also very grateful to Reinhard Bürsing and Birgit Freyberg for their technical assistance.

Furthermore, I would like to acknowledge Dirk Schwarzer, Jessalyn DeVine, Daniel Delony and Inge Dreger for proofreading this thesis. In addition, many thanks to Ian Brock from the University of Bonn for uploading such a nice and easy-to-use Latex template.

I would especially like to appreciate Anna Schönemann for her continuing support and being so understanding—especially in my final phase of writing.

Finally, this thesis would not have been possible without the continuing support of my parents, Corinna and Stefan Lau, and my grandparents. With their help, I was able to do what I love.

Contents

Introduction

Industrially used catalysts are far too complex to study the atomic scale processes in surface reactions directly. An alternative approach is offered by the field of surface science, in which these molecular processes are studied at well-defined single crystal surfaces prepared under clean ultra-high vacuum (UHV) conditions. Understanding the formation of NH_3 from N_2 and H_2 in the Haber-Bosch process is probably one of the most prominent achievements of surface science, for which Gerhard Ertl was awarded the Nobel Prize in 2007. The group of Ertl studied the energetics of the individual steps of the ammonia synthesis on different iron surfaces and showed that the mechanism obtained from the experiments on single crystals could be related to the industrial reaction. [1] This example suggests that even reactions at complicated gas-surface systems can, in principle, be predicted if all relevant atomic scale processes are understood. [2]

Molecular vibrations can have a strong influence on reactivity, as they are closely connected to the breaking and formation of chemical bonds. From detailed gas phase studies, we know that vibrational excitation of the reactants can significantly increase the rate of a chemical reaction by providing sufficient energy along the reaction coordinate to overcome the activation barrier. [3–5] To give a few examples, reaction of a hydrogen atom with a HOD molecule occurs preferentially via abstraction of a hydrogen atom when the O-H stretching vibration is excited (H + HOD $\rightarrow$ H_2 + OD). On the other hand, abstraction of a deuterium atom is preferred when the O-D stretching vibration is excited (H + DOH $\rightarrow$ HD + OH). [3] Similarly, enhanced reaction rates and vibrational mode-selective behavior are found for the dissociation of vibrationally excited methane on metal surfaces. [6–8]

Measuring the dynamics of highly vibrationally excited molecules adsorbed to solid

surfaces can be challenging, due to the decreased vibrational lifetimes compared to molecules in the gas phase. The lifetime of CO adsorbed on metal surfaces is only on the order of picoseconds [9–11]. On the silicon surface, vibrational excitation decays within nanoseconds. [12–15] In contrast, the much smaller vibrational relaxation efficiency on insulators [16, 17] makes it much easier to study highly vibrationally excited molecules directly at the surface, for example with surface infrared spectroscopy. [18, 19]
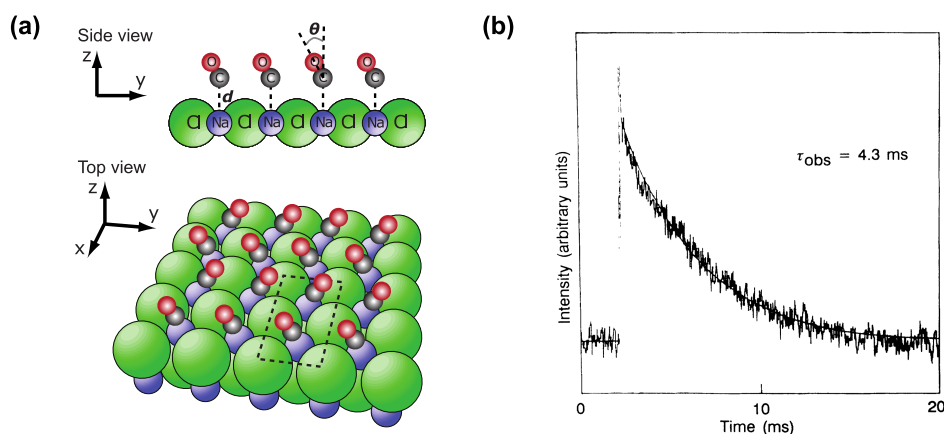
Figure 1.1: (a) Schematic representation of the CO/NaCl(100) monolayer structure at 7 K. Black, red, green and purple spheres represent carbon, oxygen, chlorine and sodium atoms, respectively. From Ref. [20]. Adapted with permission from AAAS. (b) Time-resolved total fluorescence from a $^{13}C^{16}O$ monolayer on NaCl(100) after infrared laser excitation of the first vibrationally excited state. Reprinted with permission from Ref. [16]. Copyright 1990 by the American Physical Society.

CO adsorbed to NaCl(100), whose monolayer structure is illustrated in Fig. 1.1a, is possibly the best studied model system for the vibrational dynamics of physisorbed molecules. [21–23] But despite the detailed investigation of all possible relaxation pathways for CO in the $v = 1$ state, [16, 24–26] much less is known about the dynamics of higher vibrational states. The only experimental evidence of vibrational excitation beyond $v = 1$ was reported by Ewing and co-workers in 1990. [16] In that work, the authors monitored the time-dependence of the total infrared fluorescence originating from the CO monolayer on NaCl(100) after laser excitation of the $v = 0 \rightarrow 1$ transition (see Fig. 1.1b), revealing a long effective vibrational lifetime of 4.3 ms. By applying suitable optical filters, the authors showed that most of the emission signal originated from vibrational states between $v = 2$ to 15. The population of vibrational states beyond $v = 1$ clearly indicated the presence of vibrational energy pooling (VEP), a process

in which some CO molecules collect vibrational quanta on the expense of other CO molecules via the following vibration-to-vibration (V-V) energy transfer processes:

$$CO(v = n) + CO(v = m) \longrightarrow CO(v = n + 1) + CO(v = m - 1).$$

However, vibrational state-resolved fluorescence measurements, although reported for thick CO overlayers, [27] were not possible for a single adsorbate layer at that time—limited by the sensitivity of conventional semiconductor-based infrared detectors. With the advent of more sensitive infrared detectors, such as superconducting nanowire single-photon detectors (SNSPDs), [28–30] those limitations can be overcome.

In this thesis, I will extend the previous experimental studies of CO on NaCl(100) by exploring the vibrational energy transfer dynamics of highly vibrationally excited CO molecules up to $v = 30$. For this purpose, I used an improved version of the first mid-infrared emission spectrometer based on SNSPDs that was recently developed in the group of Alec Wodtke. [31] This state-of-the-art emission spectrometer allowed me to measure the dispersed and time-resolved laser-induced fluorescence (LIF) from the CO monolayer and thus to probe the dynamics of individual vibrational states.

The structure of the thesis will be as follows. Chapter 2 gives an overview of the fundamentals to understand vibrational energy transfer and infrared spectroscopy of the CO/NaCl(100) system needed to interpret the experiments in the following chapters. Chapter 3 describes the experimental apparatus that is used to prepare CO samples on NaCl(100) single crystals and perform infrared emission and absorption experiments, including modifications of the experimental setup introduced over the course of this work. In Chapter 4, the mechanisms for VEP and relaxation of vibrational states up to $v = 27$ in a $^{13}C^{18}O$ monolayer are investigated with kinetic Monte Carlo simulations and compared to previously measured experimental results. Chapter 5 deals with the discovery of a metastable orientational isomer of the CO molecules in the monolayer emission spectrum, which is formed in the highest vibrational states from the stable C-down orientation and could be observed with the improved emission spectrometer. Based on the understanding of vibrational energy transfer in the CO monolayer from the preceding chapters, Chapter 6 presents a successful attempt to control the direction of vibrational energy transport across the CO monolayer/overlayer interface with isotopic substitution. In Chapter 7, coverage-dependent infrared absorption measurements are used to discuss the effect of intermolecular interactions on the absorption cross section of the $v = 0 \rightarrow 1$ transition and to provide an estimate of the isolated adsorbate cross section. Finally, Chapter 8 gives an overview of the conclusions drawn from this work.

Scientific background

This chapter gives an overview of the literature and fundamental concepts necessary to interpret the laser-induced fluorescence (LIF) and Fourier-transform infrared (FTIR) absorption experiments of CO on NaCl(100). Section 2.1 gives an overview of the adsorption structure and infrared absorption spectroscopy of CO on NaCl(100). Section 2.2 discusses vibrational energy transfer between adsorbates and the surface as well as vibrational energy transfer between adsorbates, including the most relevant theoretical models for the CO/NaCl(100) system. In Section 2.3, fundamental aspects and general challenges of LIF spectroscopy in the infrared region are presented. In addition, a brief introduction to superconducting nanowire single-photon detectors (SNSPDs), which are used in the present work, is given. Section 2.4 focuses on the concepts needed for a quantitative description of infrared absorption spectra, including two models that consider collective vibrations of the adsorbates (vibrational excitons). Finally, Section 2.5 gives an overview of the fundamental equations needed to describe electrostatic interactions, which are highly relevant to a large fraction of the presented results. In addition, the specific electrostatic properties of gas phase CO are discussed.

2.1 Structure and spectroscopy of CO adsorbed to NaCl(100)

Already early measurements of CO adsorbed to NaCl films led to the conclusion that CO preferentially binds to the Na^+ ions. [32] Due to the small dipole moment of ground state CO, a large fraction of the binding energy comes from the interaction between the quadrupole moment of CO and the electric field gradient of the NaCl surface, [32] whereas the orientation of the octopole moment defines the molecular orientation with

the carbon atom closer to the surface (C-down orientation). [33] In 1987, Ewing and co-workers reported the first absorption spectrum of CO on a single crystal NaCl(100) surface. [34] The infrared absorption spectra of CO on NaCl(100) at submonolayer, monolayer and multilayer coverages, measured by the groups of Ewing and Heidberg, will be introduced in the following, together with the corresponding adsorption structures.

Isolated $^{12}C^{16}O$ molecules are oriented perpendicular to the surface and show a vibrational frequency of $2159.9\,cm^{-1}$, which is blue-shifted from the gas phase value by $16.6\,cm^{-1}$. In addition, the isolated CO adsorbates show very narrow absorption lines ($0.05\,cm^{-1}$ at 11 K). [35] At submonolayer coverages, much broader absorption peaks are observed at slightly lower frequencies, which is attributed to islanding. [35–37]

At temperatures below ~35 K, the structure of the CO monolayer is characterized by a (2×1) unit cell with the plane group symmetry pg. [38, 39] A schematic representation of the (2×1) structure can be found in Fig. 1.1a. Here, the two CO molecules are tilted by about 25° with respect to the surface normal in opposite directions. In addition, the CO molecules are slightly displaced with respect to the glide plane. [40] Above ~35 K, a continuous phase transition to a (1×1) structure occurs, in which the CO molecules are oriented perpendicular to the surface. [36, 38, 39] The lattice constant of this (1×1) structure (3.96 Å) agrees well with the lattice constant of the lattice formed by the Na$^+$ ions on the NaCl(100) surface (3.99 Å), which indicates that each Na$^+$ adsorption site is occupied by a CO molecule. [39]

The polarized infrared absorption spectra of the CO monolayer at different temperatures are shown in Fig. 2.1 (taken from Ref. [36]). As a result of the (2×1) unit cell, two absorption peaks are observed at low temperatures. The high frequency peak at $2154.89\,cm^{-1}$ (at 6 K) corresponds to a symmetric, in-phase vibration of the two molecules in the unit cell and is observed only with p-polarized light. The low frequency peak at $2148.61\,cm^{-1}$ (at 6 K) corresponds to the asymmetric, out-of-phase vibration and is observed with both p- and s-polarized light. The polarization dependencies of the symmetric and asymmetric modes indicate transition dipole moments that are perpendicular and parallel to the surface, respectively. [36, 38] The frequency splitting between the two modes is a result of the collective vibrations of the molecules, which are coupled by dipole-dipole interactions (often referred to as exciton splitting, correlation field or Davydov splitting; [41, 42] see Section 2.4.3 for details). At high temperatures, the low-frequency peak disappears and only the high-frequency peak remains, corresponding to the symmetric mode in the (1×1) structure.

CO overlayers can be grown epitaxially on top of the CO monolayer because the mismatch between the lattice constant of the CO monolayer and that of the CO crystal is small. [43, 44] α-CO shows a cubic crystal structure with the space group symmetry
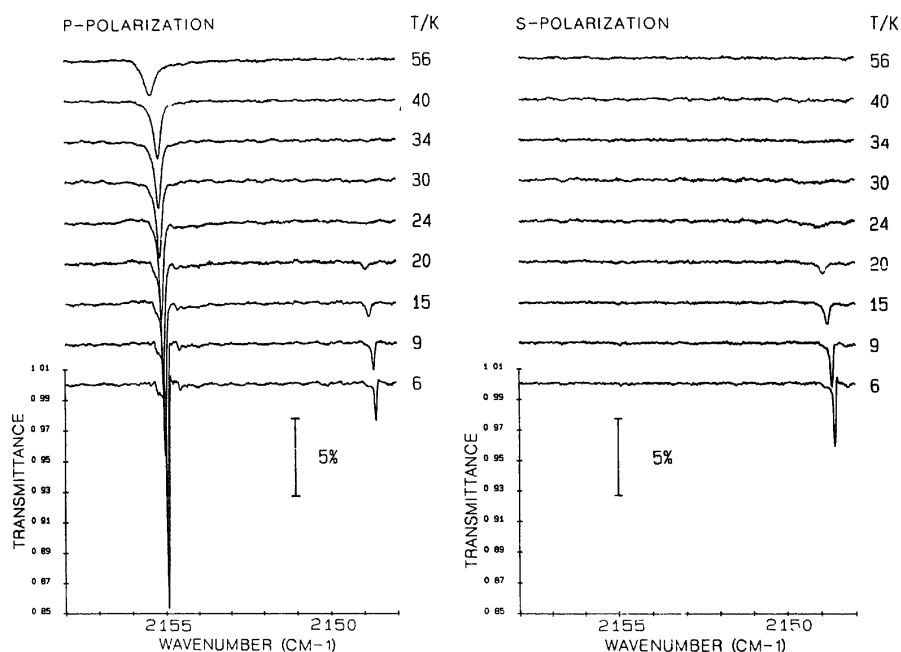
Figure 2.1: Polarized infrared absorption spectra of a $^{12}C^{16}O$ monolayer on NaCl(100) at an incidence angle of 50° and various temperatures. Reprinted from Ref. [36], Copyright 1992, with permission from Elsevier.

$P2_13$ and four molecules per unit cell. [43, 45] In this ideal structure, the lattice constant is 5.63 Å, the distance between two layers is thus ~2.82 Å, and the four CO molecules are oriented along the four space diagonals of the cube. [45] An excellent graphical representation of this idealized α-CO structure can be found in Ref. [45]. The exact orientation of the molecules is, however, randomized due to head-to-tail disorder. [46]

Whereas the spectrum of an α-CO crystal shows a single infrared absorption line, corresponding to a three-fold degenerate vibration, [47] the degeneracy is lifted for CO overlayer slabs with a thickness that is smaller than infrared wavelengths. [43, 48] Polarized infrared absorption spectra of CO overlayer samples of different thickness are shown in Fig. 2.2 (taken from Ref. [44]). Due to the symmetry of the thin slab, the overlayer shows two absorption lines. The transverse optical (TO) mode at 2138.9 cm^{-1}, which is two-fold degenerate, has a transition dipole moment parallel to the surface plane and is thus observed with both s- and p-polarization; the longitudinal optical (LO) mode at 2142.6 cm^{-1}, which is non-degenerate, has a transition dipole moment perpendicular to the surface and is thus only observed with p-polarization. [44]
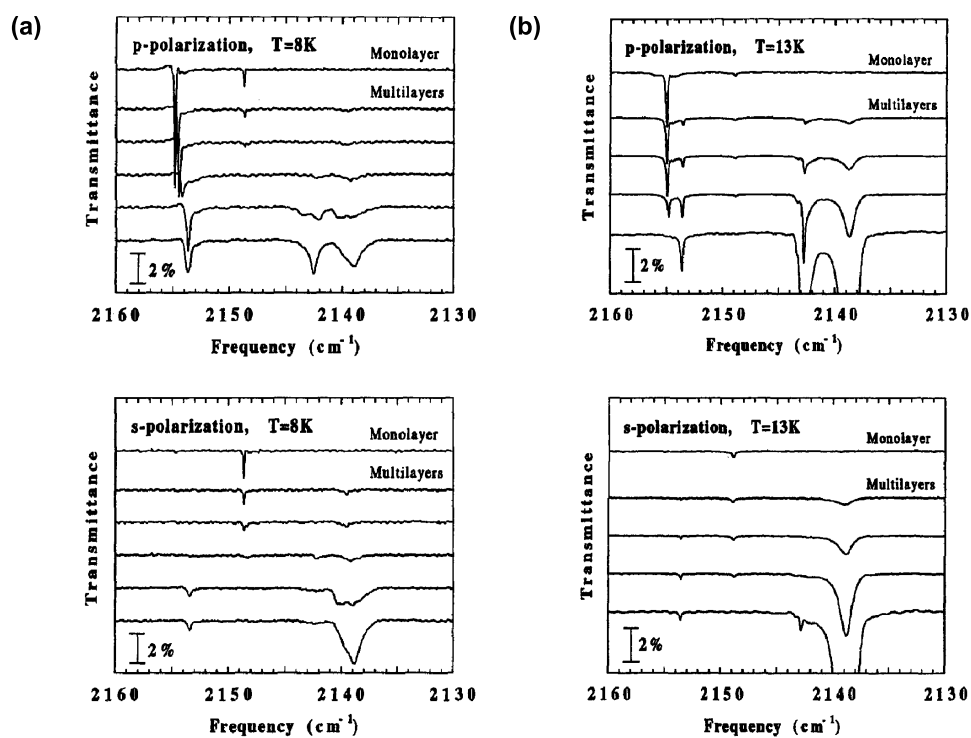
Figure 2.2: (a) Polarized infrared transmittance spectra of the $^{12}C^{16}O$ monolayer and $^{12}C^{16}O$ overlayers at 8 K. The coverages are 1 ML, 1.2 ML, 1.3 ML, 3.1 ML 9.3 ML, and 15.6 ML (from top to bottom). Reprinted from Ref. [44], Copyright 1993, with permission from Elsevier. (b) Polarized infrared transmittance spectra of the $^{12}C^{16}O$ monolayer and $^{12}C^{16}O$ overlayers at 13 K. The coverages are 1 ML, 3.5 ML, 5.8 ML, 16 ML, and 125 ML (from top to bottom). Reprinted from Ref. [44], Copyright 1993, with permission from Elsevier.

For dosing at 8 K, the peak of the symmetric mode of the monolayer shifts continuously from 2154.9 to 2153.6 cm^{-1}, while the peak of the asymmetric mode disappears. This is attributed to stochastic growth of the overlayers at 8 K (layer-by-layer growth). [44] For dosing at 13 K, the peaks of the bare monolayer (2154.9 cm^{-1}) and the buried monolayer (2153.6 cm^{-1}) coexist with varying ratios, depending on the number of overlayers. This is interpreted as the formation of 3D multilayer islands, such that bare monolayer and buried monolayer areas are present at the same time. [44]

2.2 Vibrational energy transfer at surfaces

This section gives an overview of the vibrational energy transfer processes relevant to adsorbed molecules. For diatomic molecules adsorbed on solid surfaces, two major vibrational energy transfer channels need to be considered: vibrational relaxation to the substrate and vibration-to-vibration (V-V) energy transfer between the molecules. Intramolecular vibrational energy redistribution (IVR) between different vibrational modes of the same molecule presents another important vibrational energy transfer channel for polyatomic molecules. [49] However, IVR will not be explicitly discussed because only vibrational energy transfer between CO molecules is investigated in this work.

Vibrational relaxation, in which the vibrational energy of the molecule is transferred to the substrate (see Eq. 2.1), is introduced in Section 2.2.1. In addition, two specific models for vibrational relaxation to phonons of the substrate are described.

$$CO(v = n) \longrightarrow CO(v = n - 1) \tag{2.1}$$
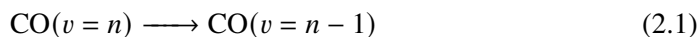
V-V energy transfer between the molecules (see Eq. 2.2) is introduced in Section 2.2.2. Furthermore, a theoretical model that describes V-V transfer in the CO/NaCl(100) system is presented.

$$CO(v = n) + CO(v = m) \longrightarrow CO(v = n + 1) + CO(v = m - 1) \tag{2.2}$$
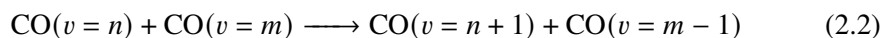
2.2.1 Vibrational relaxation

The lifetime of vibrationally excited molecules strongly depends on the substrate. Relaxation of CO in the first vibrationally excited state shows picosecond lifetimes on metal surfaces, [9, 10] nanosecond lifetimes on semiconductor surfaces (Si(100)), [12, 13] and millisecond lifetimes on insulator surfaces (NaCl(100)). [16] The fundamental

difference in the lifetimes is attributed to different vibrational relaxation mechanisms that occur on the various types of substrates. Generally, relaxation can occur via excitation of electronic degrees of freedom (DOFs) (electron-hole-pairs) of the substrate and excitation of vibrational DOFs (phonons and frustrated adsorbate motions[1]).

The short lifetimes on metal surfaces are typically explained by coupling between the molecular vibration and the electron-hole-pairs of the metal, which involves a breakdown of the Born-Oppenheimer approximation. A manifold of such electronically non-adiabatic effects has been reported for the interaction of small molecules with metal surfaces. [50] As a result, the vibrational lifetimes for CO chemisorbed to metal surfaces are extremely short (~2 ps). [9, 10] Even for CO physisorbed on Au(111), the vibrational lifetime is only 49 ps. [11] In this case, the longer lifetime is explained by the strong distance-dependence of coupling to electron-hole pairs. [11, 51] However, vibrational relaxation via electronic excitation of the NaCl crystal cannot occur because NaCl has a direct bandgap of ~9 eV [52] that is much larger than the typical energy of a vibrational quantum of CO (~0.25 eV). Similarly, coupling to electron-hole pairs is not possible for CO adsorbed on Si(100), due to the comparatively large bandgap of 1.12 eV at 300 K. [53] Therefore, electron-hole pair coupling will not be further discussed here. An overview of different models can be found in Ref. [54], for example.

Despite the different vibrational lifetimes of CO on NaCl(100) and Si(100), vibrational relaxation must occur via transfer to vibrational DOFs in both systems. Sakong *et al.* were able to reproduce the 2.3 ns lifetime of CO on Si(100) almost quantitatively by considering relaxation to four quanta of frustrated CO rotations and translations, and a single Si phonon. [55] The authors suggested that coupling to frustrated rotations and translations of CO is particularly effective due to the large frequencies of 400 to 500 cm^{-1}, attributed to the strong chemisorption bond between CO and Si(100). In addition, the highest phonon frequencies of the Si substrate are equally large (650 cm^{-1}). In summary, the short vibrational lifetime of CO on Si(100) can be explained by energy transfer to only four quanta of frustrated motion and the Si phonons. A similar explanation was used to explain the nanosecond vibrational lifetime of the covalent Si-H bond on hydrogen-covered Si(111) surfaces. [14, 15].

In contrast, the frequencies of the frustrated rotational and translational modes of CO on NaCl(100) are much lower (40 to 140 cm^{-1}). [56] The lower vibrational frequencies can be attributed to the weaker adsorbate-surface bond for CO physisorbed on NaCl(100) (20 kJ mol^{-1}). [21, 55] Therefore, relaxation of CO on NaCl(100) is expected to occur exclusively via multiphonon relaxation since the NaCl phonon frequencies are higher than

---

[1] Low-frequency vibrations of the adsorbate that correspond to frustrated rotations and translations.

the frequencies of the frustrated modes (Debye frequency of $223\,\mathrm{cm}^{-1}$ [57]). However, at least 10 phonons are required for $v = 1 \rightarrow 0$ relaxation of $^{12}\mathrm{C}^{16}\mathrm{O}$, which makes vibrational relaxation on NaCl(100) less efficient compared to relaxation on Si(100).

Corcelli and Tully developed a quantum mechanical model for multiphonon relaxation in the CO/NaCl(100) system. [57, 58]. On the other hand, Ewing and coworkers proposed that their measurements of the total fluorescence decay of vibrationally excited CO on NaCl(100) is consistent with a vibrational relaxation model based on classical electrodynamics, which was developed by Chance, Prock and Silbey. [16, 59] However, no vibrational state-resolved experiments, which could test the predictions of the two models, have been reported so far. Chapter 4 provides an analysis of the first vibrational state-resolved measurements in the CO/NaCl(100) system and therefore the two models are presented in the following.

Anharmonic adsorbate-surface coupling

Corcelli and Tully developed a theory for multiphonon relaxation rate constants in the CO/NaCl(100) system, [57, 58] based on the theory by Egorov and Skinner derived for solid crystals. [60] This model will be referred to as the Skinner-Tully (ST) model in the following and it describes the rate constant of the relaxation process in Eq. 2.3. The full derivation of the relaxation rate constant expressions can be found in Refs. [57] and [58]. Here, I will only outline the most important steps of that derivation.

$$\mathrm{CO}(n) \xrightarrow{k_n} \mathrm{CO}(n-1) \tag{2.3}$$

The Hamiltonian of the coupled adsorbate-surface system is given by Eq. 2.4, where $\hat{H}_\mathrm{S}$, $\hat{H}_\mathrm{B}$ and V refer to the Hamiltonian of the unperturbed CO molecule, the Hamiltonian of the phonon bath and the anharmonic CO-bath coupling, respectively.

$$\hat{H} = \hat{H}_\mathrm{S} + \hat{H}_\mathrm{B} + V. \tag{2.4}$$

The unperturbed CO molecule, oriented perpendicular to the surface, is modeled as a Morse oscillator:

$$\hat{H}_\mathrm{S} = \frac{p^2}{2\mu} + D\left[\exp(-2\alpha x) - 2\exp(-\alpha x)\right]. \tag{2.5}$$

Here, p is the momentum operator and $\mu = m_\mathrm{C} m_\mathrm{O}/(m_\mathrm{C} + m_\mathrm{O})$ is the reduced mass of CO. D desribes the well depth of the Morse potential and α is a width parameter. $x = r - r_e$

represents the displacement of the CO bond length, r, from its equilibrium position, r_e. The energy eigenvalues, E_n, can be written in terms of D and a dimensionless parameter, $B^2 = \hbar^2 \alpha^2 / (2\mu D)$:

$$E_n = 2DB\,(n + 1/2) - DB^2\,(n + 1/2)^2\,. \tag{2.6}$$

Note that this expression is equivalent to the standard spectroscopic notation based on the harmonic frequency, ω_e, and anharmonicity constant, $\omega_e x_e$:

$$E_n = hc\left[\omega_e\,(n + 1/2) - \omega_e x_e\,(n + 1/2)^2\right]\,. \tag{2.7}$$

Therefore, the energy that is dissipated to the phonon bath in Eq. 2.3 is given by:

$$\Delta E_n = \hbar\omega_n = E_n - E_{n-1}\,. \tag{2.8}$$

The phonon bath is described as an ensemble of harmonic oscillators with angular frequencies ω_α:

$$\hat{H}_{\text{B}} = \sum_\alpha \hbar\omega_\alpha\left(b_\alpha^\dagger b_\alpha + 1/2\right)\,. \tag{2.9}$$

Here, $b_\alpha^\dagger$ and b_α are creation and annihilation operators for a phonon of frequency ω_α. A collective phonon coordinate, z, can be defined, which describes the motion of the Na atom underneath the CO molecule perpendicular to the surface. The collective phonon coordinate can be related to a weighted phonon density of states (DOS), $\Gamma(\omega)$. For the ST model, Corcelli and Tully assumed a Debye DOS coupled with the deformation potential approximation:

$$\Gamma(\omega) = \begin{cases} \lambda\frac{4\omega^3}{\omega_{\text{D}}^4} & 0 \le \omega \le \omega_{\text{D}} \\ 0 & \omega > \omega_{\text{D}}. \end{cases} \tag{2.10}$$

Here, λ is an empirical coupling parameter with values between 0 and 1 that captures the average coupling strength between the CO vibration and the substrate phonons. ω_D is the angular Debye frequency.

To achieve coupling between the adsorbate vibration and the phonon bath, the adsorbate-surface coupling, V, must include the CO vibrational coordinate, x, and the collective phonon coordinate, z. In the ST model, the adsorbate-surface interaction potential is also described by a Morse potential, where D' and α' are the corresponding well depth and width parameter, respectively. It depends on the displacement, $x' = m_{\text{O}}/(m_{\text{O}} + m_{\text{C}})x - z$,

which is related to the relative distance between the carbon atom and the Na atom underneath, while the center-of-mass position of the CO molecule is assumed to be fixed: [57]

$$V = D' \left[\exp(-2\alpha'x') - 2\exp(-\alpha'x') \right]. \tag{2.11}$$

Taylor expansion of V round $x' = 0$ gives:

$$V \approx \sum_{p=1}^{\infty} \frac{f_p}{p!} xz^p = \sum_{p=1}^{\infty} V^{(p)}. \tag{2.12}$$

The xz^p coupling terms result in single-quantum relaxation of the CO vibration via excitation of p phonons (p-phonon processes). Higher-order terms in x, which would correspond to multi-quantum relaxation of the CO vibration, are neglected in Eq. 2.12. Based on the expression for the anharmonic adsorbate-surface coupling in Eq. 2.12 and Fermi's golden rule, Corcelli and Tully arrive at the following expression[2] for the vibrational relaxation rate constants, k_n^{ST}:

$$k_n^{\mathrm{ST}} = \sum_{p=p_{\min}}^{p_{\max}} k_n^{(p)}, \tag{2.13}$$

$$k_n^{(p)} = \frac{1}{\hbar} \left| \langle n|x|n-1 \rangle \right|^2 \left[n\left(\frac{\Delta E_n}{p} \right) + 1 \right]^p \frac{f_p^2 I_p}{\Delta E_n p!}, \tag{2.14}$$

$$n(\Delta E) = \left(\exp\left(\frac{\Delta E}{k_{\mathrm{B}} T} \right) - 1 \right)^{-1}, \tag{2.15}$$

$$f_p = (-1)^p (2^{p+1} - 2) D' \alpha'^{p+1} a_0^p \frac{m_{\mathrm{O}}}{m_{\mathrm{O}} + m_{\mathrm{C}}}, \tag{2.16}$$

$$I_p \approx \lambda^p \frac{\Delta E_n}{\hbar \omega_{\mathrm{D}}} \sqrt{\frac{75\pi}{p}} \exp\left[-\frac{75}{4p} \left(\frac{\Delta E_n}{\hbar \omega_{\mathrm{D}}} - \frac{4p}{5} \right)^2 \right]. \tag{2.17}$$

The matrix elements, $\langle n|x|n-1 \rangle$, can be calculated analytically for a Morse oscillator according to Eq. 2.42. $k_n^{(p)}$ represent individual contributions from p-phonon processes. The summation in Eq. 2.13 runs from the minimum number of phonons, $p_{\min}$, needed to dissipate the energy, ΔE_n, and is typically truncated at a maximum number of phonons, $p_{\max}$. The corresponding p-phonon integral, I_p, was evaluated analytically

---

[2] Note that the equations above are written in SI units by adding $\hbar$ and the Bohr radius a_0 at appropriate positions, whereas Corcelli and Tully used atomic units in Refs. [57] and [58]. As pointed out in Ref. [61], there are two typographical errors in the equations presented in Ref. [57]; however, Ref. [58] contains the correct equations.

by Corcelli and Tully for the Debye DOS, $\Gamma(\omega)$. In first approximation, I_p decreases exponentially with increasing ΔE_n, which is consistent with the energy gap law for vibrational relaxation. [60] Relaxation according to the ST model mainly depends on the parameters of the adsorbate-surface interaction potential, D' and α', and the coupling strength parameter, λ. D' and α' can be extracted from the measured adsorption energy and the frequency of the frustrated translation of CO on NaCl. [57] λ, on the other hand, is the only adjustable parameter.

Coupling via the near-field of an emitting dipole

In contrast to the ST model, which is based on quantum-mechanical perturbation theory, vibrational relaxation can also occur via a mechanism based on classical electrodynamics. The corresponding theory was developed by Chance, Prock and Silbey (CPS) [59, 62–64] to describe the pioneering experiments by Kuhn and Drexhage. [65, 66] In those experiments, monolayers of dye molecules were prepared at controlled distances from a metal surface, d, and the fluorescence lifetime was measured as a function of distance. For distances on the order of the emission wavelength ($d \approx 1000\,\text{Å}$), they found that the dependence of the fluorescence lifetime on d shows an oscillatory pattern. Kuhn and Drexhage successfully interpreted the modulation of the fluorescence lifetime as an interference effect between the electromagnetic wave emitted by a classical, oscillating dipole and its own reflection at the metal surface. [67, 68] However, they were not able to quantitatively describe the rapid decrease in the lifetime at small distances ($d \to 0$) because they only considered the far-field of the dipole, which is responsible for radiative relaxation (fluorescence).

For a correct description at short distances, non-radiative energy transfer to the surface via the near-field of the oscillating dipole must be considered. The CPS model, which had its origin in Sommerfeld's description of the propagation of radio waves along the surface of the Earth, [69] provides an exact description within the framework of classical electrodynamics and can describe the short-range behavior correctly. [62–64] Furthermore, the CPS model is not limited to metal surfaces or electronic relaxation but can also be applied to dielectric interfaces and vibrational relaxation. [70, 71] The result obtained for the non-radiative relaxation rate constants will be given in the following. A comprehensive review of the CPS theory can be found in Ref. [59]. Additionally, Ref. [72] provides an excellent review for a more qualitative understanding of the CPS relaxation mechanism.

In the limit of $d \to 0$, the following analytical expression can be used to calculate the

non-radiative relaxation rate, k_{nr}^{CPS}, according to the CPS model: [59]

$$\frac{k_{nr}^{CPS}}{k_{fl}} = \frac{\lambda^3 q \theta \varepsilon_1 n_2 \kappa_2}{8\pi^3 \left|\varepsilon_1 + \varepsilon_2\right|^2 d^3}.$$

(2.18)

In Eq. 2.18, the CPS rate constant is given relative to the fluorescence rate constant of the gas phase molecule, k_{fl}. λ is the corresponding emission wavelength. The molecules are located in a non-absorbing medium, which is characterized by the real dielectric constant $\varepsilon_1 = n_1^2$; in this case, the non-absorbing medium is vacuum ($\varepsilon_1 = 1$). The half-space of the absorbing surface is represented by the complex dielectric constant $\varepsilon_2 = (n_2 + i\kappa_2)^2$, where n_2 and κ_2 are the real and imaginary parts of the complex index of refraction, respectively. θ is an orientation factor with values of 1.5 and 0.75 for perpendicular and parallel oriented dipoles, respectively. q represents the quantum yield for radiative relaxation versus thermal quenching of the fluorescence. For vibrationally excited diatomic molecules, q is assumed to be 1, since no relevant quenching channels exist that could compete with fluorescence. Even for fluorescence of excited dye molecules, the experimentally determined quantum efficiencies do not differ much from unity. [59]

Under the given assumptions, the final expression for vibrational relaxation according to the CPS model is given by Eq. 2.19, where $\tilde{\nu} = 1/\lambda$ is the emission wavenumber.

$$\frac{k_{nr}^{CPS}}{k_{fl}} = \frac{\theta n_2 \kappa_2}{8\pi^3 \tilde{\nu}^3 \left|1 + \varepsilon_2\right|^2 d^3}.$$

(2.19)

The CPS relaxation rates are significantly enhanced in the case of resonances with surface plasmons for metal surfaces [70, 72] and surface polaritons for dielectric surfaces [71]. A similar effect is expected for bulk excitations. The NaCl bulk resonance that is closest to the emission wavelength of CO ($\sim$4.7 μm for $v = 1$) is an optical phonon resonance at $\lambda = 60.98$ μm. The small extinction coefficient at 4.7 μm, $\kappa = 1.7 \times 10^{-9}$, can be partially attributed to the wing of this resonance, which is broadened by multiphonon damping. [73] Therefore, both the CPS model and the ST model rely on multiphonon relaxation for the NaCl substrate. However, relaxation is mediated by dipole-dipole coupling to optical phonons in the CPS model, whereas it is mediated by anharmonic coupling between the adsorbate and the surface via the surface bond in the ST model.

2.2.2 Vibrational energy pooling

In 1968, Treanor *et al.* proposed that vibrational population inversion can be achieved for an ensemble of anharmonic oscillators via the following V-V energy transfer

processes: [74]

$$CO(v = n) + CO(v = m) \longrightarrow CO(v = n + 1) + CO(v = m - 1). \qquad (2.20)$$
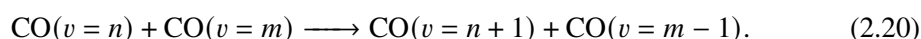
These V-V transfer processes involve an energy mismatch due to the anharmonicity of the CO oscillators, which has to be transferred to translational or rotational DOFs of the molecules during a collision. For low translational temperatures, Treanor *et al.* showed that the increasing anharmonicity greatly favors energy transfer to higher vibrational states, which results in highly non-thermal vibrational population distributions. This process is referred to as vibrational energy pooling (VEP) because individual molecules collect or "pool" vibrational quanta at the expense of other molecules.

Rich *et al.* were the first to observe the predicted vibrational population inversion experimentally in 1975. [75] By exciting a CO/Ar mixture with a continuous-wave (cw) CO laser, they were able to detect dispersed infrared fluorescence from a manifold of highly vibrationally excited states up to $v = 30$. In the following years, VEP has been extensively studied in gas phase CO and NO, [76–79] matrix-isolated CO, [80, 81], α-CO crystals, [82, 83] and CO dissolved in liquid Ar. [84] Most of these experiments relied o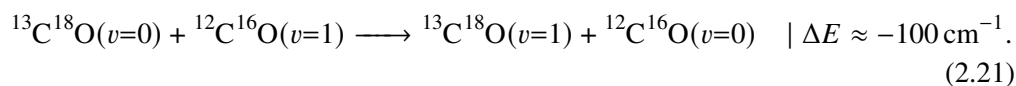n the detection of infrared fluorescence from the excited vibrational states. Through VEP, CO molecules could be pumped to vibrational states up to $v = 40$ (approx. 8.1 eV of internal vibrational energy), which is likely limited by vibration-to-electronic (V-E) transfer to electronically excited states of CO [79] and larger vibration-to-translation (V-T) transfer rates. [74] Also the formation of reaction products has been observed; this includes C_2, CN and CO_2 produced in CO/Ar and CO/N_2/Ar mixtures, [76, 85, 86] and NO_2 produced in NO/Ar mixtures. [78]

In CO samples that contain isotopic impurities, vibrational energy is preferentially transferred to the heavy isotopologues with lower vibrational frequencies even if isotopologues with higher vibrational frequencies are excited. As a result, increased emission yields compared to the abundance of the isotopologues can be observed experimentally. This effect has been observed in most VEP studies in gas phase CO, [76, 77, 86] matrix-isolated CO, [80, 81] and CO crystals. [27, 83] It can be rationalized by considering the energy transfer from a $^{12}C^{16}O$ molecule in $v = 1$ to a heavier $^{13}C^{18}O$ isotopologue in $v = 0$:

$$^{13}C^{18}O(v{=}0) + {}^{12}C^{16}O(v{=}1) \longrightarrow {}^{13}C^{18}O(v{=}1) + {}^{12}C^{16}O(v{=}0) \quad | \ \Delta E \approx -100\,\text{cm}^{-1}.$$
$$(2.21)$$

Because the V-V energy transfer process from $^{12}C^{16}O$ to $^{13}C^{18}O$ is energetically favored, preferential energy transfer to the heavier isotopologues is expected, similar to the

preference for the population of higher vibrational states according to see Eq. 2.20, due to their lower vibrational frequencies. In Chapter 6, I will show that this effect can be utilized to achieve controlled, directed vibrational energy transport.

Despite the number of VEP experiments conducted in the gas phase and the solid state, little is known about VEP of adsorbed molecules. As mentioned in Chapter 1, the only clear observation of VEP in an adsorbate layer was made by Ewing and co-workers by measuring the total fluorescence of a CO/NaCl(100) monolayer. [16] However, no dispersed fluorescence measurements have been reported so far. This is likely attributed to the much higher sensitivity needed for detecting infrared fluorescence from a single adsorbate layer compared to the larger detection volumes in matrix and gas phase samples.

Despite the lack of vibrational state-resolved experiments, Corcelli and Tully derived rate constant equations for V-V energy transfer and vibrational relaxation in order to model the undispersed fluorescence experiments in Ref. [16] with kinetic Monte Carlo (KMC) simulations. [57, 87]. The theory for V-V energy transfer developed by Corcelli and Tully is presented in the following section. The KMC simulations were restricted to nearest-neighbor interactions between the CO molecules and modeled the phonon bath with a Debye DOS, which accepts the excess energy. One of their key findings was that the highest frequency of the phonon DOS determines the shape of the vibrational distribution. They predicted that VEP stops at $v = 10$ to 11, because the excess energy associated with nearest-neighbor energy transfer for these states cannot be dissipated to a single phonon anymore. Similar KMC simulations were performed to model VEP after excitation with intense free-electron laser radiation. [61] Under these extreme excitation conditions, the chance of finding two interacting nearest-neighbor molecules in high vibrational states is significantly increased, leading to much higher vibrational excitation (up to $v = 32$). Another approach to explain the single exponential decay in the experiments of Ref. [16] was based on a quasi-equilibrium between all vibrational states such that all states decay with the same rate constants. [88] However, this approach requires that all V-V transfer processes are much faster than vibrational relaxation, which may be questionable.

Vibrational energy pooling in adsorbates

To calculate the rate constants for the V-V energy transfer process in Eq. 2.22, Corcelli and Tully used a similar approach as for the derivation of the vibrational relaxation rate constants presented in Section 2.2.1. Again, the full derivation can be found in Refs. [57]

and [58] and only the most important aspects are outlined in the following.

$$CO(n) + CO(m) \xrightarrow{k_{nm}} CO(n{+}1) + CO(m{-}1) \tag{2.22}$$
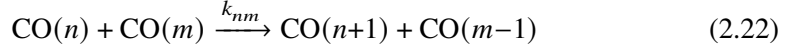
The Hamiltonian of the two CO molecules molecules is described by two independent Morse oscillators with displacements x_1 and x_2, similar to Eq. 2.5:

$$\begin{aligned}
\hat{H}_S ={}& \frac{p_1^2}{2\mu} + D\left[\exp(-2\alpha x_1) - 2\exp(-\alpha x_1)\right] \\
&+ \frac{p_2^2}{2\mu} + D\left[\exp(-2\alpha x_2) - 2\exp(-\alpha x_2)\right].
\end{aligned} \tag{2.23}$$

The two CO molecules are characterized by vibrational quantum numbers n and m. The corresponding energy eigenvalues are E_n and E_m, as in Eqs. 2.6 and 2.7. The excess energy in Eq. 2.22, which is accepted by the phonon bath, is therefore given by:

$$\Delta E_{nm} = \hbar\omega_{nm} = E_n + E_m - E_{n+1} - E_{m-1} \tag{2.24}$$

Note that ΔE_{nm} is defined such that it is positive when energy transfer is energetically favored. The Hamiltonian of the phonon bath is described by a sum of two independent collections of phonons, similar to Eq. 2.9:

$$\hat{H}_B = \sum_\alpha \hbar\omega_\alpha \left(b_{1\alpha}^\dagger b_{1\alpha} + b_{2\alpha}^\dagger b_{2\alpha} + 1\right). \tag{2.25}$$

Two collective phonon coordinates, y_1 and y_2, describe the motion of the two Na atoms underneath the CO molecules within the surface plane. y_1 and y_2 can be related to a normalized phonon DOS, $\rho(\omega)$. Although Corcelli and Tully assumed the normalized Debye DOS in Eq. 2.26, any normalized phonon DOS can be used in principle.

$$\rho(\omega) = \begin{cases} 3\dfrac{\omega^2}{\omega_D^3} & 0 \le \omega \le \omega_D \\ 0 & \omega > \omega_D. \end{cases} \tag{2.26}$$

The adsorbate-bath coupling term, V, must account for the coupling between the two CO vibrations and the phonon bath. The dominant coupling between the two CO molecules, oriented perpendicular to the surface, is dipole-dipole coupling:

$$V = \frac{\mu_1(x_1)\mu_2(x_2)}{4\pi\varepsilon_0 R^3}. \tag{2.27}$$

Here, $\mu_1(x_1)$ and $\mu_2(x_2)$ are the electric dipole moment functions (EDMFs) of the two CO molecules, which can be approximated by a linear function, $\mu(x) = \mu(0) + \mu'x$ (see also Section 2.5.3). μ' is the derivative of the EDMF at $x = 0$. $R = R_0 + y$ is the momentary intermolecular distance between the center-of-mass positions of the CO molecules. To model the coupling to the phonon motion, the equilibrium distance between the molecules (R_0) is modulated by the relative motion of the two Na atoms underneath the CO molecules ($y = y_1 - y_2$).[3] Therefore, Eq. 2.27 becomes:

$$V = \frac{\mu'^2 x_1 x_2}{4\pi\varepsilon_0 (R_0 + y)^3}.$$
(2.28)

Here, all terms that do not contain the product $x_1 x_2$ and therefore do not include coupling between the CO molecules were neglected. Equation 2.28 is then expanded into a Taylor series in y:

$$V = \frac{\mu'^2 x_1 x_2}{4\pi\varepsilon_0 R_0^3} + \sum_{p=1}^{\infty} f_p x_1 x_2 y^p.$$
(2.29)

The first term in Eq. 2.29 does not depend on y and is responsible for resonant V-V energy transfer between the CO molecules. Based on this coupling term, Corcelli and Tully derived the following expression for the resonant rate constants:

$$k_{n,n+1} = \frac{\mu'^2 |\langle n+1|x|n\rangle|^2}{\hbar \arccos(e^{-1/2}) 4\pi\varepsilon_0 R_0^3}.$$
(2.30)

Most importantly, the resonant rate constants are proportional to R_0^{-3} and to the square of the transition dipole moment of the $n \rightarrow n+1$ transition ($\mu'\langle n+1|x|n\rangle$).

The second term in Eq. 2.29 is responsible for non-resonant energy transfer, where the individual $x_1 x_2 y^p$ terms involve dissipation to p phonons. Based on this non-resonant coupling term and Fermi's golden rule, Corcelli and Tully arrived at the following

---

[3] In principle, motion in the two perpendicular directions also give a modulation of the intermolecular distance. However, the modulation by the parallel y component has the largest effect.

equations[4] for the non-resonant V-V transfer rate constants, k_{nm}:

$$k_{nm} = \sum_{p=1}^{p_{\max}} k_{nm}^{(p)}, \tag{2.31}$$

$$k_{nm}^{(p)} = \frac{2\pi}{\hbar} p! f_p^2 2^p \, |\langle n+1|x|n\rangle|^2 \, |\langle m-1|x|m\rangle|^2 \left(\frac{(n(\Delta E_{nm}/p) + 1)\hbar}{2m_{\mathrm{Na}}}\right)^p I_p, \tag{2.32}$$

$$n(\Delta E) = \left(\exp\left(\frac{\Delta E}{k_{\mathrm{B}}T}\right) - 1\right)^{-1}, \tag{2.33}$$

$$f_p = (-1)^p \frac{\mu'^2 (p+1)(p+2)}{8\pi\varepsilon_0 R_0^{p+3}}, \tag{2.34}$$

$$I_p = \int_0^\infty \mathrm{d}\omega_1 \cdots \int_0^\infty \mathrm{d}\omega_p \frac{\rho(\omega_1)}{\omega_1} \cdots \frac{\rho(\omega_p)}{\omega_p} \frac{\delta(\omega_{nm} - \omega_1 - \cdots - \omega_p)}{\hbar}. \tag{2.35}$$

$k_{nm}^{(p)}$ represents the contribution from a p-phonon process. The summation is typically truncated at a maximum number of phonons, $p_{\max}$, because processes that involve a small number of phonons are most effective. The rate constants depend critically on the p-phonon integral, I_p, which can be evaluated numerically for any given DOS normalized in angular frequency units. Furthermore, the rate constants depend on the squared transition dipole moments of the $n \to n+1$ and $m \to m-1$ transitions ($\mu'\langle n+1|x|n\rangle$ and $\mu'\langle m-1|x|m\rangle$, respectively). Another important result is that the rate constant of a one-phonon process, $k_{nm}^{(1)}$, is proportional to R^{-8} and therefore strongly distance-dependent.

2.3 Infrared laser-induced fluorescence spectroscopy

Laser-induced fluorescence (LIF) in the ultraviolet-visible (UV-Vis) spectral range has become a standard tool with applications in spectroscopy, combustion kinetics, biological microscopy and other fields. [89] In infrared laser-induced fluorescence (IR-LIF), fluorescence from purely vibrational transitions instead of electronic transitions is detected. But despite the fact that vibrational frequencies provide valuable information about the molecular environment, IR-LIF is less commonly used. The challenges associated with infrared fluorescence detection are mainly related to the low sensitivity of

---

[4] Note that the equations above are written in SI units by adding $\hbar$ and $4\pi\varepsilon_0$ at appropriate positions, whereas Corcelli and Tully used atomic units in Refs. [57] and [58]. Also note that there is a missing factor 2 in Ref. [57]; however, Ref. [58] contains the correct equations.

conventional infrared detectors, smaller emission rates and larger background compared to UV-Vis fluorescence detection. These three points are discussed in the following.

One of the greatest advantages of LIF is its great sensitivity compared to absorption spectroscopy. [89] While small changes in large signals are measured in absorption spectroscopy, typically individual photons are detected against an ideally absent background in LIF. In the UV-Vis region, highly sensitive single-photon detectors exist, such as photomultiplier tubes, allowing for measurements with high signal-to-noise ratios (SNRs). [30] SNSPDs are similarly promising single-photon detectors for infrared applications and are introduced in Section 2.3.1. If the SNR is only limited by photon shot noise, which is due to the fundamental fluctuation in the number of detected photons, the photon counts follow a Poisson distribution and the noise is given by the square root, $\sqrt{N}$, of the total number of detected photons in the observed time window, N. [90] Discriminating between signal counts, S, and unwanted background counts, BG, the SNR can be written as:

$$\text{SNR} = \frac{S}{\sqrt{S + BG}}.$$

(2.36)

Equation 2.36 emphasizes the sensitivity of single photon counting when the background is small compared to the signal. In this case, the SNR increases with $\sqrt{S}$ and can therefore simply be improved by increasing the measurement time.

Generally, much less photons are emitted in vibrational transitions compared to electronic transitions. The rate for fluorescence from an upper state n into a lower state m is given by the Einstein A coefficient: [91]

$$A_{nm} = \frac{16\pi^3 \tilde{\nu}_{nm}^3}{3\varepsilon_0 h} \left| \mu_{nm} \right|^2.$$

(2.37)

where $\tilde{\nu}_{nm}$ is the emission wavenumber, μ_{nm} is the transition dipole moment, ε_0 is the vacuum permittivity, and h is the Planck constant. Due to the cubic dependence on the emission wavenumber, the rates of vibrational transitions are at least 1000 times lower than the rates of electronic transitions, for which the emission frequencies are about one order of magnitude higher.

The reduction of background photons in the mid-infrared region, which are emitted by any room temperature object, is much harder to eliminate than visible photon background. It can, however be accomplished through shielding the optical path with cryogenically cooled surfaces. For demonstration purposes, consider the spectral radiance (in units of

$W\,cm^{-2}\,nm^{-1}\,sr^{-1}$) of a black body, which is given by Planck's law:[5] [92]

$$L_e(\lambda,T) = \frac{c}{4\pi}\rho(\lambda) = \frac{2hc^2}{\lambda^5}\frac{1}{\exp\left(\frac{hc}{\lambda k_B T}\right) - 1}. \tag{2.38}$$

For single photon counting, it is useful to divide the spectral radiance in Eq. 2.38 by the photon energy to obtain the spectral photon radiance (in units of photons $s^{-1}\,cm^{-2}\,nm^{-1}\,sr^{-1}$), which describes the photon flux into a solid angle emitted by a given area in a small wavelength region:

$$L_q(\lambda,T) = L_e(\lambda,T)\frac{\lambda}{hc}. \tag{2.39}$$

The spectral photon radiance curves for a black body at room temperature and different cryogenic temperatures are shown in Fig. 2.3. With decreasing temperature, the number of emitted photons is significantly reduced and the spectrum shifts to longer wavelengths (note the double-logarithmic scale). At 10 and 40 K, temperatures that can be achieved with helium cryostats, almost no photons are emitted at wavelengths below 10 µm, making those ideal temperatures for mid-infrared emission experiments. Also at 80 K, a temperature that can be achieved with liquid nitrogen cryostats, the number of background photons is suppressed reasonably well compared to a surface at room temperature.

2.3.1 Superconducting nanowire single-photon detectors

Superconducting nanowire single-photon detectors (SNSPDs) are one of the most promising single-photon detectors for infrared applications and are used in the present work. Therefore, the current section will focus on a basic introduction to SNSPDs, including their operating principle and recent advances in the development of SNSPDs that are made of amorphous tungsten silicide (a-$W_x Si_{1-x}$). An overview of other infrared single photon detectors, such as single photon avalanche photodiodes or superconducting transition edge sensors, can be found in Ref. [30]

 SNSPDs feature a very thin (~5 nm) superconducting wire with a width on the order of ~100 nm. To increase the filling factor and the efficiency for photon absorption, they are typically manufactured in a meander geometry inside an optical cavity. [93] They can show fast temporal response down to a few picoseconds, [94] operate at count rates as high as 1×10^7 photons/s, [95] and show system detection efficiencies[6] of up to 98 %

---

[5] Note that $\rho(\lambda) = \rho(\nu)c/\lambda^2$. Also note that the spectral radiance of a real emitter will be generally reduced compared to that of an ideal black body.

[6] The system detection efficiency not only includes the internal quantum efficiency of the SNSPD but also
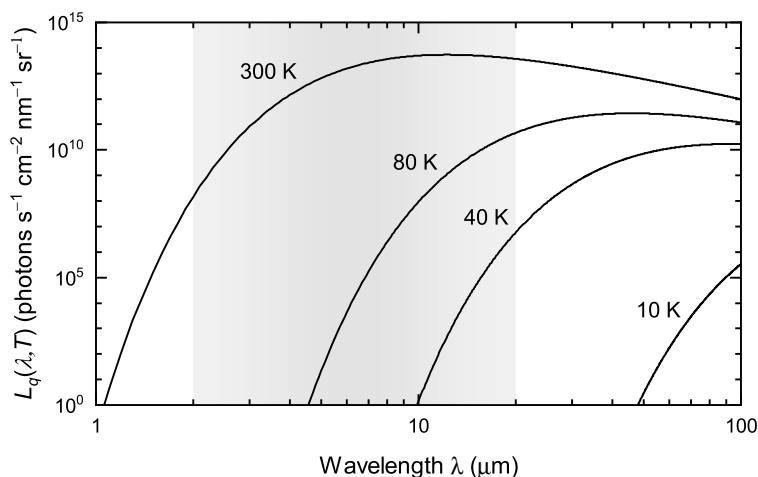
Figure 2.3: Spectral photon radiance of a black body as a function of the wavelength at room temperature and different cryogenic temperatures. The shaded area indicates a wavelength region between 2 and 20 μm that covers the fundamental and overtone vibrational transitions of most molecules.

at 1550 nm. [96]

The basic operating mechanism of a SNSPD is shown in Fig. 2.4. [28, 29] During operation, the detector is held below its critical temperature in a superconducting state. In addition, a constant bias current is applied, which is close to the critical current (switching current), where the SNSPD switches to the normal-conducting state. When a photon is absorbed on the detector, it has a chance to locally break the superconductivity and create a resistive hotspot (panel a), which then extends due to electron diffusion out of the hotspot region (panel b). Due to the finite resistance of the hotspot, the current density around the spot also increases above the critical current density, leading to growth of the non-superconducting region (panel c) until it extends across the whole width of the nanowire (panel d). The resulting voltage pulse across the wire can be amplified and detected. After that, the superconducting state is recovered on the order of 100 ns (dead time) before detection of another photon becomes possible. The dead time determines the decay time of the voltage pulses and depends on the length and cross-sectional area of the nanowire. [29] It is immediately clear from the hotspot mechanism that the photon detection efficiency increases the closer the bias current is to the critical current and the

---

the losses due to optical coupling and the absorption of the incident photons

higher the photon energy is.[7]
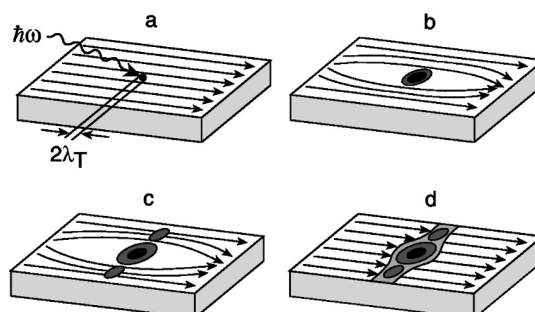
Figure 2.4: Schematic operating principle of a SNSPD for the detection of a single photon. Arrows indicate the current density due to the applied bias current. $2\lambda_T$ indicates the size of the hotspot formed by a photon with energy $\hbar\omega$. Reprinted from Ref. [28], with the permission of AIP Publishing.

While early SNSPDs were made of polycristalline NbN [28], nanowires made of amorphous a-W_xSi_{1-x} produce larger hotspots, and therefore wider nanowires can be built. [97] In addition, WSi nanowires can be operated at relatively high temperatures,[8] due to the large critical temperature of about 3.5 K. [98, 99] The first application of a WSi-SNSPD (size: 16 µm × 16 µm) for infrared spectroscopy was reported by Wodtke and co-workers. [31] More recently, a significantly larger kilo-pixel array made of WSi-SNSPDs with an active area of 0.96 mm × 0.96 mm and almost saturated detection efficiency for 1550 nm was demonstrated. [100] The possibility of producing large SNSPD arrays could potentially lead to more widespread applications of SNSPDs in physical chemistry in the future.

2.3.2 The rate of spontaneous emission

Knowledge of the vibrational state dependence of the rate constants for spontaneous emission, $k_{fl}(v)$, is incredibly useful. One can, for example, derive the population of individual vibrational states, $P(v)$, from experimental emission intensities, $I(\lambda_v)$,

---

[7] See, for example, the Supporting Information of Ref. [31].

[8] Although Refs. [98, 99] show that a-W_xSi_{1-x} SNSPDs perform well even at 2 to 2.5 K for 1550 nm wavelengths, operation at lower temperatures below 1 K is still recommended for larger wavelengths.

observed at the corresponding emission wavelengths, λ_v, according to:

$$P(v) = \frac{I(\lambda_v)}{k_{\mathrm{fl}}(v)}. \tag{2.40}$$

As mentioned in Section 2.3, the fluorescence rate constants are generally described by the Einstein A coefficients in Eq. 2.37. While the emission wavenumbers can be directly extracted from the emission spectra, the transition dipole moments are usually less well known. Assuming a linear electric dipole moment function (EDMF) (see also Section 2.5.3), the transition dipole moment for vibrational transitions can be written as:

$$\mu_{nm} = \mu' \langle m|x|n \rangle . \tag{2.41}$$

Here, n and m denote the quantum numbers of the upper and lower vibrational states, respectively. μ' is the derivative of the EDMF. The matrix elements, $\langle m|x|n \rangle$, can be calculated analytically for a Morse oscillator, [101] which serves as a reasonably accurate model for the vibration of CO—even for the high vibrational states relevant to the present work. For the $n \rightarrow n-1$, $n \rightarrow n-2$ and $n \rightarrow n-3$ transitions, the matrix elements were specifically calculated in Ref. [31]:

$$\langle n-1|x|n \rangle = \frac{1}{\alpha(k-2n)} \left(\frac{n(k-2n-1)(k-2n+1)}{(k-n)} \right)^{1/2} , \tag{2.42}$$

$$\langle n-2|x|n \rangle = \frac{-1}{2\alpha(k-2n+1)} \left(\frac{n(n-1)(k-2n-1)(k-2n+3)}{(k-n)(k-n+1)} \right)^{1/2} , \tag{2.43}$$

$$\langle n-3|x|n \rangle = \frac{1}{3\alpha(k-2n+2)} \left(\frac{n(n-1)(n-2)(k-2n-1)(k-2n+5)}{(k-n)(k-n+1)(k-n+2)} \right)^{1/2} . \tag{2.44}$$

Here, the width parameter $\alpha = (8\pi^2 c\mu\omega_e x_e/h)^{1/2}$ [102] and $k = \omega_e/\omega_e x_e$ characterize the Morse oscillator. ω_e, the harmonic frequency, and $\omega_e x_e$, the anharmonicity constant of the Morse oscillator, can be readily extracted from the experimental emission frequencies.

Therefore, the fluorescence rate constants for one-quanta ($\Delta v = 1$), two-quanta ($\Delta v = 2$) and three-quanta ($\Delta v = 3$) transitions can be calculated according to Eqs. 2.45 to 2.47 when ω_e, $\omega_e x_e$ and μ' are known—where μ' is the only parameter that cannot be

determined from the emission spectra.

$$k_{\text{fl}}^{\Delta v=1}(n) = \frac{16\pi^3 \tilde{v}_{n,n-1}^3}{3\varepsilon_0 h} \mu'^2 \left| \langle n-1|x|n \rangle \right|^2, \tag{2.45}$$

$$k_{\text{fl}}^{\Delta v=2}(n) = \frac{16\pi^3 \tilde{v}_{n,n-2}^3}{3\varepsilon_0 h} \mu'^2 \left| \langle n-2|x|n \rangle \right|^2, \tag{2.46}$$

$$k_{\text{fl}}^{\Delta v=3}(n) = \frac{16\pi^3 \tilde{v}_{n,n-3}^3}{3\varepsilon_0 h} \mu'^2 \left| \langle n-3|x|n \rangle \right|^2. \tag{2.47}$$

2.4 Infrared spectroscopy of adsorbates

This section gives an overview of the concepts fundamental to understanding the infrared absorption spectra of adsorbed molecules, mainly focusing on the special case of the fundamental $v = 0 \to 1$ transition. The most important differences of surface spectroscopy compared to gas phase spectroscopy are (1) the fixed orientation of the molecules in the condensed phase (Section 2.4.1), (2) the change in the electric field of light waves at the gas-solid interface (Section 2.4.2), and (3) the interactions between the molecules (Section 2.4.3).

2.4.1 Beer-Lambert law and the oriented gas model

One of the most fundamental equations relevant to absorption spectroscopy is the Beer-Lambert law, which is given in the following form applicable to solutions and gas phase samples:

$$A = -\log_{10}\left(\frac{I}{I_0}\right) = \frac{1}{\ln(10)}\sigma_{\text{eff}}Cd. \tag{2.48}$$

The decadic absorbance, A, is defined by the decadic logarithm of the transmittance $T = I/I_0$, where I and I_0 are the intensities of the radiation incident on the sample and transmitted through the sample, respectively. d is the sample thickness. In Eq. 2.48, C is given as a number concentration (units of molecules cm^{-3}) and therefore σ describes the effective absorption cross section of a single molecule (units of cm^2 molecule^{-1}). The absorption cross section can be related to the decadic, molar extinction coefficient, ε, by $\sigma_{\text{eff}} = \varepsilon \ln(10)/N_A$, where N_A is the Avogadro constant.

It is useful to define the integrated absorbance, $\tilde{A}$, integrated over the complete absorption line:

$$\tilde{A} = \int_{\tilde{v}} -\log_{10}\left(\frac{I}{I_0}\right) d\tilde{v} = \frac{1}{\ln(10)}\bar{\sigma}_{\text{eff}}Cd. \tag{2.49}$$

Here, integration is carried out in wavenumber units and therefore the effective integrated cross section, $\bar{\sigma}_{\text{eff}}$, has units of cm molecule^{-1}.

Equation 2.50 gives a form of the Beer-Lambert law that is applicable to the absorption of light by adsorbate layers, characterized by the surface density $S = Cd$ (in units of molecules cm^{-2}): [25]

$$\tilde{A} = \frac{S}{\ln(10)\cos(\theta_1)}\bar{\sigma}_{\text{eff}}. \tag{2.50}$$

Here, it is assumed that the light hits the absorbing sample under the incidence angle θ_1, measured relative to the surface normal. The $\cos(\theta_1)$ term must be included to account for the effective increase of the illuminated surface area when the incidence angle differs from normal incidence ($\theta_1 = 0°$). [25]

It is important to note that $\bar{\sigma}_{\text{eff}}$ describes an effective, integrated cross section, which depends on the orientation of the molecular transition dipole moment, $\boldsymbol{\mu}$, relative to the polarization of the light, given by the electric field vector, $\mathbf{E}$: [103]

$$\bar{\sigma}_{\text{eff}} \propto |\boldsymbol{\mu} \cdot \mathbf{E}|^2. \tag{2.51}$$

In the gas phase or in solution, this effect is usually averaged over all possible orientations and therefore gives $\bar{\sigma}_{\text{eff}} = \bar{\sigma}_z/3$. [25] $\bar{\sigma}_z$ is the integrated cross section of a single molecule when $\boldsymbol{\mu}$ and $\mathbf{E}$ are aligned. Note that for diatomic molecules, the direction of the transition dipole moment is parallel to the molecular bond axis. Within the oriented gas model, the effective cross section can therefore be related to the integrated cross section along the bond axis, $\bar{\sigma}_z$, via:

$$\bar{\sigma}_{\text{eff}} = \bar{\sigma}_z|\mathbf{e} \cdot \boldsymbol{\varepsilon}|^2. \tag{2.52}$$

Here, $\mathbf{e}$ and $\boldsymbol{\varepsilon}$ represent the unit vectors of $\boldsymbol{\mu}$ and $\mathbf{E}$, respectively. With Eqs. 2.50 and 2.52, the integrated absorption in the oriented gas model is given by:

$$\tilde{A} = \frac{S}{\ln(10)\cos(\theta_1)}\bar{\sigma}_z|\mathbf{e} \cdot \boldsymbol{\varepsilon}|^2. \tag{2.53}$$

The oriented gas model considers only the absorption of gas phase molecules with a fixed orientation, by considering the relative orientation of $\boldsymbol{\mu}$ and $\mathbf{E}$. However, it does not include the change of the electric field at the gas-solid interface or a possible change of the cross section of the oriented molecules compared to the gas phase, discussed in the following sections.

2.4.2 Light at the gas-solid interface

The electric field of an electromagnetic wave at the interface between two media with different refractive indices differs from the electric field in vacuum, due to the interference between the incoming, reflected and transmitted light. The electric field amplitudes of the reflected and transmitted waves are related to the amplitude of the incoming wave by the Fresnel equations. [104] Therefore one can define the following normalized field intensity components that describe the square of the electric field components at the surface (E_x, E_y and E_z) relative to the electric field in vacuum ($|E_{vac}|$): [19, 105]

$$T_x = \left(\frac{E_x}{|E_{vac}|}\right)^2 , \; T_y = \left(\frac{E_y}{|E_{vac}|}\right)^2 , \; \text{and } T_z = \left(\frac{E_z}{|E_{vac}|}\right)^2 . \tag{2.54}$$

Light of any polarization can be decomposed into two components with the polarization perpendicular (s-polarization) and parallel (p-polarization) to the plane of incidence. In the present work, s-polarized light is defined such that it has a polarization vector along the y-direction, whereas p-polarized light has a polarization vector in the xz-plane and can thus have both non-zero x- and z-components (see Fig. 2.5). Based on the Fresnel equations of a three-layer slab (medium 1: vacuum, medium 2: CO, medium 3: NaCl), Richardson *et al.* derived equations that describe the absorbance in an external transmission geometry under the Brewster angle and effectively take the field intensity components into account. [25] In this three-layer model, medium 1 (vacuum) and 3 (NaCl) are assumed to be non-absorbing and they are characterized by the refractive indices n_1 and n_3, respectively. Medium 2 (CO) is absorbing and is characterized by a complex index of refraction, $n_2 + i\kappa_2$. This is also indicated in Fig. 2.5. Chabal derived more general expressions for the T_x and T_z terms, which are relevant to p-polarized light, as a function of the incidence angle θ_1: [19]

$$T_x = \frac{2\cos(\theta_1)\sqrt{1 - (n_1/n_3)^2 \sin^2(\theta_1)}}{(n_3/n_1) + 1/\cos(\theta_1)\sqrt{1 - (n_1/n_3)^2 \sin^2(\theta_1)}}, \tag{2.55}$$

$$T_z = \frac{2\sin^2(\theta_1)}{1 + (n_1/n_3)/\cos(\theta_1)\sqrt{1 - (n_1/n_3)^2 \sin^2(\theta_1)}}. \tag{2.56}$$

A similar expression for T_y, the only component relevant to s-polarized light, is derived
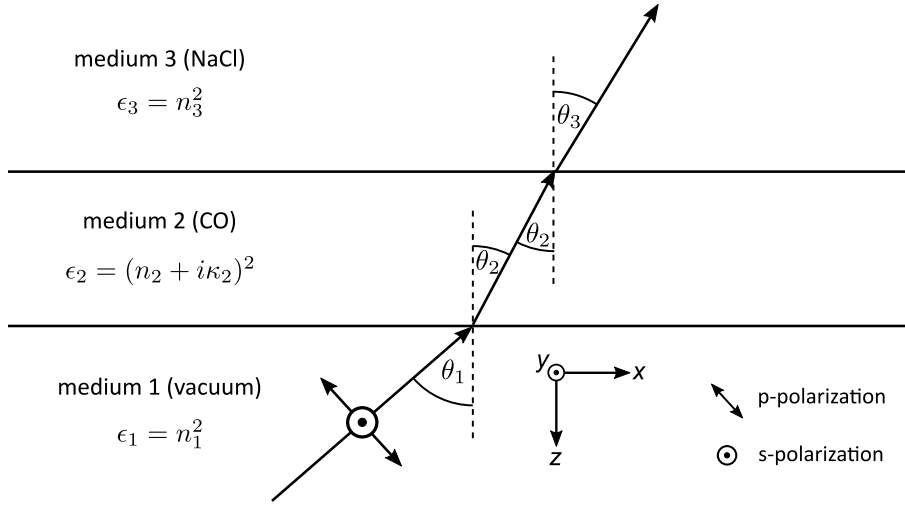
Figure 2.5: Schematic representation of the three-layer model presented in Ref. [25].

in Appendix A of the present work:

$$T_y = \frac{2}{1 + (n_3/n_1)/\cos(\theta_1)\sqrt{1 - (n_1/n_3)^2 \sin^2(\theta_1)}}. \tag{2.57}$$

Note how the field intensity terms only depend on the refractive indices of medium 1 and 3, but not on that of medium 2. They effectively describe the squared components of the electric fields at a vacuum-substrate interface, without the absorbing film, relative to the electric field in vacuum. For the vacuum-NaCl interface ($n_1 = 1$ and $n_3 = 1.52$), the field intensity components are plotted in Fig. 2.6 as a function of incidence angle. For comparison, also the results for $n_1 = n_3$ are shown as dashed lines. In the latter case, the field intensity components correspond to simple projections of the electric field unit vectors in vacuum ($\boldsymbol{\varepsilon}_p$ for p-polarization and $\boldsymbol{\varepsilon}_s$ for s-polarization) onto the interface and reduce to:

$$T_x = \varepsilon_{p,x}^2 = \cos^2(\theta_1), \ T_y = \varepsilon_{s,y}^2 = 1, \ \text{and} \ T_z = \varepsilon_{p,z}^2 = \sin^2(\theta_1). \tag{2.58}$$

29

Figure 2.6: Solid lines correspond to the normalized electric field components for the vacuum-NaCl interface ($n_1 = 1$ and $n_3 = 1.52$). For comparison, also the corresponding normalized electric field components for $n_1 = n_3$, which correspond to simple projections, are shown as dashed lines. T_x: black curve, T_y: red curve, T_z: blue curve.
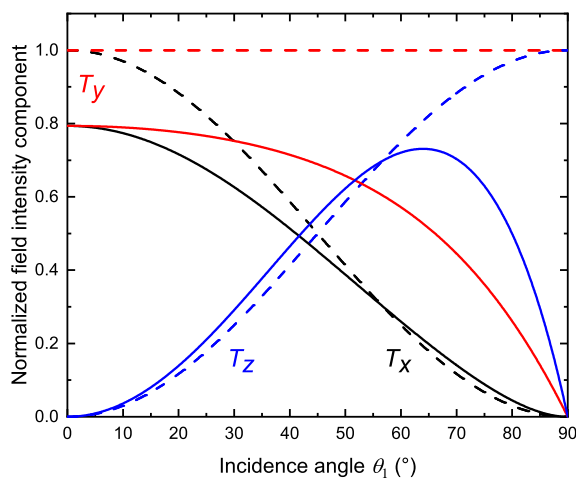
2.4.3 Vibrational excitons

Interactions between molecules, in particular dipole-dipole coupling, lead to collective, vibrational motions of the molecules, which are called vibrational excitons.[9] Similar to phonons, which are coupled motions of the atoms in solids, vibrational excitons l can also be characterized by a frequency, $\tilde{\nu}_l$, and a wavevector, $\mathbf{K}_l$.

The wavelength, λ, of infrared light is much larger than the molecular dimensions. Therefore, only vibrational excitons with $K_l = 2\pi/\lambda \approx 0$ can be excited with infrared absorption spectroscopy. For other modes, molecules in different unit cells would not vibrate in phase and the sum of their transition dipole moments would cancel. Therefore, only n infrared-active exciton modes exist for an adsorption structure with n molecules per unit cell. [106]

In the following, two different models are presented, which describe the infrared spectroscopy of adsorbate layers while considering vibrational excitons. The first model treats the interactions between the molecules with first-order perturbation theory and is especially useful to understand the frequency shifts of vibrational excitons compared to the uncoupled vibrations. The second model takes the effective change of the infrared

---

[9] The definition of vibrational excitons as coupled vibrations should not to be confused with the definition of excitons in solid matter physics.

cross section due to dipole-dipole interactions between the molecules into account.

Static and dynamic frequency shifts

The exciton model presented in this section [107, 108] is extremely useful to understand the nature of the vibrational frequency shift compared to the vibration of uncoupled molecules.

Since the coupling between the molecules is typically weak, the model is based on first-order perturbation theory. The unperturbed, vibrational wavefunction of an individual, uncoupled molecule i is given by ϕ_i in the vibrational ground state and by ϕ_i' in a vibrationally excited state (e.g., $v = 1$). Therefore, the zeroth-order wavefunctions of the total system in the ground state and the vibrationally excited state are given as:

$$\psi_0 = \phi_1 \phi_2 \cdots \phi_N, \tag{2.59}$$

$$\psi_l = C_{l1} \phi_1' \phi_2 \cdots \phi_N + C_{l2} \phi_1 \phi_2' \cdots \phi_N + \cdots + C_{lN} \phi_1 \phi_2 \cdots \phi_N'. \tag{2.60}$$

The ground state wavefunction, ψ_0, is a product of the vibrational ground state wavefunctions of N uncoupled molecules, whereas $\tilde{\nu}_0$ characterizes their unperturbed frequencies. The excited state wavefunction, ψ_l, is a linear combination of N products, in which a single molecule is vibrationally excited. Note that N excitons and thus N excited state wavefunctions exist, which are described by the expansion coefficients C_{li}. The perturbation operator describes the sum over all dipole-dipole interactions between the molecules:

$$\hat{H}' = \sum_{i=1}^{N} \sum_{j<i}^{N} \mu_i \mu_j f_{ij} \tag{2.61}$$

Here, μ_i and μ_j are the EDMFs of molecules i and j, respectively. f_{ij} is the orientation- and distance-dependent interaction term for the dipole-dipole interaction between molecules i and j (see also Section 2.5.2):

$$f_{ij} = \frac{1}{4\pi\varepsilon_0 R_{ij}^3} \left[\mathbf{e}_i \cdot \mathbf{e}_j - 3 \left(\mathbf{e}_i \cdot \mathbf{r}_{ij} \right) \left(\mathbf{e}_j \cdot \mathbf{r}_{ij} \right) \right]. \tag{2.62}$$

$\mathbf{e}_i$ and $\mathbf{e}_j$ are the unit vectors that describe the orientations of the two molecules, whereas $\mathbf{r}_{ij}$ is the unit vector of the intermolecular separation vector, $\mathbf{R}_{ij}$, that connects molecules i and j. R_{ij} is the corresponding intermolecular distance. The implementation of multipole interactions beyond the dipole-dipole interaction in Eq. 2.61 would be straightforward (see also Section 2.5.2). [108] However, only the leading dipole-dipole

interaction term will be discussed here for simplicity.

With Eqs. 2.59 and 2.61, the first-order energy correction to the vibrational ground state is given by:[10]

$$E_0^{(1)} = \langle \psi_0 | \hat{H}' | \psi_0 \rangle = \mu_{00}^2 \sum_{i=1}^{N} \sum_{j<i}^{N} f_{ij}. \tag{2.63}$$

Here, $\mu_{00} = \langle \phi_i | \mu_i | \phi_i \rangle$ is the permanent dipole moment in the vibrational ground state.

The first-order correction of the excited state must be calculated with perturbation theory for N-fold degenerate zeroth-order states. With Eqs. 2.60 and 2.61, the diagonal elements of the corresponding Hamiltonian matrix are given by:

$$H'_{kk} = \langle \psi_k | \hat{H}' | \psi_k \rangle = \mu_{00}^2 \sum_{i=1, i\neq k}^{N} \sum_{j<i, j\neq k}^{N} f_{ij} + \mu_{00}\mu_{11} \sum_{i=1, i\neq k}^{N} f_{ik}. \tag{2.64}$$

Here, $\mu_{11} = \langle \phi_i | \mu_i | \phi_i \rangle$ is the permanent dipole moment in $v = 1$. Equation 2.64 can be greatly simplified by subtracting the energy correction of the vibrational ground state (Eq. 2.63) from all diagonal elements:

$$\Delta H'_{kk} = H'_{kk} - E_0^{(1)} = (\mu_{11} - \mu_{00})\,\mu_{00} \sum_{i=1, i\neq k}^{N} f_{ik}. \tag{2.65}$$

The off-diagonal elements take a much simpler form:[11]

$$H'_{ij} = \langle \psi_i | \hat{H}' | \psi_j \rangle = \mu_{01}^2 f_{ij}. \tag{2.66}$$

Here, $\mu_{01} = \langle \phi'_i | \mu_i | \phi_i \rangle$ is the transition dipole moment.

To find the excitonic frequency shifts and transition dipole moments, the Hamiltonian matrix, H', defined by the matrix elements in Eqs. 2.65 and 2.66, must be diagonalized. The eigenvalues of H', $\Delta E_l^{(1)}$, can be related to the frequency shifts of the vibrational excitons relative to the frequency of the unperturbed molecules:

$$\Delta \tilde{\nu}_l = \frac{1}{hc} \Delta E_l^{(1)}. \tag{2.67}$$

The eigenvectors of H', $\mathbf{C}_l$, define the expansion coefficients of the excitonic wavefunctions (Eq. 2.60). The corresponding integrated absorption cross sections along the

---

[10] Note that $\langle \phi_i | \phi_i \rangle = \langle \phi'_i | \phi'_i \rangle = 1$.

[11] Note that $\langle \phi_i | \phi'_i \rangle = 0$.

direction of the transition dipole moments are given by: [108]

$$\bar{\sigma}_{z,l} = \frac{8\pi^3 \tilde{\nu}_l}{4\pi\varepsilon_0 hc} \frac{\left| \sum_{i=1}^N \langle \psi_l | \mu_i \mathbf{e}_i | \psi_0 \rangle \right|^2}{N} = \frac{8\pi^3 \tilde{\nu}_l}{4\pi\varepsilon_0 hc} \frac{\left| \sum_{i=1}^N C_{li} \mu_{01} \mathbf{e}_i \right|^2}{N}. \tag{2.68}$$

Within the oriented gas model (Eq. 2.53), the integrated absorbance for an exciton absorption line at frequency $\tilde{\nu}_l = \tilde{\nu}_0 + \Delta\tilde{\nu}_l$ is therefore given as:

$$\tilde{A}_l = \frac{S}{\ln(10)\cos(\theta_1)} \frac{8\pi^3 \mu_{01}^2 \tilde{\nu}_l}{4\pi\varepsilon_0 hc} \frac{\left| \sum_{i=1}^N C_{li} (\mathbf{e}_i \cdot \boldsymbol{\varepsilon}) \right|^2}{N}. \tag{2.69}$$

There are two different contributions to the frequency shift in Eq. 2.67, arising from the diagonal and off-diagonal matrix elements. The diagonal elements in Eq. 2.65 describe the difference in the interaction energies of a single molecule k excited from $v = 0$ to $v = 1$ with all other molecules in $v = 0$ via their permanent dipole moments. This frequency shift is called the static frequency shift because it only involves interactions between permanent multipole moments. The off-diagonal elements in Eq. 2.66 can be interpreted as the coupling between the transition dipole moments of the two molecules. This coupling explains the formation of the vibrational excitons and leads to different vibrational frequency shifts for different collective exciton modes. Only these dynamic contributions can cause a frequency splitting, whereas the static shift is often similar for different excitons. The frequency splitting caused by the dynamic frequency shift is also often called Davydov splitting or correlation-field splitting. [41, 42]

The dynamic frequency splitting, as observed in the absorption spectra of the CO monolayer in the (2×1) structure (see Section 2.1), depends strongly on the magnitude of the transition dipole moment. Dai and Ewing showed experimentally that the dynamic frequency shift vanishes for small transition dipole moments, as for the $v = 0 \rightarrow 2$ absorption line, and for molecules that are separated by large distances, as for $^{13}C^{16}O$ diluted in $^{12}C^{16}O$ (and vice versa). [107] These observations are of great importance to the VEP experiments in the present work, where molecules in highly vibrationally excited states are surrounded by molecules in much lower vibrational states, leading to inefficient dynamic coupling. Therefore, only static frequency shifts are expected for LIF experiments,[12] whereas both static and dynamic frequency shifts can be observed in infrared absorption experiments.

---

[12] Except for the $v = 1 \rightarrow 0$ transition, which cannot be probed with the present experimental setup because the $v = 0 \rightarrow 1$ transition is excited.

Effective absorption strength for collective vibrations

Although the exciton model presented in the previous section gives insight into the frequency shifts, it cannot describe the effective change of the infrared absorption that arises due to the collective motion of the molecules. To envision this, consider an array of perpendicularly oriented molecules. For the single infrared-active exciton mode ($\mathbf{K} = \mathbf{0}$), all molecules vibrate in phase with each other when they are excited with infrared light. Therefore, each molecule will experience an electric field due to the in-phase motion of the surrounding molecules, leading to an induced dipole moment that opposes the original transition dipole moment.

Due to the strong dependence of the effective reduction of the infrared absorption on the intermolecular distances, this effect is strongly coverage-depent. The coverage dependence of the absorption strength of CO on various metal surfaces is well studied, [109–113] and theoretical models exist, which consider the effect of the molecular polarizability during the collective motion. [114–116] However, all these models assume that the dipole moments of the CO molecules are perpendicular to the surface and form (1×1) structures. While this is well-justified for CO on metal surfaces, CO on NaCl(100) is not always oriented perpendicular to the surface and shows a (2×1) structure at low temperatures (see also Section 2.1).

Snigur and Rozenbaum developed a model that can describe the effective change of the infrared absorption due to dipole-dipole interactions in an adsorbate layer with n different molecules per unit cell that can have arbitrary orientations. [117] In addition, analytical solutions to the equations can be derived for simple adsorption structures, such as a slightly simplified version of the (2×1) structure in the CO/NaCl(100) monolayer. [118, 119] The model by Snigur and Rozenbaum [117] will be presented in the following and is applied in Chapter 7.

Similar to the quantum mechanical model in the previous section, also in the model by Snigur and Rozenbaum, the collective motion is characterized by an interaction matrix, $W_{jj'}$ (see Eqs. 2.70 to 2.72). Here j and j' denote molecules within the same unit cell, whereas the summation runs over the position vectors, $\mathbf{R}$, of all unit cells. e_j^{α} and $e_{j'}^{\beta}$ are the x, y and z components of the orientation unit vectors, $\mathbf{e}_j$ and $\mathbf{e}_{j'}$, of the two

molecules.

$$W_{jj'} = \sum_{\alpha=x,y,z} \sum_{\beta=x,y,z} e_j^\alpha V_{jj'}^{\alpha\beta}(\mathbf{K}=\mathbf{0}) e_{j'}^\beta, \tag{2.70}$$

$$V_{jj'}^{\alpha\beta}(\mathbf{K}) = \sum_{\mathbf{R}} \left[\frac{\delta_{\alpha\beta}}{|\mathbf{R}+\mathbf{r}_{jj'}|^3} - 3\frac{\left(\mathbf{R}+\mathbf{r}_{jj'}\right)_\alpha \left(\mathbf{R}+\mathbf{r}_{jj'}\right)_\beta}{|\mathbf{R}+\mathbf{r}_{jj'}|^5} \right]$$
$$\times \exp\left(-i\left(\mathbf{R}+\mathbf{r}_{jj'}\right)\cdot\mathbf{K}\right), \tag{2.71}$$

$$V_{jj'}^{\alpha\beta}(\mathbf{K}=\mathbf{0}) = \sum_{\mathbf{R}} \left[\frac{\delta_{\alpha\beta}}{|\mathbf{R}+\mathbf{r}_{jj'}|^3} - 3\frac{\left(\mathbf{R}+\mathbf{r}_{jj'}\right)_\alpha \left(\mathbf{R}+\mathbf{r}_{jj'}\right)_\beta}{|\mathbf{R}+\mathbf{r}_{jj'}|^5} \right]. \tag{2.72}$$

Rewriting $W_{j,j'}$ in terms of the orientation vectors gives:

$$W_{jj'} = \sum_{\mathbf{R}} \left[\frac{\mathbf{e}_j \cdot \mathbf{e}_{j'}}{|\mathbf{R}+\mathbf{r}_{jj'}|^3} - 3\frac{\left(\mathbf{e}_j \cdot \left(\mathbf{R}+\mathbf{r}_{jj'}\right)\right)\left(\mathbf{e}_{j'} \cdot \left(\mathbf{R}+\mathbf{r}_{jj'}\right)\right)}{|\mathbf{R}+\mathbf{r}_{jj'}|^5} \right]. \tag{2.73}$$

Comparison of Eq. 2.73 and Eq. 2.62 shows that Eq. 2.73 essentially describes the summation over the dipole-dipole interaction terms $4\pi\varepsilon_0 f_{ij}$ between all molecules in real space. Therefore, the matrix elements $W_{jj'}$ in Eq. 2.73 are essentially identical to the off-diagonal matrix elements H'_{ij} in Eq. 2.66, except for a constant factor. A minute difference between the models is, however, that the model by Snigur and Rozenbaum is based on the molecules in a single unit cell assuming a periodic structure, while individual molecules are considered in the other model. Diagonalization of W gives n eigenvalues, W_l, and eigenvectors, $\mathbf{C}_l$, which characterize the exciton modes, labelled by the index l. The integrated absorbance of a given exciton absorption line (in units of angular frequency) is given by:

$$\tilde{A}_l^\omega = \frac{S}{\ln(10)\cos(\theta_1)} \frac{2\pi^2 \chi_v \omega_0^2}{c} \frac{|\boldsymbol{\varepsilon}\cdot\mathbf{P}_l|^2}{n(1+\chi_e W_l)^2}. \tag{2.74}$$

Here, χ_v and χ_e are the vibrational and electronic polarizabilities of the molecules parallel to the bond axis. $\mathbf{P}_l = \sum_j C_{lj}\mathbf{e}_j$ is a vector that is proportional to the transition dipole moment vector. ω_0 is the unperturbed frequency of the molecule. Other quantities are defined as for Eq. 2.53. Conversion from angular frequencies to wavenumbers

($\omega = 2\pi c \tilde{\nu}$) finally gives:

$$\tilde{A}_l^{\tilde{\nu}} = \frac{S}{\ln(10)\cos(\theta_1)} 4\pi^3 \chi_v \tilde{\nu}_0^2 \frac{|\boldsymbol{\varepsilon} \cdot \mathbf{P}_l|^2}{n(1 + \chi_e W_l)^2}. \tag{2.75}$$

The vibrational polarizability describes the dynamic polarizability associated with the $v = 0 \to 1$ transition and can be related to the integrated cross section and the transition along the bond axis via: [25, 91]

$$\bar{\sigma}_z = 4\pi^3 \chi_v \tilde{\nu}_0^2 = \frac{8\pi^3 \mu_{01}^2 \tilde{\nu}_0}{4\pi\varepsilon_0 hc}. \tag{2.76}$$

With the relations in Eq. 2.76 in mind, note the strong similarity between Eqs. 2.69 and 2.75, differing only by $1/(1 + \chi_e W_l)^2$. This term essentially describes the effective change in the infrared cross section due to collective vibrational motion, quantified by W_l, leading to the induction of additional transition dipole moments via the electronic polarizability, χ_e. Also note that this term cannot only lead to a reduction of the effective cross section, but also to an effective increase when $W_l < 0$. [117]

Within this model, also the vibrational frequencies of the exciton absorption lines can be calculated according to: [117]

$$\tilde{\nu}_l^2 = \tilde{\nu}_0^2 \left(1 + \frac{\chi_v W_l}{1 + \chi_e W_l}\right). \tag{2.77}$$

2.5 Electrostatic interactions

For CO on NaCl(100), electrostatic interactions and dispersion interactions are the most important long-range interactions whereas repulsive interactions dominate at short distances. [120, 121] Although all these interactions are relevant to describe the absolute binding strength of CO to NaCl(100), electrostatic interactions depend strongly on molecular orientation and the CO bond distance and therefore strongly influence the vibrational dynamics. Therefore, only electrostatic interactions will be discussed in this section. For an extensive introduction to other interactions, the reader is referred to Ref. [122].

2.5.1 Molecules in an external electric field

This section describes the electrostatic interaction between a molecule placed in an external, non-homogeneous electric field. It is mainly based on Ref. [122, 123] and

only highlights the most important results. See Ref. [122] for full derivations. Since the electrostatic interaction energies are typically small compared to the energies of the molecule, they can be described by perturbation theory. The corresponding Hamiltonian that describes the perturbation is given by:

$$\hat{H}' = \sum_{\mathbf{a}} e_a V(\mathbf{a}). \tag{2.78}$$

It describes the interaction of the molecular charge distribution, where the individual charges e_a are placed at positions a, with an electric potential, $V(\mathbf{a})$. Taylor expansion of the potential around the position of the molecule makes it possible to write the Hamiltonian in terms of contributions from interactions between traceless multipole moment operators of the molecule and partial derivatives of the external potential:

$$\hat{H}' = qV + \hat{\mu}_\alpha V_\alpha + \frac{1}{3}\hat{\Theta}_{\alpha\beta}V_{\alpha\beta} + \frac{1}{15}\hat{\Omega}_{\alpha\beta\gamma}V_{\alpha\beta\gamma} + \dots \tag{2.79}$$

Here, a repeated greek index, which can take the values of the cartesian coordinates x, y and z, implies a summation over that index (Einstein summation convention). For example, $\hat{\Theta}_{\alpha\beta}V_{\alpha\beta}$ represents the following sum:

$$\hat{\Theta}_{\alpha\beta}V_{\alpha\beta} = \sum_{\alpha=x,y,z}\sum_{\beta=x,y,z}\hat{\Theta}_{\alpha\beta}V_{\alpha\beta}. \tag{2.80}$$

q is the total charge of the molecule. $\hat{\mu}_\alpha$, $\hat{\Theta}_{\alpha\beta}$ and $\hat{\Omega}_{\alpha\beta\gamma}$ are components of the dipole, quadrupole and octopole moment operators, respectively (see Ref. [122] for their definitions). Interactions beyond the octopole moment are not considered in this thesis. V_α, $V_{\alpha\beta}$ and $V_{\alpha\beta\gamma}$ are derivatives of the electric potential evaluated at the position of the molecule, for example $V_{\alpha\beta} = \partial V/\partial r_\alpha \partial r_\beta$. Note that the electric field of the potential is given by $F_\alpha = -V_\alpha$ and the corresponding electric field gradients also differ from the potential derivatives by a minus sign: $F_{\alpha\beta} = -V_{\alpha\beta}$ and $F_{\alpha\beta\gamma} = -V_{\alpha\beta\gamma}$. Thus, the Hamiltonian can also be written in terms of the electric field (derivatives):

$$\hat{H}' = qV - \hat{\mu}_\alpha F_\alpha - \frac{1}{3}\hat{\Theta}_{\alpha\beta}F_{\alpha\beta} - \frac{1}{15}\hat{\Omega}_{\alpha\beta\gamma}F_{\alpha\beta\gamma} - \dots \tag{2.81}$$

Because the vibrational state-dependence will be most important for the present work, consider a given vibrational state v in the electronic ground state, characterized by the

wavefunction $\Psi_{X,v}$. The corresponding first-order energy correction is obtained by

$$E^{(1)} = \langle \Psi_{X,v} | \hat{H}' | \Psi_{X,v} \rangle = qV - \mu_\alpha F_\alpha - \frac{1}{3} \Theta_{\alpha\beta} F_{\alpha\beta} - \frac{1}{15} \Omega_{\alpha\beta\gamma} F_{\alpha\beta\gamma} - \ldots \quad (2.82)$$

It is important to recognize the difference between the components of the multipole moment operators in Eq. 2.81 and the components of the vibrational state-dependent expectation values of the multipole moments in Eq. 2.82. For example: $\mu_\alpha = \langle \Psi_{X,v} | \hat{\mu}_\alpha | \Psi_{X,v} \rangle$. Equation 2.82 shows that the molecular charge, dipole moment, quadrupole moment and octopole moment interact with the electric potential, the electric field, the electric field gradient and the second gradient of the field, respectively.

2.5.2 Electrostatic interactions between two molecules

This section describes the electrostatic interaction between two molecules. It also follows the derivations in Ref. [122, 123] and only the most important aspects are highlighted. Equation 2.79 is used to calculate the Hamiltonian for the interaction of the multipole moments of molecule B with the electric potential generated by molecule A:

$$\hat{H}' = q^B V^A + \hat{\mu}_\alpha^B V_\alpha^A + \frac{1}{3} \hat{\Theta}_{\alpha\beta}^B V_{\alpha\beta}^A + \frac{1}{15} \hat{\Omega}_{\alpha\beta\gamma}^B V_{\alpha\beta\gamma}^A + \ldots \quad (2.83)$$

The electric potential of A at position $\mathbf{B}$ is:

$$V^A(\mathbf{B}) = \sum_a \frac{e_a}{4\pi\varepsilon_0 |\mathbf{R}_{AB} - \mathbf{a}|}. \quad (2.84)$$

Here, $\mathbf{R}_{AB} = \mathbf{B} - \mathbf{A}$ is the intermolecular separation vector, pointing from molecule A to B. $\mathbf{a}$ defines the positions of the charges e_a relative to the position of molecule A. The potential $V^A(\mathbf{B})$ could again be expressed in terms of the multipole moments of molecule A by a Taylor expansion around the position of molecule A. However, an extremely useful, alternative approach to derive the multipole-multipole interaction energies makes use of spherical multipole moments, $Q_{l\kappa}$, where the potential in Eq. 2.84 is expanded into spherical harmonics instead of cartesian coordinates. In this case, the total interaction energy due to multipole-multipole interactions can be written as:

$$E^{(1)} = \sum_{l_1=0}^{\infty} \sum_{l_2=0}^{\infty} \sum_{\kappa_1,\kappa_2} Q_{l_1\kappa_1}^A T_{l_1\kappa_1,l_2\kappa_2}^{AB} Q_{l_2\kappa_2}^B. \quad (2.85)$$

The great advantage of the spherical tensor formulation is that the spherical multipole moments are defined in the local coordinate systems of the molecules whereas the spherical interaction tensors, $T^{AB}_{l_1\kappa_1,l_2\kappa_2}$, take the relative orientation of the molecules and the intermolecular distance into account. Furthermore, only spherical multipole moments with $\kappa = 0$ are non-zero for diatomic molecules. Those spherical multipole moments agree with the "z^l"-components of the cartesian multipole moments.[13] The correspondence between the cartesian and spherical multipole moments is as follows: $Q_{00} = q$ (charge), $Q_{10} = \mu_z = \mu$ (dipole), $Q_{20} = \Theta_{zz} = \Theta$ (quadrupole) and $Q_{30} = \Omega_{zzz} = \Omega$ (octopole). Remember that the individual multipole moments are expectation values for a given vibrational state v. Therefore, Eq. 2.85 reduces to Eq. 2.86 (for neutral diatomic molecules).

$$
\begin{aligned}
E^{(1)} &= \sum_{l_1=1}^{\infty} \sum_{l_2=1}^{\infty} Q^A_{l_1,0} T^{AB}_{l_1,0,l_2,0} Q^B_{l_2,0} \\
&= \mu^A \mu^B T^{AB}_{\mu\mu} + \left(\Theta^A \mu^B - \mu^A \Theta^B \right) T^{AB}_{\Theta\mu} + \left(\Omega^A \mu^B - \mu^A \Omega^B \right) T^{AB}_{\Omega\mu} \\
&\quad + \Theta^A \Theta^B T^{AB}_{\Theta\Theta} + \left(\Omega^A \Theta^B - \Theta^A \Omega^B \right) T^{AB}_{\Omega\Theta} + \Omega^A \Omega^B T^{AB}_{\Omega\Omega} + \cdots .
\end{aligned}
\tag{2.86}
$$

The interaction terms T^{AB}_{tu} that describe the interactions between the various multipole moments in Eq. 2.86 are tabulated in Ref. [124]. Up to the octopole-octopole interaction, they can also be found in Table D.1 (see Appendix D). To give an example, the important interaction term for the dipole-dipole interaction is given by Eq. 2.87, where $\mathbf{e}_A$ and $\mathbf{e}_B$ are orientation unit vectors of molecules A and B and $\mathbf{r}_{AB} = \mathbf{R}_{AB}/R_{AB}$.

$$
T^{AB}_{\mu\mu} = \frac{1}{4\pi\varepsilon_0 R^3_{AB}} \left[\mathbf{e}_A \cdot \mathbf{e}_B - 3 \left(\mathbf{e}_A \cdot \mathbf{r}_{AB} \right) \left(\mathbf{e}_B \cdot \mathbf{r}_{AB} \right) \right] .
\tag{2.87}
$$

2.5.3 Electric dipole moment function of CO

Due to the great importance of dipole interactions in many aspects of this work, the dipole moment of CO will be explicitly considered here. The expectation value of the dipole moment in a given state, whose wavefunction, $\Psi_{N,v}$, is a product of the electronic wavefunction $\psi_N(\tau; \mathbf{R})$ and the vibrational wavefunction $\phi_v(\mathbf{R})$ within the

---

[13] When the "z^l"-components are calculated in the local coordinate system where the the diatomic molecule is aligned with the z-axis.

Born-Oppenheimer approximation, is given by:

$$\mu = \langle \Psi_{N,v} | \hat{\mu} | \Psi_{N,v} \rangle = \langle \phi_v | \langle \psi_N | \hat{\mu} | \psi_N \rangle | \phi_v \rangle. \tag{2.88}$$

Here, $\hat{\mu}$ is the dipole moment operator in the local coordinate system of the molecule. When integration is only carried out over the electronic coordinates, τ, the electric dipole moment function (EDMF), $\mu(\mathbf{R})$, which describes the dipole moment of the molecule as a function of the nuclear coordinates, $\mathbf{R}$, can be defined as:

$$\mu(\mathbf{R}) = \langle \psi_N | \hat{\mu} | \psi_N \rangle. \tag{2.89}$$

Therefore, the components of the permanent dipole moments in Eq. 2.88 can be written in terms of the vibrational wavefunction with quantum number v and the EDMF:

$$\mu_{vv} = \langle \phi_v | \mu(\mathbf{R}) | \phi_v \rangle. \tag{2.90}$$

Similarly, the components of the transition dipole moment between two different vibrational states characterized by ϕ_v and $\phi_{v'}$ can be written as:

$$\mu_{vv'} = \langle \phi_{v'} | \mu(\mathbf{R}) | \phi_v \rangle. \tag{2.91}$$

A theoretical EDMF, $\mu(r)$, and the corresponding permanent dipole moments of gas phase CO for vibrational quantum numbers up to $v = 27$ are shown in Fig. 2.7. [125] Here, r denotes the CO bond length. At the equilibrium bond length, r_e, the dipole moment has a small, negative value, which implies $C^{\delta-}O^{\delta+}$ polarity. The same applies to the permanent dipole moment in the vibrational ground state, μ_{00}. However, the polarity of the dipole moment reverses when the C-O bond is stretched, leading to a reversal of the polarity of the permanent dipole moments for $v = 5$ and higher. In addition to the sign change, the magnitude in $v = 27$ is about 6 times higher than in $v = 0$. In contrast to the small value at r_e, the derivative of the EDMF near the equilibrium value has a relatively large value of about $\mu' = 3.2 \, \mathrm{D} \, \text{Å}^{-1}$, leading to large transition dipole moments. In addition, the function remains linear for most CO bond lengths relevant to vibrational states up to $v = 30$, such that the EDMF is well approximated by:

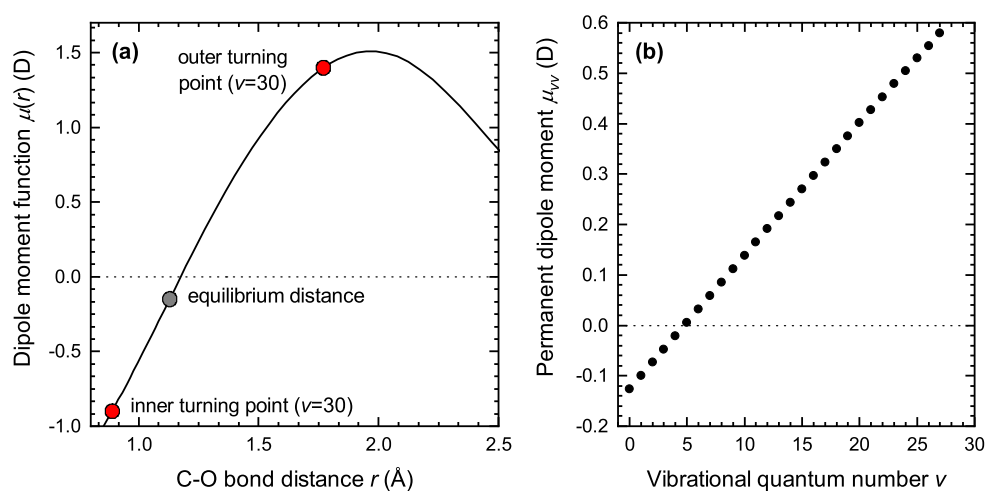$$\mu(r) = \mu(r_e) + \mu'(r - r_e). \tag{2.92}$$

Figure 2.7: (a) Electric dipole moment function of gas phase CO. The dipole moments at the equilibrium bond length and at the estimated positions of the classical turning points of $v = 30$, the highest vibrational state observed in this work for a CO monolayer, are indicated. A negative value implies a $C^{\delta-}O^{\delta+}$ polarity. (b) Corresponding permanent dipole moments for vibrational quantum numbers up to $v = 27$. Both the EDMF and the permanent dipole moments are taken from the theoretical "aV6Z (field)" results in Ref. [125].

Experimental

In this chapter, the experimental methods that were to used to obtain the results in Chapters 4 to 7 will be introduced. Section 3.1 presents the experimental apparatus, including several modifications that were installed over the course of this work—in particular, a molecular beam source chamber for the preparation of layered samples and an improved version of the mid-infrared emission spectrometer. Section 3.2 deals with the experimental conditions and measurement procedures.

3.1 Experimental setup

An overview of the main experimental components is shown in Fig. 3.1. A NaCl single crystal is mounted inside a ultra-high vacuum (UHV) chamber with a typical base pressure of 2×10^{-10} mbar. The central part of the UHV chamber is built around a 6-way cube and is pumped by a turbomolecular pump (Turbovac MAG W 600 iP, Leybold; backed by Turbovac SL 80H, Leybold) attached to the bottom of the chamber. NaCl(100) crystal planes are prepared by cleaving the crystal under UHV with a blade attached to the cleavage tool (wobble stick). The NaCl sample holder is cooled by a 4 K helium cryocooler that is attached to a UHV manipulator mounted on the top flange of the chamber. A homebuilt, cryogenically-cooled mid-infrared emission spectrometer based on SNSPDs is flanged to one side of the UHV chamber. The emission spectrometer is used for temporal and spectral measurements of infrared fluorescence induced by an infrared excitation laser, which is indicated by the red arrow. On the opposite side, a dual-molecular beam source is attached for dosing the surface with two different types of gases. On the other two sides of the UHV chamber, two vacuum compartments

(typical operating pressures of 4×10^{-2} mbar) house the optical components for the infrared excitation laser as well as a FTIR spectrometer set up in an external transmission geometry. In addition, a residual gas analyzer (RGA) can be used for residual gas analysis and temperature-programmed desorption (TPD) experiments. All experimental components are described in detail in the following sections.
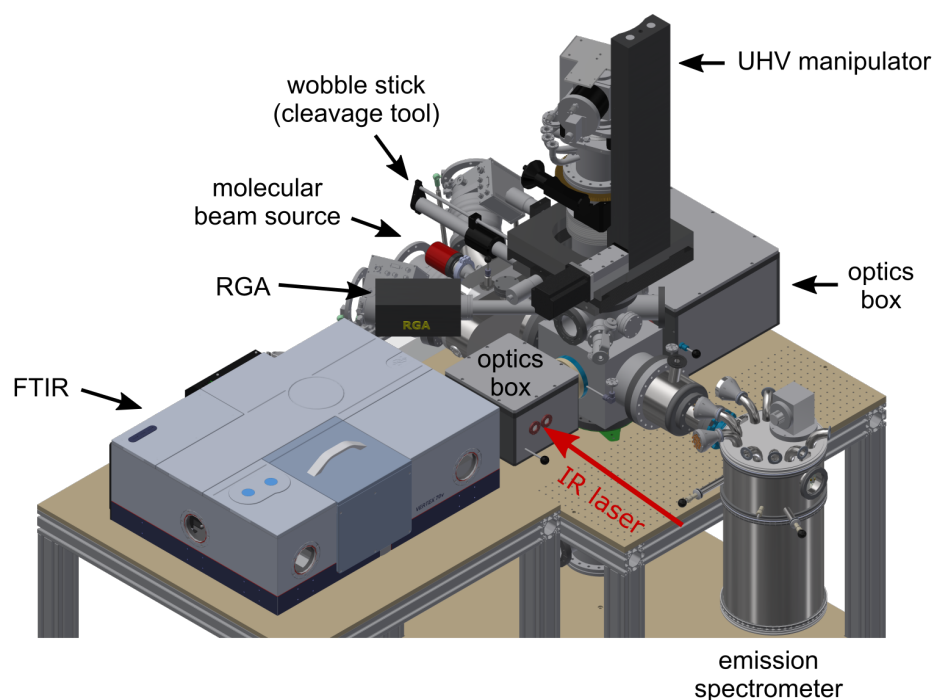

Figure 3.1: Overview of the complete experimental apparatus and its main components built around the central UHV chamber. The infrared excitation laser is indicated by a red arrow.

3.1.1 Cryogenic NaCl sample holder

The NaCl single crystal sample holder (see Fig. 3.2a) is attached to a closed-cycle 4 K helium cryocooler (RDK-408D2, Sumitomo), which is mounted on a 4-axis manipulator (UHV manipulator MEGA 25-500 and differentially pumped rotary feedthrough DDF 160 P, VAb Vakuum-Anlagenbau). The sample holder consists of two copper parts: The upper part is connected to the cryocooler while the lower part holds the NaCl crystal. Spring-loaded screws ensure mechanical and thus thermal contact between the two parts during operation at cryogenic temperatures.

The NaCl crystal (W×H: 15 mm × 10 mm, Korth Kristalle) is fixed on the lower part, using a U-shaped copper piece attached with two spring-loaded screws. A resistive cartridge heater and a silicon diode temperature sensor (Lakeshore, DT-670) are attached close to the NaCl sample to control its temperature with a cryogenic temperature controller (Lakeshore, Model 335). The upper part of the sample holder serves as a thermal connection between the lower part and the 4 K cold head of the cryocooler. A helium gas reservoir between the upper sample holder part and the cold head ensures thermal contact but reduces mechanical vibrations transferred to the sample holder (see Fig. 3.2b). Since typical helium pressures between 0.2 and 1.0 bar are used, the helium reservoir is equipped with a pressure relief valve and a helium balloon. The temperature on the upper sample holder part is also monitored using an E-type thermocouple.

The two parts can be thermally decoupled using the decoupling mechanism indicated in Fig. 3.2a, which can be rotated by 90° using the wobble stick. This is only used to avoid heating of the cryocooler when the NaCl crystal is heated above 60 K for cleaning.

To avoid heating of the sample holder due to thermal radiation, the whole upper sample holder part is gold-coated and is further shielded by an additional, outer gold-coated layer (radiation shield). The length of this radiation shield is chosen such that the gap between the radiation shield and the liquid-nitrogen cold shield is minimized when the NaCl crystal is in position for LIF experiments (see also Fig. 3.3).

3.1.2 SNSPD-based mid-infrared emission spectrometer

A drawing of the mid-infrared emission spectrometer used for the LIF experiments is presented in Fig. 3.3. The main components are an infrared excitation laser to excite adsorbates adsorbed to the NaCl crystal, a liquid-nitrogen cold shield, and a spectrometer chamber separated from the UHV chamber by a CaF_2 window flange. The spectrometer chamber contains a 40 K cold monochromator and the dispersed light is directed to a SNSPD held near 0.3 K. The emission spectrometer presented in Fig. 3.3 is an improved version of a previously reported setup, which was based on a liquid nitrogen-cooled monochromator that was separated from the spectrometer chamber. [31]

The liquid-nitrogen cold shield (see Fig. 3.4) is used to shield the NaCl sample and the optical path from thermal radiation, mainly emitted by the walls of the vacuum chamber, which are at room temperature. The left part of the cold shield contains two pairs of apertures for transmission of the infrared excitation laser and the light from the FTIR spectrometer source through the shield. The extension on the top is used to shield the sample holder and is designed such that the gap between the cold shield and the radiation shield is minimized when the NaCl crystal is in position for LIF measurements (indicated
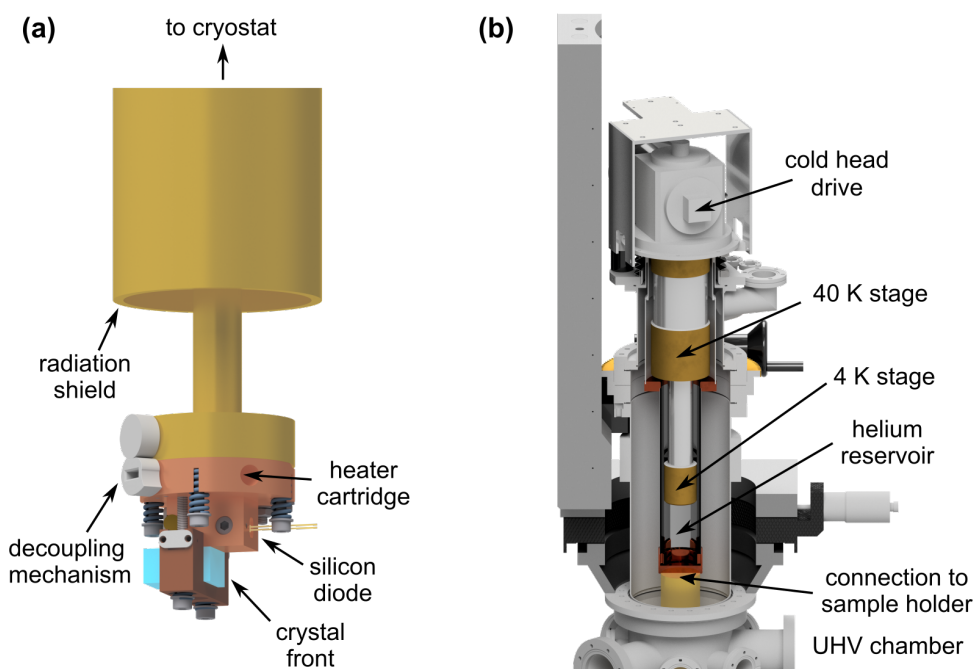
Figure 3.2: (a) Rendered image of the cryogenic NaCl sample holder, which consists of an upper (gold-coated) and a lower (uncoated) copper part. The upper part is connected to the 4 K cryocooler, shielded with an outer radiation shield and can be thermally decoupled from the lower part. In addition, the positions of the heater cartridge and the silicon diode temperature sensor are indicated. Furthermore, the crystal front, which is exposed to the infrared laser and FTIR light, is labeled. (b) Rendered image of the helium cold head, which is connected to the sample holder and mounted on the UHV manipulator. The 4 K stage of the cold head is not directly connected to the sample holder. Instead thermal contact comes from helium gas which surrounds the cold head.
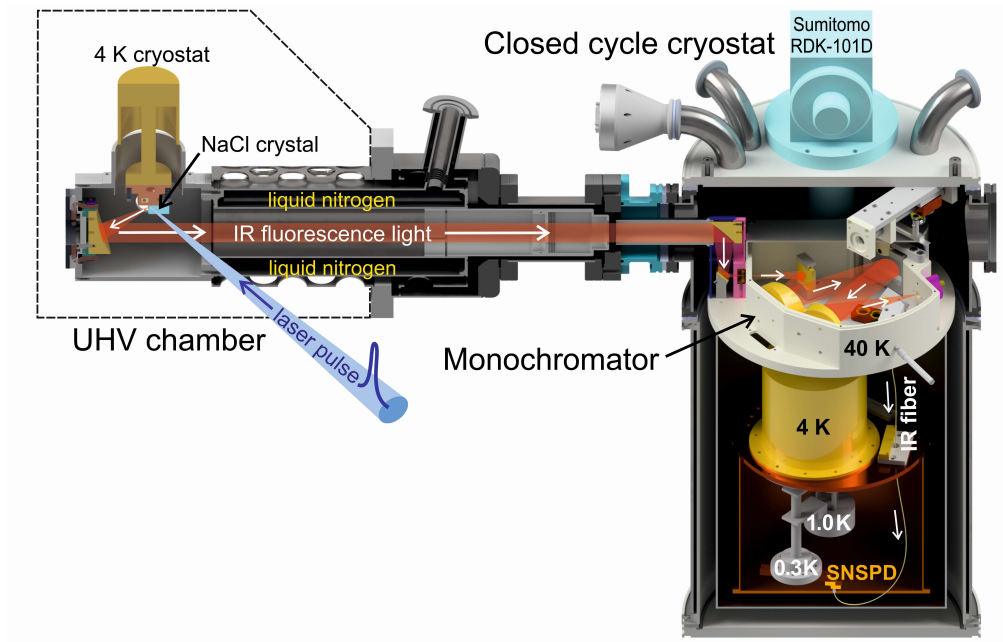
Figure 3.3: Overview of the mid-infrared emission spectrometer components. The red beam and white arrows indicate the optical path of the collected infrared fluorescence light. From Ref. [126]. Reprinted with permission from AAAS.

by "LIF"). This position overlaps with the focal point of a 30° off-axis parabolic mirror (reflected focal length: 54.5 mm),[1] which collects and collimates the fluorescence from the NaCl surface and directs it toward the monochromator. Two additional apertures in the parabolic mirror holder allow the pulses from the molecular source (see Section 3.1.5) to enter the cold shield. The cold shield is separated from the spectrometer chamber with a CaF_2 window flange so that the spectrometer chamber can be vented separately from the UHV chamber. In front of the CaF_2 window, the inner part of the cold shield contains two apertures that match the size of the first parabolic mirror inside the spectrometer and avoid collection of stray light that enters through the cold shield apertures.

The separate spectrometer chamber contains a Czerny-Turner type monochromator which is connected to a SNSPD, held ideally at 0.3 K, via a mid-infrared multimode As_2S_3 fiber (IRF-S-100, IRflex). A two-stage sub-Kelvin ^{3}He cooler (CRC-GL7-009, Chase Research Cryogenics) is attached to the 4 K stage of a helium cryocooler (RDK-101D, Sumitomo) and provides the sub-Kelvin temperature needed for operation of the

---

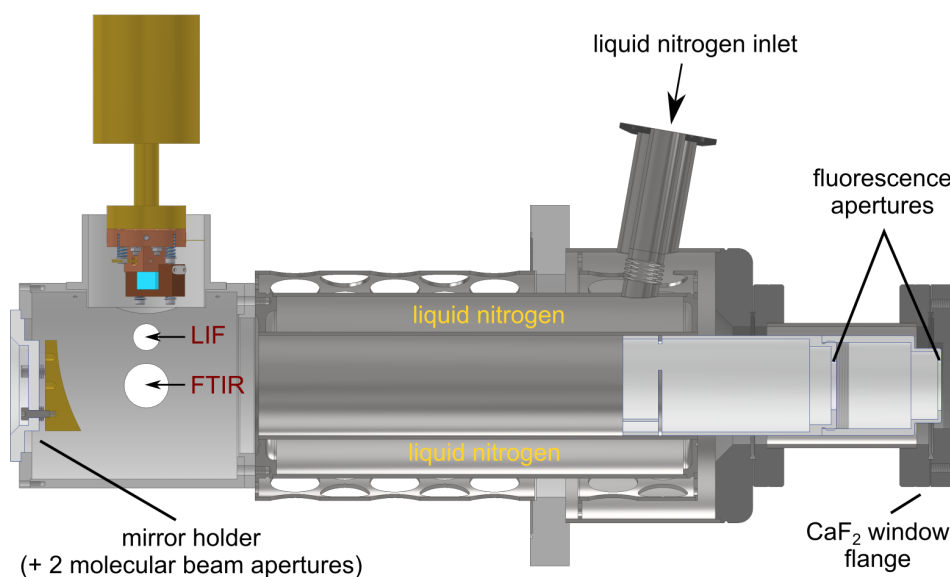[1] Note that all mirrors in the mid-infrared emission spectrometer are gold mirrors.

Figure 3.4: Drawing of the liquid-nitrogen cold shield and description of its main components.

SNSPD. The two-stage cryocooler consists of a ^{4}He and ^{3}He gas reservoir, both of which consist of a sorption pump and a cold head. The ^{4}He and ^{3}He cold heads are labeled in Fig. 3.3 with their final temperatures ("1.0 K" and "0.3 K", respectively). The cold heads are thermally connected such that the liquified ^{4}He can be used to pre-cool the ^{3}He stage. Each sorption pump can be individually heated to desorb helium gas, which can then be liquified by opening a heat switch to establish a thermal connection between the pump and the 4 K base plate. The complete cooldown procedure is found in Section 3.2.4.

To reduce background from thermal radiation on the SNSPD, the different temperature stages are shielded by two additional chambers within the spectrometer chamber, as implied in Fig. 3.3. The ^{4}He and ^{3}He stages are shielded by a layer made of gold-plated aluminum. An additional outer layer of aluminum, coated with cryogenic insulation foil, further shields the 4 K stage and the ^{4}He and ^{3}He stages and is attached to the bottom of the monochromator. The spectrometer chamber is separately pumped by a turbomolecular pump (Turbovac 150, Leybold-Heraeus) and reaches a base pressure of approx. 1×10^{-5} mbar. Inside the radiation shields, the pressure is expected to be higher than 1×10^{-5} mbar as no additional apertures, which would improve gas conductivity, are added to these shields. This is necessary because additional apertures would drastically increase the amount of thermal radiation reaching the SNSPD. Because of the inefficient

pumping speed for the inner chamber, sufficient pumping times (approx. 1 day) are required before activation of the helium cryostat to avoid condensation of background gas.

The monochromator (see Fig. 3.5) is attached to the 40 K stage baseplate and is further shielded from thermal radiation by a gold-plated aluminum cover. Realistic operating temperatures lie between 50 and 70 K. The collimated infrared light collected by the 30° off-axis parabolic mirror (reflected focal length: 54.5 mm) inside the UHV chamber is focused onto a 100 μm entrance slit using another 90° parabolic mirror (M1, reflected focal length: 76 mm). After passing through the entrance slit, the light is collimated by parabolic mirror M4, dispersed by a ruled diffraction grating (300 lines/mm, blaze wavelength: 3 μm, blank size: $30 \times 40 \times 10$ mm^3, Horiba) and then refocused by mirror M5 and flip mirror M6 onto the 100 μm exit slit to which the mid-IR fiber is connected. Note that the entrance and exit slit widths match the core diameter of the mid-IR fiber. The grating angle is controlled using a linear stepper motor (AZM26AK, Orientalmotor) that sets the position of the lever connected to the grating mount. The maximum grating angle is approx. 45°, which corresponds to a minimum emission frequency of 2200 cm^{-1} using the 300 lines/mm grating. At the entrance and exit slits of the monochromator, optical filters can be readily inserted into the optical path using two multi-filter holder plates.

The present experimental setup supports SNSPD arrays with up to four detector elements while the previous setup has used a single detector element (16 μm $\times$ 16 μm). [31, 93] The SNSPD array used in this work consists of four 25 μm $\times$ 100 μm detector stripes made of amorphous tungsten silicide (a-WSi) that were provided by Varun Verma (NIST, Boulder, Colorado, USA). The composition of the 150 nm wide and 4 nm thick WSi film is $W_{0.75}Si_{0.25}$. Theoretically, the 4-pixel array would give a total detection area that matches the 100 μm fiber core diameter and is ~31 times larger than that of the previously used detector. However, the relative detection efficiency of the individual elements, which depends strongly on the switching current (see also Section 2.3.1), restricts the useful detection area. Since higher switching currents correlate with larger detection efficiencies and the switching current is limited by imperfections along the nanowire, the best quality SNSPD element typically outperforms the other detector elements. Therefore, an ideal detector array would contain four identical detector elements. However, the SNSPD element highlighted in Fig. 3.6a, exhibiting a switching current of 5.8 μA, showed a much higher sensitivity than all other elements such that only this SNSPD element has been used for all LIF experiments. As estimated from the overlap between detector element and fiber core, only 20 % of the potential detection area are used. Thus, the active detection area is about 6 times larger than with the previous
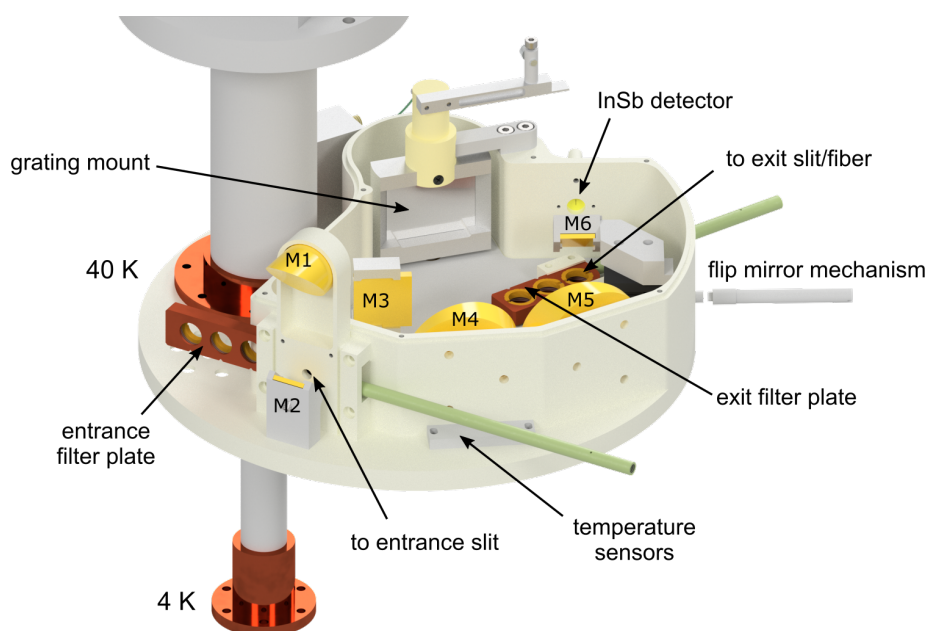
Figure 3.5: Rendered image of the Czerny-Turner monochromator, which is attached to the 40 K baseplate of the cryocooler inside the spectrometer chamber. Note that most light colored materials are gold-coated for shielding against thermal radiation. Additional gold-coated covers that shield the optical path are not shown for clarity.

detector but leaves room for further improvement.

A schematic diagram of the SNSPD bias and readout circuit for a single detector element is shown in Fig. 3.6b. A DC bias voltage on the order of 0 to 100 mV is supplied by an isolated voltage source (SIM928 isolated voltage source mounted on a SIM900 mainframe, Stanford Research Systems), which provides bias currents between 0 and 10 µA with low noise levels. A low-pass filter (BLP-1.9+, Mini-Circuits) is used in addition. A second low-pass filter is used in front of a voltmeter (SIM970, Stanford Research Systems) that can be used to measure the voltage across the nanowire. The measured voltage can be used to identify events in which the SNSPD switches to its non-superconducting state due to external influences and automatically reset it to its superconducting state by interrupting the bias voltage for a short period of time. A bias tee (JEBT-4R2GW+, Mini-Circuits) is used to pass only the radio frequency (RF) signal from the SNSPD to an amplifier (SGL0622Z, Qorvo), which is mounted on the 40 K plate of the monochromator to reduced amplification noise. A multi-channel scaler

(MCS) (MCS6A-2, FAST ComTec) with 100 ps resolution is used to detect the amplified voltage pulses. In principle, the present setup provides four separate circuits for each detector element. After passing separate Schmitt triggers, the counts from all detector elements can be combined using an OR gate, which outputs a single pulse if any of the four SNSPD elements detects a photon. However, since only a single detector element was used in this work, this circuit has not been used and the output of the single SNSPD element was directly connected to the MCS.
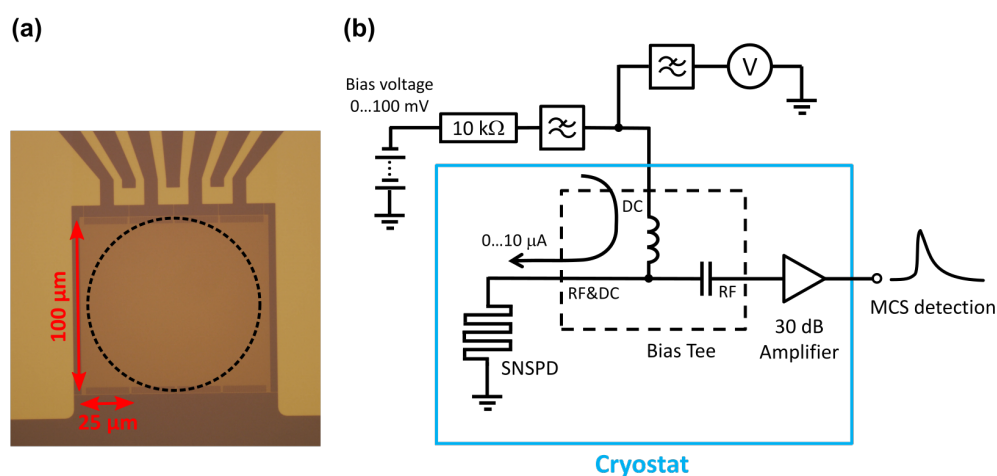
(a)   **(b)**

Figure 3.6: (a) Optical microscope image of the 4×1 SNSPD array, with dimensions of 25×100 μm^2 for each element. The single detector element that was used in this work is indicated by red arrows. The dashed circle indicates the dimensions of the mid-IR fiber core, which is centered on the SNSPD array. The microscope image was kindly provided by Varun Verma. (b) Schematic diagram of the bias and readout circuit for a single SNSPD element.

3.1.3 Infrared excitation laser setup

The infrared excitation laser setup operates in the fundamental vibrational frequency region of CO and relies on difference frequency generation (DFG). A seeded Nd:YAG laser (Continuum Surelite III-10EX, 10 Hz repetition rate, 6 ns pulse width, 0.005 cm^{-1} bandwidth) is used to generate 1064 nm pulses and pump a dye laser (Sirah Cobra-Stretch, laser dye: LDS867 in ethanol) via its second harmonic. Type-I difference frequency mixing of the p-polarized 1064 nm Nd:YAG laser pulse (~120 mJ/pulse) and the s-polarized dye laser pulse (~15 mJ/pulse) in a LiIO$_3$ crystal held at 100 °C is used to generate p-polarized mid-IR pulses. The frequency of the mid-IR light is tunable

between approx. 1900 and 2700 cm^{-1} using the LDS867 dye. A schematic of the laser setup including a typical pulse energy spectrum is shown in Fig. 3.7. The dip between 2250 and 2400 cm^{-1} is due to absorption by atmospheric CO_2. For excitation of the fundamental $^{12}C^{16}O$ and $^{13}C^{18}O$ vibrations, laser powers typically lie between 100 to 150 μJ/pulse.

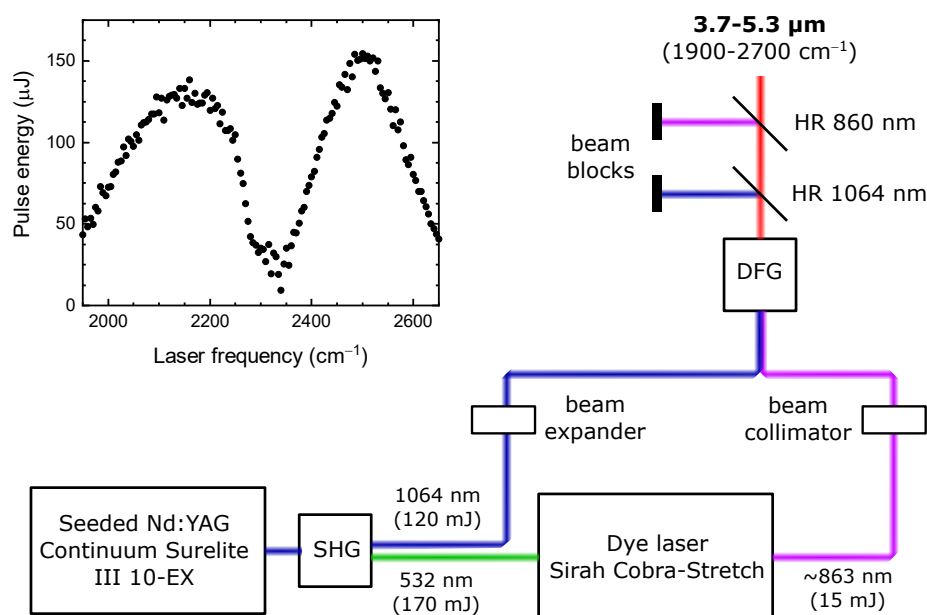Figure 3.7: Schematic drawing of the laser setup for generating mid-infrared (MIR) nanosecond pulses between approx. 1900 and 2700 cm^{-1}. Blue and green beams represent 1064 and 532 nm light. The purple beam represents the output from the dye laser (center frequency: 863 nm), which is pumped by the 532 nm output of the Neodymium-doped yttrium aluminum garnet (Nd:YAG) laser. The MIR light, produced by DFG of 1064 and 863 nm, is indicated in red. A typical pulse energy spectrum is shown as an inset.

The excitation laser frequencies are calibrated against rovibrational spectra measured with a photoacoustic cell filled with ∼10 mbar of CO in natural abundance. For this purpose, absorption lines in the $^{12}C^{16}O$ fundamental region between 2050 and 2170 cm^{-1} have been observed and compared to line positions from the HITRAN database. [127] The estimated accuracy of this calibration is ±0.2 cm^{-1} for this range.

Figure 3.8a shows the typical optical path of the mid-IR light in the LIF experiments. A planoconvex CaF_2 lense (f = 500 mm) is used to focus the excitation laser beam onto the NaCl surface, under an incidence angle of 45°. The diameter of the laser

focus at the surface is estimated as ∼1 mm, which is larger than the focus of the off-axis parabolic mirror that collects the fluorescence and reflects the collimated light toward the monochromator. Laser light that is transmitted through the crystal is blocked to avoid damage of the InSb detector of the FTIR spectrometer. Note that also the molecular beams cross at the focus position of the parabolic mirror .
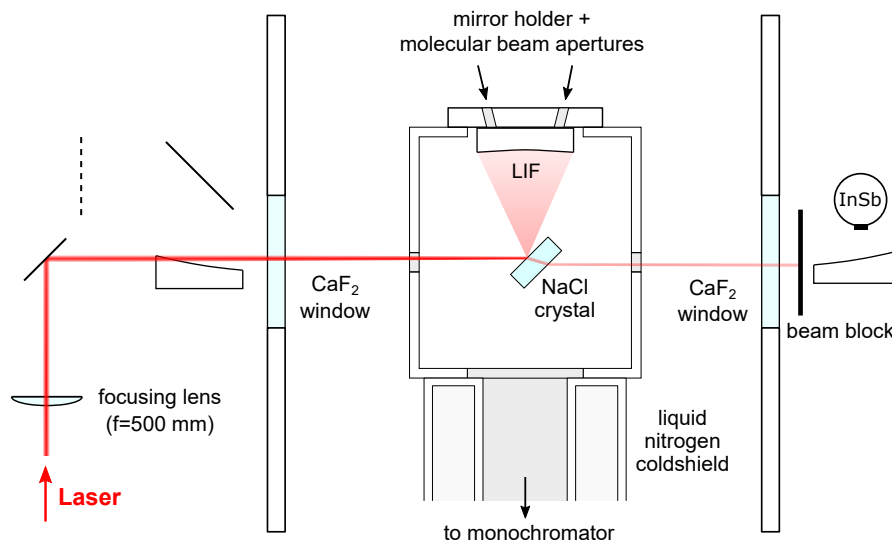
3.1.4 Fourier transform infrared spectrometer

The FTIR spectrometer (Vertex 70v, Bruker) is set up in external transmission geometry (see Fig. 3.8b). MIR light from the globar source of the FTIR spectrometer passes throughh the NaCl crystal and is detected with a liquid-nitrogen cooled InSb detector (ID413, InfraRed Associates). Two vacuum compartments (optics boxes) are connected to the UHV chamber via differentially pumped CaF_2 windows; the first compartment connects the UHV chamber with the FTIR spectrometer and the second box contains the InSb detector. The vacuum compartments as well as the FTIR spectrometer are under vacuum ($\sim 4 \times 10^{-2}$ mbar) to avoid atmospheric absorption along the optical path.

In the first optics box, a wire grid polarizer (WP50H-K, Thorlabs) is used to selectively block p- or s-polarized light from the unpolarized mid-infrared light source. An aperture wheel in front of parabolic mirror that collects light from the MIR source and sends it into the interferometer can be used to select the size of the FTIR beam at the surface. The size of the FTIR beam is approximately twice as large as the selected aperture size because the reflected focal length of the 90° off-axis parabolic mirror differs from that of the parabolic mirror inside the spectrometer. An elliptical mirror is used to refocus the light that passes through the crystal onto the InSb detector.

3.1.5 Pulsed molecular dual-beam source

A molecular beam source chamber that provides two pulsed molecular beams that cross at the LIF position under an angle of 30° has been installed for controlled dosing of layered adsorbate structures (see Fig. 3.9). The source chamber consists of three differentially pumped chambers, each of which is pumped by a $300 \, \mathrm{L \, s^{-1}}$ turbomolecular pump (first and second stage: STP-301C, Edwards; third stage: HiPace 300M, Pfeiffer). Solenoid valves (Pulse Valve 009-0582-900, Parker) are used to create gas pulses which undergo a supersonic expansion. A nickel skimmer with a 1.0 mm orifice (Beam Dynamics) is placed 3.5 cm downstream from each nozzle. The skimmers are installed on sliding valves to allow the first differential stage to be separated from the other two stages for maintenance reasons, e.g. replacement of the nozzles. The other differential stages are

(a) LIF measurement

mirror holder +
molecular beam apertures

LIF

InSb

CaF$_2$
window

NaCl
crystal

CaF$_2$
window

beam block

focusing lens
(f=500 mm)

liquid
nitrogen
coldshield

Laser

to monochromator

(b) FTIR measurement

wire grid
polarizer

FTIR

InSb

parabolic
mirror

CaF$_2$
window

NaCl
crystal

CaF$_2$
window

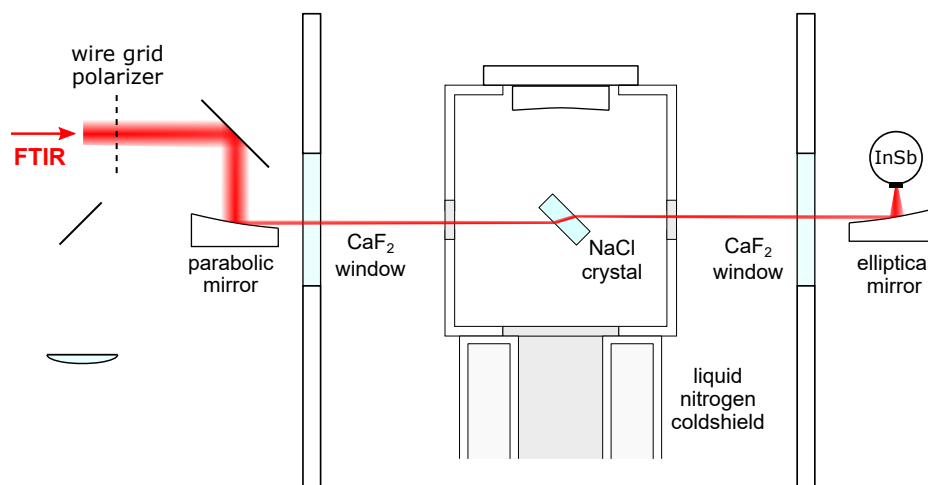elliptical
mirror

liquid
nitrogen
coldshield

Figure 3.8: Optical path and components for (a) the LIF experiments and (b) the infrared absorption measurements using the FTIR spectrometer. The area between the two CaF$_2$ windows represents the UHV chamber whereas the outer areas represent the optics boxes, which are also evacuated ($\sim 4 \times 10^{-2}$ mbar). Note that the optical paths are at different z-positions and orientations of the NaCl crystal. Furthermore, the two molecular beams propagate at the same height as the LIF focus.

separated by apertures whose sizes are chosen to match the size of the molecular beam, which is about 10 to 11 mm in diameter at the surface.

Both nozzles are operated by a single valve driver (Iota One, Parker) and a LabView program is used to switch between the nozzles and trigger a predefined number of pulses. Typical stagnation pressures between 1 to 2 bar and repetition rates between 40 to 50 Hz are used. Typical pressures for each chamber under these operating conditions are also indicated in Fig. 3.9. The two nozzles were connected to different variants of CO gas: CO gas in natural abundance (99.997% chemical purity, Linde), isotopically pure $^{12}C^{16}O$ (99.9% chemical purity, 99.99% ^{12}C, 99.95% ^{16}O, Sigma-Aldrich) and isotopically pure $^{13}C^{18}O$ (99.8% chemical purity, 99.9% ^{13}C and 99.2% ^{18}O, Sigma-Aldrich). The typical gas type used with each nozzle for dosing isotopically layered samples of $^{12}C^{16}O$ and $^{13}C^{18}O$ are also indicated in Fig. 3.9.
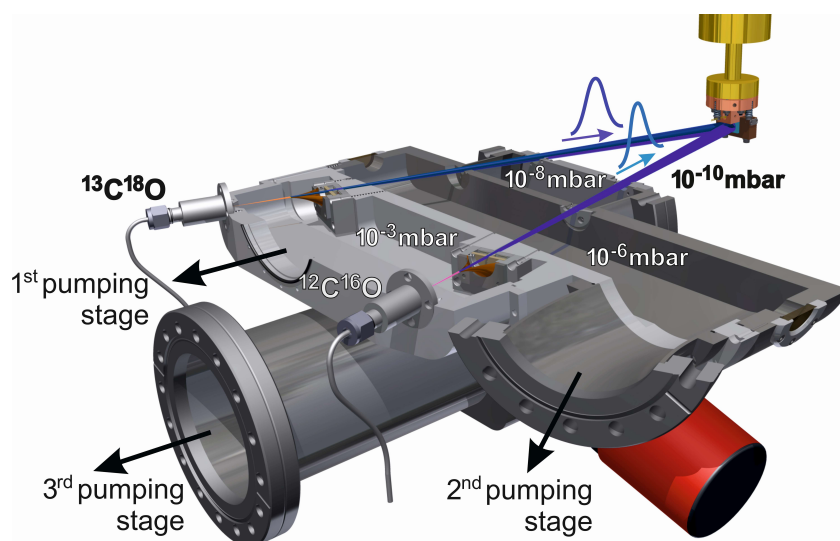

Figure 3.9: Rendered image of the three differentially pumped stages of the molecular beam source chamber. Furthermore, the directions of the molecular beams, which cross at the surface position, are indicated. Typical operating pressures and gases are shown as well. From Ref. [126]. Reprinted with permission from AAAS.

3.1.6 Temperature-programmed desorption

TPD has been used to acquire the experimental results in Chapter 7. For these experiments, the mass spectrometer (RGA200, Stanford Research Systems) that is typically used as a residual gas analyzer was slightly modified. First, the mass spectrometer was separated

from the main chamber by a 2 mm aperture. Second, the standard metal tube that surrounds the ionizer and quadrupole mass analyzer was replaced by a tube with an additional port for differential pumping.

3.2 Experimental procedures

3.2.1 NaCl(100) surface preparation and cleaning

Clean NaCl(100) surfaces are prepared by cleaving NaCl single crystals under UHV conditions. For the cleaving procedure, a stainless steel blade mounted on the wobble stick is positioned under the NaCl sample. Downward motion of the NaCl sample drives the blade into the crystal until it cleaves along the (100) plane. The NaCl crystal is cleaved both on the front of the crystal, which is exposed to the infrared excitation laser and the molecular beams during dosing, and the back of the crystal, which is only relevant to FTIR measurements (see also Fig. 3.8). After cleavage, the length of the crystal is typically 15 to 20 mm, which allows transmission of light in the FTIR experiments at a 45° tilt angle.

Between experiments, the NaCl crystal is decoupled from the helium cryostat and is heated to 380 K to avoid contamination of the surface by residual gas in the chamber. In particular, adsorption of water can lead to surface degradation over time and can be avoided at 380 K. [128] Using this procedure, a cleaved NaCl surface can be used for several months without significant degradation. The absorption linewidth of an adsorbed CO monolayer measured with FTIR spectroscopy is used as an indicator for the quality of the crystal surface.

During experiments, the NaCl crystal is in thermal contact with the helium cryostat to achieve cryogenic temperatures (base temperatures are typically around 6 K if the sample is inside the liquid-nitrogen cold shield and 11 K outside the cold shield). While cooling the NaCl crystal from 380 K to cryogenic temperatures prior to the experiment, the upper part of the sample holder heats up significantly, which leads to desorption of adsorbed gases. Therefore, CO samples are prepared immediately after cooling of the NaCl crystal to minimize surface contamination by gases that desorb from the upper sample holder parts in the cooldown procedure, in particular water. For desorption of CO layers during the experiments, the crystal is heated to 60 K.

3.2.2 CO sample preparation

Unless otherwise stated, CO samples adsorbed on the NaCl surface were prepared using molecular beam dosing with the setup described in Section 3.1.5. Alternatively, a leak valve could be used to introduce CO background gas to the chamber at a defined pressure. Note that both sides of the NaCl crystal are covered using leak valve dosing while only the front of the crystal is covered using molecular beam dosing.

For molecular beam dosing, the front of the NaCl crystal is oriented such that it faces the molecular beam source chamber (see also Fig. 3.9), which corresponds to an incidence angle of 15°. Thus, only the crystal front is covered using molecular beam dosing. The size of the molecular beams (10 to 11 mm), which overlap at the surface position, is slightly smaller than the crystal width (15 mm). CO monolayers were prepared at a surface temperature of 25 K. The number of molecular beam pulses was chosen such that a complete monolayer was formed. Before cooling to lower temperatures for LIF experiments, FTIR spectra of the monolayer are measured. If any additional multilayer absorption is detected in the FTIR spectra, the sample is kept at 25 K until the residual overlayer has desorbed. CO multilayers are prepared epitaxially on top of the monolayer sample at a crystal temperature of 22 K, where desorption of the multilayer is avoided. The multilayer coverage can be controlled by the number of molecular beam pulses which is directly proportional to the coverage. After dosing, the sample is typically cooled to 6-7 K for LIF or FTIR measurements.

With leak valve dosing, a CO monolayer is prepared by introducing a CO pressure of approx. 2×10^{-7} mbar for 3 min at a surface temperature of 55 K. While slowly closing the leak valve, the sample is cooled to 35 K and held at that temperature until the pressure drops below 2×10^{-9} to 3×10^{-9} mbar to avoid absorption of multilayers. For multilayer dosing, the crystal is cooled to 22 K and CO background pressure of 2×10^{-6} mbar, corresponding to a growth rate of about 20 layers/min, is used. After dosing, the sample is cooled to 6-7 K for LIF or FTIR measurements.

3.2.3 FTIR absorption measurements

Infrared absorption spectra are used to characterize the samples before and after the LIF experiments and are recorded using the OPUS 7 software provided by Bruker. Reference spectra are measured with a clean NaCl crystal under the same experimental conditions as the sample spectra before dosing. Typically, FTIR spectra are measured with p- and s-polarized light at an incidence angle close to 45° to be able to probe vibrations parallel and perpendicular to the surface. Furthermore, spectra are recorded at the

highest possible resolution ($0.2\,\text{cm}^{-1}$) since the absorption features of the CO monolayer are even narrower. [129] With $0.2\,\text{cm}^{-1}$ resolution, a 4-point (trapezoidal) apodization function is used, which causes little broadening of the peak shape but suppresses side lobes better than a boxcar apodization function. Interferograms are averaged over 128 scans (single sided, forward-backward). A zero-filling factor of 4 and a Mertz phase correction is used for the discrete Fourier transform. For most experiments, a 1.5 mm aperture has been used which corresponds to a spot size of 3 mm at the surface. Since the FTIR light passes the NaCl crystal under an incidence angle of approx. 45°, the crystal position is chosen such that clipping of the FTIR beam is avoided and that only CO covered crystal areas are probed.

Some spectra show periodic baseline modulations with a period of ~$0.7\,\text{cm}^{-1}$, which are attributed to interference effects due to multiple reflections within the optical path, and are particularly pronounced if the baseline signal changes over the course of the measurements. However, these modulations can be efficiently removed by lowering the effective resolution of the spectra, which is particularly useful for quantitative analysis, for example to determine the integrated absorbance of a peak. In this case, the absorbance spectra are recalculated from the high-resolution interferograms with lower ($0.4\,\text{cm}^{-1}$) resolution and a 4-term Blackman-Harris apodization function, giving an effective resolution of ~$0.7\,\text{cm}^{-1}$.

3.2.4 SNSPD cool-down procedure

The critical superconducting temperature of the SNSPDs made of amorphous WSi used in this work is about 3.7 K and lower temperatures are advantageous to achieve better detection efficiencies and lower dark count rates. [98] Thus, the SNSPD is cooled to 0.6 K using the two-stage sub-Kelvin ^{3}He cryocooler described in Section 3.1.2 prior to LIF measurements. The cool-down procedure is illustrated in Fig. 3.10 and described in the following.

First, two sorption pumps connected to the ^{4}He and ^{3}He gas reservoirs (^{4}He pump and ^{3}He pump) are regenerated by heating to ~50 K. The pumps kept at this temperature until the ^{4}He and ^{3}He cold heads (^{4}He head and ^{3}He head) reach their base temperature, typically between 4.2 and 4.5 K. At this temperature, a maximum amount of ^{4}He is liquified. In a second step, the ^{4}He pump is thermally connected to the 4 K stage of the 4 K crycooler by opening an adjustable heat switch. Adsorption of gaseous ^{4}He results in a lower vapor pressure and thus in a lower boiling point, as evident from the decrease of the ^{4}He and ^{3}He head temperatures between 60 and 80 min. Once the ^{4}He head reaches 1 K, which is thermally connected with the ^{3}He stage via the film burner,
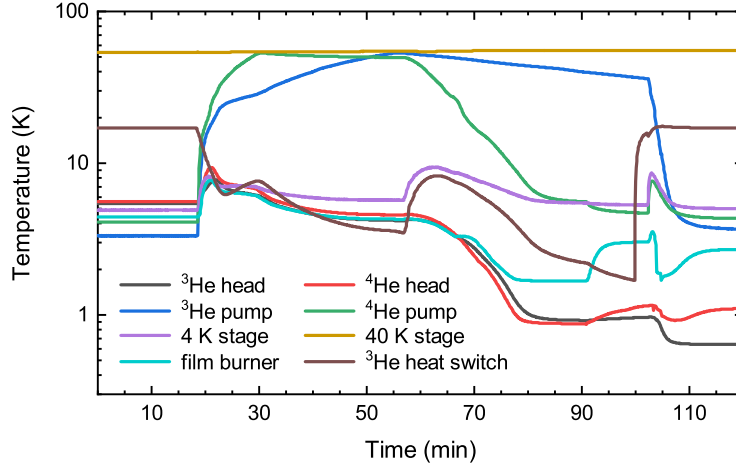
Figure 3.10: Time-dependent temperature curves of different parts of the two-stage sub-Kelvin cryocooler that are involved in cooling the SNSPD to 0.6 K.

a large amount of ^{3}He is liquified in the ^{3}He head. Finally, the ^{3}He pump is thermally connected with the 4 K stage by opening another heat switch (^{3}He heat switch) to reduce the vapor pressure of ^{3}He and lower the temperature of the ^{3}He head and the attached SNSPD to 0.6 K. The complete cool-down procedure is completed within 1.5 h and the final temperature is held for about 20 h before the SNSPD warms up.

3.2.5 Monochromator calibration

With the chosen monochromator design, the position of the linear stepper motor should ideally be directly proportional $\sin(\theta)$, where θ denotes the tilt angle of the grating relative to its zeroth order position (shown in Fig. 3.5), and thus to the emission wavelength, λ. To account for deviations from this linear relationship, a wavelength calibration is carried out by scattering light from a cw Nd:YAG laser (SI-2000 Seeder System, Continuum), normally used as a seed laser in the excitation laser setup, from the NaCl crystal under the same conditions as in the LIF experiments. Furthermore, the calibration is done at cryogenic temperatures, which differs from a room temperature calibration due to thermal contraction. With the 300 lines/mm grating used for this work (maximum wavelength observable in first order: approx. 4.5 µm), the first to fourth diffraction orders

of the 1064 nm fundamental can be detected.[2] The exact wavelength of the Nd:YAG laser, λ_{YAG}, was independently determined with a wavemeter (Wavelength meter WS-7, HighFinesse). For a selected calibration measurement, the stepper motor positions, x, in units of motor revolutions (rev), relative to the zero order position are presented in Fig. 3.11, for the four effective diffraction order wavelengths, $n\lambda_{\mathrm{YAG}}$, where n is the diffraction order. The observed dependence is nearly linear, where B_1 is the slope, but an additional quadratic term, $B_2\lambda^2$, is necessary for a proper description:

$$x = B_1\lambda + B_2\lambda^2. \tag{3.1}$$

Replacing λ with $\lambda = 1/\tilde{v}$ gives the emission wavenumbers as a function of motor position:

$$\tilde{v} = \frac{B_1}{2x} + \sqrt{\left(\frac{B_1}{2x}\right)^2 + \frac{B_2}{x}}. \tag{3.2}$$

The residuals in Fig. 3.11 are less than 0.015 rev which translates to an error less than $4\,\mathrm{cm}^{-1}$ in the range of interest (2750-4250 cm^{-1}). For selected frequencies in this range, the maximum calibration errors based on the 0.015 rev uncertainty are given in Table 3.1. The wavelength resolution of the monochromator is constant and has been determined experimentally as $\sim 7\,\mathrm{nm}$ from the full width at half maximum (FWHM) of single emission lines. Since the emission wavenumbers are inversely proportional to λ, the resolution in the wavenumber domain depends on the absolute emission wavenumbers and corresponding values are also shown in Table 3.1 for the spectral region of interest. For all frequencies, the achieved frequency accuracy is at least three times better than the spectrometer resolution.

It should be noted that the mochromator calibration stays accurate within the given frequency accuracy even if the temperature of the monochromator changes, as an increase in the temperature of the 40 K stage from 50 to 70 K typically occurs over the course of weeks. Also venting of the spectrometer chamber, for example to replace the mid-IR fiber or the SNSPD, does not affect the calibration.

---

[2] Because the mid-IR fiber does not transmit light below 1.5 μm wavelength, visible alignment lasers (e.g. HeNe lasers) cannot be used although they would provide more calibration points in this frequency range. The cw Nd:YAG laser light (1064 nm), however, has sufficiently large intensity to be transmitted through the fiber.
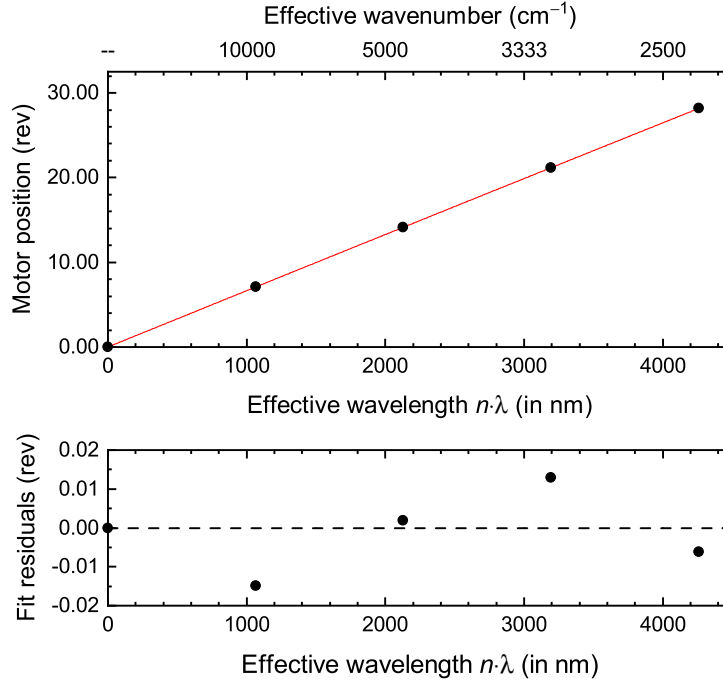
Figure 3.11: In the upper panel, dots represent the stepper motor position as a function of the effective wavelengths, $n\lambda_{YAG}$, of the first four diffraction orders from the seed laser used for the monochromator calibration. The exact wavelength of the fundamental is 1064.49 nm. The red, solid line shows a quadratic fit to the data ($B_1 = 6.668 \times 10^{-3}$ rev nm^{-1} and $B_2 = -1.3 \times 10^{-8}$ rev nm^{-2}). The lower panel shows the corresponding fit residuals.

Table 3.1: Maximum calibration errors and absolute spectral resolution for frequencies between 2750 and 4250 cm^{-1}, which are the most relevant frequencies for this work.

Emission frequency (cm^{-1})	4250	4000	3750	3500	3250	3000
Max. calibration error (cm^{-1})	4.1	3.6	3.2	2.8	2.4	2.0
Resolution (cm^{-1})	13	11	10	9	7	6.3

3.2.6 Laser-induced fluorescence alignment

For the laser-induced fluorescence experiments, the excitation laser focus and the focus of the fluorescence collection optics in the UHV chamber (see also Figs. 3.3 and 3.8a) need to be overlapped. In a pre-alignment procedure, a visible He-Ne fiber laser is connected to the fiber connector at the exit slit of the monochromator instead of the mid-IR fiber. The He-Ne laser light follows the reverse optical path of the infrared fluorescence and is focused onto the NaCl sample holder by the parabolic collection mirror attached to the cold shield. This focus spot is overlapped with another He-Ne laser, which later defines the optical path of the pulsed infrared excitation laser. This pre-alignment procedure gives sufficient overlap between the excitation laser and the focus of the collection optics for the detection of LIF signal.

To determine the crystal position at which the CO covered NaCl surface is imaged by the collection optics, about 50 layers of CO are prepared on the NaCl surface. Using this sample, the total fluorescence signal is monitored with the grating positioned at zeroth order while the CO multilayer absorption band (2138.6 cm^{-1} for $^{12}C^{16}O$) is excited with the infrared laser. The resulting fluorescence signal is then used to determine the correct crystal position. At this position, the excitation laser alignment is fine-adjusted to increase the overlap with the collection optics and, afterward, a focusing lens ($f = 500$ mm) is inserted into the optical path. Utilizing the optimized fluorescence signal, the zero order position of the grating can be accurately determined. This is necessary as the zero order position depends slightly on the exact temperature of the 40 K stage, which is found to increase with time from approx. 45 to 70 K. Note that only the last two steps need to be repeated on a daily basis to compensate for small changes in the optical path.

3.2.7 Laser-induced fluorescence measurements

This section describes the measurement conditions and procedures to obtain time-resolved measurements of single vibrational states as well as time-integrated excitation and emission spectra using LIF. Photon detection events from the SNSPD are counted by the MCS as a function of time (see also Section 3.1.2). The MCS has a maximum time-resolution of 100 ps and, using a picosecond laser, we have achieved sub-nanosecond time resolution with an SNSPD similar to the ones used in this work. [93] For the experiments presented here, the time resolution is limited by the temporal width of the the pulsed nanosecond laser (4.7 ns FWHM). [20] Thus, data is typically collected with a comparable bin time of 12.8 ns, defining the theoretical time resolution. However, the effective resolution of the experiments depends on the SNR; while excitation of

samples with 50-100 layers can realistically provide sufficient SNR at 12.8 ns resolution, excitation of a monolayer typically requires rebinning of the data for a comparable SNR, effectively lowering the resolution. The fluorescence signals are recorded up to ~50 ms after laser excitation because rates for vibrational relaxation in CO/NaCl(100) are small and can be on the order of $10\,s^{-1}$.

Typical time profiles, measured for fluorescence from a single emission line, are shown in Fig. 3.12. Figure 3.12a illustrates an example of a time profile measurement observing a high intensity emission line after excitation of a $^{12}C^{16}O$ monolayer covered by 100 $^{13}C^{18}O$ overlayers, which gives the best SNR for excitation of a single layer (see also Chapter 6). With 12.8 ns bins, barely any trend can be observed; rebinning to 640 ns allows a rising time of about ~10 µs to be resolved. $t = 0$ corresponds to the arrival time of the excitation laser pulse which can be readily determined by observing stray light from the excitation laser, which is blocked here using optical filters (see below for further details). Fig. 3.12b, on the other hand, shows the temporal decay for an emission line with about 10 times smaller intensity observed when a $^{13}C^{18}O$ monolayer covered by 100 $^{12}C^{16}O$ overlayers is excited (see Chapter 6), which is at the limit of what can still be clearly seen in the corresponding emission spectra. In this case, the initial rising part is not resolved within the 640 ns resolution and the SNR is obviously worse than in the first example.

Time-integration of these profiles allows measurements of LIF emission spectra, i.e., emission frequency is varied at a fixed excitation frequency, or excitation spectra, i.e., the excitation frequency is varied at a fixed emission frequency. Integration time windows are chosen such that they cover different parts of the time-dependent signal. The size of the integration windows ranges from 10 µs and 9 ms but the lower integration limit of each window is identical and placed close to the arrival time of the excitation laser pulse ($t = 0$), either at 0.005 or 0.05 ms (illustrated in Fig. 3.12c). Background is recorded simultaneously by integrating over the 45-50 ms window after laser excitation, in which no fluorescence signal is observed. Because time-integrated spectra do not require the 12.8 ns time resolution used for time-resolved measurements of a single emission line, data is acquired with lower 819.2 ns resolution to reduce the amount of data transferred from the MCS and thus speed up the data acquisition process.

The measured time profiles reflect the kinetic traces of the measured vibrational states as long as the maximum number of counts per bin (i.e., the event count rate) is below a threshold that avoids overlapping detection events. This maximum count rate can be determined from the recovery time of the SNSPD. The dead time of the detector extends over approx. 400 ns, which corresponds to count rate 2.5×10^6 counts s^{-1}. To avoid two detection events within the dead time, the SNSPD is operated with a bias current
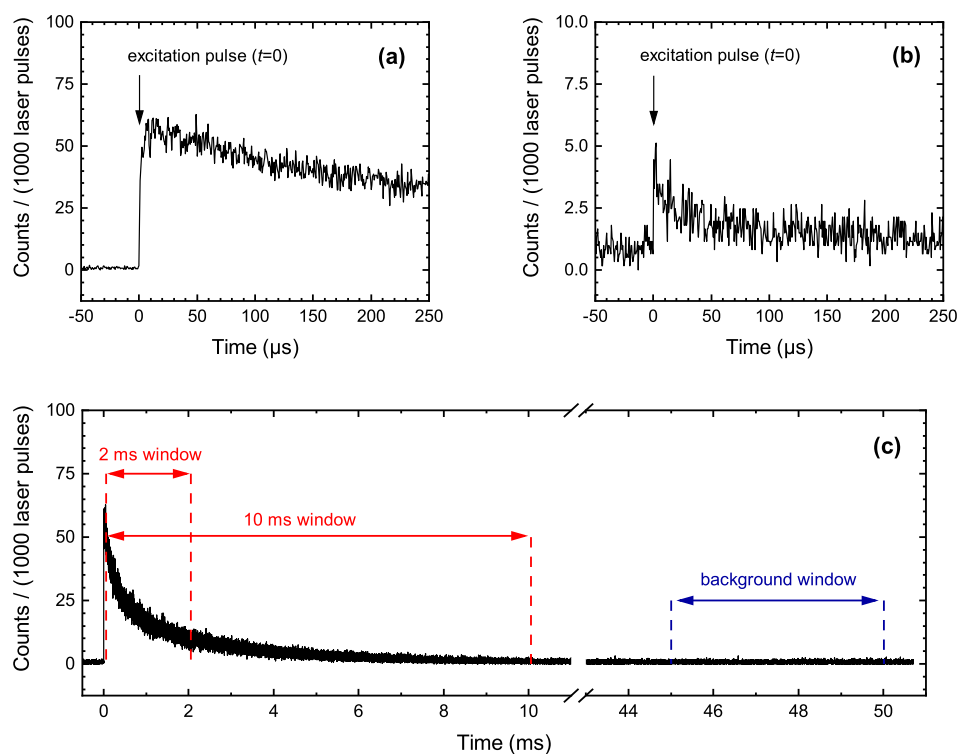
Figure 3.12: (a) Temporal profile for a high intensity emission line in the region where laser excitation occurs ($t = 0$). The line corresponds to the $3677\,\mathrm{cm}^{-1}$ emission line observed for excitation of a $^{12}\mathrm{C}^{16}\mathrm{O}$ monolayer covered by $^{13}\mathrm{C}^{18}\mathrm{O}$ overlayers (see Chapter 6). (b) Temporal profile for a low intensity emission line that can still be clearly detected in the emission spectrum. The line corresponds to the $3695\,\mathrm{cm}^{-1}$ emission line observed for excitation of a $^{13}\mathrm{C}^{18}\mathrm{O}$ monolayer covered by $^{12}\mathrm{C}^{16}\mathrm{O}$ overlayers (see Chapter 6). (c) The same temporal profile as in a) is shown for long times up to $50\,\mathrm{ms}$. In addition, selected integration time windows for time-integrated excitation and emission spectra are indicated. Measurement windows start shortly after the laser pulse (here: $0.05\,\mathrm{ms}$) to avoid integration over $t = 0$, which may contain contributions from scattered light. For demonstration purposes, only 2 and $10\,\mathrm{ms}$ windows are shown. For background, the 45-50 ms time window is used. All time profiles share the same bin size of $640\,\mathrm{ns}$.

that ensures a maximum count rate of 10^5 counts s^{-1} that is one order of magnitude smaller. For a typical bin time of 640 ns accumulated over 1000 laser pulses, this would correspond to a maximum number of 64 counts, which is not exceeded for the high intensity emission line in Fig. 3.12a.

In addition, double counting of the peaks should be avoided. This can result from noise during the detector dead time which triggers another detection event on the MCS. The amplified pulse shape in the current setup is clearly distorted by the amplifier circuit, as apparent in Fig. 3.13. It consists of two sharp peaks followed by a broad oscillatory pattern that reflects the 400 ns dead time of the SNSPD. Setting the detection threshold of the MCS at the value indicated in Fig. 3.13 helps to avoid double counting while the distorted pulse shape does not compromise the temporal resolution. The rising edge of the pulse (Fig. 3.13b) extends over only 2 ns and the observed timing jitter, observed by monitoring several detection events with the oscilloscope, is similarly small. This 2 ns uncertainty is likely limited by the 500 MHz bandwidth of the oscilloscope (Wavejet 354A, LeCroy). Thus, the actual timing jitter is expected to be much smaller than the limit to the temporal resolution imposed by the laser pulse.
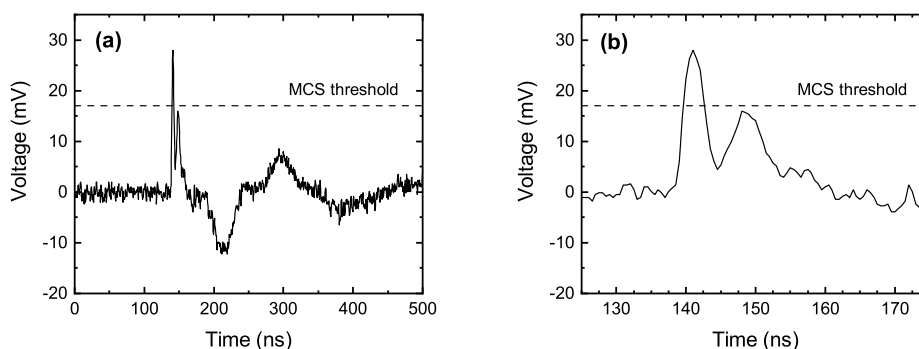
Figure 3.13: (a) Oscilloscope trace of a single, amplified SNSPD voltage pulse measured at a bias current of 5.4 µA. The dashed line indicates a typical detection threshold value used for the MCS, which avoids double counting of pulses. (b) Rising edge of the pulse presented in (a).

Optical filters can be applied at the entrance and exit slits of the monochromator to block unwanted frequencies (see also Section 3.1.2). In this work, mainly the overtone emission region of the C-O stretching vibration, ranging from ~4250 to 2600 cm^{-1}, is used as a compromise between large SNSPD detection efficiencies at short wavelengths and comparatively small background from thermal background radiation that originates from the UHV chamber. Thus, an optical bandpass filter (center wavelength: 3100

nm, bandwidth: 1300 nm, Andover) for this spectral region is used. The bandpass filter is particularly important for blocking light with frequencies above ~5500 cm^{-1}, which would otherwise be observed as second-order peaks in the CO overtone region. Furthermore, an optical longpass filter (PW-S-00501, 3 mm thick Infrasil, Laseroptik) is used to block stray light from the excitation laser pulse that is scattered into the detector, which can potentially saturate the SNSPD and thus effectively lower the time resolution near $t = 0$. The transmission spectra of these optical filters, as measured with the FTIR spectrometer, are presented in Fig. 3.14.
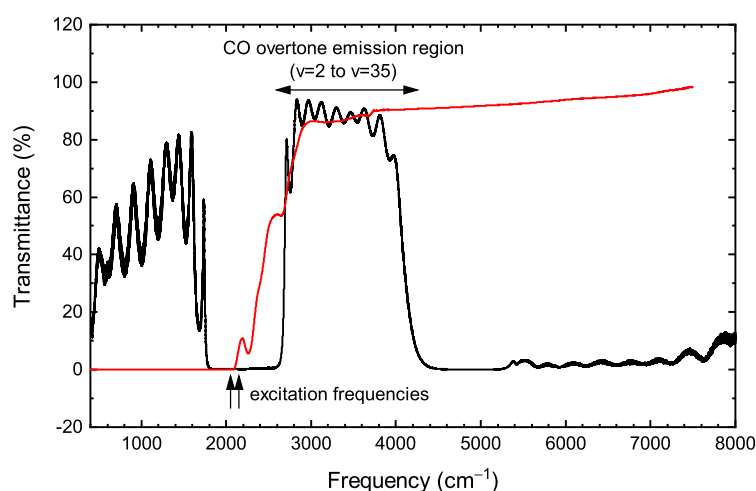

Figure 3.14: Infrared transmission spectra of the optical filters that are used to remove artifacts that appear due to second-order diffraction or stray laser light. The positions for $^{13}C^{18}O$ and $^{12}C^{16}O$ excitation at ~2050 and ~2150 cm^{-1}, respectively, are indicated by arrows. In addition, the C-O overtone spectral region is indicated.

3.2.8 Wavelength-dependent SNSPD intensity calibration

A wavelength-dependent relative detection efficiency (RDE), $\eta(\lambda)$, is necessary to convert the detected photon flux measured in LIF emission spectra to actual photon intensities emitted from the NaCl interface. These quantities differ due wavelength-dependent absorption of the SNSPD-fiber system, [93] optical filters, etc. along the optical path but can be converted if the RDE is known. In the following, photon intensities emitted from the NaCl interface will be called "corrected (emission) intensity". The corrected emission intensity is particularly useful to derive vibrational state populations when

vibrational state-dependent fluorescence rate constants are known (see Section 2.3.2).

To determine the RDE, s-polarized light from the globar light source of the FTIR spectrometer is directed at the NaCl crystal surface under conditions similar those for the excitation laser. The scattered mid-IR light is detected with the SNSPD-based emission spectrometer. A wavelength-dependent spectrum of the globar source can thus be measured with the SNSPD and is compared to a spectrum obtained with the external InSb detector of the FTIR spectrometer with a known spectral response function in the range from 2.5 μm (4000 cm^{-1}) to 6.1 μm (∼1600 cm^{-1}). For frequencies above 4000 cm^{-1}, the response curve of the InSb is extrapolated. Fig. 3.15 shows two RDE curves relevant to Chapters 5 and 6. Note that the RDE strongly depends on the bias current and the applied optical filters and thus needs to be determined individually for different measurement conditions.
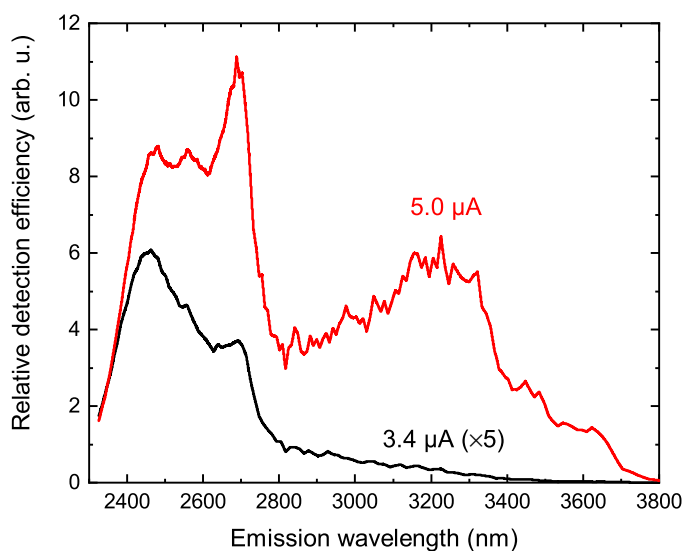

Figure 3.15: RDE curves for two different SNSPD bias current, 3.4 and 5.0 μA, which are used for LIF experiments with multilayer and monolayer excitation, respectively. For both RDE measurement, the two optical filters from Fig. 3.14 were used. From Ref. [130]. Reproduced with permission from Springer Nature.

To calculate the corrected intensity spectrum, $I(\lambda)$, the spectrum measured at the SNSPD, $\tilde{I}(\lambda)$, is simply divided by $\eta(\lambda)$. Further correction by vibrational state-dependent fluorescence rate constants, $k_{\mathrm{fl}}(v)$, gives the relative vibrational population (Eq. 3.3), where λ_v is the emission wavelength of the vibrational state with quantum

number v.

$$P(v) = \frac{I(\lambda_v)}{k_{\mathrm{fl}}(v)} = \frac{\tilde{I}(\lambda_v)}{\eta(\lambda_v) k_{\mathrm{fl}}(v)} \tag{3.3}$$

3.2.9 Temperature-programmed desorption measurements

TPD measurements are used in Chapter 7 to determine the absolute coverage of CO molecules adsorbed to the surface. For these experiments, the front of the NaCl crystal is dosed with CO using molecular beam dosing. Afterward, the surface is positioned about 3.5 cm in front of a 2 mm aperture that separates the UHV chamber from the mass spectrometer for the TPD measurements. The surface temperature is ramped at a constant heating rate of $20\,\mathrm{K\,min^{-1}}$ controlled by the cryogenic temperature controller. This heating rate cannot be exceeded due to the large cooling power of the 4 K cryocooler. Background due to desorption from the sample holder was reduced by minimizing the thermal contact between the upper and lower part of the NaCl sample holder while ensuring that low base temperatures below 10 K could still be achieved.

TPD spectra for $^{12}\mathrm{C}^{16}\mathrm{O}$ were measured at a mass-to-charge ratio of $m/z = 28$. For all measurements, the built-in electron multiplier was used for ion detection. Mass traces measured simultaneously at a nearby m/z ratio where no signal was observed were used to correct for drift in the ion signal over the course of the measurement, which was found to be identical for all mass traces.

Vibrational energy transfer dynamics in the CO/NaCl(100) monolayer

As a first step to advance the understanding of vibrational energy transfer between CO molecules adsorbed to NaCl(100), the mechanisms for vibrational energy pooling (VEP) as well as vibrational relaxation in a $^{13}C^{18}O$ monolayer are explored in this chapter. These will serve as a foundation for interpreting the experiments in Chapters 5 and 6. A set of time- and vibrational state-resolved experimental data of pooling in the two-dimensional CO/NaCl(100) system is interpreted using kinetic Monte Carlo (KMC) simulations based on the rate constant expressions in Section 2.2.2. Based on these simulations, the VEP mechanism and its relation to the phonon bath of NaCl will be discussed. Furthermore, two completely different vibrational relaxation mechanisms will be considered (see Section 2.2.1). For this chapter, I performed the KMC simulations that enabled the interpretation of the experimental data. Note that the experimental data presented in this chapter was measured by Li Chen using a previous version [20, 31] of the emission spectrometer presented in Chapter 3. The results presented in this chapter have been first published in Ref. [20] by the American Association for the Advancement of Science (AAAS).

4.1 Results

4.1.1 Experimental observations by time-resolved LIF

The experimental data that is analyzed and interpreted in the current chapter was measured by Li Chen with an older version of the experimental apparatus. [20, 31].

The main differences of the previous version to the current experimental setup are: the use of 16 µm × 16 µm instead of a larger 25 µm × 100 µm superconducting nanowire single-photon detector (SNSPD); the use of a liquid-nitrogen cooled 80 K monochromator instead of a 40 K monochromator; lower spectral resolution of about 12 nm compared to 6 nm with the new setup (see also Chapter 3). All monolayer experiments were performed at ~7 K using the heaviest isotopologue of CO, $^{13}C^{18}O$.

Fourier-transform infrared (FTIR) absorption and laser-induced fluorescence (LIF) excitation spectra of the $^{13}C^{18}O$ monolayer on NaCl(100) are presented in Fig. 4.1. Comparison of the monolayer and multilayer FTIR spectra in the inset of Fig. 4.1a shows that the absorption peaks of the bare monolayer at 2049.0 and 2055.0 cm^{-1} can be clearly distinguished from the monolayer covered with multilayers, for which only one peak at ~2053.5 cm^{-1} is observed. Also the multilayer absorption features appear at different frequencies (2039.4 and 2043.4 cm^{-1}). Except for the absolute frequencies, the assignment of all observed $^{13}C^{18}O$ absorption peaks is consistent with the literature for $^{12}C^{16}O$. [36, 38, 44] The lineshapes in the FTIR peaks are clearly limited by the instrument function because the monolayer linewidth is narrower than the FTIR resolution (0.2 cm^{-1}, using a four-point apodization function). The linewidth observed in the LIF spectra is even broader (~0.4 cm^{-1} for the 2055 cm^{-1} line) although the bandwidth of the laser is smaller than 0.05 cm^{-1}, as determined from photoacoustic spectra of CO. This is probably attributed to either saturation of the $v = 0 \rightarrow 1$ transition or heterogeneous broadening induced by the laser excitation. Despite that, the good agreement between the FTIR spectra and the LIF excitation spectra with respect to the absorption frequencies and the polarization dependence confirms that the bare monolayer is probed in the LIF experiments.

Laser excitation of the symmetric vibrational mode at 2055 cm^{-1} results in overtone emission from a large range of CO vibrational states between $v = 5$ and 27, as seen in the time-integrated emission spectrum in Fig. 4.2. Furthermore, a distinctive pattern in the intensity distribution with peaks at $v = 7$, 16 and 25 is observed.

Time-resolved measurements are available for each of the observed vibrational states, shown in Fig. 4.3 with a logarithmic time-axis. Note that the bin time, which is ~1 µs at early times, is increased at later times to improve the signal-to-noise ratio (SNR). The emission intensities in Fig. 4.3 were corrected for the wavelength-dependent relative detection efficiency (RDE) of the old experimental setup and calculated, vibrational state-dependent fluorescence rate constants (see Section 3.2.8 and Appendix B) to yield time-dependent, relative vibrational populations. Absolute vibrational populations, $P_v(t)$, are obtained by scaling the relative populations such that the average vibrational quanta, $\sum_v vP_v(t)$, are 73 % at $t = 1$ µs, a time for which vibrational relaxation has not
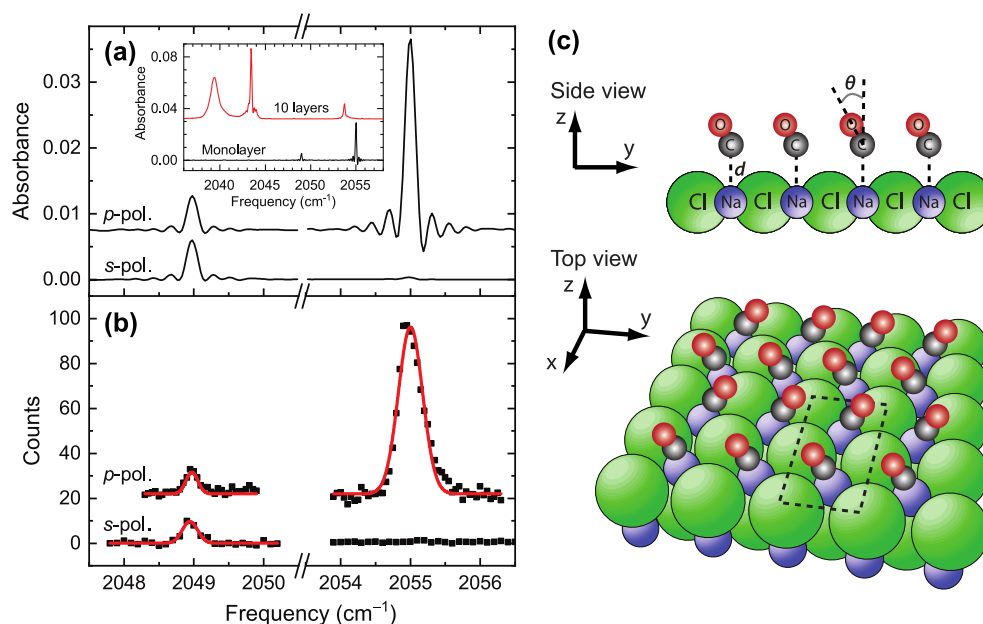
Figure 4.1: (a) FTIR absorption spectra of a $^{13}C^{18}O$ monolayer adsorbed on NaCl(100) for p- and s-polarized light. The inset shows the p-polarized monolayer spectrum (black line) in comparison to a spectrum obtained for 10 CO layers (red line) adsorbed on top of the monolayer. The shown monolayer absorption spectra for p- and s-polarization have been corrected to account for an offset of 18° in the polarizer alignment, which resulted in a mixture of s- and p-polarized light in the raw spectra. (b) LIF excitation spectra of the monolayer obtained with p- and s-polarized laser light while detecting fluorescence at zeroth order of the grating monochromator. The spectra are integrated over a time window of 1 ms after laser excitation. Black squares represent experimental data and red lines are Gaussian fits to the data. Note that the p-polarized spectra in panels (a) and (b) are offset for clarity. (c) Schematic representation of the (2×1) structure of the CO monolayer at 7 K, which features rows of CO molecules tilted in different directions. The (2×1) unit cell is indicated by dashed lines. From Ref. [20]. Adapted with permission from AAAS.
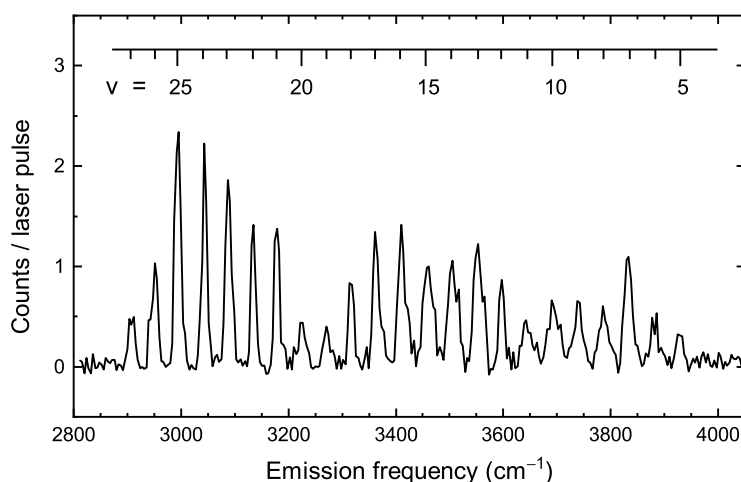
Figure 4.2: Background-subtracted LIF emission spectrum obtained after laser excitation of the symmetric vibrational mode at $2055\,cm^{-1}$ with a pulse energy of $120\,\mu J$. Emission is collected in the CO overtone region and integrated over a $50\text{-}250\,\mu s$ time window after laser excitation measured at a $5.2\,\mu A$ bias current. Vibrational quantum numbers of the emitting states are indicated by the comb. From Ref. [20]. Adapted with permission from AAAS.

yet occurred. The excitation of $73\,\%$ implies saturation of the $v = 0 \rightarrow 1$ transition and was chosen to match the initial average quanta in the KMC simulations in Section 4.1.2. Initial population of the lowest observed vibrational states (up to $v = 12$) cannot be resolved with the $1\,\mu s$ resolution and only their decay is seen. Generally, the maxima of $P_v(t)$ shift to later times for higher vibrational quantum numbers, reaching $100\,\mu s$ for $v = 25$. The different time scales on which the vibrational states are populated indicate sequential population of increasingly higher vibrational states on different time scales. However, a state-by-state comparison of the time profiles is unlikely to give detailed insight into the vibrational energy transfer mechanism because all states are highly coupled among each other. Thus, the following analysis in Section 4.1.2 will focus on the time-integrated emission spectrum and the time-dependent vibrational state distributions obtained from the time profiles at different times, which will be compared to KMC simulations.
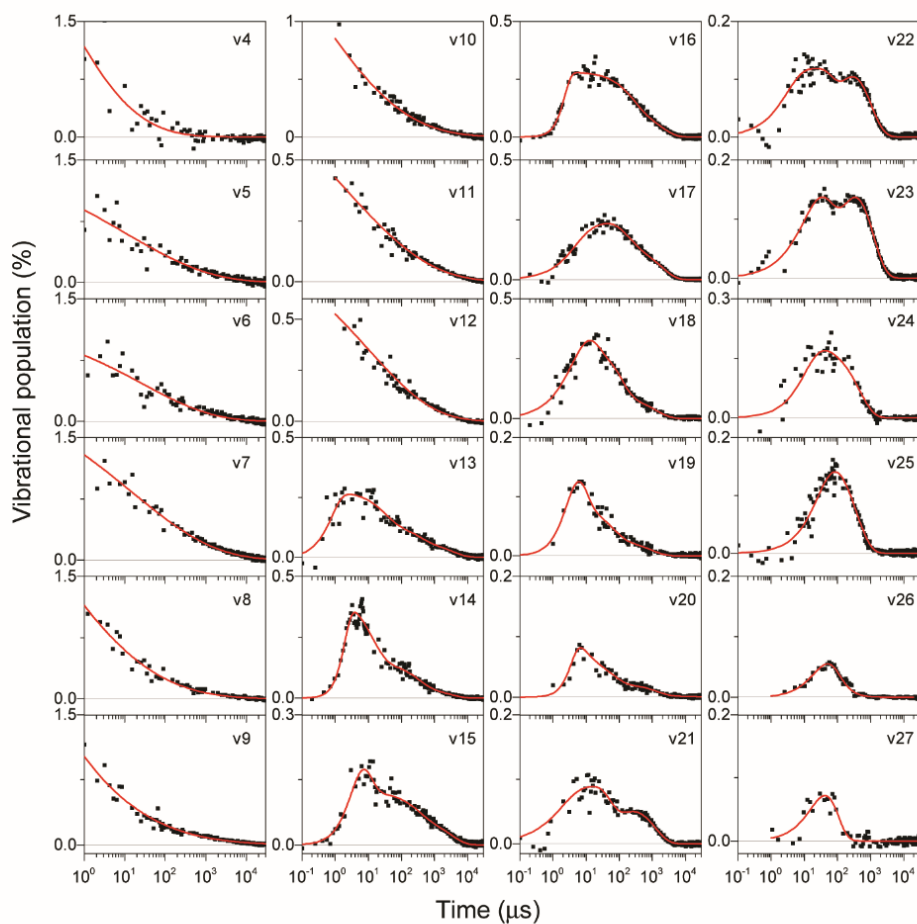
Figure 4.3: Temporal profiles for the absolute populations (in %, where 100 % corresponds to the complete monolayer) of all vibrational states observed in the emission spectrum in Fig. 4.2. Black squares represent binned data points whereas the bin time increases with time to improve the SNR. Red lines are empirical fits to the data. Absolute populations are found as described in the text. From Ref. [20]. Reprinted with permission from AAAS.

4.1.2 Kinetic Monte Carlo simulations

KMC simulations are used to model the temporal evolution of the vibrational population distribution in the CO monolayer after laser excitation, using an adapted version of the Fortran code by Corcelli and Tully [57, 58, 87]. Details regarding the KMC simulations and rate constant calculations can be found in Appendix B and only a brief summary of the most important aspects will be given in the following.

To simplify the description of CO-CO interactions, all CO molecules are assumed to adsorb perpendicular to the surface on top of the Na^+ ions, thus forming a square lattice with a lattice constant of 3.96 Å [39]. The simulation box consists of a 100×100 supercell of this (1×1) structure with periodic boundary conditions. Initially, all molecules are in their vibrational ground state, $v = 0$, and the highest vibrational state that can be populated is $v = 35$. The following energy transfer processes are included: pulsed laser excitation, vibration-to-vibration (V-V) transfer between CO molecules at varying distances, vibrational relaxation to the phonon bath, vibrational relaxation due to infrared emission, and a vibrational loss process attributed to vibration-to-electronic (V-E) energy transfer. All interactions between two CO molecules are considered up to a maximum interaction radius of 8 lattice constants (~ 32 Å) unless otherwise stated. A surface temperature of 11 K is chosen, which is only slightly larger than the experimental temperature of 7 K.

Laser excitation

Laser excitation of the $v = 0 \rightarrow 1$ transition is implemented by a time-dependent excitation rate constant, $k_{\text{stim}}(t)$, for stimulated absorption and emission (see Eq. 4.1). $k_{\text{stim}}(t)$ is modeled as a Gaussian pulse with a full width at half maximum (FWHM) of 4.7 ns and a peak excitation rate of 3.44×10^9 s^{-1}, representing the experimental excitation conditions.

$$CO(v = 0) \underset{k_{\text{stim}}(t)}{\overset{k_{\text{stim}}(t)}{\rightleftharpoons}} CO(v = 1) \tag{4.1}$$
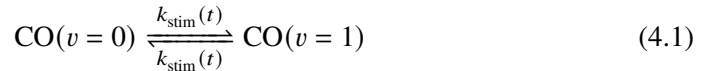
V-V energy transfer

The rate constants k_{nm} for vibration-to-vibration (V-V) transfer (Eq. 4.2) are based on the theory by Corcelli and Tully [57, 58], presented in Section 2.2.2, with two major improvements[1]: Firstly, interactions between two molecules at intermolecular distances up to 32 Å are considered, in contrast to the nearest-neighbor approximation that has

---

[1] Both improvements do not require any modifications of the original rate constant equations.

been made in Refs. [57] and [58]. Secondly, a more realistic phononic density of states (DOS) is used instead of a simple Debye density, whose function is to compensate the energy mismatch, ΔE_{nm}, associated with the reaction. The realistic DOS is shown in Fig. 4.4 and was used for all simulations unless otherwise stated. It was calculated by Jörg Meyer and is obtained from a NaCl bulk DOS, which is projected onto the motion of the Na atoms in the (100) plane. This projection models the coupling assumed in Section 2.2.2, which depends only on the parallel motion of the Na atoms underneath the CO molecules. Furthermore, only transverse phonons are considered. Details of the density functional theory (DFT) calculations and the projections can be found in the Supplementary Material of Ref. [20]. The most important difference between the realistic and the Debye DOS is the sharp drop at $\sim$170 cm^{-1} instead of 223 cm^{-1}. Section 4.1.3 will discuss how different choices of the DOS affect the results.

$$CO(v = n) + CO(v = m) \xrightleftharpoons[k_{m-1,n+1}]{k_{nm}} CO(v = n + 1) + CO(v = m - 1) \quad | \Delta E_{nm} \quad (4.2)$$
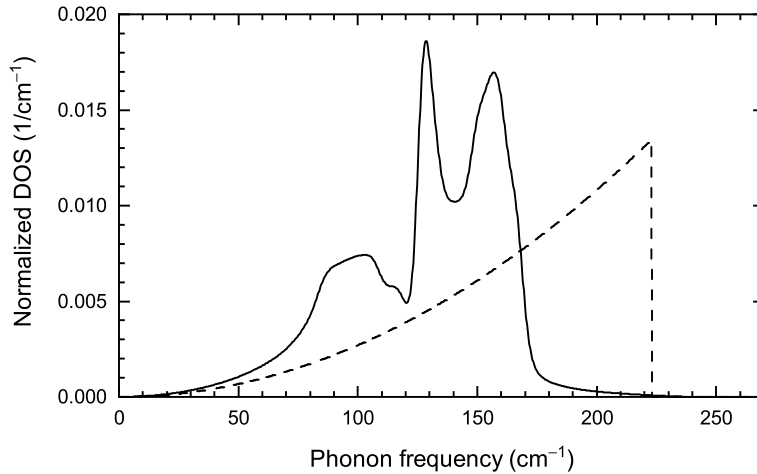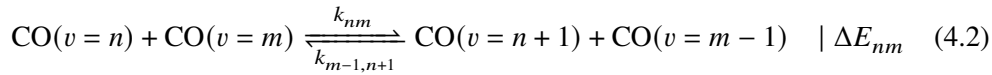

Figure 4.4: The solid line shows the realistic phonon DOS, which is used in all KMC simulations unless otherwise stated. It is based on a DFT-based bulk DOS of NaCl, which is projected onto the motion of Na atoms in the (100) plane. Furthermore, it contains only contributions from transverse phonons. For comparison, the Debye DOS of NaCl is shown as a dashed line. The integrals of both spectra are normalized to 1.

Non-radiative relaxation

Vibrational relaxation rate constants according to Eq. 4.3 are calculated for the Chance-Prock-Silbey (CPS) model (k_{nr}^{CPS}) and the Skinner-Tully (ST) model (k_{nr}^{ST}). The former describes non-radiative relaxation via the near-field of an oscillating dipole whereas the latter describes relaxation to substrate phonons via anharmonic adsorbate-surface coupling (see also Section 2.2.1).

$$CO(v = n) \xrightarrow{k_{nr}^{CPS/ST}} CO(v = n - 1) \tag{4.3}$$
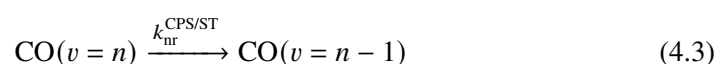
Radiative relaxation

Radiative relaxation rate constants, $k_{fl}^{\Delta v}$, are considered for fundamental, first overtone, and second overtone emission ($\Delta v = 1, 2,$ and 3, respectively):

$$CO(v = n) \xrightarrow{k_{fl}^{\Delta v}} CO(v = n - \Delta v). \tag{4.4}$$
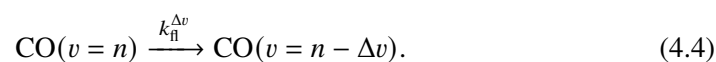
V-E energy transfer

An additional V-E energy transfer channel is based on the empirical observation that no vibrational states above $v = 27$ are observed, which coincides with the fact that $v = 28$ has an energy of 6.0 eV, which is comparable to the energy of the first electronically excited state of CO. [131] This is implemented by transferring molecules in these vibrational states to $v = 0$, assuming a rate constant of $k_{V-E} = 1 \times 10^5$ s^{-1}:

$$CO(v \geq 28) \xrightarrow{k_{V-E}} CO(v = 0) \tag{4.5}$$
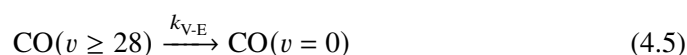
Rate constants

Selected rate constants of the above-mentioned energy transfer processes are shown in Fig. 4.5. Note that the rate constants for V-V energy transfer depend strongly on the intermolecular distance R and that only the rate constants for next-neighbor reactions ($R = 3.96$ Å) are shown.[2] The pooling rate constants $k_{n,1}$ increase with increasing n up to $n = 6$, feature a sudden drop between $n = 6$ and $n = 8$, and decrease even further for larger quantum numbers n. This vibrational state-dependence can be correlated with the appearance of peaks in the realistic phonon spectrum (Fig. 4.4). Higher quantum

---

[2] The rate constants are approximately proportional to R^{-8} for a one-phonon process.

numbers m also result in larger pooling rate constants k_{nm}. However, the overall shape of the rate constant curves as a function of the difference $\Delta v = n - m$ is not affected and is still determined by the phonon spectrum. The ST and CPS models for non-radiative relaxation are characterized by distinct vibrational dependencies. Whereas the ST rate constants increase almost exponentially with increasing quantum number, the CPS rate constants show a moderate dependence on v, which follows the v-dependence of the fundamental fluorescence rate constants.
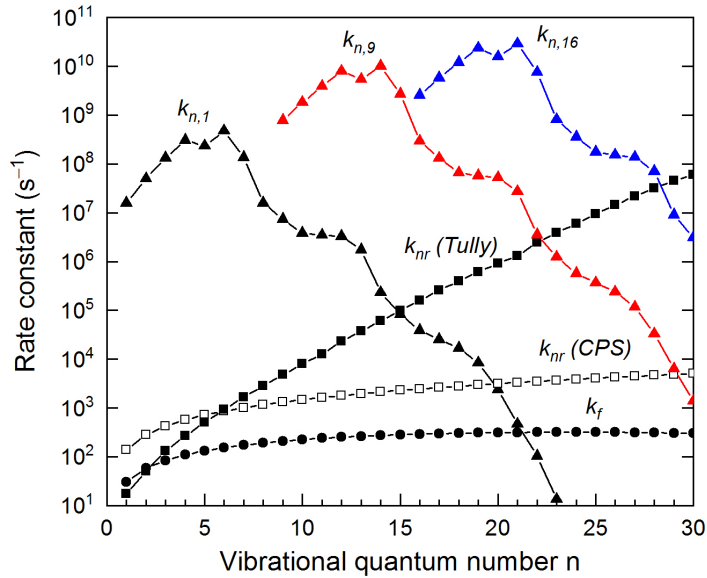

Figure 4.5: Overview of selected rate constants for V-V transfer (triangles), non-radiative relaxation (squares) and fundamental fluorescence (circles), as used in the KMC simulations. Black, red and blue triangles represent the rate constants k_{nm} for nearest neighbor pooling reactions with molecules in $m = 1$, 9 and 16, respectively, assuming the realistic DOS in Fig. 4.4. Filled squares correspond to ST rate constants, k_{nr}^{ST}, and empty squares correspond to CPS rate constants, k_{nr}^{CPS}. From Ref. [20]. Reprinted with permission from AAAS.

4.1.3 Vibrational energy pooling

This section compares the experimental data and the KMC simulations, described in the previous sections, within the initial period after laser excitation where VEP occurs. After showing the comparison, the VEP mechanism and the role of the substrate phonons will be discussed.

Figs. 4.6a and 4.6b shows a comparison of the experimentally derived overtone emission spectrum and two simulated spectra obtained from the KMC simulations. To calculate the simulated spectra, the time-dependent vibrational populations are integrated over the same time window as in the experiments and multiplied with the calculated overtone fluorescence rate constants, the RDE and an additional scaling factor. This is essentially the reverse correction used to obtain relative vibrational populations, which is presented in Section 3.2.8. The corrected, time-integrated populations are convoluted with Gaussians of constant width ($14\,\mathrm{cm}^{-1}$ FWHM) to produce the spectrum.

The simulated spectrum in Fig. 4.6a only considers V-V energy transfer between nearest neighbor molecules, the same assumption as in Refs. [57, 58, 87]. In this case, the simulation shows a peak around $v = 8$, which is comparable to the peak in the experimental spectrum near $v = 7$; however, it clearly fails to describe the population of vibrational states above $v = 11$. Increasing the interaction radius to 8 lattice constants (~$32\,\text{Å}$), shown in Fig. 4.6b, results in much better agreement with the experimental spectrum. Not only are the higher vibrational states up to $v = 27$ populated, but also the peaks in the intensity distribution at $v = 7$, 16 and 25 are well reproduced.

Fig. 4.6c directly compares the experimental and simulated vibrational distributions at different times after laser excitation, where the experimental population distributions, $P_v(t)$, were derived from the time profiles in Fig. 4.3. Overall, there is good agreement between the experimental and simulated distributions. At $1\,\mu\text{s}$, the experimental population distribution shows a peak at $v = 7$, but little population in higher vibrational states. The simulated distribution shows a comparable peak at $v = 7$, but additionally features another small peak at $v = 17$, which is not seen in the experiment. For comparison, the simulated distribution at $100\,\text{ns}$, which is plotted in the same panel, shows less population for $v = 17$. After $10\,\mu\text{s}$, two additional peaks around $v = 17$ and 23 emerge in the experimental distribution, whereas the population in the lower vibrational states is depleted. The corresponding simulation looks very similar although the exact peak positions and populations are, of course, not reproduced. Finally, the experimental peaks around $v = 7$ and 17 decreased further after $100\,\mu\text{s}$, whereas the peak around $v = 23$ became slightly more pronounced. A similar change in the simulated peak structure is observed after $93\,\mu\text{s}$.

Discussion of the vibrational energy pooling mechanism

The three peaks or groups of vibrational states in the emission spectrum and the experimental population distributions, which will be referred to as "base-camps" hereafter, are sequentially populated over time. This can be rationalized by a sequential "base-camp
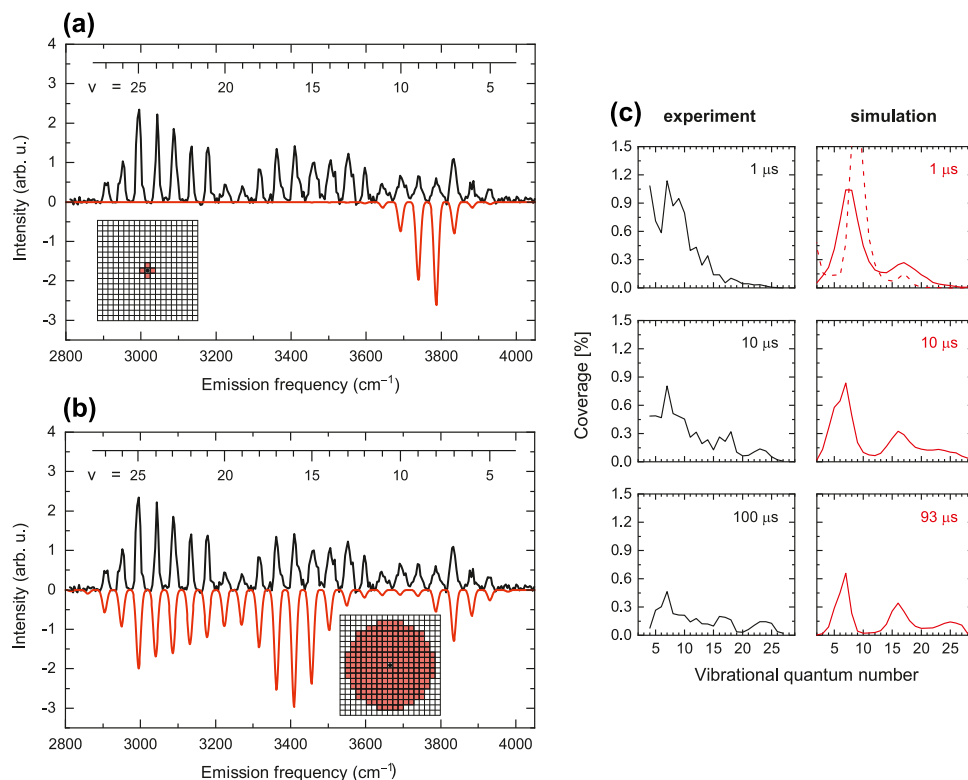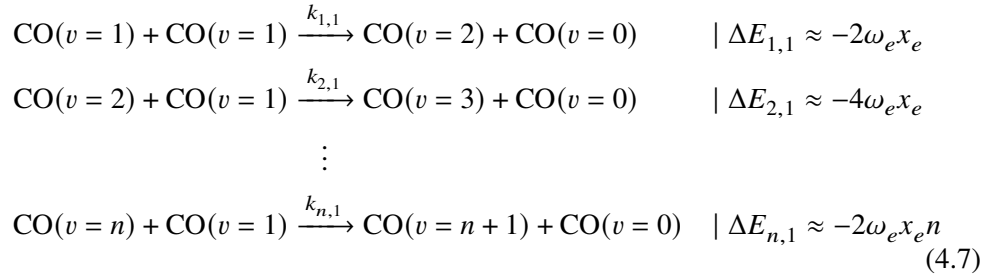
Figure 4.6: (a) The black curve shows the experimental overtone emission spectrum of the CO/NaCl(100) monolayer, time-integrated over a 50–250 μs window after laser excitation of the $v = 0 \rightarrow 1$ transition (same spectrum as in Fig. 4.2). Quantum numbers of the upper vibrational levels, from which fluorescence originates ($v \rightarrow v - 2$), are indicated by the comb. The red curve shows a simulated spectrum derived from the time-integrated vibrational population distributions in the KMC simulations. The inset shows a 21×21 square grid, where each square represents a CO molecule. All molecules that are allowed to interact with the center molecule (black dot) in the simulations are shaded in red. Here, V-V transfer is allowed only for nearest-neighbor pairs. (b) In this case, all molecules within an interaction radius of 8 lattice constants (approx. 32 Å) can interact via V-V energy transfer as implied by the red shaded area in the inset. (c) shows a comparison of the experimental and simulated vibrational population distributions at different times after laser excitation, which are indicated in each panel. In addition, the red, dashed line in the top-right panel represents the simulated population distribution at 100 ns. Vibrational populations are given as absolute coverages in both cases, where 100% would correspond to all molecules in the monolayer being in the given vibrational state. From Ref. [20]. Adapted with permission from AAAS.

mechanism", which will be described in the following. This proposed mechanism will be further supported by the KMC simulation, which are in good agreement with the experiments as demonstrated before.

Initially, over 50 % of the molecules are excited to their $v = 1$ state. Following excitation, the molecules in $v = 1$ can undergo resonant energy exchange with other molecules in $v = 0$, according to Eq. 4.6. The rate constant for this process is calculated as $k_{0,1} = 1.8 \times 10^{11} \, \text{s}^{-1}$, much faster than typical rate constants for non-resonant energy transfer. Therefore, the resonant rate constants were scaled down by a factor of 0.01 in the KMC simulations, without any noticeable impact as confirmed by test simulations using a scaling factor of 0.1.

$$CO(v = 0) + CO(v = 1) \xrightarrow{k_{0,1}} CO(v = 1) + CO(v = 0) \quad | \, \Delta E_{0,1} = 0 \qquad (4.6)$$
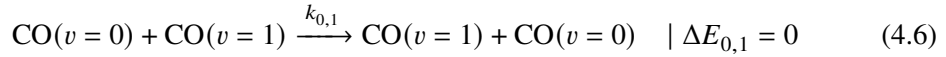
The fast "diffusion" of $v = 1$ excitation via resonant exchange makes energy transfer between two neighboring $CO(v = 1)$ molecules highly probable. This process produces one $CO(v = 2)$ and one $CO(v = 0)$ molecule and the associated energy that dissipated to the substrate phonons is given by $-2\omega_e x_e$, where $\omega_e x_e = (12.22 \pm 0.04) \, \text{cm}^{-1}$ is the anharmonicity constant of $^{13}\text{C}^{18}\text{O}$ on NaCl(100). CO molecules that have been excited to $v = 2$ can accept further vibrational energy from $CO(v = 1)$ molecules according to the generalized V-V energy transfer sequence in Eq. 4.7. Note that the energy mismatch in these subsequent processes, $\Delta E_{n,1}$, grows with increasing vibrational quantum number n.

$$CO(v = 1) + CO(v = 1) \xrightarrow{k_{1,1}} CO(v = 2) + CO(v = 0) \qquad | \, \Delta E_{1,1} \approx -2\omega_e x_e$$

$$CO(v = 2) + CO(v = 1) \xrightarrow{k_{2,1}} CO(v = 3) + CO(v = 0) \qquad | \, \Delta E_{2,1} \approx -4\omega_e x_e$$

$$\vdots$$

$$CO(v = n) + CO(v = 1) \xrightarrow{k_{n,1}} CO(v = n + 1) + CO(v = 0) \quad | \, \Delta E_{n,1} \approx -2\omega_e x_e n$$
$$(4.7)$$

As apparent from the $k_{n,1}$ rate constants in Fig. 4.5, these processes become more efficient with higher vibrational quantum numbers $n < 7$ due to the increased energy release. However, the rate constants decrease drastically for $n \geq 7$ because barely any phonons are available to compensate energies larger than $\Delta E_{7,1} \approx -171 \, \text{cm}^{-1}$, as apparent from the realistic phonon DOS in Fig. 4.4. $\Delta E_{6,1} \approx -147 \, \text{cm}^{-1}$, on the other hand, can be dissipated efficiently because the phononic DOS shows a peak at the corresponding frequency. The resulting kinetic bottleneck prevents further reaction of $CO(v = 7)$ with
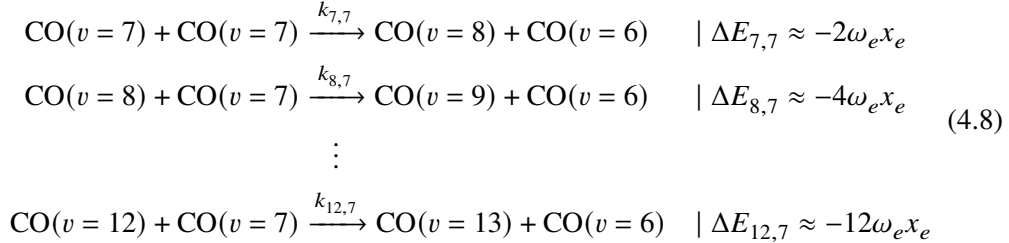
other $v = 1$ molecules and produces a large transient population in $v = 7$—the first base-camp. All energy transfer processes that populate the first base-camp can proceed via nearest-neighbor reactions, due to the rapid diffusion of $v = 1$ excitation. This is consistent with the two simulations in Figs. 4.6a and 4.6b, which were performed for different possible interaction distances and both produced peaks around $v = 7$.

To understand the population of vibrational states beyond the first base-camp, it is important to realize that vibrational energy pooling according to Eq. 4.7 concentrates many vibrational quanta in single molecules. The concentration of quanta not only decreases the number of available molecules in $v = 1$, but also reduces the chance of finding molecules in the first base-camp next to each other. Remember that absolute populations are on the order of 1 % after 1 μs (see Fig. 4.6c for example). Furthermore, higher vibrational states will be immobilized because they cannot undergo resonant exchange with the highly abundant $v = 0$ molecules, which is only possible for $v = 1$.[3] This immediately explains why almost no vibrational states beyond $v = 7$ are populated in Fig. 4.6a, given that only nearest-neighbor reaction were allowed in this simulation. Population of vibrational states in higher base-camps is, however, clearly observed in Fig. 4.6b, where interactions beyond the nearest-neighbor distance were allowed. Formation of higher base-camps must therefore be related to interactions over larger distances.

Formation of the second base-camp can be understood from the same concepts that lead to formation of the first base-camp. Although energy transfer from $CO(v = 1)$ to $CO(v \geq 7)$ becomes inefficient, energy transfer sequences as in Eq. 4.8 can occur over larger distances. I would like to emphasize that the excess energies in Eqs. 4.7 and 4.8 are identical if the difference in vibrational quantum numbers, $\Delta v = n - m$, is the same. Therefore, a similar dependence of the rate constants on the vibrational state is expected—including the kinetic bottleneck occuring at $\Delta v = 6$ defined by the highest frequency phonons of the substrate. Indeed, Fig. 4.5 shows that the rate constant curve for formation of the second base-camp ($k_{n,7}$) has a similar shape as the curve for formation of the first base-camp ($k_{n,1}$, only shifted to higher vibrational quantum number. In fact, if formation of the second base-camp occurred at nearest-neighbor distances, the corresponding rate constants would be even higher than for formation of the first base-camp. According to the rate constants in Fig. 4.5, the second base-camp would be therefore expected at $n = 13$, which is slightly lower than the second base-camp peak seen both in the experiment and the simulation. Following the same arguments, the

---

[3] In fact, resonant energy transfer between two immobilized CO molecules in high vibrational states is possible. However, it can only exchange the vibrational quantum numbers of the two molecules and will not lead to "diffusion" across the whole surface.

third base-camp peak is subsequently formed over even larger distances and should be found at $v = 19$, which is again slightly lower than in the experiment and the simulation.

$$
\begin{aligned}
\text{CO}(v=7) + \text{CO}(v=7) &\xrightarrow{k_{7,7}} \text{CO}(v=8) + \text{CO}(v=6) &| \ \Delta E_{7,7} \approx -2\omega_e x_e \\
\text{CO}(v=8) + \text{CO}(v=7) &\xrightarrow{k_{8,7}} \text{CO}(v=9) + \text{CO}(v=6) &| \ \Delta E_{8,7} \approx -4\omega_e x_e \\
&\qquad\quad \vdots \\
\text{CO}(v=12) + \text{CO}(v=7) &\xrightarrow{k_{12,7}} \text{CO}(v=13) + \text{CO}(v=6) &| \ \Delta E_{12,7} \approx -12\omega_e x_e
\end{aligned}
\tag{4.8}
$$

Mode-selective coupling to phonons

As the discussion of the base-camp mechanism in the previous section shows, the base-camp positions in the vibrational distributions depend critically on the phononic DOS. Therefore, information on the coupling to different phonon modes can be obtained from a comparison of the experimental and simulated emission spectra.

Fig. 4.7 compares the experimental emission spectrum with simulated emission spectra based on different phononic DOSs. The upper three simulations are based on phonon DOSs that are derived from a DOS for bulk NaCl, in which only phonons that include displacement of the Na atoms in the (100) plane are considered (see Supplementary Material of Ref. [20] for technical details). Projection onto the (100) plane mimics the NaCl(100) surface DOS, neglecting surface-localized modes, while projection onto the Na atom motion satisfies the coupling assumed in Ref. [57], in which the coupled CO molecules follow the parallel motion of the underlying Na atoms. The simulation for this projected DOS is shown as a blue curve in Fig. 4.7, whereas simulations that only consider its contributions from transverse and longitudinal phonons are shown as red and green curves, respectively. In addition, a simulation based on the Debye DOS of NaCl is shown, which was also used in Ref. [57].

The transverse DOS clearly agrees best with the experimental data and reproduces the positions of the three base-camp peaks with good accuracy. For the complete projected DOS, however, a third base-camp peak is barely observed and the positions of the peaks are shifted to larger v. The longitudinal DOS and the Debye DOS give very similar spectra with only two base-camp peaks, whose positions clearly differ from the experiment. The observed shift in the base-camp positions for different DOSs is consistent with the idea that the base-camp peaks mainly depends on the highest phonon frequency. This also explains the similarity between the emission spectra belonging to the longitudinal DOS and the Debye DOS, which show similar cutoff frequencies. Furthermore, the
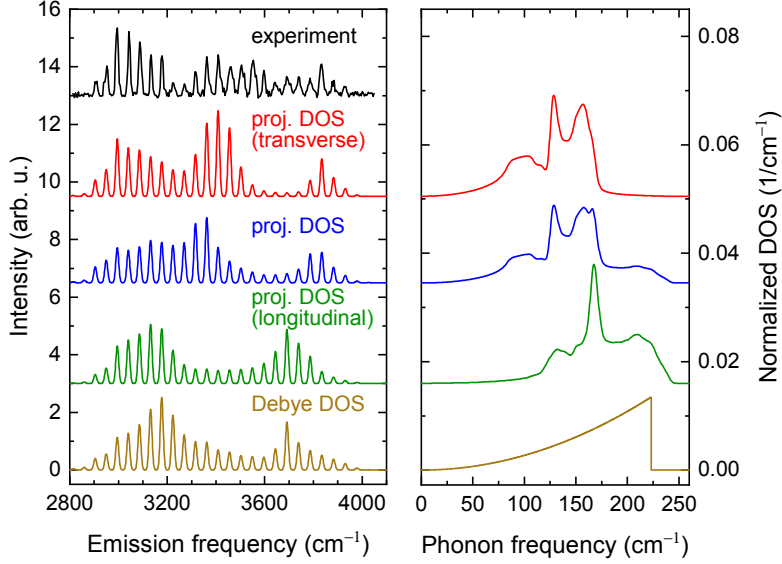
Figure 4.7: Left panel: The same experimental emission spectrum as in Fig. 4.6 is shown in black. Other spectra correspond to simulated emission spectra for different phononic DOSs: a NaCl bulk DOS projected onto the Na atom motion in the (100) plane (blue spectrum); contributions of transverse and longitudinal phonons to the projected density (red and green spectra, respectively); and a Debye DOS with a Debye frequency of $\omega_D = 223\,\mathrm{cm}^{-1}$ (brown spectrum). Right panel: The corresponding, normalized DOSs are shown in the same colors as the simulated spectra. From Ref. [20]. Reprinted with permission from AAAS.

disagreement between simulation and experiments increases the stronger the contribution from the longitudinal, optical phonons at high frequencies around $200\,\mathrm{cm}^{-1}$ is. Thus, it can be concluded that coupling to the longitudinal, optical phonons is inefficient, whereas coupling to the transverse, optical phonons is consistent with the experiment.

Additional evidence for the base-camp mechanism in the KMC simulations

While the simplified base-camp mechanism explains the key features of the experiment, the actual dynamics are more complex and involve a large number of coupled energy transfer sequences, similar to the one shown in Eq. 4.8. Furthermore, V-V energy transfer processes involving two phonons can still occur at finite rates, although they are less likely than one-phonon processes. More complete information and additional evidence for the base-camp mechanism can be extracted from the KMC simulation in Fig. 4.6b,

which will be presented in the following.

Fig. 4.8 shows the total number of energy transfer processes

$$CO(v = n) + CO(v = m) \xrightarrow{k_{n,m}} CO(v = n + 1) + CO(v = m - 1) \qquad (4.9)$$
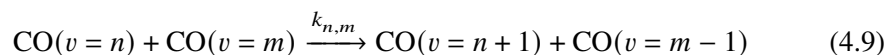
per trajectory that occur within two different time windows. The number of resonant V-V energy transfer processes (yellow diagonal, $m = n + 1$) is much larger than that of all non-resonant processes. Therefore, exact numbers for the resonant processes are not shown to highlight differences between the non-resonant reactions. Most non-resonant energy transfer processes can be characterized as single-phonon processes ($n - m < 6$) and only a few are two-phonon processes ($n - m \geq 6$). Also the proposed sequential mechanism for formation of the three base-camps is clearly observed and highlighted in Fig. 4.8. In the 0-10 µs time window, the most common processes are the same as in the energy transfer sequence in Eq. 4.7, describing the formation of the first base-camp. Some processes that form the second base-camp are also observed in this time interval; however, they are more clearly seen between 10 to 110 µs where they are indicated by the second ellipse. Although the proposed energy transfer sequence in Eq. 4.8 is definitely observed, many reactions with m between 5 and 10 contribute to formation of the second base-camp. This also explains why the base-camp peak positions predicted by the simplified mechanism do not perfectly agree with the simulation. Similar trends as for the second base-camp are also seen for formation of the third base-camp. As a final note, reverse pooling processes that are energetically uphill and are located to the left of the resonant diagonal in Fig. 4.8 are only important for the smallest vibrational states $v \leq 5$.

By analyzing the number of V-V energy transfer processes with respect to the distance over which they occur, the average distance between molecules in the different base-camps can be extracted from the simulation. For this purpose, three groups of energy transfer processes are defined, which represent formation of the different base-camps (base-camp 1: reactions with $m = 1$; base-camp 2: reactions with $m = 6$ to 10; base-camp 3: reactions with $m = 13$ to 19). I determined the corresponding average distances for the same time interval as in the measured emission spectrum (50–250 µs). While the first base-camp is formed over an average distance of 4.1 Å, base-camps 2 and 3 are formed over average distances of 11.7 Å and 17.6 Å, respectively. Recall that the nearest-neighbor distance is about 4.0 Å and that the rates constants for single-phonon processes scale approximately with R^{-8}. Therefore, the increase in the average distance is qualitatively consistent with the different timescales for formation of the three base-camps.

In Fig. 4.9, vibrational quantum numbers of five different molecules that become
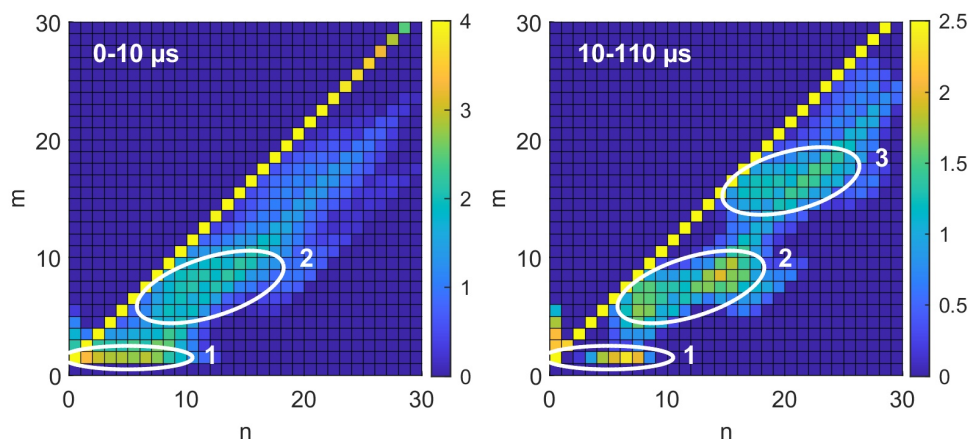
Figure 4.8: Decadic logarithm, $\log_{10}(N)$, of the number of V-V energy transfer reactions per KMC trajectory between $CO(v = n)$ and $CO(v = m)$ for two different time windows: 0 to 10 μs (left panel), and 10 to 110 μs (right panel). Note that reactions that occur less than once per trajectory ($\log_{10}(N) < 0$) are not explicitly shown (dark blue color). Reactions that occur more frequently than 10^4 (left panel) or $10^{2.5}$ times (right panel) per trajectory are also not shown with their true values (yellow color). Frequent reactions that lead to formation of the first, second and third base-camp are indicated by ellipses and labels "1", "2" and "3", respectively.

highly vibrationally excited over the course of the KMC trajectory are plotted as a function of time. In the initial phase after excitation, the quantum number of all five molecules oscillates between $v = 0$ and 1, which demonstrates the rapid diffusion of $v = 1$ excitation. Between 0.01 and 0.1 μs, the quantum number of all molecules increases abruptly because the first base-camp is formed. Within the next 1 to 100 μs, all of the selected molecules either reach the second or the third base-camp and finally lose their vibrational excitation due to vibrational relaxation on the millisecond timescale. This again shows the sequential population of the three base-camps. More importantly, Fig. 4.9 directly shows that high vibrational states become immobilized, since none of the molecules return to $v = 0$ before vibrational relaxation sets in.

4.1.4 Vibrational relaxation

The previous section focused on vibrational energy pooling, which occurs on timescales between nano- and microseconds. In the following, I will focus on vibrational relaxation, which occurs mainly on the millisecond timescale in the CO/NaCl(100) system.

Fig. 4.10a shows the long-term decays of selected experimental time profiles on
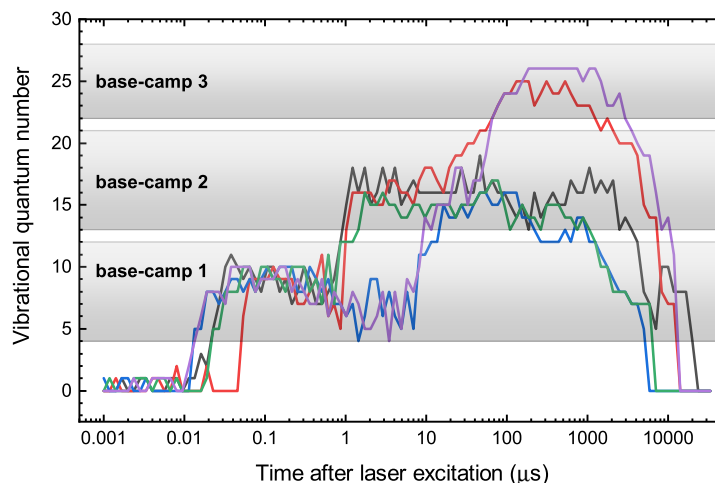
Figure 4.9: Temporal change in the vibrational quantum numbers of five immobilized CO molecules. These five molecules were chosen randomly out of all molecules in a single KMC trajectory that reached $v > 1$ at $10\,\mu s$. The three shaded areas roughly indicate the positions of the first, second and third base-camps.

a millisecond timescale. In addition, exponential fits to the decays are shown. The obtained effective, exponential lifetimes obtained from these fits are plotted in Fig. 4.10b. The effective lifetime decreases from 7 ms for $v = 5$ to $70\,\mu s$ for $v = 27$, whereas it is approximately constant between $v = 5$ and 11.

It should be emphasized that the effective lifetimes in Fig. 4.10b are comparable to the corresponding fluorescence lifetimes, which are inversely proportional to the fluorescence rate constants in Fig. 4.5. However, the effective lifetimes will not exactly correspond to the actual rate constants for vibrational relaxation, i.e., the sum of all radiative and non-radiative contributions. Instead, the effective decay of a given vibrational state is expected to be slowed down due to relaxation of higher vibrational states. Therefore, the effective, experimental lifetimes are compared to effective lifetimes extracted from the long-term decay in KMC simulations, assuming two different models for non-radiative vibrational relaxation that were introduced in detail in Section 2.2.1: The CPS model and the ST model. The former describes non-radiative relaxation via the near-field of a classical oscillating dipole whereas the latter describes relaxation to substrate phonons via anharmonic coupling due to the adsorbate-surface interaction potential. Radiative relaxation is also included but the corresponding rate constants are small compared to non-radiative relaxation for both models.
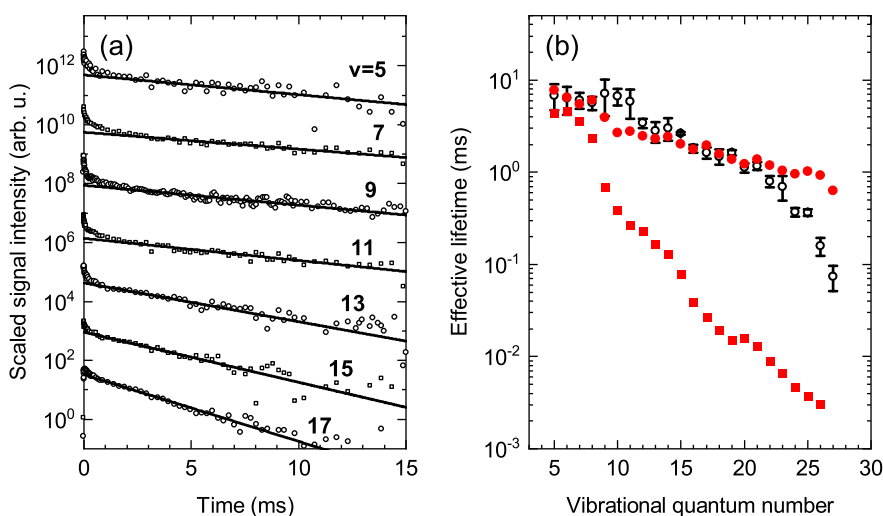
Figure 4.10: (a) Selected experimental time profiles (squares and circles) on the millisecond timescale of selected vibrational states are shown together with exponential fits to the long-term decay (solid lines). The time profiles and fits are arbitrarily scaled such that they are shifted with respect to each other on the logarithmic intensity scale. (b) Black, open dots with error bars (1σ) show the effective lifetimes extracted from the exponential fits in panel (a). Red symbols show the effective lifetimes extracted from the long-term decays in KMC simulations for two different relaxation models. Red dots correspond to the CPS relaxation model and the simulation is the same as in Fig. 4.6b. Red squares correspond to the ST model based on a Debye DOS. From Ref. [20]. Adapted with permission from AAAS.

As apparent from Fig. 4.10b, the simulated lifetimes based on the CPS model agree extremely well with the experimental lifetimes for $v \lesssim 23$, but deviate for higher vibrational states. It is worth mentioning that the vibrational state-dependence of the CPS rate constants closely follows that of the fundamental fluorescence rate constants (see Fig. 4.5). Thus, the relatively weak v-dependence, which is also observed experimentally, is fundamentally consistent with the CPS model. The simulation based on the ST model, on the other hand, agrees poorly with the data. Furthermore, it shows an extremely strong vibrational state-dependence, which leads to changes of the effective lifetime over three orders of magnitude.

It should be noted that the ST rate constants are based on a Debye DOS and the same coupling parameter λ as determined in Ref. [57]. Although the absolute values of the rate constants depend strongly on these two parameters, the strong v-dependence is rather insensitive to changes in λ and ω_{D} (see Fig. 4.11). Therefore, no major change in the

vibrational state-dependence of the effective lifetimes is expected for different parameters. Furthermore, the efficiency of vibrational relaxation according to the ST model is mainly determined by the highest phonon frequency, because it defines the number of phonons needed to dissipate the energy. Since variation of the Debye frequency does not change the v-dependence, also a more realistic phonon spectrum will therefore result in a similarly strong dependence.
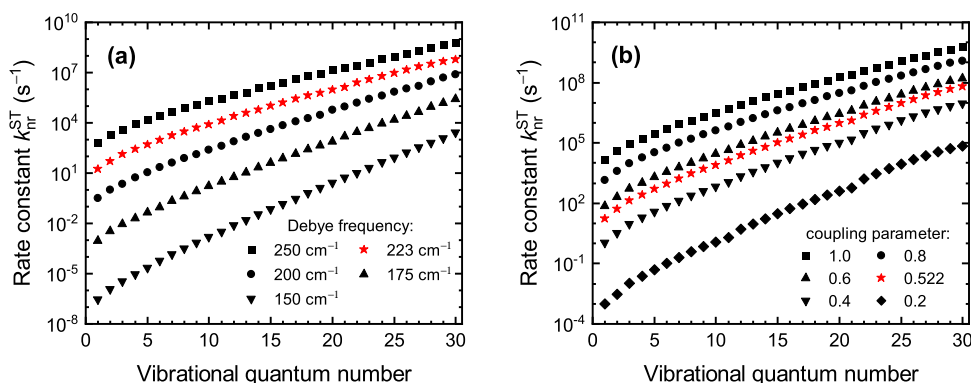

Figure 4.11: Non-radiative vibrational relaxation rate constants, k_{nr}^{ST}, obtained from the Skinner-Tully model for different Debye frequencies, ω_D, and coupling strength parameters, λ. (a) Variation of the Debye frequency in a range from 150 to $250\,\mathrm{cm}^{-1}$ for a fixed coupling strength parameter $\lambda = 0.522$. The red stars correspond to the ST rate constants used to obtain the results in Fig. 4.10b. (b) Variation of the coupling strength parameter in the range from 0.2 to 1.0 for a fixed Debye density $\omega_D = 223\,\mathrm{cm}^{-1}$. The red stars correspond to the same rate constants as in panel (a).

4.2 Discussion

4.2.1 Vibrational energy pooling dynamics

The good agreement between the experimental results and the KMC simulations, presented in Section 4.1 clearly shows the accuracy of the proposed base-camp mechanism for VEP. To achieve agreement with the experiment, the implementation of a more realistic phonon DOS and V-V energy transfer beyond nearest-neighbor molecules turn out to be the most critical factors. The phonon cutoff, defined by the highest available phonon frequencies, determines for which vibrational states the kinetic bottleneck occurs and thus the position of the different base-camps. Without energy transfer over larger

distances, VEP would stop after formation of the first base-camp, which is exactly what was observed in the simulations by Corcelli and Tully. [57, 58, 87]

The finding that vibrational energy pooling specifically excites transverse surface phonons is particularly interesting and a qualitative explanation is given in the following. [132] The V-V energy transfer process can be seen as individual CO molecules that change their respective vibrational quantum number by $\Delta v = 1$ due to dipole-dipole coupling. Since the two molecules are oriented almost perpendicular to the surface, the change in linear momentum that is associated with the $\Delta v = 1$ transitions of the two CO oscillators must also be perpendicular to the surface. To ensure momentum conservation, the wavevector of the phonons that accept the energy released in the V-V transfer process should point along the same direction. Transverse phonons that propagate perpendicular to the surface involve motion of the Na atoms in the surface plane, which is expected to result in the largest coupling between the two CO molecules (see Section 2.2.2). Longitudinal modes, on the other hand, would involve Na atom motion perpendicular to the surface, which is expected to modify the dipole-dipole coupling between the molecules less strongly.

4.2.2 The Sommerfeld ground-wave limit

The good agreement between the effective vibrational lifetimes in the experiment and in simulations based on the CPS model, which is purely based on classical electrodynamics, reflects the extraordinarily weak chemical coupling between CO and the NaCl(100) surface. In this system, long-range interactions that are responsible for VEP and vibrational relaxation via the CPS mechanism are much more important than vibrational relaxation through anharmonic coupling between the CO vibration and the surface phonons via the surface bond. We referred to this limit as the Sommerfeld ground-wave limit in Ref. [20], reflecting the origin of the CPS theory in Sommerfeld's electrodynamic description of radio wave propagation along the surface of the Earth. [69]

The unimportance of the adsorbate-surface bond seems counterintuitive at first sight, even for a physisorbed molecule. However, the weak anharmonic coupling between the CO vibration and other vibrational modes can be rationalized based on the understanding of vibrational relaxation on other surfaces (see Section 2.2.1 for a detailed introduction). For example, the nanosecond lifetime of CO on Si(100) [12, 13] was explained by energy transfer to four quanta of the frustrated rotations and translations and a single phonon. [55] In this case, the relatively strong CO-surface bond facilitates energy transfer because it increases the anharmonic coupling between the modes and the phonon bath, and only a few quanta of the high frequency modes between 400 and $500\,\mathrm{cm}^{-1}$

are needed to take up the energy. The small adsorption energy of CO on NaCl(100) ($20 \, \text{kJ} \, \text{mol}^{-1}$ [21]), however, results in weak coupling and relatively low frequencies of the frustrated rotational and translational modes (between 40 and $140 \, \text{cm}^{-1}$ [56]). The weak coupling to the frustrated translational mode perpendicular to the surface was specifically determined in laser-induced desorption experiments. [24] There, a lower limit of 100 s for the desorption lifetime of CO($v = 1$) was estimated. In addition, no evidence for desorption was found in the experiments described in Section 4.1.1, despite the population of much higher vibrational states. Also the phonon frequencies of the NaCl substrate are relatively small compared to the vibrational frequency of $^{13}\text{C}^{18}\text{O}$ ($\sim 2050 \, \text{cm}^{-1}$). Even for the Debye DOS used in the ST model ($\omega_\text{D} = 223 \, \text{cm}^{-1}$) at least 10 phonons are required for relaxation. Thus, long-range electrostatic interactions, which are responsible for VEP and CPS relaxation, can be more efficient than anharmonic couplings.

However, the sudden change of the effective lifetimes for vibrational states above $v = 23$ (see Fig. 4.10b), which cannot be explained by the CPS model, might indicate a transition from the CPS mechanism to the ST mechanism, although the currently used ST rate constants are clearly too high. Preliminary rate constant calculations by the group of Jörg Meyer, based on the ST model and more realistic phonon spectra, indicate that the sudden change could indeed be consistent with the ST mechanism. [132] Another possible explanation for deviations from the CPS model at high vibrational states might be related to the orientational isomerization of CO from its C-down orientation to an O-down orientation, which is discussed in detail in Chapter 5. This process is assumed to occur in the highest vibrational states and therefore a drop in the effective lifetime could be related to the onset of isomerization.

In the Sommerfeld ground-wave limit, the CPS relaxation rate constants (see Eq. 2.19) are mainly determined by the squared transition dipole moment of the adsorbate and the imaginary refractive index of the substrate, κ, which describes absorption of light at the corresponding transition wavelength. Even weaker coupling to the substrate would thus be expected for adsorbates with smaller transition strengths than CO. Two examples are H_2 and N_2, which are not infrared-active in the gas phase but show weak transition dipole moments when adsorbed to NaCl(100). [133, 134] Furthermore, the relaxation rate can be tuned by changing the absorption of the substrate, characterized by κ. For example, KCl shows values of κ that are up to two orders of magnitude lower compared to NaCl at $5 \, \mu\text{m}$. [73, 135] By lowering κ, one could imagine that the interaction of the CO adsorbate with the surface becomes so weak that its lifetime is only limited by the radiative lifetime of CO.

Laser-induced orientational isomerization in the CO/NaCl(100) monolayer

In the previous chapter, the mechanisms for vibrational energy pooling (VEP) and vibrational relaxation in a $^{13}C^{18}O$/NaCl(100) monolayer after infrared laser excitation were explored based on experimental data measured with the first version of the mid-infrared emission spectrometer [31, 93]. The observation of a second orientational isomer of CO that is populated in the VEP pooling process is reported in this chapter, enabled by the improved resolution and sensitivity of the new emission spectrometer presented in Section 3.1.2. The assignment of the laser-induced fluorescence (LIF) emission spectra to two different orientational isomers of CO is supported by an electrostatic model that predicts the vibrational frequency shifts with respect to gas phase CO. The most likely mechanism that leads to orientational isomerization in this system will be proposed based on the available experimental data and recent theoretical work. In addition, the potential for experimental studies of quantum state-resolved isomerization in the condensed phase will be discussed. The results presented in this chapter have been first published in Ref. [126] by the American Association for the Advancement of Science (AAAS).

5.1 Results

5.1.1 Observation of additional CO/NaCl(100) emission lines

The key observation for this chapter resulted from reproducing the LIF emission spectrum shown in Fig. 4.2 with the improved emission spectrometer presented in Section 3.1.2. Overall, the emission spectrum was measured with doubled resolution (~7 nm), while

the improved thermal shielding inside the 40 K monochromator and the use of a larger superconducting nanowire single-photon detector (SNSPD) ($25 \times 100 \, \mu m^2$) increased the sensitivity. A monolayer of isotopically enriched $^{13}C^{18}O$ was prepared with molecular beam dosing at 25 K (see Section 3.2.2) and subsequently cooled to 7 K to perform LIF experiments. The symmetric mode near 2055 cm^{-1} was excited and the corresponding emission spectrum, measured in the CO overtone region, is presented in Fig. 5.1. As in Fig. 4.2, the presented data is integrated over a 200 μs time window after laser excitation with the background subtracted to allow for an easier comparison.

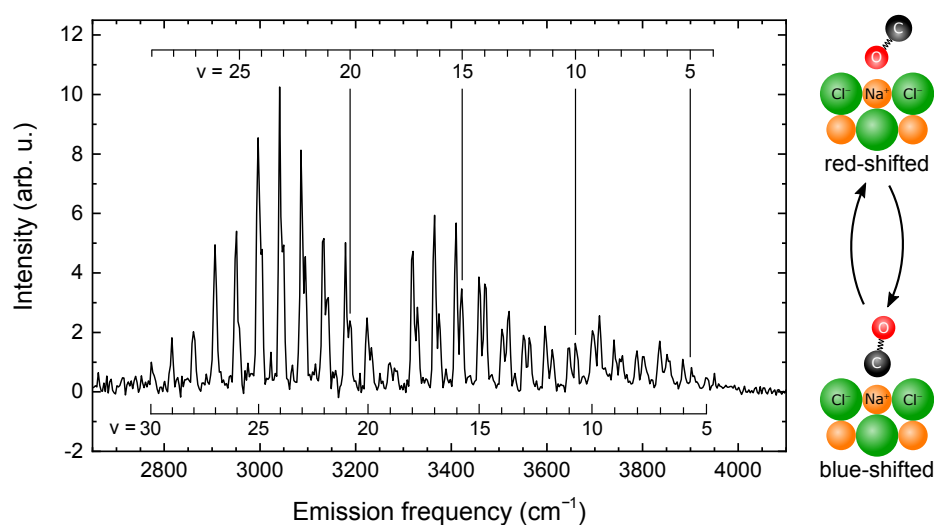Figure 5.1: Overtone emission spectrum of the $^{13}C^{18}O$/NaCl(100) monolayer obtained with the improved emission spectrometer after laser excitation of the symmetric mode at 2055 cm^{-1} with a pulse energy of 145 μJ. Emission signal is integrated over a 5-205 μs time window after laser excitation and measured at a 5.0 μA bias current. Two vibrational progressions are observed and the vibrational assignment for both species is indicated by combs. The quantum numbers, v, correspond to the upper vibrational levels from which fluorescence originates ($v \rightarrow v - 2$). The two schematic pictures illustrate the C-down and O-down orientations of CO that are assigned to these two progressions in the following. From Ref. [126]. Reprinted with permission from AAAS.

Figure 5.1 clearly shows two separate vibrational progressions, which could not be resolved with the previous experimental setup. The vibrational assignment for those progressions will be explained in Section 5.1.2 and it will be shown that the progressions indicated by the upper and lower combs, respectively, are red-shifted and blue-shifted with respect to those of $^{13}C^{18}O$ in the gas phase. In Section 5.1.3, the blue-shifted

species will be assigned to the usual orientation of CO on the surface, in which the carbon atom binds closer to the Na$^+$ ion. For clarity, I will thus refer to the blue-shifted species as "C-down" (or Na$^+$–CO) already in the following. The red-shifted species will be assigned to a flipped orientation, in which the oxygen atom binds closer to the Na$^+$ ion. I will thus refer to the red-shifted species as "O-down" (or Na$^+$–OC).

Both progressions are observed over a large range of vibrational states between $v = 5$ and 30. While the two progressions are clearly separated for low vibrational states, the O-down lines are only seen as a shoulder for $v = 23$ to 26 and they cannot be distinguished from the C-down lines for higher states. The intensity distribution of both progressions is very similar and consistent with the distribution observed in Fig. 4.2, which was explained by a base-camp mechanism in which groups of vibrational states are populated sequentially on different time scales. Interestingly, the emission frequencies of the C-down progression are consistent with the peak positions observed in Fig. 4.2, indicating that mainly this species has been probed in Chapter 4.

Two similar vibrational progressions are observed when the ^{13}C^{18}O monolayer is covered by ~100 overlayers of ^{12}C^{16}O (buried monolayer) and the monolayer excitation line near 2053.5 cm^{-1} is excited (see Fig. 5.2). The emission peak positions for the C-down species in the bare and buried monolayer spectra agree within the experimental accuracy. The peak positions of the O-down species in the buried monolayer are close to the emission frequencies observed in the bare monolayer but slightly shifted to larger emission frequencies by 3-6 cm^{-1}. However, the relative contribution of the O-down species to the overall emission intensity is significantly larger for the buried monolayer than for the bare monolayer. In addition, the overall emission intensity is smaller in the buried monolayer case and lower vibrational states ($v \leq 17$) are populated.

5.1.2 Spectroscopic assignment

Using the vibrational assignment in Section 5.1.1, the observed emission wavenumbers can be used to extract the vibrational constants ω_e, $\omega_e x_e$ and $\omega_e y_e$ of the two species. The term values for an anharmonic oscillator (in cm^{-1}) are given by

$$G(v) = \omega_e (v + 1/2) - \omega_e x_e (v + 1/2)^2 + \omega_e y_e (v + 1/2)^3 . \tag{5.1}$$

ω_e is the harmonic frequency. $\omega_e x_e$ and $\omega_e y_e$ are anharmonicity constants. Based on Eq. 5.1, the corresponding emission wavenumbers for overtone transitions ($v \rightarrow v - 2$) are

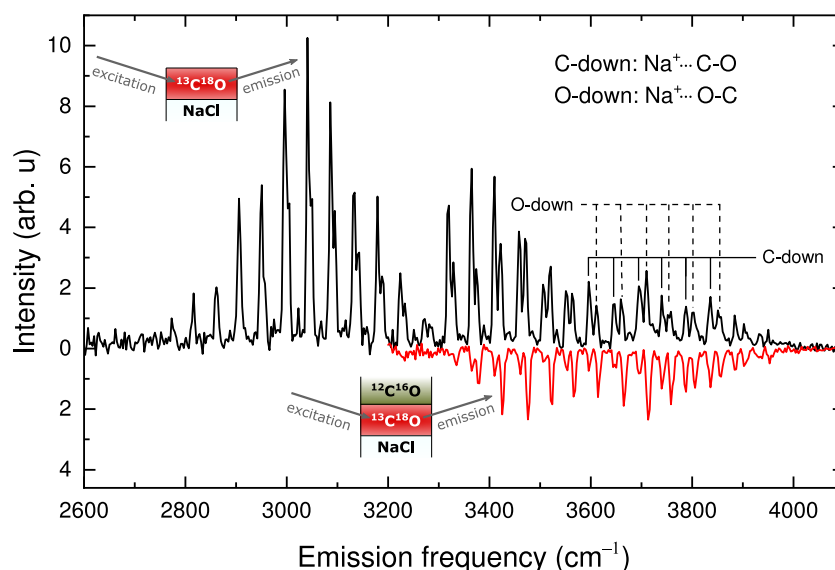$$\tilde{\nu}_v = G(v) - G(v - 2) = 2\omega_e + (-4v + 2)\omega_e x_e + (6v^2 - 6v + 7/2)\omega_e y_e . \tag{5.2}$$

Figure 5.2: The emission spectrum of a $^{13}C^{18}O$/NaCl(100) monolayer covered by 100 additional $^{12}C^{16}O$ overlayers (buried monolayer), obtained after excitation of the absorption line near $2053.5\,cm^{-1}$ with $145\,\mu J$/pulse at a $5.0\,\mu A$ bias current, is shown in red. This is compared to the bare monolayer emission spectrum in Fig. 5.1, shown in black. For both spectra, two vibrational progressions with similar emission frequencies are observed, which are indicated by combs for selected emission lines. The absolute vibrational assignment can be found in Fig. 5.1. From Ref. [126]. Reprinted with permission from AAAS.

By fitting the observed emission wavenumbers to the expression in Eq. 5.2, the spectroscopic constants ω_e, $\omega_e x_e$ and $\omega_e y_e$ for the C-down and O-down species in the bare and buried monolayer can be derived. Their values are shown in Table 5.1. In addition, the spectroscopic constants for $^{13}C^{18}O$ and $^{12}C^{16}O$ multilayers, obtained from the corresponding multilayer emission spectra, and of the $^{12}C^{16}O$ C-down species, obtained from $^{12}C^{16}O$ monolayer emission spectra, are presented (the spectra are not explicitly shown). The same spectroscopic constants of different isotopologues of gas phase CO are also shown for comparison. For the most relevant species, the extrapolated fundamental frequencies of the $v = 0 \rightarrow 1$ transitions, $\tilde{v}_{0\rightarrow1} = G(1) - G(0)$, are calculated based on the listed spectroscopic constants and compared to the corresponding gas phase isotopologue.

   Comparison of the harmonic frequencies of the C-down and and O-down species in the bare monolayer with the harmonic frequency of $^{13}C^{18}O$ in the gas phase ($\omega_e = 2067.80\,cm^{-1}$) shows frequency shifts in opposite directions: The C-down species

Table 5.1: Vibrational constants ω_e, $\omega_e x_e$ and $\omega_e y_e$ of various CO isotopologues in the gas phase, in the multilayer, in the buried monolayer and in the bare monolayer. C-down and O-down species are denoted as Na^+–CO and Na^+–OC, respectively. $^{13}C^{18}O$ species are highlighted in grey. In addition, the calculated fundamental frequencies, $\tilde{\nu}_{0\rightarrow1}$, and the vibrational frequency shifts, $\Delta\tilde{\nu}_{0\rightarrow1}$, relative to the corresponding gas phase isotopologue are also given for the bare monolayer and the buried monolayer. From Ref. [126]. Adapted with permission from AAAS.

sample	isotopologue/ isotomer	ω_e (cm^{-1})	$\omega_e x_e$ (cm^{-1})	$\omega_e y_e$ (10^{-3} cm^{-1})	$\tilde{\nu}_{0\rightarrow1}$ (cm^{-1})	$\Delta\tilde{\nu}_{0\rightarrow1}$ (cm^{-1})
gas-phase*	$^{12}C^{16}O$	2169.81	13.29	10.5	2143.3	0
	$^{12}C^{17}O$	2142.17	12.95	10.1	–	–
	$^{13}C^{16}O$	2121.45	12.70	9.8	–	–
	$^{12}C^{18}O$	2117.40	12.65	9.8	–	–
	$^{13}C^{17}O$	2093.16	12.37	9.4	–	–
	$^{13}C^{18}O$	2067.80	12.07	9.1	2043.7	0
multilayer†	$^{12}C^{16}O$	2166.6±1.0	13.39±0.07	14.8±1.3	2139.8	–
	$^{13}C^{18}O$	2065.6±1.1	12.19±0.08	13.2±1.5	2041.3	–
buried monolayer†	Na^+–$^{13}C^{18}O$	2073.7±4.0	12.05±0.39	8±12	2049.6	+5.9
	Na^+–$^{18}O^{13}C$	2061.8±3.3	12.31±0.37	14±12	2037.2	−6.5
monolayer†	Na^+–$^{13}C^{18}O$	2075.7±0.7	12.21±0.05	11.5±1.1	2051.3	+7.6
	Na^+–$^{18}O^{13}C$	2058.8±0.9	12.18±0.08	9.2±1.8	2034.4	−9.3
	Na^+–$^{12}C^{16}O$	2176.8±1.0	13.35±0.08	11.2±1.8	2150.2‡	+6.9

∗ The gas-phase values for $^{12}C^{16}O$ are taken from Ref. [136] and are actually available with much higher accuracy than shown here. The values for other isotopologues were calculated based on the scaling relations of the Dunham coefficients with the reduced mass μ ($\omega_e \propto \mu^{-1/2}$, $\omega_e x_e \propto \mu^{-1}$ and $\omega_e y_e \propto \mu^{-3/2}$). The rounded values for $^{13}C^{16}O$ and $^{12}C^{18}O$ calculated in this way agree extremely well with the experimental data by Todd *et al.*, which indicates that the values are accurate for all isotopes within the given precision.

† The error bars represent 95 % confidence intervals (2σ). They were derived by calculating the weighted average of the spectroscopic constants and the corresponding errors from several fits to different measurements except for the buried monolayer where the constants were derived from a single spectrum shown in Fig. 5.2.

‡ Note that this value is in excellent agreement with the experimental value of 2150.5 cm^{-1} found when $^{12}C^{16}O$ is diluted in $^{13}C^{16}O$ [107], conditions where the influence of the excitonic splitting in absorption spectroscopy is essentially removed. In emission spectroscopy, the splitting also does not appear. We have observed emission lines for the O-down isomer of $^{12}C^{16}O$, but the data is not sufficient to derive its spectroscopic constants accurately.

($\omega_e = (2075.7 \pm 0.7)$ cm^{-1}) is blue-shifted with respect to the gas phase value while the O-down species ($\omega_e = (2058.8 \pm 0.9)$ cm^{-1}) is red-shifted. The blue- and red-shifts are, of course, also reflected in the fundamental frequency shifts, $\Delta\tilde{\nu}_{0\rightarrow1}$, relative to the gas phase frequency. Furthermore, the extrapolated fundamental frequency of the C-down species in the bare monolayer (2051.3 cm^{-1}) is consistent with the Davydov doublet at 2049 and 2055 cm^{-1} observed in absorption. The same trends are found for the buried monolayer. Because the bare monolayer system is less complex and its spectroscopic constants are obtained with higher accuracy, the following analysis will mostly focus on the bare monolayer.

Since isotopically enriched ^{13}C^{18}O has been used for the experiments with less than 1 % ^{13}C^{16}O and ^{13}C^{17}O impurities (see also Section 3.1.5), it is reasonable to assume that the vibrational progressions observed in the monolayer emission spectrum can be assigned to two different ^{13}C^{18}O species. This hypothesis is supported by the clear mass dependence seen in the gas phase spectroscopic constants of the various CO isotopologues listed in Table 5.1. To be more specific, the following scaling relations apply, [136] where μ is the reduced mass of the molecule:

$$\omega_e \propto \mu^{-1/2}, \ \omega_e x_e \propto \mu^{-1} \text{ and } \omega_e y_e \propto \mu^{-3/2}. \tag{5.3}$$

Thus, the spectroscopic constants show characteristic values depending on the isotopologue and can be used to assign the C-down and O-down species in the bare monolayer to ^{13}C^{18}O (see Table 5.1). The harmonic frequencies of both species are clearly located near the ^{13}C^{18}O gas phase value. In addition, $\omega_e x_e \approx 12.2$ cm^{-1} is only 0.1 cm^{-1} larger than the ^{13}C^{18}O gas phase value and identical for both species within experimental errors; the difference to the next isotopologue (^{13}C^{17}O) is slightly larger ($\sim$0.15 cm^{-1}). A similar value of $\omega_e x_e$ is also observed for the ^{13}C^{18}O multilayer, providing further evidence that both species can be assigned to different ^{13}C^{18}O species. To definitely exclude that the O-down progression can simply be assigned to a C-down progression of a different isotopologue, the spectroscopic constants of Na$^+$ – ^{13}C^{18}O are used to predict the spectroscopic constants of Na$^+$ – ^{13}C^{16}O and Na$^+$ – ^{13}C^{17}O using the isotopic relations in Eq. 5.3. The predicted constants can then be used to predict the corresponding emission frequencies (Eq. 5.2). Figure 5.3 clearly shows that the predicted emission frequencies of Na$^+$ – ^{13}C^{16}O and Na$^+$ – ^{13}C^{17}O do not agree with the observed emission peaks of the O-down species.

The spectroscopic constants in Table 5.1, in particular the resulting red-shift for the O-down isomer, strongly rely on the vibrational assignment in Fig. 5.1. The infrared absorption spectra of the buried monolayer in Fig. 5.4 give strong evidence that the given
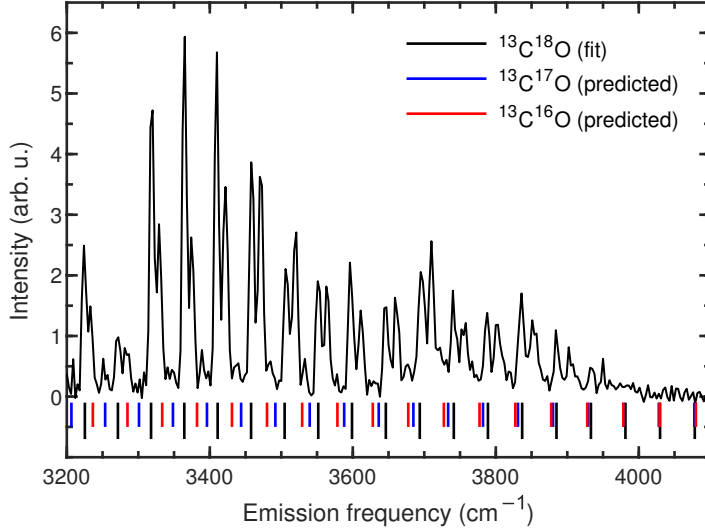
Figure 5.3: Black lines indicate the emission frequencies calculated with the fitted spectroscopic constants of the C-down species in the bare monolayer (Na$^+$ – ^{13}C^{18}O). Blue and red lines indicate predictions for the emission peak positions of Na$^+$ – ^{13}C^{17}O and Na$^+$ – ^{13}C^{16}O based on the isotopic relations in Eq. 5.3 and the spectroscopic constants of Na$^+$ – ^{13}C^{18}O.

assignment is indeed correct. Figure 5.4a shows the polarized Fourier-transform infrared (FTIR) absorption spectra of the freshly prepared buried monolayer sample, measured at 7 K. The spectra show an intense peak at 2053.5 cm^{-1} and a tiny peak at 2048.2 cm^{-1}, both of which are observed with p- and s-polarization. The intense peak is consistent with the absorption peak at 2153.6 cm^{-1} reported for a buried ^{12}C^{16}O monolayer, [44] considering that the fundamental frequencies of ^{13}C^{18}O and ^{12}C^{16}O differ by almost exactly 100 cm^{-1}. The low intensity peak, on the other hand, has not been reported previously. Observation of a doublet can be explained by exciton splitting if the unit cell consists of two inequivalent CO molecules, similar to the doublet observed for the bare monolayer (see also Section 2.1). [36, 38] Based on simulations of the absorption spectra, we estimated the structure of the buried monolayer in the Supplementary Materials of Ref. [126].[1] In addition, this simulation provided an estimate of the fundamental frequency if the dynamic exciton splitting was not present. The estimate of this unsplit frequency is indicated in Fig. 5.4 and agrees well with the extrapolated fundamental frequency value obtained from the C-down emission lines and indicated by the blue bar.

---

[1] A slightly better estimate for the tilt angle of the C-down and O-down species is shown in Appendix C.

However, no absorption peak is observed for the red-shifted O-down species before laser excitation.

Following laser excitation of the $^{12}C^{16}O$ overlayer,[2] a second absorption peak appears at ~2037 cm^{-1}, accompanied by a redshift and broadening of the C-down peak (Fig. 5.4b). This second peak is in good agreement with the extrapolated fundamental frequency of the O-down species indicated by the red bar, thus confirming the vibrational assignment of the two species made above. At 7 K, no change in the O-down absorption peak is observed over the course of 12 h but the laser-induced change can be fully reversed by annealing at 22 K for 20 min (Fig. 5.4c). Only the long lifetime of the O-down species makes the observation with conventional absorption spectroscopy possible in the buried monolayer case. For the bare monolayer, the red-shifted species could not be observed in absorption, suggesting that its lifetime at 7 K is shorter than the typical time required to measure an FTIR spectrum (approx. 5 min), which is significantly shorter than the lifetime observed for the buried monolayer.

5.1.3 Orientation dependence of the vibrational frequency shift

The results presented in the previous section indicate that both vibrational progressions observed in the monolayer emission spectra result from different $^{13}C^{18}O$ species, featuring emission frequencies that are blue- and red-shifted with respect to gas phase CO. In this section, it will be shown that the peculiar blue- and red-shifts relative to the gas phase molecule can be explained by two different orientational isomers of $^{13}C^{18}O$ adsorbed to NaCl. Whereas the blue-shifted species corresponds to the well-known, stable monolayer structure where CO binds with the carbon atom facing the NaCl surface (C-down orientation), the observed metastable red-shifted species binds with the oxygen atom closer to the surface (O-down orientation).

The vibrational frequency shift relative to the gas phase molecule is mainly determined by electrostatic interactions between CO and its environment, which by their very nature are strongly dependent on molecular orientation. [122] The vibrational frequency of the CO stretching vibration, characterized by the quantum number v, is much higher than the frequencies for frustrated translation and rotation (2050 vs. 40-140 cm^{-1}). [56] Hence, a vibrationally adiabatic [137] potential energy surface (PES), $V_v(\mathbf{r}, \theta, \phi)$, can be constructed, which is a function of the vibrational state v and depends parametrically on the position and orientation of the molecule. Here, $\mathbf{r} = (x, y, z)$ represents the center of mass coordinates of the CO molecule relative to the NaCl surface, θ is the

---

[2] $^{12}C^{16}O$ excitation provides the most efficient way to pump the $^{13}C^{18}O$ monolayer in the buried monolayer sample. See Chapter 6 for a detailed discussion of this effect.
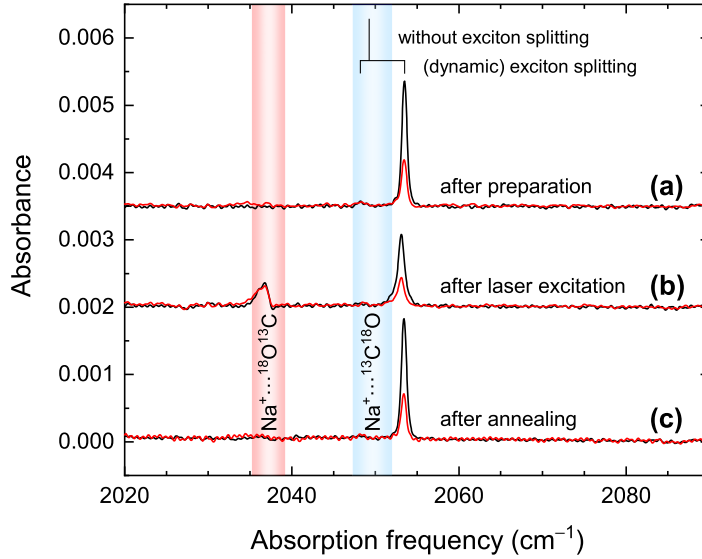
Figure 5.4: (a) p-polarized (black curve) and s-polarized (red curve) FTIR spectra of the buried monolayer sample at 7 K, measured immediately after preparation at an incidence angle of 34°. The doublet at 2048.2 cm^{-1} and 2053.5 cm^{-1} is indicated by two vertical lines that are labeled "(dynamic) exciton splitting". The estimate of the fundamental frequency as it would appear in emission is indicated by another vertical line labeled "without exciton splitting". Red and blue bars indicate the positions of the extrapolated fundamental frequencies, $\tilde{\nu}_{0\rightarrow1}$, of the C-down and O-down species in the buried monolayer, respectively (see Table 5.1). (b) shows the polarized absorption spectra after excitation of the $^{12}C^{16}O$ overlayer excitation line at 2138.6 cm^{-1} with ~6000 laser pulses. (c) shows the absorption spectra of the same sample measured after annealing at 22 K for about 20 min. Note that the three sets of spectra are offset for clarity. Furthermore, absorption peaks assigned to iron carbonyl impurities in the $^{12}C^{16}O$ overlayer (see Appendix E), which are identical for all three panels, were subtracted for clarity. From Ref. [126]. Adapted with permission from AAAS.

tilt angle of the molecule and ϕ describes its azimuthal orientation. This position- and orientation-dependent PES includes all first-order energy corrections to the vibrational levels of an unperturbed CO molecule due to electrostatic interactions with the NaCl surface, $V_v^{CO\leftrightarrow NaCl}(\mathbf{r}, \theta, \phi)$, and surrounding CO molecules, $V_v^{CO\leftrightarrow CO}(\mathbf{r}, \theta, \phi)$:

$$V_v(\mathbf{r}, \theta, \phi) = V_v^{CO\leftrightarrow NaCl}(\mathbf{r}, \theta, \phi) + V_v^{CO\leftrightarrow CO}(\mathbf{r}, \theta, \phi). \tag{5.4}$$

The corresponding first-order correction to the fundamental frequency, i.e., the fundamental frequency shift relative to gas phase CO, is simply given by

$$\Delta\tilde{\nu}_{0\to 1}(\mathbf{r}, \theta, \phi) = \frac{1}{hc}\left[V_{v=1}(\mathbf{r}, \theta, \phi) - V_{v=0}(\mathbf{r}, \theta, \phi)\right]. \tag{5.5}$$

To illustrate the effect of orientation-dependent electrostatic interactions on the vibrational frequency shift, consider the simplified case where a CO molecule interacts solely with the electric field of the NaCl surface via its dipole moment. The dipole moment of CO in its vibrational ground state, μ_{00}, is positive, corresponding to a direction of the dipole vector from the carbon atom to the oxygen atom ($C^{\delta-}O^{\delta+}$ polarity). The electric field vector above a sodium ion points away from the surface. Therefore, interaction between the dipole moment and the surface electric field is attractive when CO is adsorbed perpendicular and in a C-down orientation. If CO is excited to $v = 1$, the magnitude of the permanent dipole moment, μ_{11}, is reduced but still positive. Thus the interaction will be less attractive ($V_{v=1} > V_{v=0}$). This results in a positive value of $\Delta\tilde{\nu}_{0\to 1}$ and therefore in a blue-shift. In contrast, the dipole-electric field interaction for CO adsorbed in a flipped O-down configuration is repulsive and the interaction in the $v = 1$ state will be less repulsive than in the $v = 0$ state ($V_{v=1} < V_{v=0}$). In this case, the flipped orientation results in a negative value of $\Delta\tilde{\nu}_{0\to 1}$ and thus in a red-shift. However, considering only the dipole-electric field interaction is clearly not sufficient to give a proper description of the orientation-dependent frequency shift. Instead, all electrostatic CO-NaCl and CO-CO interactions within the bare monolayer should be considered.

The CO monolayer is modeled using the parameters of the experimentally known (2×1) structure (see also Refs. [38, 39]): In the (2×1) unit cell, both CO molecules are tilted with respect to the surface normal ($\theta = 25°$), but in opposite directions along the short unit cell vector ($\phi = +90$ and $-90°$). Note that $\theta = 0°$ corresponds to a C-down orientation with the bond axis perpendicular to the surfaces. $\phi = 0$ corresponds to the direction of the long unit cell vector. It is assumed that the CO molecules adsorb on top of the Na$^+$ ions ($x = y = 0$) in the first surface layer at a distance $z = 2.35$ Å, corresponding to the equilibrium z-distance of the C-down orientation. [120, 138] The (2×1) unit cells

are repeated in a supercell with periodic boundary conditions that contains (20×20) molecules. The lattice constant of the underlying Na^+ lattice, $a = a_{NaCl}/\sqrt{2} = 3.99\,Å$, defines the nearest-neighbor distance between CO molecules, where $a_{NaCl} = 5.64\,Å$ is the bulk lattice constant of NaCl.

The PES for rotation of a single CO molecule around its center of mass is obtained by calculating $V_v(\mathbf{r}, \theta, \phi)$ according to Eq. 5.4 for different orientational angles, θ and ϕ, and different quantum numbers v. The positions and orientations of all other molecules in the monolayer structure are kept fixed and those molecules are assumed to be in their vibrational ground state. Each CO molecule in the monolayer structure is represented by the v-dependent expectation values of the dipole moment, μ_{vv}, the quadrupole moment, Θ_{vv}, and the octopole moment, Ω_{vv}, located in the center of mass of the molecule. The vibrational state-dependent expectation values of the multipole moments that are used can be found in Table 5.2 (including references) and should be valid at least for $v \leq 5$ (see the footnote in Table 5.2). Within this model, each CO molecule interacts with the electric field and the electric field gradients of the NaCl surface via its dipole moment and the higher multipole moments. CO-CO pairs can interact within a radius of $10a \approx 40\,Å$ via multipole-multipole interactions. Equations describing the individual contributions to the CO-NaCl and CO-CO interaction terms can be found in Appendix D. With the calculated electrostatic PES, $V_v(\mathbf{r}, \theta, \phi)$, and Eq. 5.5, calculation of the fundamental frequency shift as a function of molecular orientation and vibrational states is straightforward. However, note that the model only describes the rotation of a single molecule while all other degrees of freedom (DOFs) are frozen.

Fig. 5.5 shows the calculated results for rotation of a single molecule within the bare CO monolayer structure. The fundamental frequency shift is shown in Fig. 5.5a as a function of the two orientational angles θ and ϕ. Figs. 5.5b and 5.5c illustrate the corresponding electrostatic PES for the molecule in $v = 0$. Two distinct, stable minima are predicted: the first minimum at $\theta = 4°$ and $\phi = 90°$ corresponds to a C-down orientation, where CO is adsorbed almost perpendicular to the surface; the second minimum at $\theta = -134°$ and $\phi = 90°$ corresponds to an O-down orientation, where the CO bond axis is tilted by $46°$ with respect to the surface normal.[3] The C-down minimum is predicted to be $750\,cm^{-1}$ more stable than the O-down isomer. These two minima are indicated by green and black ellipses in Fig. 5.5a and the model clearly shows a blue-shift $(+15.9\,cm^{-1})$ for the C-down species and a red-shift $(-3.9\,cm^{-1})$ for the O-down species. This is in good qualitative agreement with the experimentally observed frequency shifts for the C-

---

[3] Note that the given angles only refer to the upper half of Fig. 5.5b because the lower half essentially shows the same orientations.

Table 5.2: v-dependence of the vibrational expectation values of the dipole moment, μ_{vv}, the quadrupole moment, Θ_{vv}, the octopole moment, Ω_{vv}, and the parallel and perpendicular components of the dipole polarizability, $\alpha_{\parallel}$ and $\alpha_{\perp}$ (including references). For μ and Ω, positive values are defined such that the multipole moments point from the carbon to the oxygen atom. All given values are gas phase values of $^{12}C^{16}O$. From Ref. [126]. Reprinted with permission from AAAS.

Property	v-dependent value[*]	Unit	Ref.
μ	$0.1381 - 0.0263(v + 1/2)$	D	[125][†]
Θ	$-6.505 + 0.132(v + 1/2)$	$1 \times 10^{-40}\,C\,m^2$	[139][‡]
Ω	$8.953 + 0.051(v + 1/2)$	$1 \times 10^{-50}\,C\,m^3$	[139][‡]
$\alpha_{\parallel}$	$15.431 + 0.197(v + 1/2)$	a. u. $(1.649 \times 10^{-41}\,C\,m^2\,V^{-1})$	[140]
$\alpha_{\perp}$	$11.732 + 0.038(v + 1/2)$	a. u. $(1.649 \times 10^{-41}\,C\,m^2\,V^{-1})$	[140]

[*] While the calculated dipole moment values from Ref. [125] show a linear dependence up to $v = 27$, the highest vibrational state that can be compared to experimental data is $v = 5$. The quadrupole moments, octopole moments and polarizabilities in Ref. [139] and [140] have been calculated for internuclear separations of CO between 1.83 and 2.43 a.u., which agrees with the classical turning points of $v = 5$ [125]. We conclude that the vibrational-dependent properties used in the present work are clearly valid for $v = 5$ and lower.

[†] The values are derived from a linear fit to the "aV6Z (field)" data for all vibrational states calculated in Ref. [125].

[‡] Note that there is an error in the relative sign of μ and Ω in Ref. [139]. The correct signs of the multipole moments were taken from Ref. [141].

and O-down species ($+7.6\,cm^{-1}$ and $-9.3\,cm^{-1}$), although the model seems to predict too positive frequency shifts. Also the predicted frequency splitting between the two species ($19.8\,cm^{-1}$) is in good agreement with experiment ($16.9\,cm^{-1}$). Interestingly, the region near $\theta = \pm 70°$ where the potential barriers for interconversion of the two species are located also separates the blue-shifted from the red-shifted region. This qualitative trend further emphasizes that a blue-shift is expected for the C-down minimum while a red-shift is expected for the O-down minimum, as observed in the experimental emission spectra.

The model gives similarly good results for a single, isolated CO adsorbate that interacts only with the NaCl surface. In this zero coverage limit, the experimentally observed frequency shift with respect to the gas phase molecule is $16.6\,cm^{-1}$ and the polarization dependence of the FTIR spectra shows that the tilt angle is $\theta = 0°$. [35] Both the most stable geometry ($\theta = 0°$) and the corresponding frequency shift ($19.8\,cm^{-1}$) predicted
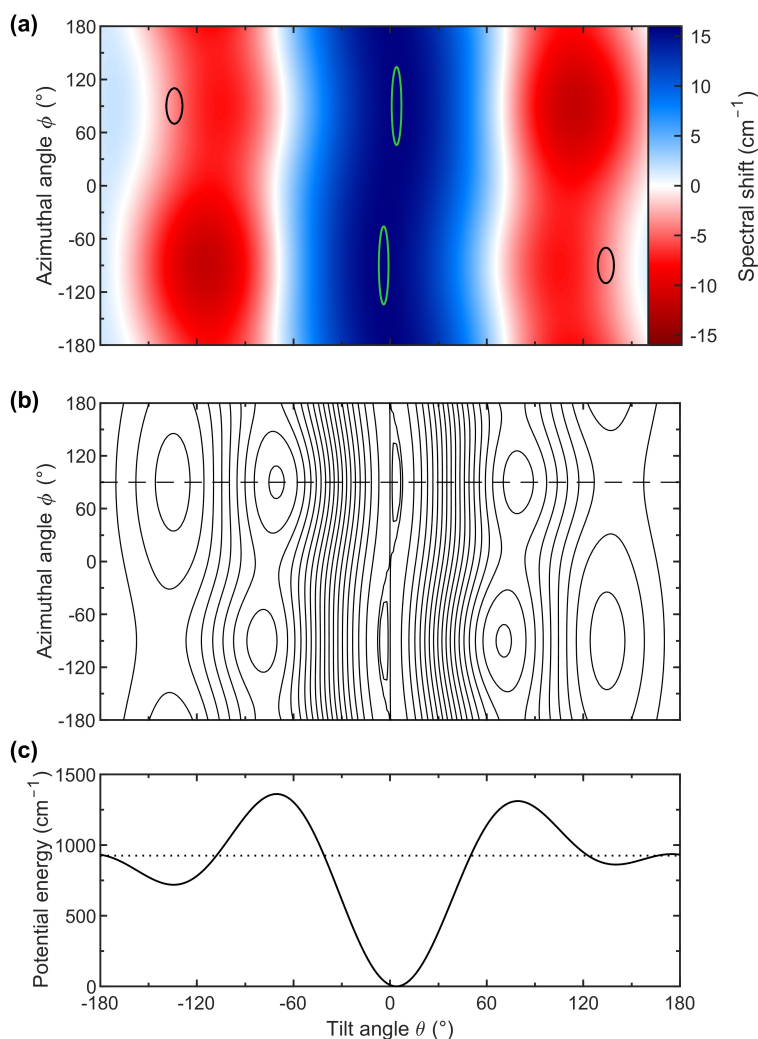
Figure 5.5: (a) Fundamental frequency shift, $\Delta\tilde{\nu}_{0\to1}$, relative to gas phase CO as a function of the tilt angle θ and the azimuthal angle ϕ. Black and green ellipses indicate the O-down and C-down orientations, respectively, which are minima on the electrostatic PES in panels (b) and (c). Note that the upper and lower halfs of the plot are related by symmetry and that ellipses of the same color correspond to the same orientation. (b) Contour plot the electrostatic PES as a function of the same two orientational angles. All contour lines are spaced by $75\,\mathrm{cm^{-1}}$, except for the two contour lines near $\theta = 0°$ at the lowest potential energies, which were added at 5 and $10\,\mathrm{cm^{-1}}$ in order to visualize the C-down minimum. (c) Cut through the PES at $\phi = 90°$, indicated by the dashed line in panel (b). Note that the potential energy of the C-down minimum is chosen as the reference energy ($0\,\mathrm{cm^{-1}}$). The potential energy at which the total electrostatic interaction energy for the rotated CO molecule is zero is shown as a dotted line for comparison. From Ref. [126]. Adapted with permission from AAAS.

by the model (see Fig. 5.6) agree well with the experimental values. However, the frequency shift is again overestimated (too positive). Furthermore, it is clearly seen that the electrostatic interaction potential for an isolated molecule in Fig. 5.6b does not differ much from the potential for a molecule inside the monolayer in Fig. 5.5c and also predicts a stable O-down species. Thus, the interaction with the NaCl surface is largely responsible for the total electrostatic interaction energy. The frequency shifts in Fig. 5.6a, on the other hand, differ slightly from the shifts in Fig. 5.5a. This is most likely due to CO-CO interactions that involve the dipole moment of the rotating molecule. Since μ is small for $v = 0$, it does not contribute much to the overall interaction energy; however, its strong dependence on v leads to a notable change in the frequency shift.
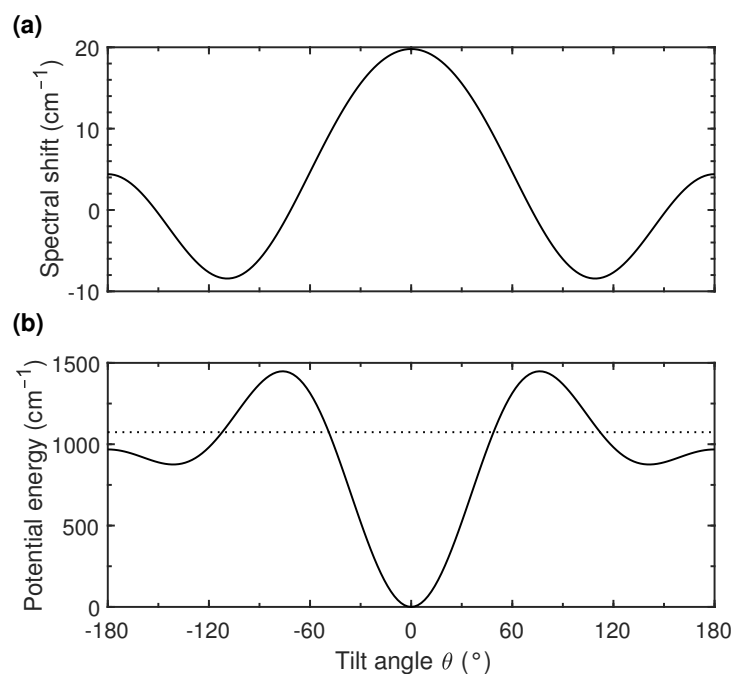

Figure 5.6: (a) Fundamental frequency shift of a single CO molecule, which is adsorbed directly on top of a sodium ion and only interacts with the electric potential of the NaCl surface, as a function of the tilt angle θ. (b) shows the corresponding potential energy curve for CO in $v = 0$. As in Fig. 5.5, the energies are referenced to the C-down minimum and the dotted line indicates the energy at which the total electrostatic interaction energy becomes zero.

The fact that the model consistently predicts frequency shifts that are too positive is likely explained by the fact that only electrostatic interactions are included, which should capture a large fraction of the orientation dependence of the frequency shift.

Contributions from induction, dispersion and repulsion are, however, not considered. The contribution of induced dipole interactions to the overall interaction energies and frequency shifts is negligible for the dipole and polarizability values given in Table 5.2. Dispersive and repulsive interactions are not explicitly considered because their dependence on orientation and vibrational quantum number is expected to be weak. Thus, they should not alter the orientation dependence of the electrostatic PES and the fundamental frequency shift much. However, one should keep in mind that their contributions to the overall binding energy of CO on NaCl(100) are large. [21, 120] In addition, the neglected interactions are expected to contribute a frequency shift that is approximately independent of orientation. To estimate this contribution, it is instructive to look at the frequency shifts observed for CO in rare gas matrices, as only those interactions are involved in CO-rare gas interactions that are neglected in the electrostatic model. The matrix shifts observed for CO in Ne ($-2.3\,\mathrm{cm}^{-1}$) and Ar ($-4.7\,\mathrm{cm}^{-1}$) are both red-shifts on the order of a few wavenumbers. [80] Such a contribution would compensate for the too positive frequency shifts predicted by the electrostatic model compared to the experiment.

5.1.4 Orientational isomerization of CO

The results obtained with the electrostatic model, presented in the previous section, clearly support the assignment of the two vibrational progressions to a stable blue-shifted C-down isomer and a metastable, red-shifted O-down isomer. In this section, the experimental data and the electrostatic model will be used to extract information on the mechanism for orientational isomerization from C-down to O-down.

It is important to realize that the C- and O-down orientations are separated by a large potential barrier. According to Fig. 5.5b, the barrier height is $\sim$1200 cm^{-1} in the vibrational ground state. Furthermore, the C-down isomer is more stable by around 720 cm^{-1} (not including zero-point energy (ZPE) corrections). Keep in mind that interactions other than electrostatic interactions are neglected and only orientational DOFs are included. Absolute energies and barriers extracted from the electrostatic model should thus be interpreted with care. Still, the estimated barrier height and energy difference between the two orientations are orders of magnitude larger than the thermal energy available at a surface temperature of 7 K ($k_{\mathrm{B}}T/hc \approx 5\,\mathrm{cm}^{-1}$). Therefore, spontaneous interconversion in the vibrational ground state is not feasible on the timescale of the experiment and the large energy difference would definitely favor population of the C-down isomer. In conclusion, isomerization can only occur for higher vibrational states.

Stabilization of the O-down isomer in high vibrational states

The strong vibrational state dependence of the electrostatic interactions, which is responsible for the fundamental frequency shift, could be relevant to the isomerization dynamics as well. Consider again the interaction of the molecular dipole moment with the surface electric field. As apparent from Table 5.2, the polarity of the dipole moment in the ground state is described by $C^{\delta-}O^{\delta+}$ polarity ($\mu \approx 0.125$ D), leading to an attractive interaction with the electric field for the C-down orientation. For $v = 5$, the sign of the dipole moment inverts and the interaction becomes repulsive. In the highest vibrational state observed in the experiments, $v = 30$, the repulsive dipole-electric field interaction would be more than five times stronger than the interaction in $v = 0$ ($\mu \approx -0.66$ D). [125] The increasingly repulsive dipole-electric field interaction for high vibrational states should therefore destabilize the C-down orientation. The O-down orientation, on the other hand, would be stabilized, effectively reducing the energy difference between the two isomers.

The electrostatic model presented in Section 5.1.3 can be used to estimate the change in the relative stability of the O-down and the C-down isomer ($\Delta E(v) = E_O(v) - E_C(v)$) in high vibrational states, assuming that the linear dependence of the multipole moments in Table 5.2 still holds. Figure 5.7 compares the calculated PES cuts of $v = 0$ and $v = 30$ at $\phi = 90°$, along which the C-down and O-down minima are located. In $v = 30$, the energy difference between the two isomers is significantly reduced from $\Delta E(v = 0) \approx 720 \, \text{cm}^{-1}$ to $\Delta E(v = 30) \approx 100 \, \text{cm}^{-1}$, resulting in a change of $-620 \, \text{cm}^{-1}$. This semi-quantitative trend shows that the vibrational dependence of the electrostatic interactions strongly stabilizes the O-down species relative to the C-down species for high vibrational states of CO. A similar trend is reported in a recent DFT study of the CO/NaCl(100) system, using $p(1 \times 1)$ and $p(2 \times 2)$ unit cells that contain a single CO molecule. [142]

The change in the relative stability can also be extracted based on the experimental emission spectra, including ZPE contributions. With the fitted spectroscopic constants of the C-down and O-down isomer in the bare monolayer (Table 5.1), it is readily calculated from the corresponding term values $G_C(v)$ and $G_O(v)$ (see Eq. 5.1):

$$\Delta E(v = 30) - \Delta E(v = 0) = \left[G_O(v = 30) - G_C(v = 30) \right] - \left[G_O(v = 0) - G_C(v = 0) \right].$$
(5.6)

The resulting value of $-540 \, \text{cm}^{-1}$ indicates a significant stabilization of the O-down isomer relative to the C-down isomer in $v = 30$ compared to $v = 0$, which is in surprisingly good agreement with the electrostatic model. Unfortunately, only the change in the energy difference can be extracted from the experiment, but not its absolute value.
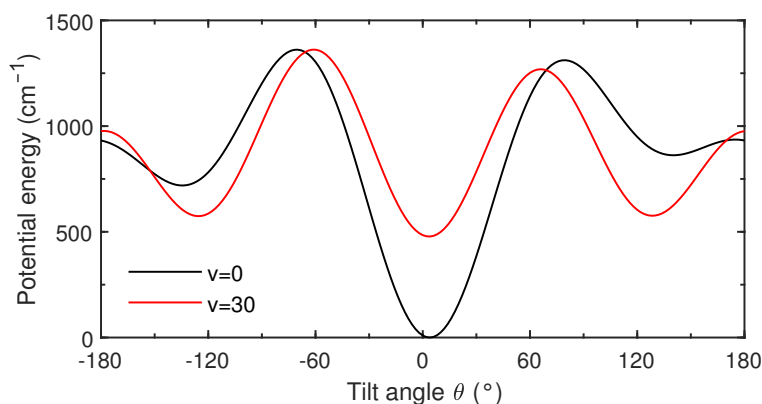
Figure 5.7: Comparison of the electrostatic PES cuts ($\phi = 90°$) obtained from the electrostatic model for different tilt angles of a single CO molecule in $v = 0$ (black curve) and $v = 30$ (red curve). As in Fig. 5.5c, both potential curves are referenced to the electrostatic interaction energy for the C-down minimum in $v = 0$. Note that only the electrostatic interaction energies relative to $CO(v)$ are considered and that the unperturbed $v = 30$ state actually lies at much higher absolute energies than the $v = 0$ state.

However, the large stabilization suggests that high vibrational excitation could favor population of the O-down isomer, whereas the C-down isomer is clearly favored in the vibrational ground state.

Kinetic interpretation of the isomerization

Although the presented results are consistent with a stabilization of the O-down species in high vibrational states, the presented vibrationally adiabatic electrostatic model cannot explain why isomerization should occur. Whereas Fig. 5.7 implies that the barrier for interconversion is reduced substantially for $v = 30$, the barrier is still too large to be overcome at cryogenic temperatures.[4] Potential mechanisms that could explain isomerization despite the large barrier will be discussed in Section 5.2.2, together with recent theoretical work. Nevertheless, some information on the isomerization dynamics can be deduced from the experimental observations, as presented in the following.

Since isomerization probably occurs in the highest vibrational states, lower vibrational states of the O-down isomer can only be populated by vibrational relaxation. However, emission from the O-down isomer is observed for all vibrational states down to $v = 4$ within the first 200 μs after laser excitation (see Fig. 5.1)—despite the fact that the effective

---

[4] Note that the cuts through the PES do not resemble the minimum energy path.

lifetimes for vibrational relaxation are much longer. Relaxation starting from the highest vibrational states of the O-down isomer would require several milliseconds to populate $v = 4$ (compare with Fig. 4.10). Therefore, the emission from low vibrational states of the O-down isomer indicates that the lifetime for back-conversion to the C-down isomer is longer than the time between two laser pulses (100 ms).[5] In this case, population in the O-down isomer survives relaxation to the vibrational ground state on the millisecond timescale and can participate in the VEP process following the next excitation laser pulse. Eventually, the competition between back-conversion to the C-down isomer and population of the O-down isomer due to laser excitation will lead to a steady-state concentration of the O-down isomer.

Further evidence for a steady-state concentration is given by the temporal behavior of selected vibrational states, which is shown for a low vibrational state ($v = 7$) and a high vibrational state ($v = 22$) in Fig. 5.8. Without a steady-state concentration, the $v = 7$ state of the O-down species could not be populated within the first microseconds after laser excitation. In addition, the shapes of the C-down and O-down time profiles barely differ for identical vibrational states during the first 300 μs after laser excitation, where VEP dominates the vibrational dynamics. Only after 300 μs, the time profile of the O-down isomer in $v = 22$ deviates from the time profile of the C-down isomer in $v = 22$. This observation indicates that the VEP dynamics of the two isomers are comparable, which is also reflected in the similar intensity patterns observed in the experimental emission spectrum (Fig. 5.1). The finding that the VEP dynamics are similar is not entirely surprising, given that the difference in the harmonic frequencies of the two isomers ($\Delta\omega_e \approx -17\,\mathrm{cm}^{-1}$) is even smaller than two times the anharmonic constant of the two species ($2\omega_e x_e \approx 24\,\mathrm{cm}^{-1}$).[6]

Alternatively, identical time profiles could indicate rapid interconversion between the O-down and the C-down species in the same vibrational state. In this case, the time profiles should also be correlated at late times and decay with the same relaxation rate, which is clearly not observed. More rapid decay of the O-down species is observed instead. Interestingly, the effective lifetimes of the O-down species are about 2 times shorter than those of the C-down species, for both $v = 7$ and 22.[7] The differences in the

---

[5] Recall that the lifetime for vibrational relaxation of the O-down molecule and the lifetime for back-conversion to the C-down isomer are two different quantities, both of which depend on v.

[6] Recall that the excess energy, which determines the rate constant of a $CO(n) + CO(m) \rightarrow CO(n+1) + CO(m-1)$ energy transfer process, is given by $\Delta E_{nm} \approx \Delta\omega_e - 2\omega_e x_e (n - m + 1)$, assuming that $\omega_e x_e$ is similar for both species.

[7] Note that the effective lifetimes observed for the C-down isomer are in excellent agreement with those in Fig. 4.10.

observed lifetimes are so small that they can probably be explained by slightly different VEP and relaxation dynamics rather than isomerization dynamics. Unfortunately, a direct comparison of the temporal profiles of C-down and O-down states above $v = 22$, where isomerization dynamics could probably be observed, is not possible because the corresponding emission lines overlap significantly.
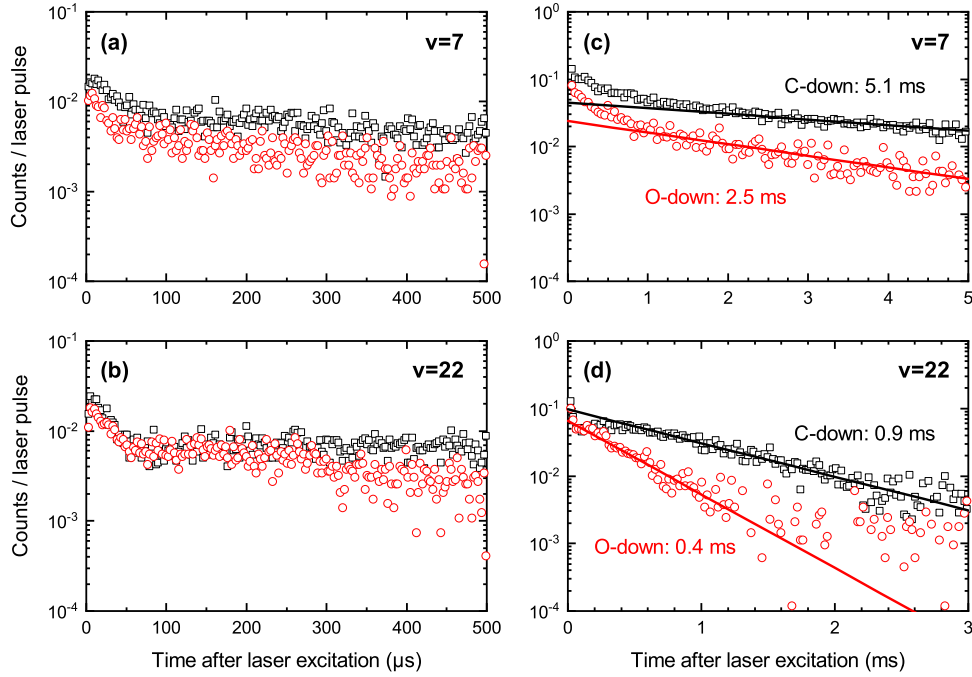

Figure 5.8: (a) Time profiles of the C-down (black squares) and O-down (red dots) isomer in $v = 7$ with a bin time of 2.56 μs. (b) Time profiles of the C-down (black squares) and O-down (red dots) isomer in $v = 22$ with a bin time of 2.56 μs. (c) Rebinned time profiles for $v = 7$ with a bin time of 40.96 μs. (d) Rebinned time profiles for $v = 22$ with a bin time of 20.48 μs. Straight lines in panels (c) and (d) indicate exponential fits to the asymptotic decays for both isomers. The corresponding effective lifetimes are also noted. For all panels, a logarithmic y-axis is chosen to emphasize the similarities of the curve shapes and to highlight the exponential decay at long times. Also note that the absolute number of counts differs between the left and right panels due to rebinning.

Back-conversion of the O-down isomer to the C-down isomer was directly observed for the buried monolayer. The lifetime of the buried $^{13}C^{18}O$ monolayer is indefinitely long at 7 K, as no change in the O-down absorption peak is detected over the course of

several hours. On the other hand, back-conversion at 22 K occured within about 20 min (see also Section 5.1.2). Recent experiments by Arnab Choudhury, using time-resolved FTIR measurements to probe the rate constants for the back-conversion in $v = 0$, reveal a large activation energy of about $500\,cm^{-1}$, [143] which is consistent with the indefinitely long lifetime at 7 K.

Unfortunately, the absorption peak of the O-down isomer in the bare monolayer has not been detected with FTIR or LIF spectroscopy so far. Those spectra require several minutes to be acquired, which gives an upper limit to the time for back-conversion of the O-down isomer to the C-down isomer. In addition, the lifetime must be longer than the time between two laser pulses (100 ms). Therefore, the lifetime for back-conversion of the O-down isomer in the bare monolayer at 7 K can be estimated between approx. 0.1 and 100 s.

5.2 Discussion

5.2.1 Relevance to quantum-state resolved isomerization

The orientational isomerization of CO on NaCl(100), in which well-resolved vibrational states from both isomers have been detected, presents an interesting system for studying isomerization on a quantum level.

The most simple isomerization reactions, 1,2-hydrogen-shift reactions, have been studied in great detail using gas phase spectroscopy to investigate how the (vibrational) eigenstates associated with the isomerization potential are affected near or above the isomerization barrier. A relatively simple example is the symmetric double-well potential for isomerization of the $(HF)_2$ dimer, in which information on the isomerization is encoded in the tunneling splitting. [144] Another well-studied example of isomerization in an asymmetric potential is the $HCP \rightleftharpoons CPH$ reaction, although the CPH isomer actually corresponds to a saddle point and not a local minimum on the PES. [145, 146] Despite that, a clear influence due to changes in the PES near the saddle point could be identified, resulting in isomerization states that are located along the isomerization coordinate. [145, 146] In contrast to $HCP \rightleftharpoons CPH$, both isomers in the $HCN \rightleftharpoons CNH$ reaction correspond to actual minima on the PES. However, no evidence for mixing with CNH states has been found for the HCN states below and near the isomerization threshold. [147–149] Possibly one of the best studied isomerization reaction is the acetylene-vinylidene isomerization $(HCCH \rightleftharpoons H_2CC)$, where vinylidene corresponds to a stable minimum on the PES with a small barrier for isomerization to acetylene. This system has been probed both from the acetylene side using stimulated emission pumping [150, 151] and from the vinylidene

side using anion photoelectron spectroscopy [152]. In the latter case, strong evidence for mixing between the vinylidene states and the acetylene states was observed below the isomerization threshold when the in-plane rocking mode was excited, indicating quantum state-selective isomerization below the classical barrier. [152]

However, most of the above-mentioned gas phase spectroscopic studies detect stationary eigenstates of one isomer, which are potentially perturbed by states of the other isomer. To investigate quantum state-resolved isomerization dynamics, it would be desirable to have transitions between the quantum states of different isomers, which can for example be induced by intermolecular interactions in condensed phase systems. However, the same interactions typically lead to unresolved vibrational spectra of condensed phase systems. Furthermore, high-level quantum chemical methods, which are essential for interpreting the quantum nature of isomerization, e.g. to interpret the corresponding wavefunctions, [145] are normally restricted to the gas phase. Some exceptions to these restrictions are molecules isolated in rare gas matrices where well-resolved infrared spectra of different isomers can be observed. As an example, matrix isolation spectroscopy enabled the study of laser-induced isomerization of formic acid from the *trans* conformation to the *cis* conformation [153] and the reverse process mediated by tunneling [154–156]. Similarly, different isomers of matrix-isolated rare gas compounds (e.g. HXeCN and HXeNC) can be easily distinguished with infrared spectroscopy. [157]

The orientational isomerization of CO on NaCl(100) observed here presents another promising exception to the restrictions mentioned above. First, well-resolved vibrational spectra for both isomers are observed, which is unusual for a condensed phase system. Second, isomerization dynamics after infrared laser excitation seem to occur on experimentally accessible timescales. Thus, one may be able to track the reaction pathways between single quantum states of the two isomers. Third, CO/NaCl(100) is a relatively simple system, which should still be accessible to high-level quantum chemical methods. In particular, building a full PES based on separate CO-CO interactions (6 DOFs) and CO-NaCl interactions (6 DOFs for a frozen surface) should be possible, as these contributions involve the same number of DOFs as for the full acetylene-vinylidene PES. [158] Efforts by other groups to construct such a full-dimensional PES are discussed in the following section.

As a final point, it is not unlikely that similar metastable orientational isomers could be observed in other physisorption systems. For example, NO has an electric dipole moment function (EDMF) that is extremely similar to that of CO, including a reversal of the dipole moment when the N-O bond is stretched. [159, 160] Also electronic excitation can lead to a reversal of the dipole moment. As an example, the $a\,^3\Pi(v = 0)$ state of CO shows a dipole moment of about 1.4 D, [161] which also corresponds to a flipped

$C^{\delta+}O^{\delta-}$ polarity and is about twice as large as the dipole moment of the $X\ ^1\Sigma^+(v=30)$ state (see Fig. 2.7b).

5.2.2 Comparison with recent theoretical work

Stimulated by the orientational isomerization reported here, several theoretical studies [142, 162–164] have been published dealing with different aspects of the isomerization dynamics and the properties of the two isomers in the CO/NaCl(100) system. In principle, three possible scenarios exist that could explain how the isomerization occurs although the activation barrier remains large even for high vibrational states according to the electrostatic model (see Section 5.1.4): (1) The DOFs that are frozen in the electrostatic model, in particular the distance from the surface, could play an important role in lowering the barrier. (2) The isomerization dynamics cannot be fully captured by the vibrationally adiabatic model, which accurately describes the vibrational frequency shifts. In this case, weak anharmonic coupling between the C-O stretching vibration and the frustrated rotation of CO could transfer energy to the frustrated rotational mode in a relaxation or VEP event, which is used to overcome the activation barrier. This scenario was also proposed in Ref. [162]. (3) Tunneling effects at energies below the isomerization threshold could play a role, although this explanation seems less likely given the relatively high mass of CO.

Ref. [142] reports density functional theory (DFT) calculations based on the PBE functional with different dispersion corrections that can reproduce the C-down adsorption structure of CO on NaCl(100) with good accuracy. The DFT calculations predict stable O-down structures (θ = 120-145° for different functionals) with harmonic vibrational frequencies that are red-shifted with respect to the C-down structures and the unperturbed gas phase molecule by a few wavenumbers, in agreement with the experiment. In addition, the authors show that the relative stability of the O-down and C-down structures inverts in favor of O-down for high vibrational states if CO is positioned above Na$^+$, similar to what is predicted by the electrostatic model (see Section 5.1.4). It should, however, be noted that the DFT calculations are performed for a single CO molecule inside (1×1) and (2×2) unit cells with periodic boundary conditions. Therefore, all CO molecules flip simultaneously, which will not quantitatively represent the experiment.

Ref. [163] reports a PES for a cluster of 12 CO molecules adsorbed on a single, frozen surface layer of NaCl, which is composed of contributions from a CO-NaCl PES (diatom-diatom potential with the Na-Cl distance fixed at the NaCl bulk value) [163] and a recently published full-dimensional CO-CO PES [162]. Also this work, which is based on highly accurate wavefunction methods, predicts a stable O-down isomer with

a similar tilt angle of the C-O bond axis (51°) as derived from the electrostatic model (46°). The tilt angle is, however, lower than the experimentally determined value for the buried monolayer (~69°, see Appendix C). According to the calculations in Ref. [163], the O-down isomer becomes stabilized for large C-O bond distances, resembling the outer turning points of high vibrational states. Furthermore, the transition state for high vibrational states lies at large distances from the surface centered around $z \approx 5.5$ Å, which is significantly further away than the equilibrium bond distances for C-down ($z \approx 3.0$ Å) and O-down ($z \approx 2.8$ Å). The authors compare the isomerization further away from the surface with a roaming reaction, a unimolecular reaction channel in the gas phase based on near-dissociation events. [165, 166]

The authors of Ref. [163] also performed quasiclassical trajectory calculations for high vibrational states ($v = 22$) in which isomerization and desorption events are observed. However, it should be noted that these trajectories start at the equilibrium adsorption geometry of the C-down isomer in the vibrational ground state, which is significantly shifted from the equilibrium geometry in high vibrational states. Isomerization (and desorption) is observed because the energy of this starting geometry lies above the isomerization threshold. This "direct excitation" to $v = 22$ associated with additional potential energy is inconsistent with the experimental conditions, in which high vibrational states will be populated by sequential one-quanta energy transfer processes—potentially allowing for dissipation of the additional energy deposited in the low frequency rotational mode. The work does, however, show that considering other DOFs, in particular the z-distance, is an important factor to decrease the barrier.

Finally, DFT calculations based on the PBE-D2 functional in Ref. [164] confirm many of the findings in Refs. [142, 162, 163] but also consider the possibility of a different isomerization mechanism. The authors found that the vibrational states obtained for a 2D potential, depending only on the z-distance and the tilt angle, and a 3D potential, which is additionally a function of the C-O bond distance, exhibit several quasi-degenerate pairs of states. For these pairs, one of the states is located in the C-down well and the other state is located in the O-down well. If these quasi-degenerate states also exist for the full-dimensional PES and have appreciable overlap, it can potentially lead to isomerization below the classical barrier. So far, this mechanism is only hypothetical as no overlap was observed for two dimensions. It could, however, be relevant to the lifetimes for back-conversion of the O-down isomer to the C-down isomer in the vibrational ground state, where vibrationally non-adiabatic $CO(v) \rightarrow CO(v-1)$ transitions cannot occur.

The discussed theoretical studies clearly lead to an improved understanding of the orientational isomerization. However, all these studies predict similarly high barriers for isomerization in high vibrational states as the electrostatic model and are thus not able to

explain how isomerization from C-down to O-down can occur. So far, breakdown of the vibrationally adiabatic approximation seems to be the most likely explanation, leading to energy transfer from the CO stretching vibration to the frustrated rotational modes. However, also tunneling contributions cannot be excluded at the present stage.

Another alternative mechanism involving vibration-to-electronic (V-E) energy transfer from high vibrational states of the electronic ground state to the $a\,^3\Pi$ state is also conceivable, as it could potentially reduce the isomerization barrier due to the large magnitude of the dipole moment in the electronically excited state (1.4 D). [161] This hypothesis has not been considered in the theoretical calculations and also the experimental emission spectra presented in this chapter do not contain information on the excited electronic state. It could, however, be tested experimentally by either monitoring infrared fluorescence after direct excitation of the $a\,^3\Pi$ state or by observing UV phosphorescence from the $a\,^3\Pi$ state populated through VEP and subsequent V-E transfer.

In conclusion, further experiments and calculations are needed for a complete understanding of the orientational isomerization dynamics. Pump-probe experiments that directly track the isomerization dynamics from quantum states of the C-down isomer to states of the O-down isomer would be incredibly helpful to investigate the role of vibrationally non-adiabatic transitions or the $a\,^3\Pi$ state. Such experiments are, however, challenging due to the coupled vibrational dynamics when the high vibrational states are prepared via VEP. Furthermore, the repetition rate of the experiment would have to be adapted to allow for back-conversion of the O-down orientation before each laser excitation cycle. Therefore, molecular dynamics calculations based on the above-mentioned full-dimensional PESs are invaluable to interpret the experimental observations presented in this chapter.

Mid-infrared light harvesting to promote orientational CO isomerization

In Chapters 4 and 5, a thorough understanding of the VEP dynamics within the monolayer was obtained. In this chapter, the vibrational energy transport across isotopically layered CO monolayer-multilayer samples will be investigated. I will show that vibrational energy transport can be controlled by choosing the right isotopic substitution patterns. For a $^{13}C^{18}O$ monolayer sample with about 100 $^{12}C^{16}O$ overlayers on top, energy transport from the overlayer to the monolayer results in higher vibrational excitation than possible with direct excitation of the monolayer and can efficiently drive the orientational CO isomerization discussed in Chapter 5. This effect will be discussed in analogy to solar light harvesting systems. Furthermore, the mechanism for vibrational energy transport across the interface will be discussed. The results presented in this chapter have been first published in Ref. [130] by Springer Nature.

6.1 Results

6.1.1 Preparation and characterization of isotopically layered samples

To investigate the effect of isotopic substitution on vibrational energy transport, different monolayer-multilayer samples were prepared using isotopically pure $^{12}C^{16}O$ and $^{13}C^{18}O$ (see Section 3.1.5 for isotopic purities of the gases). All four possible combinations were prepared and are listed in Table 6.1. Also the notation that will be used throughout the whole chapter is shown in Table 6.1. For example, a $^{13}C^{18}O$ monolayer covered by $^{12}C^{16}O$ overlayers will be labeled as "m38o26", where "m38" indicates the ^{13}C and ^{18}O

Table 6.1: Overview of the four isotopically layered samples.

Isotopologue (monolayer)	Isotopologue (multilayer)	Abbreviation
$^{12}C^{16}O$	$^{13}C^{18}O$	m26o38
$^{13}C^{18}O$	$^{12}C^{16}O$	m38o26
$^{12}C^{16}O$	$^{12}C^{16}O$	m26o26
$^{13}C^{18}O$	$^{13}C^{18}O$	m38o38

isotopes of CO in the monolayer and "o26" indicates the ^{12}C and ^{16}O isotopes of CO in the overlayer.

The samples were prepared using molecular beam dosing according to Section 3.2.2. The monolayer was prepared at 25 K and in each case about 100 overlayers were deposited epitaxially on top of the monolayer at 22 K. Only for dosing $^{13}C^{18}O$ overlayers, leak valve dosing was used to save expensive $^{13}C^{18}O$ gas. Therefore, a $^{13}C^{18}O$ monolayer and 100 $^{13}C^{18}O$ overlayers are adsorbed on the crystal back in all o38 samples, whereas molecular beam dosing only covers the front of the crystal. These additional $^{13}C^{18}O$ layers on the back of the crystal are not relevant to the laser-induced fluorescence (LIF) experiments but can be observed in the Fourier-transform infrared (FTIR) spectra, which are used to characterize the samples.

Figure 6.1 shows the FTIR spectra of the m38o26 and m26o38 samples at 7 K immediately after preparation. The spectra of the m26o26 and m38o38 samples are not explicitly shown, as they are merely combinations of the m38o26 and m26o38 spectra. The absorbing species is indicated by bold, underlined fonts: e.g., **m38**o26 means excitation of the $^{13}C^{18}O$ monolayer within the m38o26 sample; m38**o26** means excitation of the $^{12}C^{16}O$ overlayer. Note that monolayer excitation always refers to excitation of the C-down species, unless otherwise stated. The O-down species cannot be observed in the FTIR spectra of the freshly prepared samples.

The absorption spectrum of the m38o26 sample (Fig. 6.1a) only shows the buried $^{13}C^{18}O$ monolayer (**m38**o26, peaks at 2048.2 and 2053.6 cm^{-1}) and $^{12}C^{16}O$ overlayer absorption peaks (m38**o26**, peaks at 2138.6 and 2143.1 cm^{-1}), which are consistent with the literature [44] and the spectra presented in Chapter 5. No absorption due to isotopic impurities is observed. However, additional absorption peaks between 1990 and 2040 cm^{-1} are seen, which are attributed to $Fe(CO)_5$ impurities in the $^{12}C^{16}O$ overlayer (see Appendix E). Since they are only present in the overlayer and at very low concentrations (~0.01 %), they are not expected to be relevant to the LIF experiments.
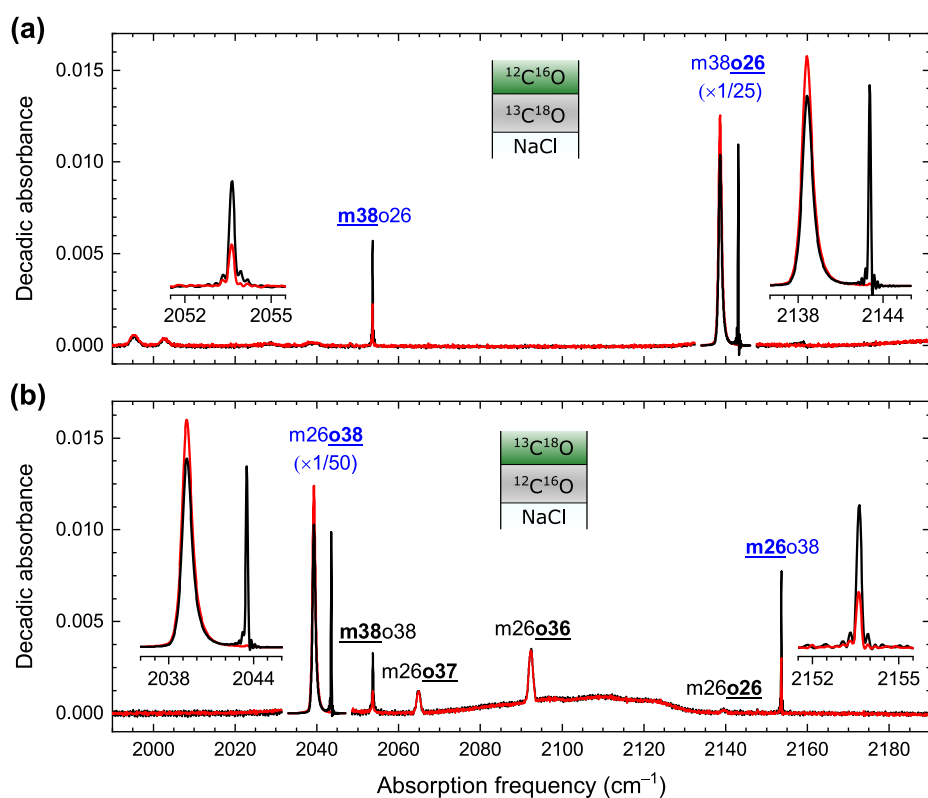
Figure 6.1: (a) FTIR spectrum of the m38o26 sample measured at 7 K. The insets on the left and right show the **m38**o26 and m38**o26** absorption peaks, respectively, which are marked in blue. (b) FTIR spectrum of the m26o28 sample measured at 7 K. The insets on the left and right show the m26**o38** and **m26**o38 absorption peaks, respectively, which are marked in blue. In addition, absorption peaks of isotopic impurities in the overlayer are indicated. In both panels, the main overlayer absorption features are scaled by the factors given in each figure. All FTIR spectra are shown for a resolution of $0.2\,\mathrm{cm}^{-1}$ and a 4-point apodization function to highlight the sharp monolayer absorption features. From Ref. [130]. Adapted with permission from Springer Nature.

In the absorption spectrum of the m26o38 sample (Fig. 6.1b), absorption peaks of the buried $^{12}C^{16}O$ monolayer (**m26**o38, peaks at 2147.8 and 2153.6 cm^{-1}) and the $^{13}C^{18}O$ overlayer (m26**o38**, peaks at 2039.3 and 2043.5 cm^{-1}) are observed, which are both shifted by almost exactly +100 cm^{-1} and −100 cm^{-1} with respect to the m38o26 sample, respectively. Note that the m26**o38** absorption is twice as strong compared to the overlayer peak in Fig. 6.1b due to adsorption of $^{13}C^{18}O$ on the crystal back, as mentioned above. Between the two absorption features, additional peaks from isotopic impurities in the $^{13}C^{18}O$ overlayer (m26**o37**, m26**o36** and m26**o26**) and from the crystal back (**m38**o38) are observed. The isotopic impurities have higher vibrational frequencies than the $^{13}C^{18}O$ overlayer and are therefore not expected to participate in any vibrational energy transfer process occuring in the overlayer. The broad background ranging from 2060 to 2130 cm^{-1} is assigned to a CO overlayer-CO crystal phonon combination band. [43]

Note that the absorption of the overlayer is significantly higher than that of the monolayer, despite the broader linewidth. The number of overlayers, N_l, can be estimated from the integrated absorbance, $\tilde{A}$, of the overlayer absorption line using a slightly modified form of Eq. 2.50: [43]

$$N_l = \frac{\ln(10)\cos(\theta_1)}{\bar{\sigma}_{\text{eff}} S_l N} \tilde{A}. \tag{6.1}$$

Here, $S_l = 6.3 \times 10^{14}$ molecules cm^{-2} is the surface density of a single layer. [45] N is the number of overlayer covered surfaces ($N = 1$ for $^{12}C^{16}O$; $N = 2$ for $^{13}C^{18}O$) and $\theta_1 = 34°$ is the incidence angle. The effective cross section of the overlayer is given by $\sigma_{\text{eff}} = 9.6 \times 10^{-18}$ cm molecule^{-1} for $^{12}C^{16}O$. [167] An isotope correction for $^{13}C^{18}O$ gives $\sigma_{\text{eff}} = 8.8 \times 10^{-18}$ cm molecule^{-1}. [83] By controlling the number of molecular beam pulses ($^{12}C^{16}O$ overlayers) or the dosing time with the leak valve ($^{13}C^{18}O$ overlayers), a comparable sample thickness of about 105-110 overlayers was achieved for all samples.

6.1.2 LIF spectroscopy of the isotopically layered samples

In the LIF experiments, either the monolayer or the overlayer is selectively excited via the corresponding absorption peaks, which are marked in blue in Fig. 6.1. Observation of the emission from different species in the monolayer and overlayer then gives information on the vibrational energy transport dynamics. The emission spectra of the mixed isotopologue samples (m26o38 and m38o26) will be presented first. After that, also the emission spectra of the m26o26 and m38o38 samples will be briefly presented. In the last part of this section, the excitation spectra of all four samples will be compared.

Emission spectra: m26o38 and m38o26

Figure 6.2 shows the overtone emission spectra of the m26o38 and m38o26 samples after selective excitation of the monolayer or the overlayer. To excite the monolayer (**m38**o26 or **m26**o38), the high intensity absorption lines at 2053.6 and 2153.6 cm^{-1} are used, respectively. To excite the overlayer (m38**o26** or m26**o38**), the low frequency absorption lines at 2138.6 and 2039.3 cm^{-1} are used, respectively.[1] In addition, comparable pulse energies were used for the different excitation peaks. Emission spectra after monolayer and overlayer excitation were measured with different bias currents of 5.0 and 3.4 μA, respectively; however, the spectra shown in Fig. 6.2 have been corrected by the corresponding relative detection efficiency (RDE) curves (see Section 3.2.8), in addition to a background correction and the conversion from wavelength to wavenumber space using the Jacobian $|d\lambda/d\tilde{\nu}| = 1/\tilde{\nu}^2$. Therefore, all spectra share the same intensity scale and can be compared directly.

Based on the known spectroscopic constants of the different CO isotopologues in the buried monolayer and the overlayer (see Table 5.1) and comparison between the different emission spectra, the observed emission lines in Fig. 6.2 can be easily assigned.

Figures 6.2a and 6.2b show the emission spectra of the m26o38 sample. m26**o38** excitation (Fig. 6.2b) results in a single vibrational progression (green comb), which is assigned to emission from the ^{13}C^{18}O overlayer. **m26**o38 excitation (Fig. 6.2a) shows an intense vibrational progression with the same emission frequencies as in Fig. 6.2b, also indicated by a green comb. This indicates efficient energy transfer from the ^{12}C^{16}O monolayer to the ^{13}C^{18}O overlayer. Furthermore, no emission from the monolayer is observed.[2] Additional emission lines, which are marked by asterisks, might be due to emission from a CO_2 impurity in the overlayer, which has a concentration of ~0.01 % (see Appendix E for details).

Figures 6.2c to 6.2e show the emission spectra of the m38o26 sample, where the isotopic labeling is reversed. For **m38**o26 excitation (Fig. 6.2c), two different vibrational progressions are observed, which are assigned to the emission of the C-down isomer (blue comb) and the O-down isomer (red comb) in the buried ^{13}C^{18}O monolayer. No overlayer emission lines are observed in this case. This indicates that energy transfer from the monolayer to the overlayer does not occur for **m38**o26; in strong contrast to **m26**o38 excitation, where most of the energy is transferred to the overlayer. Also

---

[1] The actual excitation frequencies observed in the excitation spectra are slightly different from the FTIR frequencies, which will be discussed later (see the excitation spectra in Fig. 6.4).

[2] The emission peak positions of the buried ^{12}C^{16}O monolayer can be extracted from Fig. 6.3c for comparison.
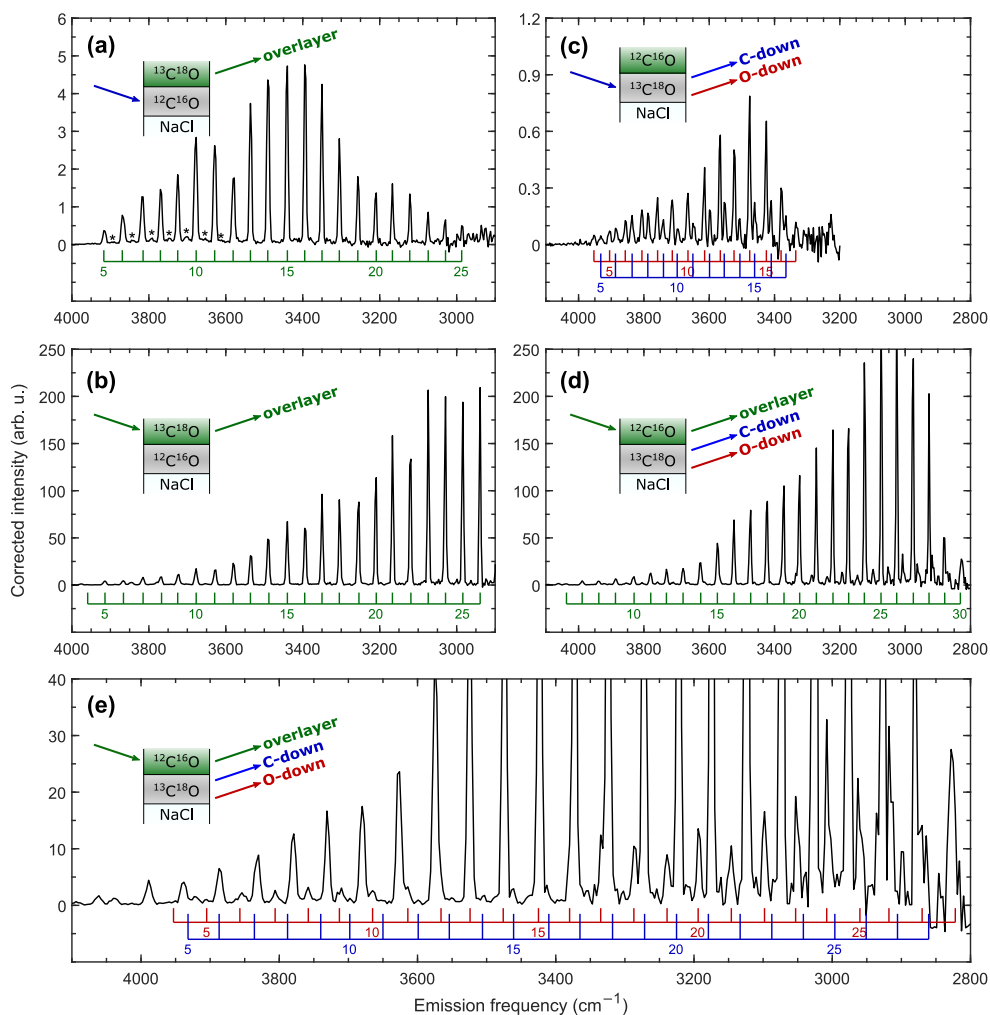
Figure 6.2: Overtone emission spectra of the m26o38 and m38o26 samples after selective laser excitation of either the monolayer or multilayer absorption lines. Colored combs indicate vibrational progressions of different CO species and the corresponding vibrational assignment (green: CO overlayer, blue: CO monolayer (C-down), red: CO monolayer (O-down)). (a) Excitation of **m26**o38 with 120 μJ/pulse. Additional emission lines, which cannot be attributed to CO emission, are indicated by asterisks. (b) Excitation of m26**o38** with 95 μJ/pulse. (c) Excitation of **m38**o26 with 145 μJ/pulse. (d) and (e) Excitation of m38**o26** with 115 μJ/pulse. Both panels show the same emission spectrum on different scales. Panel (d) shows the assignment of the overlayer emission lines, while panel (e) shows the assignment of the monolayer emission lines. All spectra are integrated over the initial 500 μs after laser excitation. In addition, the excited and emitting CO species are indicated by arrows in the schematic representations of the isotopically layered samples in each panel. From Ref. [130]. Adapted with permission from Springer Nature.

the emission spectrum after m38**o26** excitation (Figs. 6.2d and 6.2e) differs from that after m26**o38** excitation. Besides emission from the $^{12}C^{16}O$ overlayer (green comb), additional emission lines are clearly observed (blue and red combs). Comparison with Fig. 6.2c shows that the latter emission lines are consistent with emission from the C-down and O-down isomers in the monolayer.[3] Also note that most of the emission intensity originates from high vibrational states $v > 17$ for m38**o26** excitation, which are not even populated for **m38**o26 excitation. In addition, the overall emission intensities are much higher for m38**o26** excitation compared to **m38**o26 excitation and most emission occurs from the O-down isomer. Therefore, the results indicate extremely efficient energy transfer from the $^{12}C^{16}O$ overlayer to the $^{13}C^{18}O$ monolayer for m38**o26** excitation. For this reason, the m38**o26** emission spectrum will be further analyzed in Section 6.1.3.

Emission spectra: m26o26 and m38o38

Emission spectra of the m38o38 and m26o26 samples, in which both the monolayer and overlayer consist of the same CO isotopologue, are shown in Fig. 6.3 for completeness. After monolayer excitation (Figs. 6.3a and 6.3c), both spectra show contributions from all three species: the C-down isomer (blue comb), the O-down isomer (red comb) and the overlayer (green comb). In both spectra, most emission signal is observed from the O-down isomer, indicating that energy transfer to the overlayer is much less efficient compared to **m26**o38 excitation. The **m38**o38 and **m26**o26 spectra rather resemble the **m38**o26 emission spectrum, where energy transfer to the overlayer is inefficient. Emission spectra for overlayer excitation (Figs. 6.3b and 6.3d) only show emission from the corresponding overlayer species and no monolayer emission peaks are observed, indicating that potential population in the monolayer due to energy transfer from the overlayer to the monolayer is below the detection limit.

Excitation spectra

The LIF excitation spectra for the monolayer absorption lines of the four isotopically layered samples are shown in Fig. 6.4. In addition, the FTIR frequencies of the high- and low-frequency absorption lines of the C-down species are indicated. Further note that only the high frequency absorption line can be detected with LIF. Fig. 6.4 shows

---

[3] Up to $v \approx 17$, the agreement can be seen by direct comparison of the peak positions in Figs. 6.2c and 6.2e. Since states above $v = 17$ are not observed in Fig. 6.2c, the positions of the emission peaks are estimated based on the spectroscopic constants of the C-down and O-down isomers in the bare $^{13}C^{18}O$ monolayer. For this reason, also emission peak positions for $v > 17$ can be shown, which are not observed due to overlap with overlayer emission lines.
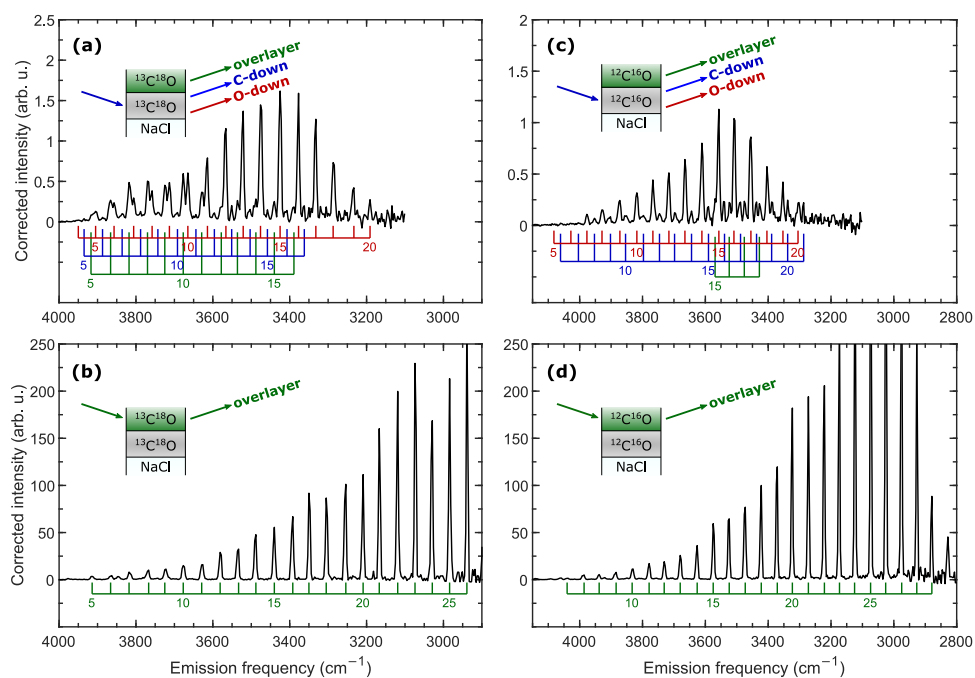
Figure 6.3: Overtone emission spectra of the m38o38 and m26o26 samples after selective excitation of either the monolayer and multilayer, which are integrated over the initial 500 µs after laser excitation. Colored combs indicate vibrational progressions of different CO species (green: CO overlayer, blue: CO monolayer (C-down), red: CO monolayer (O-down)) and the assignment to vibrational quantum numbers. In each panel, the excited and emitting CO species are indicated by the schematic representations of the isotopically layered samples. (a) Excitation of **m38**o38 with 120 µJ/pulse. (b) Excitation of m38**o38** with 100 µJ/pulse. (c) Excitation of **m26**o26 with 120 µJ/pulse. (d) Excitation of m26**o26** with 120 µJ/pulse. From Ref. [130]. Adapted with permission from Springer Nature.

that all LIF excitation peaks are red-shifted with respect to the corresponding FTIR frequencies. The magnitudes of the red-shifts are: $0.6\,\mathrm{cm}^{-1}$ (**m26**o38), $0.8\,\mathrm{cm}^{-1}$ (**m38**o38), $1.1\,\mathrm{cm}^{-1}$ (**m38**o26), and $1.6\,\mathrm{cm}^{-1}$ (**m26**o26). For **m38**o26 excitation, the red-shift increases significantly to $2.3\,\mathrm{cm}^{-1}$ when the sample is excited via m38**o26** excitation prior to measuring the **m38**o26 excitation spectrum. This additional red-shift is probably related to the efficient energy transfer from the overlayer to the monolayer in the m38o26 sample, where most of the emission originates from the O-down isomer in the monolayer. The smallest frequency shift, on the other hand, is observed for **m26**o38 excitation, where no monolayer emission is observed. Therefore, the magnitude of the red-shift seems to be correlated with the fraction of monolayer molecules converted to the O-down orientation.
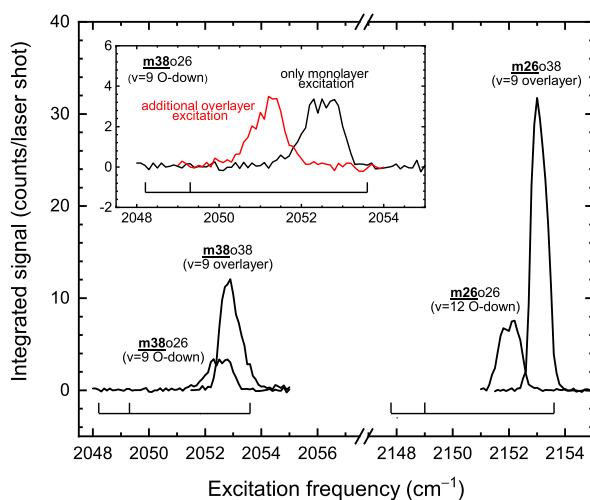

Figure 6.4: LIF excitation spectra for monolayer excitation of the m38o26, m26o38, m38o38 and m26o26 samples. All excitation spectra were obtained by monitoring high intensity emission lines. The species and vibrational state of those emission lines is indicated in brackets. In addition, two combs represent the absorption frequencies of the buried $^{12}C^{16}O$ and $^{13}C^{18}O$ monolayers, taken from the FTIR spectra in Fig. 6.1. The outer lines of the comb correspond to the FTIR absorption lines. The center line of the comb gives an estimate of the frequency without dynamic exciton splitting, similar to Fig. 5.4. The inset shows how the **m38**o26 excitation spectrum changes when overlayer excitation via the m38**o26** line was used before measuring the **m38**o26 excitation spectrum (red curve vs. black curve). All spectra are integrated over the initial $500\,\mathrm{\mu s}$ after laser excitation. From Ref. [130]. Reproduced with permission from Springer Nature.

6.1.3 Efficient vibrational energy transport in the m38o26 system

The results in Section 6.1.2 demonstrated that the small difference of $100\,\mathrm{cm}^{-1}$ between the fundamental vibrational frequencies of $^{13}\mathrm{C}^{18}\mathrm{O}$ and $^{12}\mathrm{C}^{16}\mathrm{O}$ is sufficient to achieve vibrational energy transport away from the CO monolayer and toward the monolayer, depending on the isotopic substitution of the different layers. The m38o26 system, consisting of a high-frequency overlayer and a low-frequency monolayer, is of particular interest because more photons can be absorbed in the 100 overlayers than in the monolayer. Furthermore, the results in Section 6.1.2 indicate enhanced vibrational excitation in the monolayer after m38**o26** excitation compared to **m38**o26 excitation. Therefore, the efficiency of vibrational energy transport from the $^{12}\mathrm{C}^{16}\mathrm{O}$ overlayer to the $^{13}\mathrm{C}^{18}\mathrm{O}$ monolayer is further quantified in this section.

Since the emission spectra in Fig. 6.2 are already corrected for the RDE curves, the integrated emission peak intensities[4] can be used to estimate relative vibrational populations, $P(v)$, if the corresponding fluorescence rate constants are known (see Section 2.3.2). For calculating the relevant fluorescence rate constants, the spectroscopic constants (ω_e and $\omega_e x_e$) of $^{12}\mathrm{C}^{16}\mathrm{O}$ overlayers, and of the C-down and O-down isomers in the bare $^{13}\mathrm{C}^{18}\mathrm{O}$ monolayer in Table 5.1 are used. Furthermore, the same dipole derivative as for gas phase CO ($\mu' = 3.2\,\mathrm{D\,\mathring{A}}^{-1}$) is assumed for all species. [125] The calculated overtone fluorescence rate constants are shown in Fig. 6.5. Note that the overtone fluorescence rate constants of the buried monolayer species are approximated by those in the bare monolayer because the spectroscopic constants for the bare monolayer are known to better accuracy. To support the validity of this approximation, also the fluorescence rate constants of the $^{13}\mathrm{C}^{18}\mathrm{O}$ overlayer are shown and it is clearly seen that even the difference between the rate constants of the three different $^{13}\mathrm{C}^{18}\mathrm{O}$ species is negligible.

Errors of the relative vibrational populations are estimated according to the following procedure, assuming that the error is mainly determined by photon shot noise (see also Section 2.3). In this case, the absolute errors in the uncorrected intensity and RDE measurements can be estimated as $\sqrt{N}$, where $N = S + BG$ is the total number of detected photons (counts) within a given time interval, including signal (S) and background counts (BG). Based on these two errors, the error of the corrected intensity and thus of the vibrational populations can be calculated with Gaussian error propagation. In the

---

[4] Since the emission spectra are originally measured in the wavelength domain, where the emission peak linewidths are limited by the constant monochromator resolution, the peak intensities in the wavelength domain are proportional to the peak integrals. Therefore, relative peak integrals are determined from the peak intensities in the wavelength domain, which simplifies the analysis for emission lines that partially overlap.
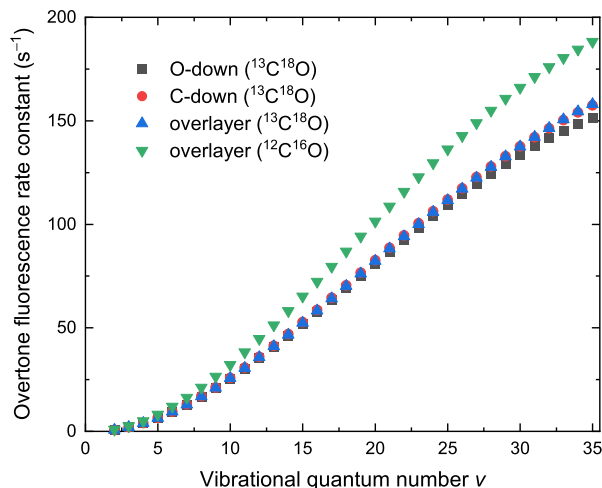
Figure 6.5: Calculated overtone fluorescence rate constants for $^{12}C^{16}O$ and $^{13}C^{18}O$ in the multilayer and the C-down species and O-down species in the bare $^{13}C^{18}O$ monolayer. Note that the bare monolayer rate constants also describe the fluorescence rate constants of the buried monolayer with sufficient accuracy. From Ref. [130]. Reproduced with permission from Springer Nature.

following, Gaussian error propagation is also used to calculate the errors of all other quantities that are related to the relative vibrational populations, e.g. the average number of vibrational quanta for each CO species.

The resulting (time-integrated) vibrational state distributions of the C-down and O-down species after **m38**o26 and m38**o26** excitation, obtained from the emission spectra in Figs. 6.2c to 6.2e after correction by the fluorescence rate constants in Fig. 6.5, are compared in Fig. 6.6. Clearly, m38**o26** excitation (blue bars) results in much larger vibrational populations than **m38**o26 excitation (orange bars). Note that only emission lines in the m38**o26** spectrum that do not overlap with the intense overlayer emission lines are analyzed in Fig. 6.6. As a result, populations for most C-down states and some O-down emission lines between $v = 12$ and 16 cannot be extracted. Therefore, the overall vibrational population after m38**o26** excitation is expected to be even higher than shown in Fig. 6.6. For **m38**o26 excitation (red bars), the shown vibrational distributions are complete and represent all emission lines that were observed.

To further quantify the amplification effect after overlayer excitation, the average
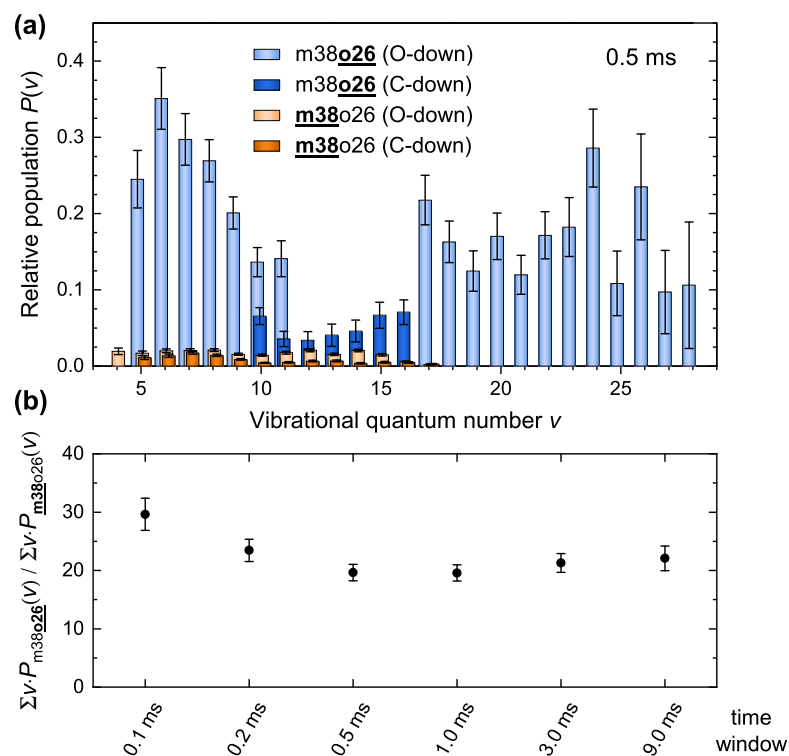
Figure 6.6: (a) Relative vibrational state populations, $P(v)$, derived from the integrated emission intensities of the O-down (light colors) and C-down (dark colors) emission peaks in Fig. 6.2c (for **m38**o26 excitation, orange) and in Figs. 6.2d to 6.2e (m38**o26**, blue). Because the emission spectra in Fig. 6.2 are integrated over a 0.5 ms time window, the obtained relative populations are also averaged over the initial 0.5 ms after laser excitation. (b) Ratio of the vibrational quanta in the monolayer (C-down + O-down) after m38**o26** and **m38**o26 excitation for different integration time windows. From Ref. [130]. Adapted with permission from Springer Nature.

number of vibrational quanta for each species will be considered because vibrational quanta are conserved during vibration-to-vibration (V-V) energy transfer, as long as vibrational relaxation can be neglected. The sum of the average vibrational quanta, $\sum_v vP(v)$, in the monolayer are compared for both excitation schemes in Fig. 6.6b (blue vs. orange distribution). In the initial 0.1 ms time window, the number of vibrational quanta in the monolayer is about 30 times larger for m38**o26** excitation compared to **m38**o26 excitation. This result implies that initially at least 30 times more vibrational quanta are deposited in the monolayer after m38**o26** excitation than possible with direct excitation of the monolayer. Increasing the integration time window to 0.5 ms and beyond 0.5 ms, gives a reduced ratio of 20. The decrease within the first 0.5 ms is interpreted as the effect of fast vibrational relaxation of high vibrational states above $v \approx 20$ (compare with Fig. 4.10), which are only populated for m38**o26** excitation.

Another measure of the amplification effect is given by the transfer efficiency, which is defined by the average number of vibrational quanta observed in the monolayer compared to the number of vibrational quanta observed in the overlayer for a given time window:

$$\text{Transfer efficiency} = \frac{\sum_v vP_{\text{C-down}}(v) + \sum_v vP_{\text{O-down}}(v)}{\sum_v vP_{\text{C-down}}(v) + \sum_v vP_{\text{O-down}}(v) + \sum_v vP_{\text{overlayer}}(v)} \quad (6.2)$$

Figure 6.7a shows the relative vibrational population distributions of the overlayer (green) and of the O-down and C-down species in the monolayer (blue). The population distributions were extracted from the m38**o26** emission spectrum in Figs. 6.2d to 6.2e and are thus averaged over the initial 0.5 ms after excitation. The corresponding transfer efficiency is shown in Fig. 6.7b different time windows after laser excitation. The resulting value of about 12 % is independent of the integration time window within the experimental uncertainty.[5]

Because about 30 times higher vibrational excitation is achieved with m38**o26** excitation, it should efficiently promote the isomerization to the O-down isomer and one might expect an increased O-down fraction compared to **m38**o26 excitation. Therefore, Fig. 6.8a shows a **m38**o26 emission spectrum measured after additional m38**o26** excitation for about 10 min (6000 laser shots). To obtain an estimate of the O-down fraction, the corresponding vibrational population distributions of the O-down and C-down species, which are again obtained after correction of the integrated emission peak intensities by the fluorescence rate constants in Fig. 6.5, are shown in Fig. 6.8b. Based on these

---

[5] Keep in mind that not all monolayer emission lines can be analyzed due to overlap with overlayer emission lines. Also note that overlayer states above $v = 30$ cannot be detected due to the applied optical filters (see Fig. 3.14).
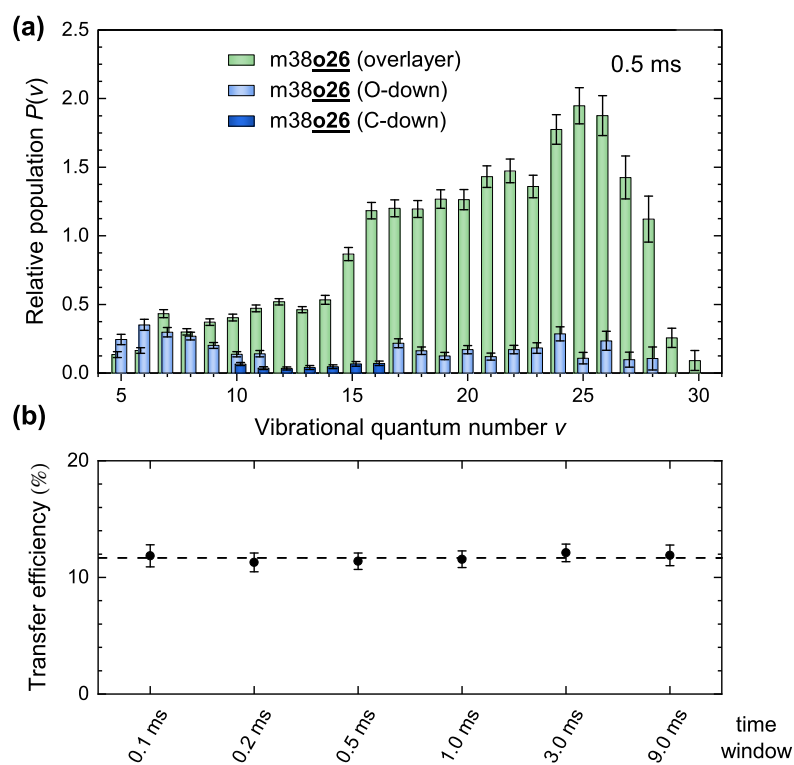
Figure 6.7: (a) Relative vibrational state populations, $P(v)$, derived from the integrated emission intensities of the multilayer (green), O-down (light blue) and C-down (dark blue) emission peaks in Figs. 6.2d to 6.2e (m38**o26**). The O-down and C-down populations are identical to those in Fig. 6.6. The relative populations are averaged over the initial 0.5 ms after laser excitation. (b) Transfer efficiency from the overlayer to the monolayer (see text for definition) for different integration time windows. From Ref. [130]. Adapted with permission from Springer Nature.

population distributions, it is inferred that a fraction of (76 ± 2) % emits from the O-down orientation. This fraction is slightly larger than the fraction of (68 ± 2) % obtained from the emission spectrum after **m38**o26 excitation only (see Figs. 6.2c and 6.6a).
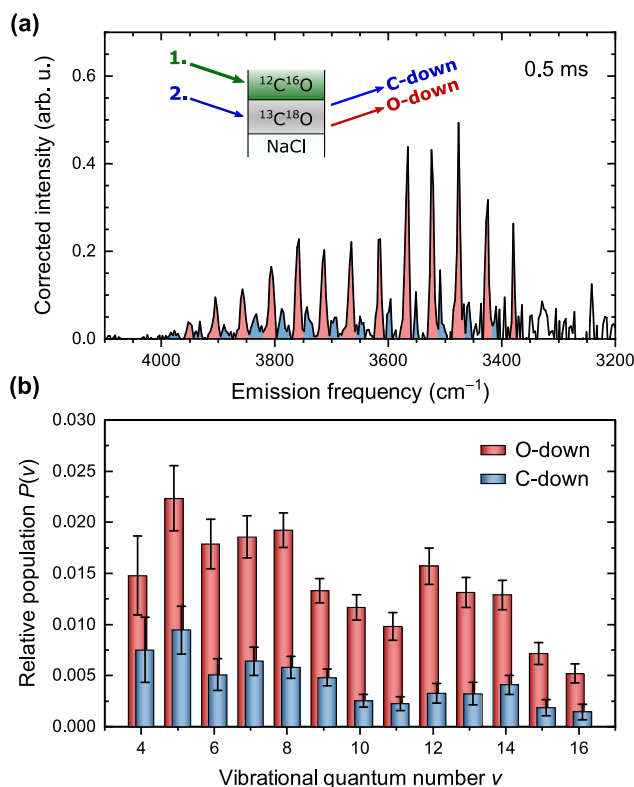

Figure 6.8: (a) **m38**o26 emission spectrum measured with 145 μJ/pulse after additional excitation of the overlayer (m38**o26**) for about 10 min. C-down and O-down emission lines are marked in blue and red, respectively. (b) Relative vibrational population distributions derived from the emission peak integrals in panel (a). From Ref. [130]. Adapted with permission from Springer Nature.

Both the increased fraction of emitting O-down molecules (Fig. 6.8) and the additional red-shift (Fig. 6.4) support an increased fraction of flipped molecules when the overlayer is excited. However, one should keep in mind that the fraction of emitting O-down molecules does not necessarily agree with the actual fraction of O-down molecules. Without energy transfer from the excited C-down species to the O-down species, no emission from the O-down species would be observed. This is demonstrated in Fig. 6.9 by

comparing the emission spectrum in Fig. 6.8a, measured after excitation of the C-down isomer at 2051.2 cm^{-1}, with an emission spectrum of the same sample, measured after excitation of the O-down isomer at 2036.2 cm^{-1}. If the emitting population corresponded to the actual population, the spectra would be expected to be identical. However, the comparison shows that almost no C-down emission is observed after O-down excitation while the O-down emission is more or less unchanged. Therefore, both the actual O-down fraction and the efficiency of energy transfer from C-down to O-down determine what fraction is observed in the emission. The estimate of 76 %, obtained after additional overlayer excitation, should therefore only be interpreted relative to the 68 % estimate, obtained without additional overlayer excitation.
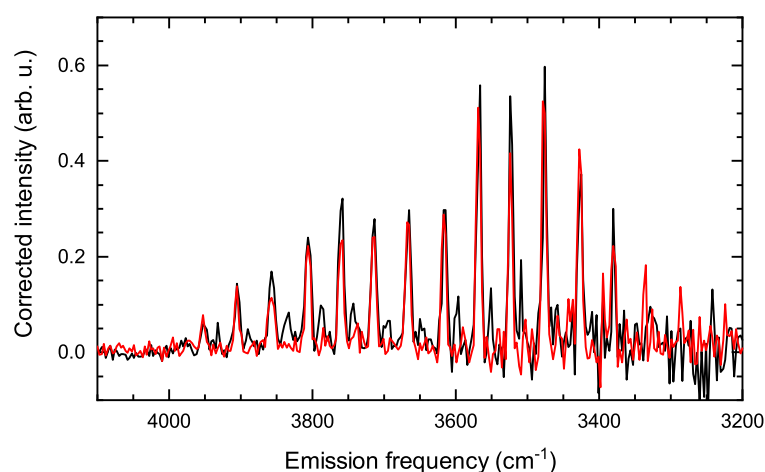

Figure 6.9: Comparison of the **m38**o26 emission spectrum for C-down versus O-down excitation in the monolayer. The black curve is the same spectrum as in Fig. 6.8a, obtained with excitation of the C-down species at 2051.2 cm^{-1} after m38**o26** had been used to produce a large fraction of the metastable O-down isomer. The red curve shows a spectrum of the same sample but the O-down species is directly excited at 2036.2 cm^{-1}.

6.2 Discussion

6.2.1 Analogy to solar light harvesting systems

The results presented in Section 6.1.3 show enhanced vibrational excitation in the $^{13}C^{18}O$ monolayer when infrared light is absorbed in the 100 times thicker $^{12}C^{16}O$

overlayer, which leads to efficient orientational isomerization of CO in the monolayer. This observation reminds of many characteristics of solar light harvesting systems: (1) enhanced absorption of visible light in spatially organized chromophores; (2) controlled transport of the resulting electronic energy; and (3) concentration of the electronic energy at a reaction center. [168, 169] In solar light harvesting systems, controlled electronic energy transport is mainly achieved by Förster resonance energy transfer (FRET) between the chromophores.[6] [170, 171] In the m38**o26** system, on the other hand, controlled vibrational energy transport is based on V-V energy transfer.

The efficiency of the light harvesting effect in the m38o26 system is characterized by the amplification factor of 30 and the transfer efficiency of 12 %, which were estimated in Section 6.1.3. The estimate of the transfer efficiency suggests that 12 of the 100 overlayers transfer their vibrational energy to the monolayer on average. The apparent discrepancy between energy transfer from 12 layers and the 30 times higher excitation achieved in the monolayer can be explained by a photobleaching effect. Since formation of the O-down isomer effectively reduces the fraction of the absorbing C-down species in the monolayer, less photons are absorbed for **m38**o26 excitation, depending on the concentration of the remaining C-down molecules. In addition, the **m38**o26 absorption line shifts with increasing O-down fraction (see Fig. 6.4). Bleaching does, however, not occur for excitation of the m38**o26** absorption line, as the overlayer is not involved in the isomerization and simply serves as a vibrational energy donor.

Most importantly, energy transfer from CO overlayers as donors is not limited to other CO molecules as acceptors. As discussed in Section 6.2.2, the efficient energy transfer can be rationalized based on V-V energy transfer between the overlayer and the monolayer. Thus, the transfer rate mainly depends on the transition dipole moments of acceptor and donor, and on their frequency mismatch, which has to be compensated by phonon spectrum (see also Section 2.2.2). Therefore, any infrared-active vibration of other (polyatomic) molecules could potentially serve as an acceptor.

To obtain efficient energy transport, V-V energy transfer from the CO overlayer to the acceptor molecule must be able to compete with vibrational energy pooling (VEP) in the overlayer, which is discussed in Section 6.2.2 in more detail. Therefore, acceptor vibrations with large transition dipole moments are expected to show more favorable energy transfer. In addition, the fundamental vibrational frequency of the acceptor must be red-shifted from the CO fundamental frequency; however, it should not exceed the highest relevant phonon frequencies to ensure energy transfer via a single-phonon

---

[6] In addition, delocalized, electronic exciton states play a role and also quantum coherence is discussed in the literature. [168]

process. Considering the magnitude of typical phonon frequencies and the high efficiency achieved for transfer from $^{12}C^{16}O$ to $^{13}C^{18}O$, a red-shift on the order of $100\,cm^{-1}$ appears to be a good choice. Promising donor-acceptor pairs that fulfill those requirements are: $^{13}C^{18}O$ overlayer ($2040\,cm^{-1}$)-NO monolayer ($1876\,cm^{-1}$ [131]) and $^{13}C^{18}O$ overlayer ($2140\,cm^{-1}$)-OCS monolayer ($2062\,cm^{-1}$ [172]).[7] By using other donor molecules than CO, the range of possible acceptor frequencies could probably be increased even further.

This mid-infrared light harvesting effect could provide an efficient method to deposit large amounts of vibrational energy in more reactive acceptor molecules. Recall that the energy of about 12 layers is efficiently transferred to the $^{13}C^{18}O$ monolayer for m38**o26** excitation. Considering that a fraction of 50 % can be excited in each layer, each molecule in the monolayer receives on average 6 vibrational quanta, which amounts to roughly 1.5 eV/molecule. This provides a large amount of energy for small polyatomic molecules, even when the energy is statistically distributed among all vibrational modes due to intramolecular vibrational energy redistribution (IVR). [49] As a result of IVR, the greatest challenge for efficient excitation of polyatomic molecule will probably be vibrational relaxation of the low frequency modes, which are expected to couple more efficiently to the crystal phonons and thus act as an energy loss channel.

6.2.2 Controlled vibrational energy transport across an interface

The emission spectra of the isotopically layered samples in Section 6.1.2 show very clear examples of selective vibrational energy transport from CO species with higher frequencies to CO species with lower frequencies. The effect is particularly pronounced in the m38o26 and m26o38 samples, in which the vibrational frequencies of the $^{12}C^{16}O$ and $^{13}C^{18}O$ molecules in the two layers differ by $\sim100\,cm^{-1}$. In the m26o38 system, all the vibrational energy deposited in the monolayer can flow into the overlayer, but energy transfer from the overlayer to the monolayer is not observed. In the m38o26 system, energy transfer from the monolayer to the overlayer is blocked, while about 12 % of the energy deposited in the 100 overlayers is effectively transferred to the monolayer. Similarly, energy transfer from the C-down species to the O-down species can occur in the monolayer, while reverse energy transfer is inefficient, despite the small vibrational frequency difference of only $\sim15\,cm^{-1}$.

Preferential energy transfer from light to heavy CO isotopologues has been observed in many experiments, including VEP in gas phase CO, [76, 77, 86] matrix-isolated CO, [80, 81] and CO crystals. [27, 83]. However, in those experiments, the heavier CO isotopologues were present as isotopic impurities. The present work, on the other hand,

---

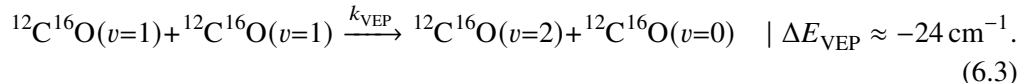[7] The cited NO and OCS frequencies are gas phase values.

describes controlled vibrational energy transport across an interface due to selective isotopic substitution.

Unfortunately, the time resolution of ~1 μs was not sufficient to resolve the initial phase of energy transfer between the isotopically labeled CO layers experimentally. Also a full microscopic treatment of the vibrational energy transport based on kinetic Monte Carlo (KMC) simulations, as in Chapter 4 for an isotopically pure CO monolayer, is beyond the scope of this work. It would require knowledge of the rate constants for VEP within the monolayer and the overlayer as well as for energy transfer between the two layers. In addition, energy transfer between the C-down and O-down isomers would need to be considered.
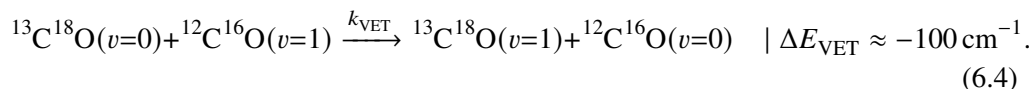
Therefore, the energy transfer mechanism will only be discussed qualitatively, based on the knowledge obtained from Chapter 4 and the rate constant expressions for V-V transfer in Section 2.2.2. Note that this discussion will explicitly focus on the energy transfer after m38**o26** excitation. Similar concepts should, however, also apply to the other systems.

The efficiency of energy transfer from the $^{12}C^{16}O$ overlayer to the $^{13}C^{18}O$ monolayer depends critically on the competition between VEP in the overlayer and V-V energy transfer from the overlayer to the monolayer. After excitation of a large fraction of the overlayer to $v = 1$, VEP is started by the following process:

$$^{12}C^{16}O(v{=}1) + {}^{12}C^{16}O(v{=}1) \xrightarrow{k_{\mathrm{VEP}}} {}^{12}C^{16}O(v{=}2) + {}^{12}C^{16}O(v{=}0) \quad | \; \Delta E_{\mathrm{VEP}} \approx -24\,\mathrm{cm}^{-1}.$$
(6.3)

Due to the strong distance-dependence of the V-V transfer rate constants, energy transfer to the monolayer is most efficient near the overlayer-monolayer interface. However, only the $v = 1$ molecules will show fast "diffusion" in the overlayer, due to resonant exchange with the abundant $v = 0$ molecules (see also Section 4.1.3). Once a molecule has been excited to $v = 2$ or higher due to VEP, it is much less mobile and unlikely to be located near the interface. Therefore, any VEP process will effectively remove vibrational quanta from the interface and $v = 1$ excitation is the most likely donor for vibrational energy transfer to the monolayer.

In the initial phase after excitation, only $v = 0$ in the monolayer can serve as the acceptor and only the following V-V energy transfer process can take place:

$$^{13}C^{18}O(v{=}0) + {}^{12}C^{16}O(v{=}1) \xrightarrow{k_{\mathrm{VET}}} {}^{13}C^{18}O(v{=}1) + {}^{12}C^{16}O(v{=}0) \quad | \; \Delta E_{\mathrm{VET}} \approx -100\,\mathrm{cm}^{-1}.$$
(6.4)

Therefore, the efficiency of vibrational energy transport (VET) will be largely determined

by the ratio $k_{\text{VET}}/k_{\text{VEP}}$. In this example, the excess energy of $\sim 100\,\text{cm}^{-1}$ allows for efficient energy transfer from $^{12}\text{C}^{16}\text{O}$ to $^{13}\text{C}^{18}\text{O}$. Remember that V-V energy transfer is generally more efficient for more negative excess energies, ΔE_{VET}, because more phonons are available at higher frequencies that can accept the energy. Only when the energy of the highest frequency phonon is exceeded, energy cannot be transferred to a single phonon anymore and a drop in the VET efficiency is expected.

As a last point, the vibrational frequency difference should be much larger than $k_{\text{B}}T$ to avoid a reduction of the transfer efficiency due to reverse energy transfer from the monolayer to the overlayer. For the process in Eq. 6.4, the rate constant of the reverse reaction, k'_{VET}, can be related to the rate constant of the forward reaction, k_{VET}, by detailed balance: [27, 173]

$$\frac{k'_{\text{VET}}}{k_{\text{VET}}} = \exp\left(\frac{\Delta E_{\text{VET}}}{k_{\text{B}}T}\right) \tag{6.5}$$

At $7\,\text{K}$ and an energy difference of $-100\,\text{cm}^{-1}$, the backward reaction is 10^{-9} slower than the forward reaction. Therefore, energy transfer is irreversible under the given experimental conditions. This not only helps to obtain a high efficiency for energy transfer from the overlayer to the monolayer but also explains why reverse energy transfer from $^{13}\text{C}^{18}\text{O}$ to $^{12}\text{C}^{16}\text{O}$ is not observed at all. Even for a much smaller energy difference of only $-15\,\text{cm}^{-1}$, the backward rate is only $5\,\%$ of the forward rate constant. This is consistent with the fact that energy can be transferred from the C-down isomer to the O-down isomer in the monolayer but not vice versa (see Fig. 6.9).

Based on this example, it can be seen that the efficiency for VET depends strongly on the difference between the fundamental vibrational frequencies of the donor and acceptor. In addition, large transition dipole moments of the acceptor would favor VET over VEP. The transition dipole moment of the donor, on the other hand, influences VEP more strongly than VET. Therefore, other vibrational energy transport systems that rely on V-V transfer should be possible with careful choice of the acceptor and donor vibrations—in analogy to electronic energy transport systems that rely on FRET and careful choice of the electronic absorption and emission spectra. [174–177]

Analogy between V-V energy transfer and FRET

That a system based on V-V energy transfer can operate similarly to a solar light harvesting system is not entirely surprising, given that V-V energy transfer and FRET rely on the same intermolecular coupling. The rate constants of both energy transfer mechanisms

can be calculated based on Fermi's golden rule: [57, 171]

$$k_{FI} = \frac{2\pi}{\hbar} \sum_i P_i \sum_f |V_{FI}|^2 \, \delta(E_F - E_I). \tag{6.6}$$

Here, the summation is over initial and final bath states, $|i\rangle$ and $|f\rangle$. This thermal bath ensures that the total energies of the systems in the initial and final state, E_I and E_F, are equal. P_i describes the Boltzmann probability for occupation of an initial bath state $|i\rangle$ at a given temperature. [57] Since energy transfer has to be resonant, the overall magnitude of the rate constant is mainly determined by the coupling matrix element $V_{FI} = \langle F|V|I \rangle$.

For both FRET and V-V energy transfer, the leading term in the interaction between acceptor and donor is the dipole-dipole interaction. [57, 58, 171] Therefore, the coupling matrix element can be generally written as:

$$V_{FI} = \left\langle n_A^*, n_D; f \left| \frac{f_{AD} \hat{\mu}^A \hat{\mu}^D}{4\pi\varepsilon_0 R^3} \right| n_A, n_D^*; i \right\rangle. \tag{6.7}$$

Here, $|n_A\rangle$ and $|n_D^*\rangle$ refer to the initial acceptor (A) and donor (D) states, whereas the asterisk denotes an excited state. Similarly, $|n_A^*\rangle$ and $|n_D\rangle$ refer to the final acceptor and donor states. $\hat{\mu}^A$ and $\hat{\mu}^D$ are dipole moment operators in the local coordinate systems of the acceptor and donor molecules. In addition, the coupling depends on the distance R between acceptor and donor and on a term f_{AD} that describes the relative orientation of the molecules (see also Eqs. 2.86 and 2.87).

For FRET, the donor and acceptor states correspond to electronic states. In this case, R is simply given by the distance, R_0, between the molecules. The rovibrational states of the two molecules act as the thermal bath that can compensate the mismatch between the electronic transition energies of acceptor and donor. This is possible because the rovibrational states typically show a quasi-continuous energy spectrum in the condensed phase due to line broadening. [171] As a result, the rate constant for FRET depends critically on the overlap between the donor emission and acceptor absorption spectrum, and on the electronic transition dipole moments of donor and acceptor. [171]

For V-V energy transfer, the donor and acceptor states correspond to individual vibrational states in the electronic ground state. Note that normally the following notation was used throughout this thesis, where n and m are vibrational quantum numbers: $|n_A\rangle = |n\rangle$, $|n_D^*\rangle = |m\rangle$, $|n_A^*\rangle = |n+1\rangle$ and $|n_D\rangle = |m-1\rangle$. For V-V transfer, the distance between the CO molecules, $R = R_0 + y$, is modulated by the lattice vibrations, which is described by the relative phonon displacement coordinate, y, and ensures

coupling between the CO molecules and the phonon bath (see also Section 2.2.2). [57, 58] Therefore, the continuous phonon spectrum allows for compensation of the typical energy mismatch on the order of $\sim 100\,\text{cm}^{-1}$. As a result, the rate constant for V-V energy transfer depends strongly on the phononic density of states (DOS) at the mismatch energy, and on the vibrational transition dipole moments of donor and acceptor. [57, 58]

The coverage dependence of the infrared absorption of CO on NaCl(100)

While the previous sections focused on the dynamics of highly vibrationally excited CO molecules on the NaCl(100) surface, the current chapter deals with the $v = 0 \rightarrow 1$ transition. It is well known that the collective vibrations of the molecules within the CO monolayer lead to an effective reduction of the infrared cross section compared to gas phase CO. [25] Absorption spectra at well-defined submonolayer coverages could provide further information on the contributions of the CO-CO and CO-NaCl interactions on the effective cross section. Therefore, polarized FTIR absorption spectra at various coverages between 0.02 ML and 1.00 ML are presented in this chapter, where the molecular beam source described in Chapter 3 provides a controlled way of dosing and temperature-programmed desorption (TPD) is used to determine the coverage quantitatively. From the coverage-dependent absorption data, the vibrational exciton model introduced in Section 2.4.3 is used to extract the infrared absorption cross section of an isolated CO molecule on the NaCl(100) surface. Its deviation from the gas phase value is also discussed. The results presented in this chapter have been first published in Ref. [178] by AIP Publishing.

7.1 Results

7.1.1 Coverage-dependent absorption spectra

To measure polarized FTIR absorption spectra at well-defined coverages, the following experimental procedure is used. First, adsorbed CO samples (natural abundance) are

prepared using a defined number of molecular beam pulses at 22 K (see Sections 3.1.5 and 3.2.2 for further details). After dosing, the sample is cooled down to 10 K to record p- and s-polarized FTIR spectra under an incidence angle of $\theta_1 = 45°$ (see Section 3.2.3 for further details). Here, it was ensured that the FTIR light source with a diameter of 3 mm at the surface only probes the center of the dosed area (diameter of ~10 mm), where a uniform surface coverage can be achieved. After the FTIR measurements, the sample is positioned in front of a mass spectrometer and heated at a constant ramp rate of 20 K/min to record TPD spectra of $^{12}C^{16}O$ (see Section 3.2.9 for further details).

The TPD spectra are used to determine the absolute surface coverage, θ. Figure 7.1a shows a selection of TPD spectra at different coverages. At low coverages, only a single desorption peak around 60 K is observed, which corresponds to desorption of CO in the first layer (submonolayer and monolayer). At increased coverages, a second desorption peak with an onset of ~26 K emerges, which can be attributed to desorption of CO overlayers. [43, 179] The TPD spectrum that corresponds to the full monolayer coverage ($\theta = 1$ ML) is identified based on the corresponding FTIR spectrum, for which complete monolayer absorption peaks but no overlayer absorption peaks are observed (shown later in Fig. 7.2). For submonolayer samples, the coverage is estimated based on the ratio between the integrals of the submonolayer desorption peak and the monolayer desorption peak, which are obtained by numerical integration. Similarly, the coverage of overlayer samples can be estimated based on the ratio between the overlayer desorption peak and the monolayer desorption peak. Only for coverages below 0.3 ML, an accurate estimate by direct integration of the submonolayer peak is not possible due to increased relative noise. However, the TPD integral depends approximately on the number of molecular beam pulses used for dosing, as seen in Fig. 7.1b. Therefore, the integrals for $\theta < 0.3$ ML are estimated from the linear fit to the high coverage data in Fig. 7.1b.

Polarized infrared absorption spectra for the monolayer and different submonolayer coverages are shown in Fig. 7.2 with an effective spectral resolution of ~0.7 cm^{-1} at 10 K. The upper left panel shows the absorption spectrum of the complete monolayer ($\theta = 1$ ML), showing the well-resolved absorption lines of the symmetric and asymmetric modes in the low temperature (2×1) structure at 2155.0 and 2148.7 cm^{-1}, respectively. (see also Section 2.1). [36, 38] In addition, the inset shows that overlayer absorption is only seen for slightly higher coverages, as mentioned earlier. Also note that the actual linewidth of the monolayer absorption peaks at 10 K is actually much narrower than the effective resolution. [129] With decreasing coverage, the absorption lines become significantly broader and a continuous shift to more positive frequencies is observed, consistent with previous measurements at submonolayer coverages. [35–37] In addition, the two peaks move closer together and the doublet disappears around $\theta = 0.3$ ML. At
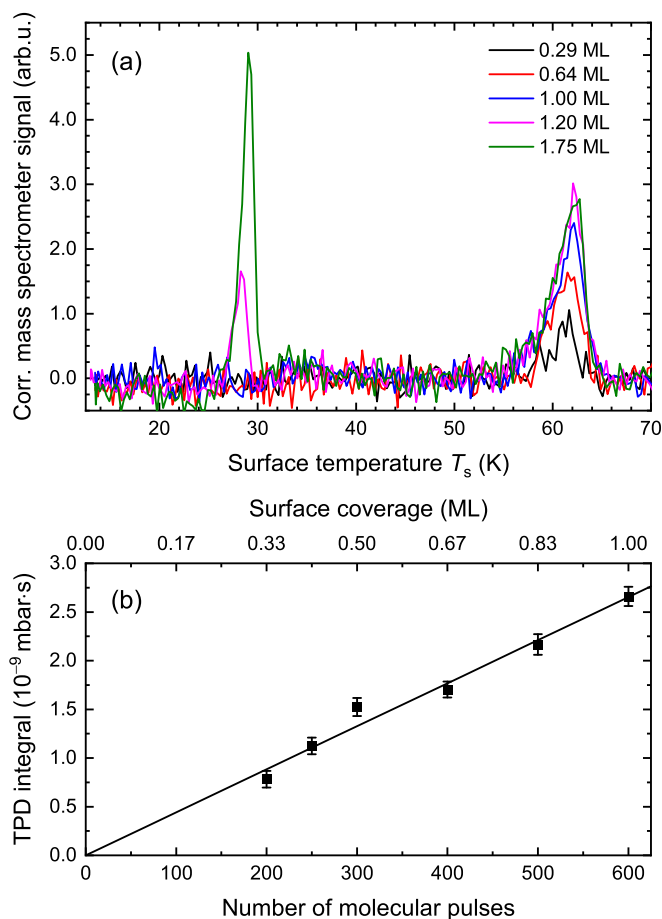
Figure 7.1: (a) Selected TPD spectra at various submonolayer, monolayer, and overlayer coverages. The corresponding coverages are determined from the desorption peak integrals, as described in the text. All spectra were corrected for a time-dependent drift in the ion signal, as described in Section 3.2.9. In addition, all spectra were corrected by subtracting a linear background. (b) The squares show the monolayer desorption peak integrals, extracted from TPD spectra at coverages above 0.3 ML, as a function of the number of molecular beam pulses. The error bars (1σ) for numerical integration are calculated as $\sigma \Delta t / \sqrt{N}$, where σ is the standard deviation of the baseline noise near the peak, Δt is the integration time window, and N is the number of data points within that time window. The straight line through the origin is a linear fit to the data, where the slope is given by $(4.42 \pm 0.12) \times 10^{-12}$ mbar s pulse^{-1}. This line can be used to estimate the low coverage integrals and the corresponding errors. Reproduced from Ref. [178], with the permission of AIP Publishing.

the lowest measured coverage, only a single, rather narrow absorption peak is observed at $2159.8\,\mathrm{cm^{-1}}$, consistent with the $0.05\,\mathrm{cm^{-1}}$ narrow line at $2159.9\,\mathrm{cm^{-1}}$ reported in Ref. [35]. In addition to the frequency shift and broadening, also a change in the polarization dependence is observed. While the low-frequency peak at high coverages shows absorption for both p- and s-polarized light, only absorption of p-polarized light is observed at the lower coverages.
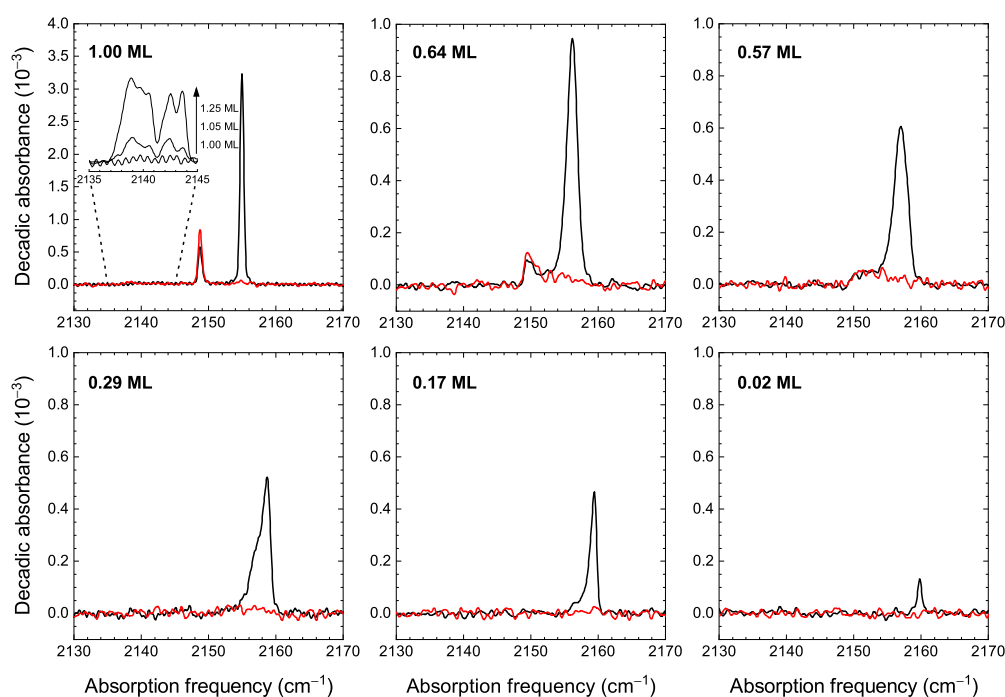
Figure 7.2: Polarized FTIR absorption spectra at the monolayer coverage and selected sub-monolayer coverages measured at $10\,\mathrm{K}$. Black and red curves show spectra measured with p- and s-polarized light, respectively. The inset in the upper, left panel shows the frequency range between 2135 and $2145\,\mathrm{cm^{-1}}$, where absorption by CO overlayers would be expected, for the complete monolayer coverage (1.00 ML) and slightly increased coverages (1.05 ML and 1.25 ML). Reproduced from Ref. [178], with the permission of AIP Publishing.

The integrated absorbance for p- and s-polarization, $A^{(p)}$ and $A^{(s)}$, extracted from the absorption spectra in Fig. 7.2, is shown in Fig. 7.3 as a function of coverage.[1] Since the low coverage spectra only feature a single peak, also the integrated absorbance for the high coverage spectra is integrated over the complete absorption band, including

---

[1] For convenience, the integrated absorbance will be labeled as A instead of $\tilde{A}$ throughout this chapter.

both the symmetric mode and the asymmetric mode. The non-linear dependence can at least partially be attributed to a change in the molecular tilt angle, as seen in the change of the $A^{(s)}/A^{(p)}$ ratio. However, also changes in the absorption strength due to intermolecular dipole-dipole interactions ("dipole screening") need to be considered. The coverage-dependent integrated absorbance will be analyzed quantitatively in the following sections while considering the dipole screening effect with an extended version of the model presented in Section 2.4.3.
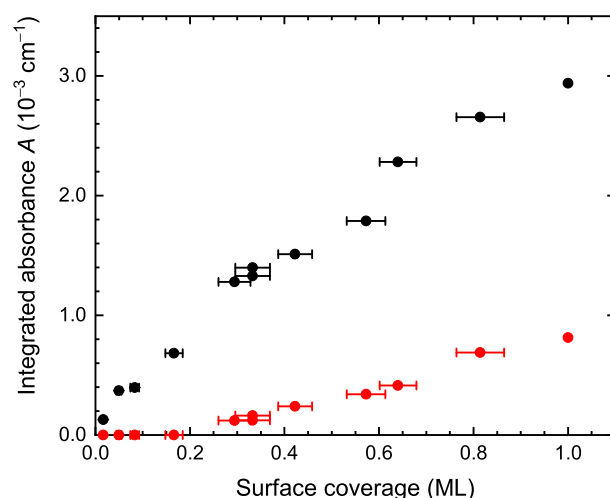
Figure 7.3: Integrated absorbance for p- and s-polarization, extracted from the monolayer and submonolayer absorption spectra in Fig. 7.2, as a function of the CO coverage. For coverages below 0.2 ML no absorption peaks are observed with s-polarized light and $A^{(s)}$ is set to zero in this case. The error bars for the coverage are calculated from the errors of the TPD integrals in Fig. 7.1. The error in the integrated absorbance is negligible and therefore not shown. Reproduced from Ref. [178], with the permission of AIP Publishing.

Before this analysis is presented, another advantage of molecular beam dosing must be mentioned. At the dosing temperature of 22 K, diffusion of CO molecules is not possible and therefore adsorption sites are occupied randomly by CO molecules. This is demonstrated in Fig. 7.4. In this experiment, a submonolayer sample is prepared at 9 K at a coverage of 0.57 ML. The corresponding p-polarized FTIR spectrum at 9 K, measured immediately after preparation, shows a single, broad peak with a maximum at 2157.4 cm^{-1}. When the sample is annealed to 20 K and subsequently cooled down to 9 K to measure another FITR spectrum, barely any change is observed. However, the spectrum obtained after annealing to 30 K (or higher) results in a significantly

altered spectrum. Now, two slightly narrower peaks at 2149.3 and 2155.3 cm^{-1} are observed, which remind of the two peaks in the monolayer spectrum. This is interpreted as the formation of monolayer islands at 30 K due to diffusion of the CO molecules, which seems to occur already 10 K below the onset for diffusion of CO on rough NaCl films. [180] Most importantly, diffusion is not important for the dosing temperature of 22 K and lower temperatures. Therefore, molecules are assumed to be randomly distributed over the adsorption sites, which greatly simplifies the following analysis.
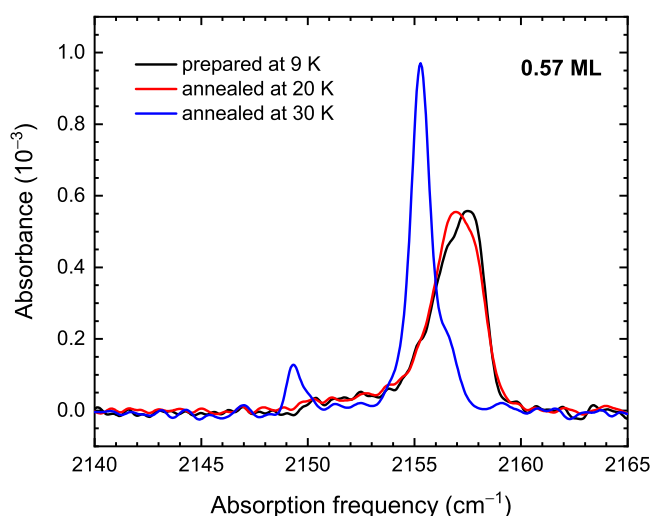
Figure 7.4: p-polarized absorption spectra of the same submonolayer sample ($\theta = 0.57$ ML) measured at 9 K after sequential annealing steps. The black curve shows the spectrum immediately after preparation at 9 K. The red curve shows a spectrum at 9 K after annealing at 20 K. The blue curve shows a spectrum at 9 K after annealing at 30 K. Reproduced from Ref. [178], with the permission of AIP Publishing.

7.1.2 Extended dipole screening model

An extension of the dipole screening model by Snigur and Rozenbaum [117] will be used to analyze the coverage-dependent absorption data in Fig. 7.3. One of the greatest advantages of this model is that it can deal with unit cells that contain more than a single molecule and that analytical equations are available for the eigenvalues and eigenvectors of the matrix that describes the vibrational excitons in the (2×1) monolayer structure of CO on NaCl(100). [117–119] A detailed introduction to the dipole screening model can be found in Section 2.4.3. Therefore, only the most important equations and parameters

will be briefly explained in the present section. Note that the present section also relies on many other concepts introduced in Section 2.4.

The integrated absorbance of a single exciton line l in the original model is given by (see Eq. 2.75):

$$A_l^{\tilde{\nu}} = \frac{S}{\ln(10)\cos(\theta_1)} 4\pi^3 \chi_\nu \tilde{\nu}_0^2 \frac{|\boldsymbol{\varepsilon} \cdot \mathbf{P}_l|^2}{n(1 + \chi_e W_l)^2}. \tag{7.1}$$

Here, the surface density, $S = 6.28 \times 10^{14}\,\text{molecules}\,\text{cm}^{-2}$, of the complete (2×1) monolayer structure is given by the lattice constant of the underlying Na^+ lattice ($a = 3.99\,\text{Å}$). The incidence angle in the absorption experiments is $\theta_1 = 45°$. χ_ν is the vibrational polarizability (in units of Å^3), which is related to the infrared absorption cross section, $\bar{\sigma}_z$, along the bond axis of a single CO molecule by $\bar{\sigma}_z = 4\pi^3 \chi_\nu \tilde{\nu}_0^2$ (see Eq. 2.76). χ_e is the electronic polarizability (in units of Å^3) of a single molecule parallel to the bond axis.[2] A constant value of $2155\,\text{cm}^{-1}$ is chosen for the unperturbed frequency, $\tilde{\nu}_0$, which approximates all absorption frequencies observed in Fig. 7.2 with sufficient accuracy.

W_l is an eigenvalue of the matrix W (see Eqs. 2.70 to 2.73), which effectively describes the sum over the dipole-dipole interaction terms between the two types of molecules in the (2×1) structure ($n = 2$). The vector $\mathbf{P}_l$ is related to the corresponding eigenvector, $\mathbf{C}_l$, by $\mathbf{P}_l = \sum_j C_{lj} \mathbf{e}_j$. Here, $\mathbf{e}_j$ is a unit vector that describes the orientation of the molecule of type j within the unit cell. Therefore, $\mathbf{P}_l/n$ can be interpreted as the unit vector of the transition dipole moment of the corresponding exciton mode. $\boldsymbol{\varepsilon}$ is a unit vector that describes the orientation of the electric field vector of the infrared light.

Equation 7.1 only describes the integrated absorbance of a single exciton line for a given absolute orientation of $\mathbf{P}_l$, i.e., for a single adsorbate domain. To describe the absorption experiments correctly, an average over all possible domains needs to be considered. [35, 117] To consider the C_{4v} symmetry of the surface, the vector $\mathbf{P}_l$ of a single rotational domain,[3] can be conveniently written in polar coordinates. $P_\parallel = (P_x^2 + P_y^2)^{1/2}$ and P_z characterize its components parallel and perpendicular to the surface. The azimuthal angles of the four rotational domains can be written as $\phi_m = \phi_0 + m\pi/2$, where the index m labels the different domains. Therefore, the domain average of the polarization-dependent $|\boldsymbol{\varepsilon} \cdot \mathbf{P}_l|^2$ term is given by Eq. 7.2 and is independent

---

[2] The perpendicular components of the electronic polarizability do not contribute.[117]

[3] In principle, also domains related by mirror symmetry exist for C_{4v} symmetry. However, they do not need to be considered explicitly because the average over all mirror domains gives the same result.

of the azimuthal domain orientation.

$$
\begin{aligned}
\left\langle \left| \boldsymbol{\varepsilon} \cdot \mathbf{P}_l \right|^2 \right\rangle &= \frac{1}{4} \sum_{m=0}^{3} \left[\cos\left(\phi_0 + \frac{m\pi}{2} \right) P_\| \varepsilon_x + \sin\left(\phi_0 + \frac{m\pi}{2} \right) P_\| \varepsilon_y + P_z \varepsilon_z \right]^2 \\
&= 0.5 P_\|^2 \left(\varepsilon_x^2 + \varepsilon_y^2 \right) + P_z^2 \varepsilon_z^2 \\
&= 0.5 \left(P_x^2 + P_y^2 \right) \left(\varepsilon_x^2 + \varepsilon_y^2 \right) + P_z^2 \varepsilon_z^2 .
\end{aligned}
\tag{7.2}
$$

Up to here, the original equations from Ref. [117] were described, although Snigur and Rozenbaum used a slightly different approach for the domain average. In the following steps, extensions beyond the original model will be introduced. To consider the proper electric fields of the infrared radiation at the surface, the squared components of the electric field unit vector, ε_x^2, ε_y^2 and ε_z^2, need to be replaced by the normalized field intensity components, T_x, T_y and T_z, given in Eqs. 2.55 to 2.57. To achieve this, the electric field unit vectors, $\boldsymbol{\varepsilon}$ can be replaced by $\mathbf{T}_p$ and $\mathbf{T}_s$ for p- and s-polarization, respectively:[4]

$$
\mathbf{T}_p = \left(T_x^{1/2} \quad 0 \quad T_z^{1/2} \right),
\tag{7.3a}
$$

$$
\mathbf{T}_s = \left(0 \quad T_y^{1/2} \quad 0 \right).
\tag{7.3b}
$$

For the vacuum-NaCl interface, the refractive indices, which define the normalized field intensity terms, are given by $n_1 = 1$ and $n_3 = 1.52$. [135] The resulting values for the field intensity terms at the incidence angle of 45° are $T_x = 0.452$, $T_y = 0.689$ and $T_z = 0.548$. With Eq. 7.3, the domain-averaged polarization-dependent terms (Eq. 7.2) become:

$$
\left\langle \left| \mathbf{T}_p \cdot \mathbf{P}_l \right|^2 \right\rangle = 0.5 \left(P_x^2 + P_y^2 \right) T_x + P_z^2 T_z,
\tag{7.4a}
$$

$$
\left\langle \left| \mathbf{T}_s \cdot \mathbf{P}_l \right|^2 \right\rangle = 0.5 \left(P_x^2 + P_y^2 \right) T_y.
\tag{7.4b}
$$

Therefore, the integrated absorbance for p- and s-polarized light of individual exciton lines is given by Eq. 7.5. It considers both the reduction of the effective cross section due to the intermolecular dipole-dipole interactions within a periodic structure and the

---

[4] Remember that, by definition, only x- and z-components are relevant to p-polarized light, whereas only the y-component is relevant to s-polarized light.

effective field at the surface.

$$A_l^{(p)} = \frac{S}{\ln(10)\cos(\theta_1)} 4\pi^3 \chi_v \tilde{v}_0^2 \frac{\left\langle |\mathbf{T}_p \cdot \mathbf{P}_l|^2 \right\rangle}{n(1 + \chi_e W_l)^2}, \tag{7.5a}$$

$$A_l^{(s)} = \frac{S}{\ln(10)\cos(\theta_1)} 4\pi^3 \chi_v \tilde{v}_0^2 \frac{\left\langle |\mathbf{T}_s \cdot \mathbf{P}_l|^2 \right\rangle}{n(1 + \chi_e W_l)^2}. \tag{7.5b}$$

Another extension of the model is made for the analytical description of submonolayer coverages. It has been shown by Persson and Ryberg that the absorption of an incomplete monolayer structure, i.e., a monolayer structure with randomly distributed vacant adsorption sites, can be calculated based on the absorption of the complete monolayer. [114] For this purpose, an average polarizability approximation (APA) is made.[5] This approximation effectively assumes a complete monolayer structure, in which each adsorption site is characterized by an average vibrational and electronic polarizability, $\bar{\chi}_v = \theta \chi_v$ and $\bar{\chi}_e = \theta \chi_e$, which depends on the coverage, θ. [114] Within the APA, Eq. 7.6 provides an analytical equation that is able to describe the absorption at submonolayer coverages if the adsorption sites are occupied randomly as shown experimentally in Section 7.1.1.

$$A_l^{(p)} = \frac{S}{\ln(10)\cos(\theta_1)} 4\pi^3 \theta \chi_v \tilde{v}_0^2 \frac{\left\langle |\mathbf{T}_p \cdot \mathbf{P}_l|^2 \right\rangle}{n(1 + \theta \chi_e W_l)^2}, \tag{7.6a}$$

$$A_l^{(s)} = \frac{S}{\ln(10)\cos(\theta_1)} 4\pi^3 \theta \chi_v \tilde{v}_0^2 \frac{\left\langle |\mathbf{T}_s \cdot \mathbf{P}_l|^2 \right\rangle}{n(1 + \theta \chi_e W_l)^2}. \tag{7.6b}$$

Analytical solution for an incomplete CO monolayer

For a simplified version of the (2×1) CO monolayer structure, analytical solutions can be obtained for the two eigenvectors and eigenvalues of the matrix W, which correspond to the symmetric $(+)$ and asymmetric $(-)$ modes. [117–119] In this simplified monolayer structure, the two molecules in the unit cell are tilted in opposite directions by an angle α and adsorb on top of the Na$^+$ ions, which form a square lattice with lattice constant

---

[5] The APA is called "average T-matrix approximation" in Ref. [114].

$a = 3.99$ Å. The corresponding eigenvalues are given by:

$$W_+ = \frac{1}{2a^3} \left[-4D_F \cos^2(\alpha) + 2D_A \sin^2(\alpha) \right], \tag{7.7a}$$

$$W_- = \frac{1}{2a^3} \left[2D_F \sin^2(\alpha) - \left(1 - \sqrt{2}\right) D_F \cos^2(\alpha) \right]. \tag{7.7b}$$

Here, $D_F = -4.516811$ and $D_A = -5.098873$ are dimensionless constants. The vectors $\mathbf{P}_l$, which are related to the eigenvectors, $\mathbf{C}_l$, are given by:

$$\mathbf{P}_+ = \begin{pmatrix} 0 & 0 & \sqrt{2}\cos(\alpha) \end{pmatrix}, \tag{7.8a}$$

$$\mathbf{P}_- = \begin{pmatrix} \sqrt{2}\sin(\alpha) & 0 & 0 \end{pmatrix}. \tag{7.8b}$$

Inserting Eqs. 7.7 and 7.8 into Eq. 7.6 gives the integrated absorbance of the symmetric and asymmetric modes in the incomplete CO/NaCl(100) monolayer structure at any given coverage θ. A schematic representation of the incomplete (2×1) monolayer structure is shown in Fig. 7.5.

$$A_+^{(s)} = 0, \tag{7.9a}$$

$$A_-^{(s)} = \frac{\theta S}{\ln(10)\cos(\theta_1)} \frac{4\pi^3 \chi_v \tilde{\nu}_0^2}{(1 + \theta \chi_e W_-)^2} \frac{T_y \sin^2(\alpha)}{2}, \tag{7.9b}$$

$$A_+^{(p)} = \frac{\theta S}{\ln(10)\cos(\theta_1)} \frac{4\pi^3 \chi_v \tilde{\nu}_0^2}{(1 + \theta \chi_e W_+)^2} T_z \cos^2(\alpha), \tag{7.9c}$$

$$A_-^{(p)} = \frac{\theta S}{\ln(10)\cos(\theta_1)} \frac{4\pi^3 \chi_v \tilde{\nu}_0^2}{(1 + \theta \chi_e W_-)^2} \frac{T_x \sin^2(\alpha)}{2}, \tag{7.9d}$$

In the equations in Eq. 7.9, the first term describes the effective surface density of the submonolayer sample and the last term describes the polarization dependence. The second term can be interpreted as the effective cross section of the collective vibrational mode along the direction of the transition dipole moment, which considers the dipole screening effect:

$$\bar{\sigma}_{z,l}^{\text{eff}} = \frac{4\pi^3 \chi_v \tilde{\nu}_0^2}{(1 + \theta \chi_e W_l)^2}. \tag{7.10}$$
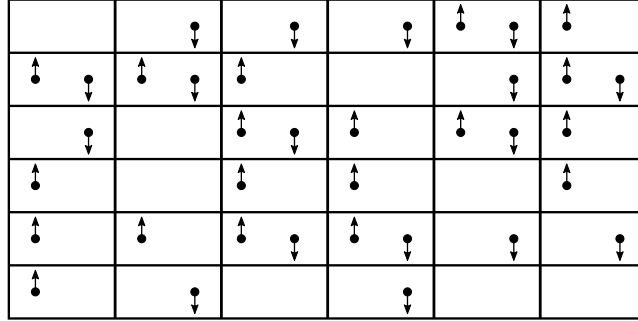
Figure 7.5: Schematic representation of the incomplete (2×1) monolayer structure of CO on NaCl(100) for $\theta = 0.5$ ML. The molecules are assumed to adsorb on top of the Na$^+$ ions, whereas the occupied adsorption sites are randomly distributed. Arrows indicate the tilt direction of the molecules. The unit cells of the complete (2×1) monolayer structure are also indicated. Reproduced from Ref. [178], with the permission of AIP Publishing.

7.1.3 Fit to the coverage-dependent integrated absorbance data

The analytical dipole screening model presented in the previous section can be used to extract the properties of isolated CO molecules on the NaCl(100) surface from the coverage-dependent integrated absorbance in Fig. 7.3. For this purpose, Eq. 7.9 is used, which describes the integrated absorbance of the symmetric and asymmetric mode of the incomplete monolayer structure by analytical functions. Since the integral over the complete absorption band was used to obtain the experimental values, the same is done for the analytical model by adding the integrated absorbance of the symmetric and asymmetric line ($A^{(p)} = A_+^{(p)} + A_-^{(p)}$ and $A^{(s)} = A_+^{(s)} + A_-^{(s)}$).

The only free parameters in the dipole screening model are the vibrational polarizability, χ_v, the electronic polarizability, χ_e, and the molecular tilt angle, α. Therefore, the analytical equations in Eq. 7.9 are fitted to the data in Fig. 7.3 using the following procedure. First, note that the $A^{(s)}/A^{(p)}$ ratio depends only on α and χ_e, but not on χ_v. Therefore, α can be calculated as a function of χ_e for all measured coverages using the experimental $A^{(s)}/A^{(p)}$ ratio.[6] This constraint removes α as a free parameter from the non-linear least square fit to the $A^{(p)}$ and $A^{(s)}$ data in Fig. 7.3, from which χ_v and χ_e are obtained as $\chi_v = (0.0435 \pm 0.0014)$ Å^3 and $\chi_e = (3.30 \pm 0.36)$ Å^3. According to Eq. 2.76, the value of χ_v can also be converted to the integrated cross section along the bond axis of an isolated CO molecule, which gives $\bar{\sigma}_z = (2.51 \pm 0.08) \times 10^{-17}$ cm molecule^{-1}.

---

[6] Note that α cannot be represented as an analytical function of χ_e and is calculated numerically.

The fit results are visualized in Fig. 7.6. Fig. 7.6b shows the tilt angles, α, that are obtained from the fit (see above). As expected from the increase of the $A^{(s)}/A^{(p)}$ ratio with increasing coverage, the tilt angles also continuously increase from 0° (at low coverages) to $(27 \pm 1)°$ (at the monolayer coverage). The solid line shows an empirical fit of the form $\alpha(\theta) = \alpha_{\mathrm{ML}} \exp(-b/\theta^n)$, where $\alpha_{\mathrm{ML}} = 26.3°$, $b = 3.18 \times 10^{-3}$, and $n = 3.91$. This function is used as an interpolation function for the tilt angle and can thus be used to visualize the fit results in Fig. 7.6a for the whole coverage range.

In addition to the standard deviations, $\sigma(\chi_v) = 0.0014\,\text{Å}^3$ and $\sigma(\chi_e) = 0.36\,\text{Å}^3$, the covariance, $\mathrm{cov}(\chi_v, \chi_e) = 4.6 \times 10^{-4}\,\text{Å}^6$, describing the correlation between the two parameters, is obtained from the fit and considered for estimating the errors in the determined tilt angles (Fig. 7.6b). Here, error propagation is done numerically because the tilt angles cannot be represented by an analytical function of χ_e. For this purpose, the standard deviations and covariance are used to draw 10^5 random numbers from the corresponding bivariate normal distribution. These random numbers are used to calculate a distribution of tilt angles and the corresponding error is determined as the standard deviation of the resulting distribution. The errors in Fig. 7.8 are calculated in the same manner.

7.1.4 Deviations from the incomplete monolayer structure

In the following, it will be shown that the incomplete monolayer structure (Fig. 7.5) assumed in the analytical model provides accurate values for the integrated absorbance at submonolayer coverage, even though the actual submonolayer structures likely differ from that idealized structure. For this purpose, the integrated absorbance will be simulated for submonolayer structures, where the CO molecules are shifted or oriented differently compared to the incomplete monolayer structure.

For the numerical simulations, the more general expression for the extended dipole screening model in Eq. 7.5 will be used, which describes the integrated absorbance of an exciton absorption line for a periodic structure with n molecules per unit cell. The corresponding interaction matrix W, which defines W_l and $\mathbf{P}_l$, is given by:

$$W_{jj'} = \sum_{\mathbf{R}} \left[\frac{\mathbf{e}_j \cdot \mathbf{e}_{j'}}{|\mathbf{R} + \mathbf{r}_{jj'}|^3} - 3\frac{\left(\mathbf{e}_j \cdot \left(\mathbf{R} + \mathbf{r}_{jj'}\right)\right)\left(\mathbf{e}_{j'} \cdot \left(\mathbf{R} + \mathbf{r}_{jj'}\right)\right)}{|\mathbf{R} + \mathbf{r}_{jj'}|^5} \right]. \tag{7.11}$$

Here, $\mathbf{e}_j$ and $\mathbf{e}_{j'}$ are the orientation vectors of molecules j and j' in the unit cell, $\mathbf{r}_{jj'} = \mathbf{r}_{j'} - \mathbf{r}_j$ is the distance between the two molecules and the summation includes all
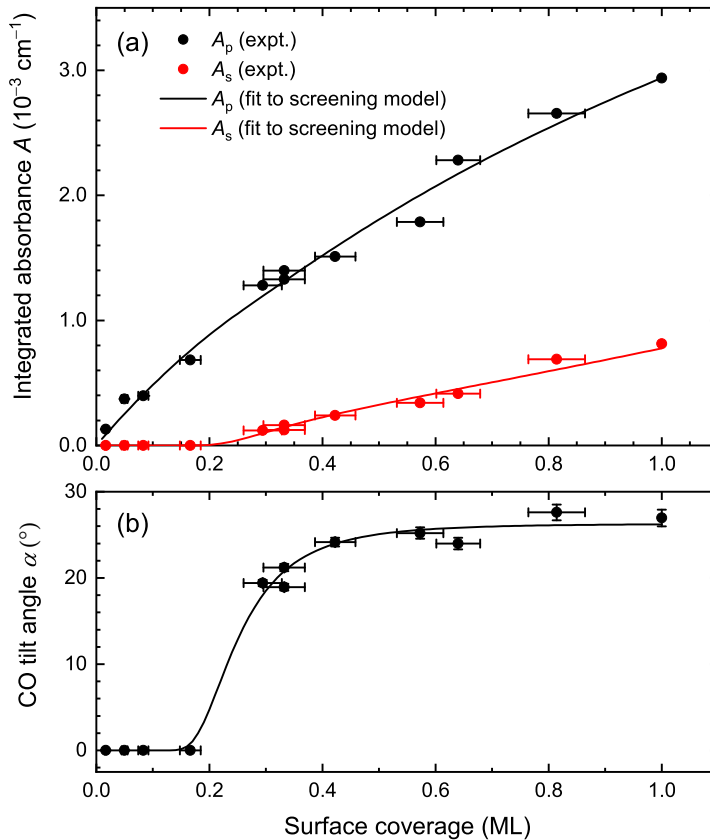
Figure 7.6: (a) The experimental data from Fig. 7.3 is shown as black and red dots for p- and s-polarization, respectively. Solid lines of the same color represent the results from the analytical dipole screening model using the fitted parameters, $\chi_v = (0.0435 \pm 0.0014)$ Å^3 and $\chi_e = (3.30 \pm 0.36)$ Å^3, and the interpolated tilt angle function, $\alpha(\theta)$, which is shown in panel b. (b) The tilt angles (black dots) obtained from the fit are shown as a function of coverage. Error bars are derived as described in the text. The solid line shows the empirical fit to the tilt angle data. Reproduced from Ref. [178], with the permission of AIP Publishing.

unit cell position vectors, $\mathbf{R}$ (see also Eqs. 2.70 to 2.73). As noted in Section 2.4.3, this corresponds to a summation over all dipole-dipole interaction terms between molecules of type j and j'. Here, a slightly different interpretation is used. If the size of the simulation cell is chosen large enough, the summation over the different unit cells can be neglected and it is sufficient to calculate $W_{jj'}$ from the interaction of molecules j and j' in a single unit cell. For this approximation, a large supercell containing 50×50 adsorption sites with periodic boundary conditions and the minimum image convention is used.

Based on this approach, the matrix W can be constructed for any adsorption structure, which is characterized by the positions and orientation vectors of the n molecules ($\mathbf{r}_j$ and $\mathbf{e}_j$). For a given coverage, θ, vacant adsorption sites are produced randomly with a probability of $1 - \theta$ and are conveniently modeled by setting the corresponding orientation vectors, $\mathbf{e}_j$, to zero. Diagonalization of W gives the corresponding eigenvalues, W_l, and the vectors $\mathbf{P}_l$, which can be used in Eq. 7.5 to calculate the integrated absorbance $A_l^{(p)}$ and $A_l^{(s)}$ of a single exciton absorption line. The integrated absorbance of the complete absorption band is then simply given as a sum over the integrated absorbance of all exciton lines ($A^{(p)} = \sum_l A_l^{(p)}$ and $A^{(s)} = \sum_l A_l^{(s)}$). The results from 50 different, random configurations are averaged for each coverage. In addition, the fitted parameters, $\chi_v = (0.0435 \pm 0.0014)\ \text{Å}^3$ and $\chi_e = (3.30 \pm 0.36)\ \text{Å}^3$, as well as the fitted tilt angle function, $\alpha(\theta)$ are used with Eq. 7.5 so that the coverage-dependent results for $A^{(p)}$ and $A^{(s)}$ can be directly compared to the analytical results in Fig. 7.6a.

First, simulations of the incomplete monolayer structure are shown in Fig. 7.7a and compared to the analytical result from Fig. 7.6a. In the simulation, exactly the same structure as in the analytical model is assumed, just with a (50×50) supercell. There, all CO molecules adsorb on top of the Na^+ ions and form a (2×1) structure, in which the two CO molecules are tilted in opposite direction by the tilt angle α. If the average polarizability approximation (APA), which was used to obtain the analytical result for the incomplete monolayer, is valid, the experimental and simulated curves in Fig. 7.7a should be identical. Indeed, the results agree well with a maximum deviation of about 1.5 %. From a convergence study at $\theta = 1\ \text{ML}$ (not explicitly shown) it can be seen that the residual deviation is due to the finite size of the (50×50) simulation cell.

In addition, displacements of the CO molecules from the Na^+ ion positions are considered. Low-energy electron diffraction (LEED) experiments show that the positions of the carbon atoms are displaced by roughly 0.4 Å along the tilt direction of the CO molecules in the (2×1) monolayer structure. [40] However, even lateral shifts along the tilt directions of 0.7 Å, appropriate for the center-of-mass positions of the CO molecules, give results that are identical to those in Fig. 7.7a within less than 0.3 % and are therefore
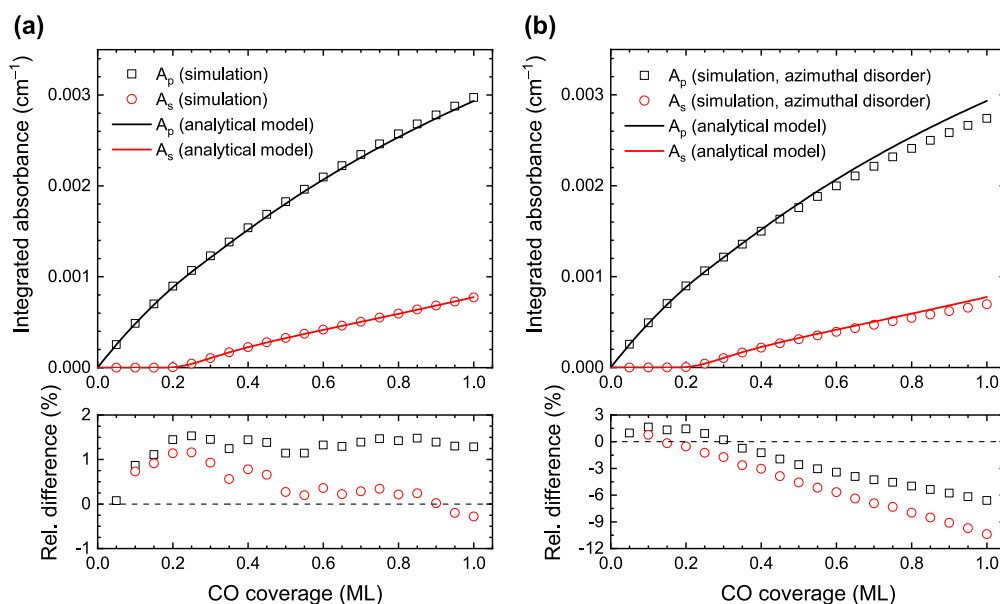
Figure 7.7: Numerical simulations of (a) the incomplete (2×1) monolayer structure and (b) the incomplete monolayer structure with random azimuthal orientations. Upper panels: Black squares and red circles show the integrated absorbance for p- and s-polarized light, respectively. Black and red solid lines show the analytical results for the incomplete monolayer structure from Fig. 7.6a. Lower panels: Relative differences between the simulations and the analytical results. Reproduced from Ref. [178], with the permission of AIP Publishing.

not further considered.

The azimuthal orientation of the molecules has the largest effect on the infrared absorption. While the (2×1) monolayer structure is highly ordered, azimuthal order becomes less likely for lower coverages. Therefore, Fig. 7.7b shows the simulation results for an incomplete monolayer sample with total azimuthal disorder. To simulate this, not only the occupied adsorption sites but also the azimuthal orientations of the molecules are chosen randomly. Below 0.5 ML, the deviations do not exceed 4 %. At coverages above 0.5 ML, the observed deviations become continuously larger and reach 6.6 % and 10.4 % at $\theta = 1$ ML for p- and s-polarization, respectively. However, the FTIR absorption spectra in Fig. 7.2 still show a doublet peak at above 0.5 ML, which indicates at least partial azimuthal order. At low coverages, azimuthal disorder is much more likely due to the larger average separation between the molecules; however, the deviations from the incomplete monolayer structure are also much smaller for the same reason. In addition, the tilt angle approaches 0° at low coverages, which makes the effect of

azimuthal disorder less relevant. In conclusion, the deviations in Fig. 7.7b rather resemble the largest possible deviations due to azimuthal disorder and the actual deviations are expected to be much smaller, especially at coverages above 0.5 ML. Therefore, the incomplete monolayer structure seems to be a reasonably accurate model for extracting χ_v and χ_e from the experimental data.

7.2 Discussion

In the previous sections, the electronic and vibrational polarizabilities of an isolated CO molecule on the NaCl(100) surface, $\chi_v = (0.0435 \pm 0.0014)\,\text{Å}^3$ and $\chi_e = (3.30 \pm 0.36)\,\text{Å}^3$, could be extracted based on the coverage dependence of the infrared absorption spectra. Although absorption spectra at submonolayer coverages and various temperatures have been previously reported, [35–37] there are two major advantages of the experimental approach used here. First, the coverage was independently determined using TPD, whereas the previous studies estimated the coverage based on the integrated absorbance of the submonolayer peaks. Second, the submonolayer samples were prepared by molecular beam dosing at 22 K, which gives access to random, non-equilibrium distributions of the CO molecules among the available adsorption sites and thus a simplified analysis. The submonolayer samples in Refs. [35–37], on the other hand, were prepared by adsorption of CO background gas at 40 K or higher, which is more likely to result in island formation.

First of all, the obtained integrated absorption cross section along the bond axis of the isolated CO molecule, $\bar{\sigma}_z = (2.51 \pm 0.08) \times 10^{-17}\,\text{cm molecule}^{-1}$, will be discussed. Its value is reduced by 18 % compared to that of gas phase CO, which is $3.05 \times 10^{-17}\,\text{cm molecule}^{-1}$. [181] Another estimate of the isolated adsorbate cross section was provided by Richardson *et al.*, who reported infrared absorption spectra of a CO monolayer at 55 K, where CO adopts the (1×1) structure. [25] They already recognized that a major fraction of the 61 % reduction of the monolayer cross section can be explained by the dipole-dipole interactions between the molecules, essentially the same mechanism as in the dipole screening model. Assuming that the electronic polarizability of the adsorbed CO molecule is unchanged from that of the gas phase molecule, they could quantitatively estimate this contribution. They concluded that the cross section of a single molecule is reduced by 30 % compared to the gas phase value, [25, 181] which is to be compared with the 18 % reduction reported here.

It was later suggested that the magnitude of the cross section reduction for the isolated CO adsorbate can be explained by the vibrational Stark effect, [21, 182] which describes

the interaction of the CO molecule with the electric field of the NaCl surface. Lambert *et al.* showed that an extension of the vibrational Stark effect that also includes the interaction with the gradients of the electric field can account for a reduction of up to 19.4 % in the CO/NaCl(100) monolayer.[7] [182] This theoretical estimate is in remarkable agreement with the 18 % reduction reported here. In conclusion, the reduction of the cross section of the isolated adsorbate can indeed be explained by the electrostatic interactions with the surface electric field.

In the present work, the fitted electronic polarizability, $\chi_e = (3.30 \pm 0.36)$ Å^3, is found to be increased compared to the gas phase value of 2.3 Å^3. [183] To some degree, this increase could also be related to the interaction with the surface electric field. However, the fitted electronic polarizability probably also contains an effective contribution from the polarizability of the substrate, since only interactions between the CO molecules are explicitly considered in the dipole screening model. In a previous microscopic model of the CO/NaCl(100) monolayer, where also the polarizability of the sodium and chlorine atoms were considered, the integrated absorbance was found to be slightly reduced compared to the estimate by Richardson *et al.*, where only the polarizability of the molecules was considered. [184, 185] This result would be consistent with an effectively increased electronic polarizability. Further analysis of the coverage-dependent absorption spectra could thus explicitly include the effect of the substrate polarizability but is beyond the scope of this work.

Monolayer samples composed of ^{12}C^{16}O/^{13}C^{16}O mixtures provide an interesting, alternative approach to control the CO coverage of the two isotopologue. Ewing and co-workers performed experiments with such isotopic mixtures for a CO monolayer at 55 K, where it forms a (1×1) structure. [37] Interestingly, they found that the monolayer cross section is independent of the isotopic mixing ratio. The results from Ref. [37] are shown in Fig. 7.8 as empty squares. For comparison, also the effective integrated cross sections for the corresponding, hypothetical ^{12}C^{16}O submonolayer experiment are predicted as a function of coverage. These effective cross sections are based on the analytical dipole screening model (see Eq. 7.10), assuming an incomplete (1×1) monolayer structure and the fitted parameters from Section 7.1.3.[8] The good agreement between the prediction and the experimental data from Ref. [37] at 1 ML shows that the prediction is accurate. At lower coverages, the predicted cross section of the submonolayer samples deviates

---

[7] Note that the concept of considering the interactions between the multipole moments of CO and the electric field (gradients) is very similar to the way the orientation-dependent static frequency shifts were obtained in Chapter 5.

[8] The incomplete (1×1) monolayer structure corresponds to the incomplete (2×1) monolayer structure with $\alpha = 0°$.

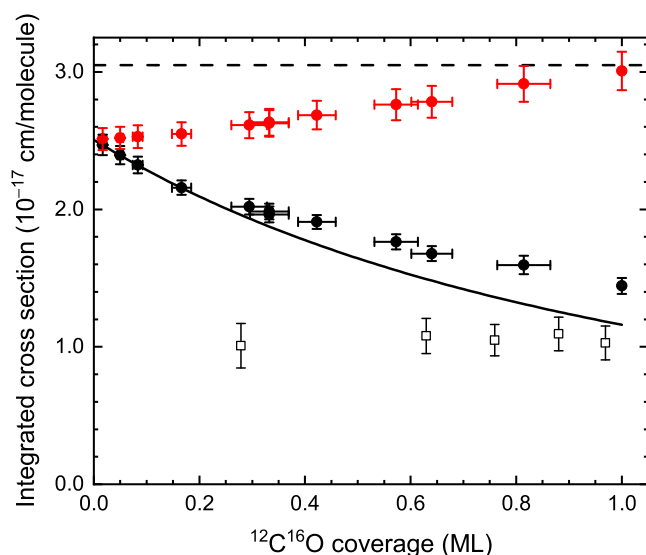significantly from that of the isotopic mixtures and approaches the isolated molecule cross section at 1 ML.

Figure 7.8: Effective integrated cross sections as a function of coverage are shown for different CO samples. Open squares show the cross sections derived in Ref. [37] for the symmetric mode of a CO monolayer at 55 K consisting of $^{12}C^{16}O/^{13}C^{16}O$ mixtures at different mixing ratios. In this case, the $^{12}C^{16}O$ coverage refers to the percentage of $^{12}C^{16}O$ in the isotopic mixture. The black, solid line corresponds to the prediction by the analytical dipole screening model for the cross section of the symmetric mode in the incomplete (1×1) monolayer structure. The dashed line indicates the integrated cross section of gas phase CO along the bond axis for comparison $(3.05 \times 10^{-17} \, \text{cm molecule}^{-1})$. [181] Black and red dots correspond to the effective cross sections of the symmetric and asymmetric modes obtained for the incomplete (2×1) monolayer structure, respectively, using the results from Fig. 7.6. Error bars are estimated as described in Section 7.1.3. Reproduced from Ref. [178], with the permission of AIP Publishing.

By considering the $1/(1 + \theta \chi_e W_l)^2$ term in the equation for the effective cross section (Eq. 7.10), the difference between the two cases becomes clearer. For the isotopic mixtures, the electronic polarizability of all molecules plays a role in the dipole screening effect and is approximately independent of the specific isotopologue. [114] Therefore, the effective cross section in the mixed monolayer sample does not depend on the isotopic mixing ratio and is identical to that of an isotopically pure monolayer. For the submonolayer sample, on the other hand, the average electronic polarizability is reduced at lower coverages, resulting in increasingly larger integrated cross sections.

For completeness, also the effective cross sections of the symmetric and asymmetric modes in the incomplete (2×1) monolayer structure, based on the experimentally determined tilt angles and fit parameters from Fig. 7.6, are shown in Fig. 7.8. Here, it should be noted that the dipole screening effect cannot only lead to a reduction of the effective cross section, as observed for the symmetric mode; it can also lead to an effective increase of the effective cross section, as seen for the asymmetric mode. [117]

Conclusions

The presented results provide new insight into the vibrational dynamics of highly excited CO adsorbed on NaCl(100). The improved kinetic Monte Carlo (KMC) simulations, which were performed to understand the mechanism of vibrational energy pooling (VEP) and vibrational relaxation in the CO/NaCl(100) monolayer, agree extraordinarily well with the experimental data. A realistic phonon spectrum that shows a lower cutoff frequency than a simple Debye density of states (DOS) can accurately reproduce the positions of the three base-camp peaks in the vibrational state distributions. To explain vibrational population up to $v = 30$, vibration-to-vibration (V-V) energy transfer over large distances up to 32 Å needs to be considered. As a consequence of the increasing dilution of vibrationally excited molecules in the pooling process and the strong distance dependence of their dipole-dipole coupling, the second and third base-camp states are populated on progressively longer timescales of up to 100 μs. The success of the simulations based on the aforementioned improvements thus validates the previously reported theory for V-V transfer rate constants in this system. [57, 58] Furthermore, the excess energy in V-V transfer processes is found to be specifically transferred to transverse phonons that involve motion of the Na atoms underneath the CO molecules—consistent with the coupling mechanism assumed in Refs. [57, 58]. The same base-camp mechanism found for VEP of CO should also apply to other diatomic adsorbates on NaCl(100), such as NO for example. For CO on other alkali halide surfaces, featuring different phonon spectra, altered base-camp positions in the vibrational distributions are expected.

Surprisingly, the mechanism for vibrational relaxation of adsorbed CO proposed in Refs. [57, 58] (Skinner-Tully (ST) model) cannot explain the effective experimental lifetimes. This mechanism is based on anharmonic coupling between the CO vibration

and the NaCl phonons via the adsorbate-surface potential, which is typically considered as the most important relaxation channel when electron-hole pair excitation is not possible. However, this quantum mechanical mechanism is not the dominant relaxation channel in the CO/NaCl(100) system, due to the weak CO-NaCl bond. Instead, relaxation of $v \leq 23$ can be explained by the Chance-Prock-Silbey (CPS) model, which is based on classical electrodynamics [59, 71] and was already proposed by Ewing and co-workers [16]— despite the lack of vibrational state-resolved information in that study. This weak coupling regime, where electrodynamics dominate vibrational relaxation, was termed the Sommerfeld ground-wave limit because the CPS theory originated in Sommerfeld's early description of radio wave propagation. [69] For CO on NaCl(100), the CPS relaxation rates are one order of magnitude larger than the corresponding fluorescence rate constants. Since the ratio between non-radiative relaxation and fluorescence rates can be modified by changing the substrate's extinction coefficent, κ, even vibrational lifetimes that are limited by the fluorescence lifetime are conceivable. For example, CO on KCl should show relaxation rates that are two orders of magnitude smaller than on NaCl, due to the reduced value of κ. [73, 135] The observed deviation of vibrational states above $v = 23$ from the CPS model could indicate a transition from the CPS model to the ST model; however, testing this hypothesis would require an improved ST model based on a more accurate phonon spectrum. Alternatively, the deviation above $v = 23$ could also be related to the formation of molecules in the O-down orientation.

With the current version of the mid-infrared emission spectrometer based on superconducting nanowire single-photon detectors (SNSPDs), the overtone emission from a CO monolayer can be routinely measured with a wavelength resolution of 7 nm and a temporal resolution of about 1 µs. The high resolution revealed spectral signatures of a previously unknown metastable O-down orientation of CO. The fundamental frequency of the O-down molecule is red-shifted by $-9.3\,\mathrm{cm}^{-1}$ from the vibrational frequency of gas phase CO, whereas the frequency of the stable C-down orientation is blue-shifted by $+7.6\,\mathrm{cm}^{-1}$. The existence of two orientations and their frequency shifts can be rationalized using a simple electrostatic model that only considers the vibrational state-dependent electrostatic interactions of CO with surrounding CO molecules and the surface. The metastable O-down orientation can only be formed in the highest vibrational states and, due its relatively long estimated lifetime between 0.1 to 100 s, a steady-state population of O-down molecules is observed in the emission spectra. When the $^{13}C^{18}O$ monolayer is covered by a $^{12}C^{16}O$ overlayer, the lifetime of the metastable O-down molecule becomes indefinitely long at 7 K such that its $v = 0 \rightarrow 1$ transition can be observed with absorption spectroscopy. It is not unlikely that similar flipped orientations exist for other physisorbed molecules that show vibrational or electronic state-dependent electrostatic properties.

The well-resolved vibrational spectra of both orientational isomers make CO on NaCl(100) an interesting system for studying isomerization dynamics with quantum state-resolution. However, it is so far unclear how the C-down molecules can overcome the large isomerization barrier, which is on the order of several hundred wavenumbers, even for the highest vibrational states. Vibrationally non-adiabatic transitions, in which CO changes its vibrational state from v to $v - 1$ and transfers the excess energy to the frustrated rotations, is speculated to be the most likely mechanism that can accumulate sufficient energy in the rotational motion. Pump-probe experiments that directly track the isomerization dynamics from quantum states of the C-down isomer to states of the O-down isomer would be incredibly helpful to investigate the importance of vibrationally non-adiabatic transitions. Such experiments are, however, challenging due to the coupled vibrational dynamics when the high vibrational states are prepared via VEP. Therefore, molecular dynamics calculations based on the recently published, full-dimensional potential energy surfaces (PESs) [142, 162, 163] are invaluable to interpret experiments that can be done with the present laser-induced fluorescence (LIF) setup. Besides vibrationally non-adiabatic transitions, tunneling due to accidental resonances between C-down and O-down states in the asymmetric isomerization potential are discussed as well. [164] Future experiments also need to explore the possibility of the isomerization taking place in the $a\ ^3\Pi$ electronic state, which might be populated due to vibration-to-electronic (V-E) energy transfer.

For the $^{13}C^{18}O$ monolayer/$^{12}C^{16}O$ overlayer system it is found that the O-down isomer can be more effectively produced when photons are absorbed by the 100 $^{12}C^{16}O$ overlayers, leading to 30 times more vibrational quanta than direct monolayer excitation. This directional vibrational energy transport across the interface is facilitated by the energetic preference for V-V transfer from $^{12}C^{16}O$ to $^{13}C^{18}O$ due to the $100\,\mathrm{cm}^{-1}$ difference in the respective fundamental vibrational frequencies, which was reported in previous VEP experiments for the low-frequency isotopic impurities [76–78, 80, 81, 83, 86] but has so far not been exploited in a controlled manner. This preferential energy transport was also demonstrated for excitation of the $^{12}C^{16}O$ monolayer, which can transfer essentially all of its energy to $^{13}C^{18}O$ overlayers. Energy transfer from $^{13}C^{18}O$ to $^{12}C^{16}O$, which is energetically uphill, was not observed.

Future experiments could use this concept of controlled vibrational energy transport from a CO overlayer to prepare highly excited (polyatomic) molecules that are more reactive than CO. In such experiments, the fundamental vibrational frequency of the acceptor should be red-shifted from the donor frequency by about $100\,\mathrm{cm}^{-1}$ to achieve efficient transfer; however, the frequency difference should not exceed the highest available phonon frequency that accepts the excess energy. Furthermore, the transition

dipole moment of the acceptor mode should be large in order to favor interlayer transfer over VEP in the CO overlayer. Therefore, promising acceptor molecules are NO and OCS, both of which show strong infrared-active transitions that lie approx. 165 and 80 cm^{-1} below the $^{13}C^{18}O$ and $^{12}C^{16}O$ frequencies, respectively. The limited range of vibrations that can accept energy from CO can probably be extended by using other diatomic donor molecules. However, it is unclear how much of the transferred energy will be lost due to intramolecular vibrational energy redistribution (IVR) in polyatomic molecules and subsequent vibrational relaxation of their low-frequency modes to the crystal phonons, which needs to be addressed in future studies.

The coverage-dependent infrared absorption measurements, enabled by combining Fourier-transform infrared (FTIR) with temperature-programmed desorption (TPD) and molecular beam dosing, revisit the dynamics of the $v = 0 \rightarrow 1$ transition. With an extended semi-empirical model that describes the absorption strength of the collective vibrational exciton states that arise from dipole-dipole coupling between the CO oscillators, [117] the measured coverage dependence of the integrated absorbance can be described quantitatively. Furthermore, the integrated cross section ($\bar{\sigma}_z = (2.51 \pm 0.08) \times 10^{-17}$ cm/molecule) and the electronic polarizability ($\chi_e = (3.30 \pm 0.36)$ Å^3) along the bond-axis of an isolated CO adsorbate can both be determined independently. The cross section of an isolated CO molecule at the NaCl surface is 18 % lower than that of gas phase CO, which is consistent with a theoretical prediction based on the vibrational Stark effect in the CO/NaCl(100) monolayer. [182] The cross section of the CO monolayer is, however, significantly smaller than that of the isolated CO adsorbate, attributed to the dipole-dipole interactions between the CO molecules. [25]

Finally, I would like to emphasize that many of the reported mechanisms and phenomena that occur in the CO/NaCl(100) system can be explained by electrostatic interactions, in particular the dipole-dipole interactions between CO molecules. Therefore, I expect that these concepts apply to physisorbed molecules in general—not only to CO on NaCl(100). To repeat some of the aforementioned examples: vibrational or electronic state-dependent multipole moments are not uncommon and therefore different orientational isomers might be accessible for many physisorbed molecules. Another example is the controlled V-V energy transfer between different CO isotopologues that can be reduced to the interaction between their transition dipole moments and the fundamental frequency difference and should therefore apply to any suitable set of donor and acceptor vibrations. In conclusion, the present work not only advances the understanding of vibrational energy transfer in CO on NaCl(100), but also provides new opportunities for exploiting vibrational energy transfer in other physisorbed molecules.

Bibliography

[1] G. Ertl, Reactions at surfaces: From atoms to complexity (Nobel Lecture), *Angew. Chem. Int. Ed.* **47**, 3524–3535 (2008).

[2] G. B. Park, B. C. Krüger, D. Borodin, T. N. Kitsopoulos, and A. M. Wodtke, Fundamental mechanisms for molecular energy conversion and chemical reactions at surfaces, *Rep. Prog. Phys.* **82**, 096401 (2019).

[3] F. F. Crim, Vibrational state control of bimolecular reactions: discovering and directing the chemistry, *Acc. Chem. Res.* **32**, 877–884 (1999).

[4] R. N. Zare, Laser control of chemical reactions, *Science* **279**, 1875–1879 (1998).

[5] F. F. Crim, Chemical dynamics of vibrationally excited molecules: controlling reactions in gases and on surfaces, *Proc. Natl. Acad. Sci. U.S.A.* **105**, 12654–12661 (2008).

[6] H. Chadwick and R. D. Beck, Quantum state–resolved studies of chemisorption reactions, *Annu. Rev. Phys. Chem.* **68**, 39–61 (2017).

[7] A. L. Utz, Mode selective chemistry at surfaces, *Curr. Opin. Solid State Mater. Sci.* **13**, 4–12 (2009).

[8] L. Juurlink, D. Killelea, and A. Utz, State-resolved probes of methane dissociation dynamics, *Prog. Surf. Sci.* **84**, 69–134 (2009).

[9] M. Morin, N. J. Levinos, and A. L. Harris, Vibrational energy transfer of CO/Cu(100): Nonadiabatic vibration/electron coupling, *J. Chem. Phys.* **96**, 3950–3956 (1992).

[10] J. D. Beckerle, R. R. Cavanagh, M. P. Casassa, E. J. Heilweil, and J. C. Stephenson, Subpicosecond transient infrared spectroscopy of adsorbates. Vibrational dynamics of CO/Pt(111), *J. Chem. Phys.* **95**, 5403–5418 (1991).

[11] S. Kumar, H. Jiang, M. Schwarzer, A. Kandratsenka, D. Schwarzer, and A. M. Wodtke, Vibrational relaxation lifetime of a physisorbed molecule at a metal surface, *Phys. Rev. Lett.* **123**, 156101 (2019).

[12] K. Laß, X. Han, and E. Hasselbrink, The surprisingly short vibrational lifetime of the internal stretch of CO adsorbed on Si(100), *J. Chem. Phys.* **123**, 051102 (2005).

[13] K. Laß, X. Han, and E. Hasselbrink, Dynamics of the C–O stretch vibration on Si(100), *Surf. Sci.* **600**, 4275–4279 (2006).

[14] P. Guyot-Sionnest, P. Dumas, and Y. Chabal, Lifetime of an adsorbate-substrate vibration measured by sum frequency generation: H on Si(111), *J. Electron. Spectros. Relat. Phenomena* **54**, 27–38 (1990).

[15] P. Guyot-Sionnest, P. Dumas, Y. J. Chabal, and G. S. Higashi, Lifetime of an adsorbate-substrate vibration: H on Si(111), *Phys. Rev. Lett.* **64**, 2156–2159 (1990).

[16] H.-C. Chang and G. E. Ewing, Infrared fluorescence from a monolayer of CO on NaCl(100), *Phys. Rev. Lett.* **65**, 2125–2128 (1990).

[17] Y. Huang, C. T. Rettner, D. J. Auerbach, and A. M. Wodtke, Vibrational promotion of electron transfer, *Science* **290**, 111–114 (2000).

[18] Y. Chabal, Surface infrared spectroscopy, *Surf. Sci. Rep.* **8**, 211–357 (1988).

[19] Y. J. Chabal, M. A. Hines, and D. Feijóo, Characterization of silicon surfaces and interfaces by optical vibrational spectroscopy, *J. Vac. Sci. Technol. A* **13**, 1719–1727 (1995).

[20] L. Chen, J. A. Lau, D. Schwarzer, J. Meyer, V. B. Verma, and A. M. Wodtke, The Sommerfeld ground-wave limit for a molecule adsorbed at a surface, *Science* **363**, 158–161 (2019).

[21] G. E. Ewing, A model system for the study of structure and dynamics of molecules on surfaces: CO on NaCl(100), *Int. Rev. Phys. Chem.* **10**, 391–425 (1991).

[22] G. E. Ewing, Energy flow from excited molecules on salt surfaces, *Acc. Chem. Res.* **25**, 292–299 (1992).

[23] H.-C. Chang, C. Noda, and G. E. Ewing, CO on NaCl(100): Model system for investigating vibrational energy flow, *J. Vac. Sci. Technol. A* **8**, 2644–2648 (1990).

[24] H.-C. Chang and G. E. Ewing, The quantum efficiency of vibrationally induced desorption for a monolayer of CO on NaCl(100), *Chem. Phys.* **139**, 55–65 (1989).

[25] H. H. Richardson, H.-C. Chang, C. Noda, and G. E. Ewing, Infrared spectroscopy of CO on NaCl(100): I. Photometry, *Surf. Sci.* **216**, 93–104 (1989).

[26] C. Noda, H. H. Richardson, and G. E. Ewing, Infrared spectroscopy of CO on NaCl(100). II. Vibrational dephasing and band shapes, *J. Chem. Phys.* **92**, 2099–2105 (1990).

[27] H. C. Chang and G. E. Ewing, Vibrational energy transfer and population inversion in carbon monoxide overlayers on sodium chloride (100), *J. Phys. Chem.* **94**, 7635–7641 (1990).

[28] G. N. Gol'tsman, O. Okunev, G. Chulkova, A. Lipatov, A. Semenov, K. Smirnov, B. Voronov, A. Dzardanov, C. Williams, and R. Sobolewski, Picosecond superconducting single-photon optical detector, *Appl. Phys. Lett.* **79**, 705–707 (2001).

[29] C. M. Natarajan, M. G. Tanner, and R. H. Hadfield, Superconducting nanowire single-photon detectors: physics and applications, *Supercond. Sci. Technol.* **25**, 63001 (2012).

[30] M. D. Eisaman, J. Fan, A. Migdall, and S. V. Polyakov, Invited review article: single-photon sources and detectors, *Rev. Sci. Instrum.* **82**, 071101 (2011).

[31] L. Chen, D. Schwarzer, V. B. Verma, M. J. Stevens, F. Marsili, R. P. Mirin, S. W. Nam, and A. M. Wodtke, Mid-infrared laser-induced fluorescence with nanosecond time resolution using a superconducting nanowire single-photon detector: New technology for molecular science, *Acc. Chem. Res.* **50**, 1400–1409 (2017).

[32] R. Gevirzman, Y. Kozirovski, and M. Folman, Infra-red spectra and spectral shifts of CO adsorbed on evaporated alkali-halides. Part 1.—Films of sodium salts, *Trans. Faraday Soc.* **65**, 2206–2214 (1969).

[33] J. E. Gready, C. Bacskay, and N. Hush, Comparison of multipole moment expansions by direct summation or finite-field SCF methods with full electrostatic interaction energies: application to CO and N_2, *Chem. Phys.* **31**, 375–390 (1978).

[34] H. H. Richardson and G. E. Ewing, Infrared spectrum of carbon monoxide on sodium chloride(100), *J. Phys. Chem.* **91**, 5833–5835 (1987).

[35] M. Thomas, Untersuchungen von Monolagen und Submonolagen der Adsorbate CO-NaCl(001) und CO-KCl(001) in Transmissions- sowie ATR-Geometrie, PhD thesis (University of Hanover, 2000).

[36] J. Heidberg, E. Kampshoff, R. Kühnemuth, M. Suhren, and H. Weiss, Fourier-transform infrared spectra of CO adsorbed on NaCl(100): Structural changes at low temperatures, *Surf. Sci.* **269–270**, 128–134 (1992).

[37] C. Noda and G. E. Ewing, Infrared spectroscopy of CO on NaCl(100) III. Submonolayers and isotopic mixtures, *Surf. Sci.* **240**, 181–192 (1990).

[38] J. Heidberg, E. Kampshoff, and M. Suhren, Correlation field, structure, and phase transition in the monolayer CO adsorbed on NaCl(100) as revealed from polarization Fourier-transform infrared spectroscopy, *J. Chem. Phys.* **95**, 9408–9411 (1991).

[39]D. Schmicker, J. P. Toennies, R. Vollmer, and H. Weiss, Monolayer structures of carbon monoxide adsorbed on sodium chloride: A helium atom diffraction study, *J. Chem. Phys.* **95**, 9412–9415 (1991).

[40]J. Vogt and B. Vogt, The structure of carbon monoxide adsorbed on the NaCl(100) surface—A combined LEED and DFT-D/vdW-DF study, *J. Chem. Phys.* **141**, 214708 (2014).

[41]J. Heidberg, E. Kampshoff, R. Kühnemuth, O. Schönekäs, H. Stein, and H. Weiss, Site symmetry and correlation field splitting in the adsorbate CO_2-NaCl(100), *Surf. Sci.* **226**, L43–L47 (1990).

[42]A. S. Davydov, The theory of molecular excitons, *Sov. Phys. Usp.* **7**, 145–178 (1964).

[43]H.-C. Chang, H. H. Richardson, and G. E. Ewing, Epitaxial growth of CO on NaCl(100) studied by infrared spectroscopy, *J. Chem. Phys.* **89**, 7561–7568 (1988).

[44]J. Heidberg, M. Suhren, and H. Weiss, Growth of CO multilayers on the monolayer adsorbate CO/NaCl(100): A high resolution Fourier-transform infrared study, *J. Electron. Spectros. Relat. Phenomena* **64–65**, 227–234 (1993).

[45]I. Vegard, Struktur und Leuchtfähigkeit von festem Kohlenoxyd, *Z. Phys.* **61**, 185–190 (1930).

[46]E. K. Gill and J. A. Morrison, Thermodynamic properties of condensed CO, *J. Chem. Phys.* **45**, 1585–1590 (1966).

[47]G. E. Ewing and G. C. Pimentel, Infrared spectrum of solid carbon monoxide, *J. Chem. Phys.* **35**, 925–930 (1961).

[48]D. Fox and R. M. Hexter, Crystal shape dependence of exciton states in molecular crystals, *J. Chem. Phys.* **41**, 1125–1139 (1964).

[49]D. J. Nesbitt and R. W. Field, Vibrational energy flow in highly excited molecules: Role of intramolecular vibrational redistribution, *J. Phys. Chem.* **100**, 12735–12756 (1996).

[50]A. M. Wodtke, Electronically non-adiabatic influences in surface chemistry and dynamics, *Chem. Soc. Rev.* **45**, 3641–3657 (2016).

[51]P. R. Shirhatti, I. Rahinov, K. Golibrzuch, J. Werdecker, J. Geweke, J. Altschäffel, S. Kumar, D. J. Auerbach, C. Bartels, and A. M. Wodtke, Observation of the adsorption and desorption of vibrationally excited molecules on a metal surface, *Nat. Chem.* **10**, 592–598 (2018).

[52]D. M. Roessler and W. C. Walker, Electronic spectra of crystalline NaCl and KCl, *Phys. Rev.* **166**, 599–606 (1968).

[53]W. H. Strehlow and E. L. Cook, Compilation of energy band gaps in elemental and binary compound semiconductors and insulators, *J. Phys. Chem. Ref. Data* **2**, 163–200 (1973).

[54]P. Saalfrank, Quantum dynamical approach to ultrafast molecular desorption from surfaces, *Chem. Rev.* **106**, 4116–4159 (2006).

[55]S. Sakong, P. Kratzer, X. Han, K. Laß, O. Weingart, and E. Hasselbrink, Density-functional theory study of vibrational relaxation of CO stretching excitation on Si(100), *J. Chem. Phys.* **129**, 174702 (2008).

[56]P. N. M. Hoang, S. Picaud, C. Girardet, and A. W. Meredith, Structure of CO monolayer adsorbed on NaCl(100) from molecular dynamics, *J. Chem. Phys.* **105**, 8453–8462 (1996).

[57]S. A. Corcelli and J. C. Tully, Vibrational energy pooling in CO on NaCl(100): Methods, *J. Chem. Phys.* **116**, 8079–8092 (2002).

[58]S. A. Corcelli, Vibrations and rare events in the condensed phase, PhD thesis (Yale University, 2002).

[59]R. R. Chance, A. Prock, and R. Silbey, Molecular fluorescence and energy transfer near interfaces, *Adv. Chem. Phys.* **37**, 1–65 (1978).

[60]S. A. Egorov and J. L. Skinner, On the theory of multiphonon relaxation rates in solids, *J. Chem. Phys.* **103**, 1533–1543 (1995).

[61]E. T. D. Boney and R. A. Marcus, On the infrared fluorescence of monolayer ^{13}CO:NaCl(100), *J. Chem. Phys.* **139**, 184712 (2013).

[62]R. R. Chance, A. Prock, and R. Silbey, Lifetime of an emitting molecule near a partially reflecting surface, *J. Chem. Phys.* **60**, 2744–2748 (1974).

[63]R. R. Chance, A. Prock, and R. Silbey, Lifetime of an excited molecule near a metal mirror: Energy transfer in the Eu_3^+/silver system, *J. Chem. Phys.* **60**, 2184–2185 (1974).

[64]R. R. Chance, A. Prock, and R. Silbey, Comments on the classical theory of energy transfer, *J. Chem. Phys.* **62**, 2245–2253 (1975).

[65]K. H. Drexhage, M. Fleck, H. Kuhn, F. P. Schäfer, and W. Sperling, Beeinflussung der Fluoreszenz eines Europiumchelates durch einen Spiegel, *Ber. Bunsenges. Phys. Chem.* **70**, 1179 (1966).

[66] H. Kuhn, Energieübertragung in monomolekularen Schichten, *Naturwissenschaften* **54**, 429–435 (1967).

[67] H. Kuhn, Classical aspects of energy transfer in molecular systems, *J. Chem. Phys.* **53**, 101–108 (1970).

[68] K.-H. Tews, O. Inacker, and H. Kuhn, Variation of the luminescence lifetime of a molecule near an interface between differently polarizable dielectrics, *Nature* **228**, 276–278 (1970).

[69] A. Sommerfeld, Über die Ausbreitung der Wellen in der drahtlosen Telegraphie, *Ann. Phys.* **333**, 665–736 (1909).

[70] L. E. Brus, Application of classical electromagnetic theory to an understanding of molecular vibrational energy transfer into metal surfaces, *J. Chem. Phys.* **73**, 940–945 (1980).

[71] L. E. Brus, Long range vibrational energy transfer to dielectric surfaces, *J. Chem. Phys.* **74**, 737–743 (1981).

[72] D. Waldeck, A. Alivisatos, and C. Harris, Nonradiative damping of molecular electronic excited states by metal surfaces, *Surf. Sci.* **158**, 103–125 (1985).

[73] E. D. Palik, Potassium chloride (KCl), in *Handbook of optical constants of solids*, edited by E. D. Palik (Academic Press, Burlington, 1997), pp. 703–718.

[74] C. E. Treanor, J. W. Rich, and R. G. Rehm, Vibrational relaxation of anharmonic oscillators with exchange-dominated collisions, *J. Chem. Phys.* **48**, 1798–1807 (1968).

[75] J. W. Rich, R. C. Bergman, and J. W. Raymonda, Vibration-vibration pumping of carbon monoxide initiated by an optical source, *Appl. Phys. Lett.* **27**, 656–658 (1975).

[76] J. Rich and R. C. Bergman, C_2 and CN formation by optical pumping of CO/Ar and CO/N_2/Ar mixtures at room temperature, *Chem. Phys.* **44**, 53–64 (1979).

[77] R. C. Bergman, G. F. Homicz, J. W. Rich, and G. L. Wolk, ^{13}C and ^{18}O isotope enrichment by vibrational energy exchange pumping of CO, *J. Chem. Phys.* **78**, 1281–1292 (1983).

[78] H. Dünnwald, E. Seigel, W. Urban, J. Rich, G. Homicz, and M. Williams, Anharmonic vibration-vibration pumping in nitric oxide by resonant IR-laser irradiation, *Chem. Phys.* **94**, 195–213 (1985).

[79] R. L. DeLeon and J. Rich, Vibrational energy exchange rates in carbon monoxide, *Chem. Phys.* **107**, 283–292 (1986).

[80] H. Dubost and R. Charneau, Laser studies of vibrational energy transfer and relaxation of CO trapped in solid neon and argon, *Chem. Phys.* **12**, 407–418 (1976).

[81] H. Dubost and R. Charneau, Role of vibrational energy migration upon V→V transfer in matrix isolated CO, *Chem. Phys.* **41**, 329–343 (1979).

[82] N. Legay-Sommaire and F. Legay, Observation of a strong vibrational population inversion by CO laser excitation of pure solid carbon monoxide, *IEEE J. Quantum Electron.* **16**, 308–314 (1980).

[83] N. Legay-Sommaire and F. Legay, Analysis of the infrared emission and absorption spectra from isotopic CO molecules in solid α-CO, *Chem. Phys.* **66**, 315–325 (1982).

[84] D. S. Anex and G. E. Ewing, Transfer and storage of vibrational energy in liquids: Collisional up-pumping of carbon monoxide in liquid argon, *J. Phys. Chem.* **90**, 1604–1610 (1986).

[85] K. A. Essenhigh, Y. G. Utkin, C. Bernard, I. V. Adamovich, and J. W. Rich, Gas-phase Boudouard disproportionation reaction between highly vibrationally excited CO molecules, *Chem. Phys.* **330**, 506–514 (2006).

[86] A. Serdyuchenko, E. Mintusov, K. Frederickson, W. Lempert, J. Rich, and I. Adamovich, Isotope effect in Boudouard disproportionation reaction in optically pumped CO, *Chem. Phys.* **363**, 24–32 (2009).

[87] S. A. Corcelli and J. C. Tully, Vibrational Energy Pooling in CO on NaCl(100): Simulation and Isotope Effects, *J. Phys. Chem. A* **106**, 10849–10860 (2002).

[88] E. T. D. Boney and R. A. Marcus, Theory of vibrational equilibria and pooling at solid-diatom interfaces, *J. Chem. Phys.* **139**, 124107 (2013).

[89] R. N. Zare, My Life with LIF: A Personal Account of Developing Laser-Induced Fluorescence, *Annu. Rev. Anal. Chem.* **5**, 1–14 (2012).

[90] B. E. A. Saleh and M. C. Teich, *Fundamentals of Photonics*, 2nd Edition (John Wiley & Sons, Inc., Hoboken, 2007).

[91] R. C. Hilborn, Einstein coefficients, cross sections, f values, dipole moments, and all that, *Am. J. Phys.* **50**, 982–986 (1982).

[92] W. Demtröder, *Laserspektroskopie 1*, 6th Edition (Berlin, Heidelberg, 2011).

[93] L. Chen, D. Schwarzer, J. A. Lau, V. B. Verma, M. J. Stevens, F. Marsili, R. P. Mirin, S. W. Nam, and A. M. Wodtke, Ultra-sensitive mid-infrared emission spectrometer with sub-ns temporal resolution, *Opt. Express* **26**, 14859–14868 (2018).

[94]B. Korzh, Q.-Y. Zhao, J. P. Allmaras, S. Frasca, T. M. Autry, E. A. Bersin, A. D. Beyer, R. M. Briggs, B. Bumble, M. Colangelo, G. M. Crouch, A. E. Dane, T. Gerrits, A. E. Lita, F. Marsili, G. Moody, C. Peña, E. Ramirez, J. D. Rezac, N. Sinclair, M. J. Stevens, A. E. Velasco, V. B. Verma, E. E. Wollman, S. Xie, D. Zhu, P. D. Hale, M. Spiropulu, K. L. Silverman, R. P. Mirin, S. W. Nam, A. G. Kozorezov, M. D. Shaw, and K. K. Berggren, Demonstration of sub-3 ps temporal resolution with a superconducting nanowire single-photon detector, *Nat. Photonics* **14**, 250–255 (2020).

[95]V. B. Verma, B. Korzh, F. Bussières, R. D. Horansky, S. D. Dyer, A. E. Lita, I. Vayshenker, F. Marsili, M. D. Shaw, H. Zbinden, R. P. Mirin, and S. W. Nam, High-efficiency superconducting nanowire single-photon detectors fabricated from MoSi thin-films, *Opt. Express* **23**, 33792–33801 (2015).

[96]D. V. Reddy, R. R. Nerem, S. W. Nam, R. P. Mirin, and V. B. Verma, Superconducting nanowire single-photon detectors with 98% system detection efficiency at 1550 nm, *Optica* **7**, 1649–1653 (2020).

[97]B. Baek, A. E. Lita, V. Verma, and S. W. Nam, Superconducting a-W_xSi_{1-x} nanowire single-photon detector with saturated internal quantum efficiency from visible to 1850 nm, *Appl. Phys. Lett.* **98**, 251105 (2011).

[98]F. Marsili, V. B. Verma, J. A. Stern, S. Harrington, A. E. Lita, T. Gerrits, I. Vayshenker, B. Baek, M. D. Shaw, R. P. Mirin, and S. W. Nam, Detecting single infrared photons with 93% system efficiency, *Nat. Photonics* **7**, 210–214 (2013).

[99]V. B. Verma, B. Korzh, F. Bussières, R. D. Horansky, A. E. Lita, F. Marsili, M. D. Shaw, H. Zbinden, R. P. Mirin, and S. W. Nam, High-efficiency WSi superconducting nanowire single-photon detectors operating at 2.5 K, *Appl. Phys. Lett.* **105**, 122601 (2014).

[100]E. E. Wollman, V. B. Verma, A. E. Lita, W. H. Farr, M. D. Shaw, R. P. Mirin, and S. W. Nam, Kilopixel array of superconducting nanowire single-photon detectors, *Opt. Express* **27**, 35279–35289 (2019).

[101]J. A. C. Gallas, Some matrix elements for morse oscillators, *Phys. Rev. A* **21**, 1829–1834 (1980).

[102]P. M. Morse, Diatomic molecules according to the wave mechanics. II. Vibrational levels, *Phys. Rev.* **34**, 57–64 (1929).

[103]J. I. Steinfeld, *Molecules and Radiation: An Introduction to Modern Molecular Spectroscopy*, 2nd Edition (MIT Press, Cambridge, 1985).

168

[104] M. Born and E. Wolf, *Principles of Optics*, 7th Edition (Cambridge University Press, Cambridge, 1999).

[105] J. Heidberg, A. Voßberg, M. Hustedt, M. Thomas, S. Briquez, S. Picaud, and C. Girardet, Monolayers of ortho-H2, para-H2, para-D2 and normal-H2 adsorbed on NaCl(001) single crystal surfaces, *J. Chem. Phys.* **110**, 2566–2578 (1999).

[106] R. Durman, U. A. Jayasooriya, S. F. A. Kettle, S. Mahasuverachai, R. Mortimer, and L.-J. Norrby, Factor group splitting and dispersion on internal vibrational modes: A qualitative discussion, *J. Chem. Phys.* **81**, 5247–5251 (1984).

[107] D. J. Dai and G. E. Ewing, Vibrational overtone spectroscopy and coupling effects in monolayer CO on NaCl(100), *Surf. Sci.* **312**, 239–249 (1994).

[108] R. Disselkamp, H.-C. Chang, and G. E. Ewing, Infrared spectroscopy of CO on NaCl(100) IV. Bandshape analysis, *Surf. Sci.* **240**, 193–210 (1990).

[109] H. Pfnür, D. Menzel, F. Hoffmann, A. Ortega, and A. Bradshaw, High resolution vibrational spectroscopy of CO on Ru(001): The importance of lateral interactions, *Surf. Sci.* **93**, 431–452 (1980).

[110] R. Hammaker, S. Francis, and R. Eischens, Infrared study of intermolecular interactions for carbon monoxide chemisorbed on platinum, *Spectrochim. Acta* **21**, 1295–1309 (1965).

[111] R. Ryberg, Carbon monoxide adsorbed on Cu(100) studied by infrared spectroscopy, *Surf. Sci.* **114**, 627–641 (1982).

[112] B. Persson and R. Ryberg, Collective vibrational modes in isotopic mixtures of CO adsorbed on Cu(100), *Solid State Commun.* **36**, 613–617 (1980).

[113] A. Crossley and D. A. King, Infrared spectra for co isotopes chemisorbed on Pt {111}: Evidence for strong absorbate coupling interactions, *Surf. Sci.* **68**, 528–538 (1977).

[114] B. N. J. Persson and R. Ryberg, Vibrational interaction between molecules adsorbed on a metal surface: the dipole-dipole interaction, *Phys. Rev. B* **24**, 6954–6970 (1981).

[115] G. D. Mahan and A. A. Lucas, Collective vibrational modes of adsorbed CO, *J. Chem. Phys.* **68**, 1344–1348 (1978).

[116] B. N. J. Persson, F. M. Hoffmann, and R. Ryberg, Influence of exciton motion on the shape of optical absorption lines: Applications to vibrations at surfaces, *Phys. Rev. B* **34**, 2266–2283 (1986).

[117] A. V. Snigur and V. M. Rozenbaum, Davydov splitting of vibrational spectra of adsorbates, *Opt. Spectrosc.* **95**, 685–689 (2003).

[118] V. Rozenbaum, Davydov splitting in the vibration spectrum for a system of inclined-oriented dipoles on a square lattice, *Phys. Lett. A* **176**, 249–253 (1993).

[119] V. M. Rozenbaum, Lateral interactions of adsorbed molecules, *J. Exp. Theor. Phys.* **80**, 289–295 (1995).

[120] A. W. Meredith and A. J. Stone, A perturbation theory study of adlayer CO on NaCl(100), *J. Chem. Phys.* **104**, 3058–3070 (1996).

[121] S. Picaud, P. Hoang, C. Girardet, A. Meredith, and A. Stone, Theoretical study of the monolayer structures of CO adsorbed on NaCl(100), *Surf. Sci.* **294**, 149–160 (1993).

[122] A. Stone, *The Theory of Intermolecular Forces*, 2nd Edition (Oxford University Press, Oxford, 2013).

[123] A. D. Buckingham, Permanent and induced molecular moments and long-range intermolecular forces, in *Advances in Chemical Physics: Intermolecular Forces, Volume 12*, edited by J. O. Hirschfelder (John Wiley & Sons, Ltd, 1967), pp. 107–142.

[124] C. Hättig and B. A. Heß, Calculation of orientation-dependent double-tensor moments for coulomb-type intermolecular interactions, *Mol. Phys.* **81**, 813–824 (1994).

[125] H.-J. Chen, J. Wu, H. Liu, and X.-L. Cheng, Electric dipole moment function and line intensities for the ground state of carbon monoxide, *Chin. Phys. B* **24**, 083102 (2015).

[126] J. A. Lau, A. Choudhury, L. Chen, D. Schwarzer, V. B. Verma, and A. M. Wodtke, Observation of an isomerizing double-well quantum system in the condensed phase, *Science* **367**, 175–178 (2020).

[127] I. Gordon, L. Rothman, C. Hill, R. Kochanov, Y. Tan, P. Bernath, M. Birk, V. Boudon, A. Campargue, K. Chance, B. Drouin, J.-M. Flaud, R. Gamache, J. Hodges, D. Jacquemart, V. Perevalov, A. Perrin, K. Shine, M.-A. Smith, J. Tennyson, G. Toon, H. Tran, V. Tyuterev, A. Barbe, A. Császár, V. Devi, T. Furtenbacher, J. Harrison, J.-M. Hartmann, A. Jolly, T. Johnson, T. Karman, I. Kleiner, A. Kyuberis, J. Loos, O. Lyulin, S. Massie, S. Mikhailenko, N. Moazzen-Ahmadi, H. Müller, O. Naumenko, A. Nikitin, O. Polyansky, M. Rey, M. Rotger, S. Sharpe, K. Sung, E. Starikova, S. Tashkun, J. V. Auwera, G. Wagner, J. Wilzewski, P. Wcisło, S. Yu, and E. Zak, The HITRAN2016 molecular spectroscopic database, *J. Quant. Spectrosc. Radiat. Transf.* **203**, 3–69 (2017).

[128] J. Estel, H. Hoinkes, H. Kaarmann, H. Nahr, and H. Wilsch, On the problem of water adsorption on alkali halide cleavage planes, investigated by secondary ion mass spectroscopy, *Surf. Sci.* **54**, 393–418 (1976).

[129] J. Heidberg, M. Grunwald, M. Hustedt, and F. Traeger, High-resolution PIRSS using a tunable infrared diode laser: The Davydov doublet of the antiferroelectric (2×1) monolayer CO adsorbed on NaCl(001), *Surf. Sci.* **368**, 126–132 (1996).

[130] J. A. Lau, L. Chen, A. Choudhury, D. Schwarzer, V. B. Verma, and A. M. Wodtke, Transporting and concentrating vibrational energy to promote isomerization, *Nature* **589**, 391–395 (2021).

[131] K. P. Huber and G. Herzberg, *Molecular spectra and molecular structure IV. Constants of diatomic molecules* (Van Nostrand Reinhold, 1979).

[132] J. Meyer, private communication, 2019.

[133] M. Grunwald and G. E. Ewing, A two-dimensional quantum crystal: H_2 on NaCl(100), *J. Chem. Phys.* **109**, 4990–4996 (1998).

[134] H. H. Richardson and T. L. McDonald, Infrared spectroscopy of submonolayer N_2 on NaCl films, *J. Electron. Spectros. Relat. Phenomena* **54-55**, 1003–1012 (1990).

[135] J. Eldridge and E. D. Palik, Sodium chloride (NaCl), in *Handbook of optical constants of solids*, edited by E. D. Palik (Academic Press, Burlington, 1997), pp. 775–793.

[136] T. Todd, C. Clayton, W. Telfair, T. McCubbin, and J. Plíva, Infrared emission of $^{12}C^{16}O$, $^{13}C^{16}O$, and $^{12}C^{18}O$, *J. Mol. Spectrosc.* **62**, 201–227 (1976).

[137] A. Staib and J. T. Hynes, Vibrational predissociation in hydrogen-bonded OH. . . O complexes via OH stretch-OO stretch energy transfer, *Chem. Phys. Lett.* **204**, 197–205 (1993).

[138] A. D. Boese and P. Saalfrank, CO molecules on a NaCl(100) surface: Structures, energetics, and vibrational Davydov splittings at various coverages, *J. Phys. Chem. C* **120**, 12637–12653 (2016).

[139] R. D. Amos, SCF and CI calculations of the one-electron properties of carbon monoxide as a function of internuclear distance, *Chem. Phys. Lett.* **68**, 536–539 (1979).

[140] R. D. Amos, A configuration-interaction study of the polarizability derivatives of carbon monoxide, *Chem. Phys. Lett.* **70**, 613–617 (1980).

[141] G. Maroulis, On the electric multipole moments of carbon monoxide, *Z. Naturforsch.* **47a**, 480–484 (1992).

[142] J. Chen, S. Hariharan, J. Meyer, and H. Guo, Potential energy landscape of CO adsorbates on NaCl(100) and implications in isomerization of vibrationally excited CO, *J. Phys. Chem. C* **124**, 19146–19156 (2020).

171

[143] A. Choudhury, unpublished results.

[144] T. R. Dyke, B. J. Howard, and W. Klemperer, Radiofrequency and microwave spectrum of the hydrogen fluoride dimer; a nonrigid molecule, *J. Chem. Phys.* **56**, 2442–2454 (1972).

[145] H. Ishikawa, R. W. Field, S. C. Farantos, M. Joyeux, J. Koput, C. Beck, and R. Schinke, HCP↔CPH isomerization: Caught in the act, *Annu. Rev. Phys. Chem.* **50**, 443–484 (1999).

[146] M. Joyeux, S. C. Farantos, and R. Schinke, Highly excited motion in molecules: Saddle-node bifurcations and their fingerprints in vibrational spectra, *J. Phys. Chem. A* **106**, 5407–5421 (2002).

[147] X. Yang, C. A. Rogaski, and A. M. Wodtke, Vibrational structure of hydrogen cyanide up to 18900 cm^{-1}, *J. Opt. Soc. Am. B* **7**, 1835–1850 (1990).

[148] D. M. Jonas, X. Yang, and A. M. Wodtke, Axis-switching transitions and the stimulated emission pumping spectrum of HCN, *J. Chem. Phys.* **97**, 2284–2298 (1992).

[149] J. M. Bowman, B. Gazdy, J. A. Bentley, T. J. Lee, and C. E. Dateo, Ab initio calculation of a global potential, vibrational energies, and wave functions for HCN/HNC, and a simulation of the $\tilde{A} - \tilde{X}$ emission spectrum, *J. Chem. Phys.* **99**, 308–323 (1993).

[150] Y. Chen, D. M. Jonas, J. L. Kinsey, and R. W. Field, High resolution spectroscopic detection of acetylene-vinylidene isomerization by spectral cross correlation, *J. Chem. Phys.* **91**, 3976–3987 (1989).

[151] M. P. Jacobson and R. W. Field, Acetylene at the threshold of isomerization, *J. Phys. Chem. A* **104**, 3073–3086 (2000).

[152] J. A. DeVine, M. L. Weichman, B. Laws, J. Chang, M. C. Babin, G. Balerdi, C. Xie, C. L. Malbon, W. C. Lineberger, D. R. Yarkony, R. W. Field, S. T. Gibson, J. Ma, H. Guo, and D. M. Neumark, Encoding of vinylidene isomerization in its anion photoelectron spectrum, *Science* **358**, 336–339 (2017).

[153] M. Pettersson, J. Lundell, L. Khriachtchev, and M. Räsänen, IR spectrum of the other rotamer of formic acid, *cis*-HCOOH, *J. Am. Chem. Soc.* **119**, 11715–11716 (1997).

[154] M. Pettersson, E. M. S. Maçôas, L. Khriachtchev, J. Lundell, R. Fausto, and M. Räsänen, *Cis→trans* conversion of formic acid by dissipative tunneling in solid rare gases: Influence of environment on the tunneling rate, *J. Chem. Phys.* **117**, 9095–9098 (2002).

[155] K. Marushkevich, L. Khriachtchev, and M. Räsänen, High-energy conformer of formic acid in solid neon: Giant difference between the proton tunneling rates of *cis* monomer and *trans-cis* dimer, *J. Chem. Phys.* **126**, 241102 (2007).

[156] A. Domanskaya, K. Marushkevich, L. Khriachtchev, and M. Räsänen, Spectroscopic study of *cis*-to-*trans* tunneling reaction of HCOOD in rare gas matrices, *J. Chem. Phys.* **130**, 154509 (2009).

[157] M. Pettersson, J. Lundell, L. Khriachtchev, and M. Räsänen, Neutral rare-gas containing charge-transfer molecules in solid matrices. III. HXeCN, HXeNC, and HKrCN in Kr and Xe, *J. Chem. Phys.* **109**, 618–625 (1998).

[158] S. Zou and J. M. Bowman, Full dimensionality quantum calculations of acetylene/vinylidene isomerization, *J. Chem. Phys.* **117**, 5507–5510 (2002).

[159] M. Drabbels and A. M. Wodtke, The determination of the infrared radiative lifetimes of a vibrationally excited neutral molecule using stimulated-emission-pumping, molecular-beam time-of-flight, *J. Chem. Phys.* **106**, 3024–3028 (1997).

[160] W. T. Rawlins, J. C. Person, M. E. Fraser, S. M. Miller, and W. A. M. Blumberg, The dipole moment and infrared transition strengths of nitric oxide, *J. Chem. Phys.* **109**, 3409–3417 (1998).

[161] B. G. Wicke, R. W. Field, and W. Klemperer, Fine structure, dipole moment, and perturbation analysis of $a\ ^3\Pi$ CO, *J. Chem. Phys.* **56**, 5758–5770 (1972).

[162] J. Chen, J. Li, J. M. Bowman, and H. Guo, Energy transfer between vibrationally excited carbon monoxide based on a highly accurate six-dimensional potential energy surface, *J. Chem. Phys.* **153**, 054310 (2020).

[163] A. Nandi, P. Zhang, J. Chen, H. Guo, and J. M. Bowman, Quasiclassical simulations based on cluster models reveal vibration-facilitated roaming in the isomerization of CO adsorbed on NaCl, *Nat. Chem.* **13**, 249–254 (2021).

[164] S. Sinha and P. Saalfrank, "Inverted" CO molecules on NaCl(100): A quantum mechanical study, *Phys. Chem. Chem. Phys.*, DOI: 10.1039/D0CP05198E (2020).

[165] A. G. Suits, Roaming atoms and radicals: A new mechanism in molecular dissociation, *Acc. Chem. Res.* **41**, 873–881 (2008).

[166] J. M. Bowman and B. C. Shepler, Roaming radicals, *Annu. Rev. Phys. Chem.* **62**, 531–553 (2011).

[167] G. J. Jiang, W. B. Person, and K. G. Brown, Absolute infrared intensities and band shapes in pure solid CO and CO in some solid matrices, *J. Chem. Phys.* **62**, 1201–1211 (1975).

[168] G. D. Scholes, G. R. Fleming, A. Olaya-Castro, and R. van Grondelle, Lessons from nature about solar light harvesting, *Nat. Chem.* **3**, 763–774 (2011).

[169] T. Brixner, J. Stenger, H. M. Vaswani, M. Cho, R. E. Blankenship, and G. R. Fleming, Two-dimensional spectroscopy of electronic couplings in photosynthesis, *Nature* **434**, 625–628 (2005).

[170] T. Förster, Energiewanderung und Fluoreszenz, *Naturwissenschaften* **33**, 166–175 (1946).

[171] T. Förster, Zwischenmolekulare Energiewanderung und Fluoreszenz, *Ann. Phys.* **437**, 55–75 (1948).

[172] T. Shimanouchi, Molecular vibrational frequencies, in *NIST Chemistry WebBook, NIST Standard Reference Database Number 69*, edited by P. J. Linstrom and W. G. Mallard (National Institute of Standards and Technology, Gaithersburg MD, 20899), retrieved December 21, 2020.

[173] B. H. Mahan, Microscopic reversibility and detailed balance. An analysis, *J. Chem. Educ.* **52**, 299–302 (1975).

[174] M. Berggren, A. Dodabalapur, R. E. Slusher, and Z. Bao, Light amplification in organic thin films using cascade energy transfer, *Nature* **389**, 466–469 (1997).

[175] J. Kim, D. T. McQuade, A. Rose, Z. Zhu, and T. M. Swager, Directing energy transfer within conjugated polymer thin films, *J. Am. Chem. Soc.* **123**, 11488–11489 (2001).

[176] C. R. Kagan, C. B. Murray, and M. G. Bawendi, Long-range resonance transfer of electronic excitations in close-packed CdSe quantum-dot solids, *Phys. Rev. B* **54**, 8633–8643 (1996).

[177] S. A. Crooker, J. A. Hollingsworth, S. Tretiak, and V. I. Klimov, Spectrally resolved dynamics of energy transfer in quantum-dot assemblies: Towards engineered energy flows in artificial materials, *Phys. Rev. Lett.* **89**, 186802 (2002).

[178] J. A. Lau, A.-M. Schönemann, D. Schwarzer, and A. M. Wodtke, The coverage dependence of the infrared absorption of CO adsorbed to NaCl(100), *J. Chem. Phys.* **153**, 154703 (2020).

[179] D. P. Engelhart, R. J. Wagner, A. Meling, A. M. Wodtke, and T. Schäfer, Temperature programmed desorption of weakly bound adsorbates on Au(111), *Surf. Sci.* **650**, 11–16 (2016).

[180] J. Heidberg, H. Stein, and I. Hussla, Infrared cryospectroscopic study of CO-NaCl adsorbates: Detection of surface diffusion at 25 and 40 K, *Surf. Sci.* **162**, 470–477 (1985).

[181] P. Varanasi and S. Sarangi, Measurements of intensities and nitrogen-broadened linewidths in the CO fundamental at low temperatures, *J. Quant. Spectrosc. Radiat. Transf.* **15**, 473–482 (1975).

[182] D. K. Lambert, G. P. M. Poppe, and C. M. J. Wijers, Vibrational Stark effect of CO on NaCl(100), *J. Chem. Phys.* **103**, 6206–6216 (1995).

[183] Y. N. Kalugina and V. N. Cherepanov, Multipole electric moments and higher polarizabilities of molecules: Methodology and some results of ab initio calculations, *Atmospheric Ocean. Opt.* **28**, 406–414 (2015).

[184] G. P. M. Poppe, C. M. J. Wijers, and A. van Silfhout, IR spectroscopy of CO physisorbed on NaCl(100): Microscopic treatment, *Phys. Rev. B* **44**, 7917–7929 (1991).

[185] G. Poppe, C. Wijers, and A. van Silfhout, Microscopic treatment of the IR spectroscopy of CO physisorbed on NaCl(100), *Surf. Sci.* **251-252**, 321–324 (1991).

[186] K. A. Fichthorn and W. H. Weinberg, Theoretical foundations of dynamical Monte Carlo simulations, *J. Chem. Phys.* **95**, 1090–1096 (1991).

[187] J. Heidberg, E. Kampshoff, O. Schönekäs, H. Stein, and H. Weiss, Correlation field splitting in a two-dimensional phase: CO_2 adsorbed on the NaCl(100) cleavage plane, *Ber. Bunsenges. Phys. Chem.* **94**, 112–118 (1990).

[188] J. E. Lennard-Jones and B. M. Dent, Cohesion at a crystal surface, *Trans. Faraday Soc.* **24**, 92–108 (1928).

[189] J. R. Rumble, ed., *CRC Handbook of Chemistry and Physics*, 101st Edition (Internet Version 2020) (CRC Press/Taylor & Francis, Boca Raton, FL).

[190] A. D. Buckingham, Molecular quadrupole moments, *Q. Rev. Chem. Soc.* **13**, 183–214 (1959).

[191] J. M. Parnis, M. G. K. Thompson, and L. M. Ashenhurst, Matrix isolation of electron bombarded gases containing Fe(CO)5: An FTIR absorption study of neutral and anion decomposition products, *J. Phys. Chem. A* **107**, 7390–7395 (2003).

[192] C. H. F. Peden, S. F. Parker, P. H. Barrett, and R. G. Pearson, Moessbauer and infrared studies of matrix-isolated iron-carbonyl complexes, *J. Phys. Chem.* **87**, 2329–2336 (1983).

[193] P. Portius, M. Bühl, M. W. George, F.-W. Grevels, and J. J. Turner, Structure and dynamics of iron pentacarbonyl, *Organometallics* **38**, 4288–4297 (2019).

[194]S. Tashkun, V. Perevalov, R. Gamache, and J. Lamouroux, CDSD-296, High-resolution carbon dioxide spectroscopic databank: An update, *J. Quant. Spectrosc. Radiat. Transf.* **228**, 124–131 (2019).

Normalized field intensity component for s-polarized light

This appendix contains the derivation of the normalized field intensity component, T_y, in the three-layer model, which is relevant to describe the effective electric field of s-polarized light at the interface relative to the electric field in vacuum. The presented derivation was published in Ref. [178]

Based on the three-layer model of Richardson *et al.*, [25] Chabal derived the following expression for the transmittance of p-polarized light with the wavelength λ: [19]

$$\frac{I}{I_0} = 1 - \frac{2\pi d}{\lambda} \frac{1}{n_1 \cos(\theta_1)} \left[T_x \operatorname{Im}(\epsilon_2) + T_z \operatorname{Im}\left(-\frac{n_1^4}{\epsilon_2} \right) \right]. \tag{A.1}$$

For a definition of the angles, θ_j, and the dielectric constants, ϵ_j, of the three media, see Fig. 2.5 (Section 2.4.2). T_x and T_z are the field intensity components relevant to p-polarization (see Eqs. 2.55 and 2.56). According to Ref. [25], d can be interpreted as an effective, optical thickness , whereas $d_x = d_y = d \operatorname{Im}(\epsilon_2)$ and $d_z = d \operatorname{Im}(-1/\epsilon_2)$ describe the effective thickness in the surface plane and perpendicular to the surface plane of the absorbing medium, respectively.

To derive a similar expression as in Eq. A.1 for s-polarized light, the intermediate result for the ratio of the transmission coefficients with and without the absorbing film,

t/t_0, for s-polarized light in Ref. [25] is used:

$$\frac{t}{t_0} = 1 + i\frac{2\pi}{\lambda}\epsilon_2^{1/2}d\cos(\theta_2)\left(1 - \frac{2r_{12}^{\rm s}r_{23}^{\rm s}}{1 + r_{12}^{\rm s}r_{23}^{\rm s}}\right), \tag{A.2}$$

$$r_{jk}^{\rm s} = \frac{p_j - p_k}{p_j + p_k}, \tag{A.3}$$

$$p_j = \epsilon_j^{1/2}\cos(\theta_j). \tag{A.4}$$

With the definitions in Eqs. A.3 and A.4, Eq. A.2 can be rewritten as:

$$\frac{t}{t_0} = 1 + i\frac{2\pi d}{\lambda}\left(\frac{p_2^2 + p_1 p_3}{p_1 + p_3}\right) \tag{A.5}$$

The transmittance, I/I_0 is related to t/t_0 by:

$$\frac{I}{I_0} = \left|\frac{t}{t_0}\right|^2 \approx 1 - \frac{4\pi d}{\lambda}\left(\frac{p_2^2 + p_1 p_3}{p_1 + p_3}\right) = 1 - \frac{4\pi d}{\lambda}\left(\frac{p_2^2}{p_1 + p_3}\right). \tag{A.6}$$

Here, it is assumed that the effective thickness, d, is small compared to the wavelength such that quadratic terms in d/λ can be neglected.[1] Furthermore, the $p_1 p_3/(p_1 + p_3)$ term can be neglected because p_1 and p_3, characterizing the two non-absorbing media, are real-valued and their imaginary part is zero.

A generalized form of Snell's law relates p_2 and p_3 in Eq. A.6 to the incidence angle, θ_1, and the refractive index, n_1, of the first medium: [25]

$$\epsilon_j\cos^2(\theta_j) = \epsilon_j - n_1^2\sin^2(\theta_1). \tag{A.7}$$

With Eq. A.7, Eq. A.6 can be written in a similar form as Eq. A.1, showing that the transmittance of s-polarized light and the corresponding T_y term are given by:

$$\frac{I}{I_0} = 1 - \frac{2\pi d}{\lambda}\frac{1}{n_1\cos(\theta_1)}\left[T_y\,{\rm Im}(\epsilon_2)\right], \tag{A.8}$$

$$T_y = \frac{2}{1 + (n_3/n_1)/\cos(\theta_1)\sqrt{1 - (n_1/n_3)^2\sin^2(\theta_1)}}. \tag{A.9}$$

---

[1] More generally, $|1 + iz|^2 = 1 - 2\,{\rm Im}(z) + |z|^2$, where z is a complex number.

Kinetic Monte Carlo simulations

The rate constant equations for the different processes involved in the kinetic Monte Carlo (KMC) simulations of Section 4.1.2 as well as details of the KMC algorithm are presented in the following.

Kinetic Monte Carlo simulations

Vibrational states between $v = 0$ and 35 are considered in the KMC simulations. The CO monolayer lattice is represented by a (100×100) square lattice of perpendicularly oriented CO molecules with a lattice constant of $R_0 = 3.96\,\text{Å}$ and all molecules are in their vibrational ground state at the start of the simulation ($t = 0$). Periodic boundary conditions are applied but interactions between CO molecules are considered up to an interaction radius of 8 lattice constants ($\sim 32\,\text{Å}$). The results are averaged over 50 different KMC simulations based on different random number seeds and are propagated for ~ 33 ms after laser excitation.

The Fortran code used for the KMC simulation is a modified version of the original code from Refs. [57, 58, 87] based on a rejection-free KMC algorithm. At each time step, t, the sum of rate constants, R, of all possible events for individual molecules i (k_i) and for all CO pairs (i, j) within the chosen interaction radius (k_{ij}) are summed for the

current lattice of vibrational states:[1]

$$R = \sum_i k_i + \sum_{ij} k_{ij}.$$ (B.1)

The individual events can be thought of as subsequent intervals of length k_i or k_{ij} on a line with total length R. To determine which event occurs in this time step, a random number, u_1, uniformly distributed between 0 and 1, is drawn. [57] The event is chosen if $u_1 R$ lies on the corresponding interval of the event. The quantum states of the involved CO molecules are changed accordingly and the system is propagated by a time step Δt. This time step is also randomly chosen from an exponential distribution:

$$\Delta t = -\frac{\ln(u_2)}{R}.$$ (B.2)

Here, u_2 is another uniformly distributed number between 0 and 1, and the exact form of Eq. B.2 ensures that the time steps are consistent with a Poisson process occurring at an average rate R. [57, 186]

Spectroscopic constants of CO

Vibrational spectroscopic constants were obtained from the emission spectra for $^{13}C^{18}O$ adsorbed to NaCl(100) measured by Li Chen (Section 4.1.1) by fitting the observed overtone emission lines to the energy eigenvalue expression for an anharmonic oscillator:

$$E_v = hc \left[\omega_e \left(v + \frac{1}{2} \right) - \omega_e x_e \left(v + \frac{1}{2} \right)^2 + \omega_e y_e \left(v + \frac{1}{2} \right)^3 \right].$$ (B.3)

Here, $\omega_e = (2074.6 \pm 0.9)\,\text{cm}^{-1}$ is the harmonic vibrational frequency and $\omega_e x_e = (12.22 \pm 0.04)\,\text{cm}^{-1}$ and $\omega_e y_e = (0.012 \pm 0.002)\,\text{cm}^{-1}$ are anharmonicity constants. These spectroscopic constants will be used to calculate transition energies in most of the following rate constant calculations.

---

[1] The rate constants k_i include stimulated absorption/emission (k_{stim}), radiative relaxation (k_{fl}), non-radiative relaxation (k_{nr}) and vibration-to-electronic (V-E) transfer (k_{VE}). The rate constants k_{ij} are identical to the vibrational energy pooling (VEP) rate constants (k_{nm}).

Excitation laser pulse

The peak excitation rate of $3.44 \times 10^9 \, \text{s}^{-1}$ is estimated from the experimental parameters and the absorption cross section of the CO monolayer. The laser fluence is estimated from the $120 \, \mu\text{J}$ pulse energy assuming a focus diameter of $1.4 \, \text{mm}$. The temporal Gaussian intensity profile of the laser, $I_{\text{laser}}(t, \tilde{\nu})$, with $4.7 \, \text{ns}$ FWHM is chosen such that it reproduces this total flux. In the frequency domain, the laser profile is modeled as a Gaussian centered at the excitation frequency, $\tilde{\nu} = 2055 \, \text{cm}^{-1}$, and the corresponding bandwidth is estimated as $0.05 \, \text{cm}^{-1}$ from photoacoustic spectra. The profile of the CO absorption cross section at $7 \, \text{K}$, $\sigma(\tilde{\nu})$, is modelled as a Lorentzian line with $0.028 \, \text{cm}^{-1}$ FWHM [129] and an integrated cross section of 1.1×10^{-17} cm/molecule [25]. The excitation rate constant is given by Eq. B.4 where $I_{\text{laser}}(t, \tilde{\nu}) * \sigma(\tilde{\nu})$ denotes a convolution of the laser and cross section profile in the frequency domain. The $\sin^2(\theta_i)/\cos(\theta_i)$ term corrects for geometrical factors due to the incidence angle $\theta_i = 45°$ while the excited absorption line has a dipole moment perpendicular to the surface. Note that the excitation laser maximum appears $6 \, \text{ns}$ later than $t = 0$ in the KMC simulations. This displacement is, however, negligible compared to the timescales considered in Section 4.1.2.

$$k_{\text{stim}}(t) = \frac{I_{\text{laser}}(t, \tilde{\nu}) * \sigma(\tilde{\nu})}{hc\tilde{\nu}} \frac{\sin^2(\theta_i)}{\cos(\theta_i)} \tag{B.4}$$

Radiative relaxation

One-quanta ($k_{\text{fl}}^{\Delta v=1}$), two-quanta ($k_{\text{fl}}^{\Delta v=2}$) and three-quanta ($k_{\text{fl}}^{\Delta v=3}$) processes are considered in the simulations. The corresponding vibrational state-dependent rate constants are calculated based on Eqs. 2.45 to 2.47. The dipole moment derivative $\mu' = 3.2 \, \text{D/Å}$ is taken as the gas phase value. [125] The transition frequencies are based on Eq. B.3 using the corresponding values for ω_e, $\omega_e x_e$ and $\omega_e y_e$. The matrix elements (Eqs. 2.42 to 2.44) are based on $k = \omega_e/\omega_e x_e \approx 169.8$ and $\alpha \approx 2.339 \, \text{Å}^{-1}$, which is calculated from $\alpha = (8\pi^2 c \mu \omega_e x_e/h)^{1/2}$ [102] where μ is the reduced mass of $^{13}\text{C}^{18}\text{O}$. Since $k_{\text{fl}}^{\Delta v=1} > k_{\text{fl}}^{\Delta v=2} > k_{\text{fl}}^{\Delta v=3}$ and $k_{\text{fl}}^{\Delta v=3}$ is at least 5 times smaller than $k_{\text{fl}}^{\Delta v=1}$ for all relevant vibrational states, other overtones do not need to be considered.

Vibrational energy pooling (V-V transfer)

The vibrational energy pooling rate constants, k_{nm}, are calculated according to Eqs. 2.31 to 2.35, which model the vibration-to-vibration (V-V) energy transfer between any pair of

CO molecules adsorbed perpendicular to the surface which couple to the in-plane motion of the Na atoms underneath the molecule, described by a projected density of states (DOS). Note that the energy mismatch, $\Delta E_{nm} = E_n + E_m - E_{n+1} - E_{m-1} \approx 2hc\omega_e x_e(n - m + 1)$, is considered positive for exothermic reactions ($n \geq m$). Endothermic reaction rates ($m > n + 1$) are calculated from the reverse, exothermic reactions by the detailed balance relationship:

$$k_{nm} = k_{m-1,n+1} \exp(\Delta E_{nm}/k_{\mathrm{B}}T) \qquad (B.5)$$

The summation is truncated at $p_{\mathrm{max}} = 3$. Unless otherwise stated, the phononic DOS that has been used in Chapter 4 is the DOS given in Fig. 4.4. The realistic DOS is implemented by evaluating the I_p integrals (Eq. 2.35) numerically. However, note that this DOS shown in Fig. 4.4 is normalized in wavenumber units but the integrals I_p in Eq. 2.35 rely on a normalized DOS in angular frequency units, which can be easily interconverted ($\rho(\omega) = \rho(\tilde{\nu})/(2\pi c)$). The energy difference Matrix elements of the type $\langle n - 1|x|n\rangle$ are calculated according to Eq. 2.42, where the same parameters k and α as for the fluorescence (radiative) rate constant calculation are used, and also μ' is assumed to be 3.2 D/Å. The CO molecules are arranged in a square lattice with a lattice constant (nearest neighbor distance) of 3.96 Å and the equilibrium distance between any pair of two interacting CO molecules, R_0, can be easily evaluated. $m_{\mathrm{Na}} = 23$ u is the mass of a Na atom.

For resonant reactions ($m = n+1$), the rate constants are calculated according to Eq. 2.30. These are typically much larger than non-resonant rate constants ($k_{0,1} = 1.8 \times 10^{11}$ s^{-1} vs. 1×10^7-1×10^8 s^{-1}). To reduce the computation time for the KMC simulations, all resonant rate constants have thus been scaled down by a factor of 100. As the resonant rate constants only lead to spatial "diffusion" of vibrational excitation but do not change the overall vibrational population distribution, this scaling was found to have little effect compared to a test simulation where the resonant rate constants were scaled down by a factor of 100.

Non-radiative relaxation

Skinner-Tully model

Non-radiative relaxation rate constants according to the Skinner-Tully (ST) model, based on energy transfer to a phonon bath that is characterized by a Debye DOS with Debye frequency $\tilde{\nu}_{\mathrm{D}} = 223$ cm^{-1}, are calculated according to Eqs. 2.13 to 2.17. The energy difference is simply given by $\Delta E_n = E_n - E_{n-1}$ (see Eq. B.3). The minimum number of

phonons, $p_{\min}$, is calculated as $\lceil \Delta E_n / (hc\tilde{\nu}_D) \rceil$ and $p_{\max} = p_{\min} + 10$ is used. The same coupling parameter as in Ref. [57], $\lambda = 0.522$ is used unless otherwise stated. However, the influence of λ and ω_D on the relaxation rates is discussed in Section 4.1.4. The same Morse parameters as in Ref. [57] ($\alpha' = 0.82\,\text{Å}^{-1}$ and $D' = 0.168\,\text{eV}$) are used for the CO-NaCl potential, as the isotope effect of $^{13}C^{18}O$ vs. $^{13}C^{16}O$ should be negligible. Matrix elements of the type $\langle n - 1|x|n\rangle$ are calculated according to Eq. 2.42, where the same parameters k and α as for the fluorescence (radiative) rate constant calculation are used. m_C and m_O are the masses for ^{13}C and ^{18}O, respectively.

CPS model

Non-radiative relaxation rate constants according to the Chance-Prock-Silbey (CPS) model, based on classical electrodynamic energy transfer via the near-field of the oscillating CO dipole, are calculated according to Eq. 2.19. As the CO molecules are perpendicular to the surface in the simulations, an orientation factor $\theta = 3/2$ is used. For k_{fl} and $\tilde{\nu}$, the fundamental fluorescence rate constants and wavenumbers as calculated above are used. The real and imaginary parts of the complex index of refraction, $n = 1.52$ and $\kappa = 1.8 \times 10^{-9}$, are approximately constant in the relevant frequency range between 1500 and 2600 cm^{-1}. [135] The distance from the surface is assumed to be 3.36 Å. [138]

V-E energy transfer

Since the energy of the highest vibrational state observed experimentally ($v = 28$, $E_{28} - E_0 \approx 48\,400\,\text{cm}^{-1}$) lies extremely close to the energy for electronic excitation to the $a^3\Pi_r\,(v = 0)$ state of gas phase CO ($\nu_{00} = 48\,473.22\,\text{cm}^{-1}$). [131] Therefore, a V-E energy transfer channel with a fixed rate of $k_{\text{V-E}} = 1 \times 10^5\,\text{s}^{-1}$ has been introduced for $v \geq 28$. Assuming that energy transferred to the $a^3\Pi_r$ state will not be involved in the vibrational energy transfer dynamics and eventually relax to the vibrational and electronic ground state, the electronic state is not explicitly modeled and V-E transfer processes are implemented by transferring population directly to the vibrational ground state:

$$\text{CO}(v \geq 28) \xrightarrow{k_{\text{V-E}}} \text{CO}(v = 0) \tag{B.6}$$
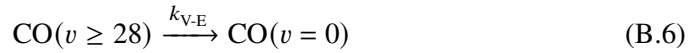
C-down and O-down structure in the buried monolayer

In the Supplementary Materials of Ref. [126], we simulated the Fourier-transform infrared (FTIR) absorption spectra of the buried $^{13}C^{18}O$ monolayer (Fig. 5.4a) to estimate the fundamental absorption frequency of the C-down species without the dynamic frequency splitting. The simulation was based on Eqs. 2.65 to 2.69 and gave an estimate of the tilt angle of the C-down species.

This estimation of the tilt angle neglected the normalized field intensity terms that describe the effective electric field at the vacuum-NaCl interface. Here, a slightly more accurate estimate of the molecular tilt angles of the C-down and O-down isomer in the buried monolayer structure will be obtained by considering these terms. The integrated absorbance of the C-down and O-down absorption peaks for p- and s-polarized light, determined from the absorption peaks in Figs. 5.4a and 5.4b, are summarized in Table C.1. For a single absorption line, the tilt angle of the transition dipole moment against the surface normal, α, can be estimated based on the $A^{(s)}/A^{(p)}$ ratio. [187] Using the results from Chapter 7 (Eqs. 7.4 and 7.5), we can write:

$$\frac{A_l^{(s)}}{A_l^{(p)}} = \frac{\left\langle \left| \mathbf{T}_s \cdot \mathbf{P}_l \right|^2 \right\rangle}{\left\langle \left| \mathbf{T}_p \cdot \mathbf{P}_l \right|^2 \right\rangle} = \frac{0.5 \sin^2(\alpha) T_y}{0.5 \sin^2(\alpha) T_x + \cos^2(\alpha) T_z}. \tag{C.1}$$

Here, the $A^{(s)}/A^{(p)}$ ratio for a single exciton absorption line only depends on the normalized field intensity terms (Eqs. 2.55 to 2.57) and the tilt angle α. Figure C.1 shows the $A^{(s)}/A^{(p)}$ ratio as a function of α for the experimental conditions under which

Table C.1: Absorption peak frequencies, integrated absorbance for p- and s-polarized light, and the $A^{(s)}/A^{(p)}$ ratio of the C-down and O-down absorption peaks in the buried $^{13}C^{18}O$ monolayer, measured for an incidence angle of 34°. The peaks at 2048.3 and 2053.5 cm^{-1} correspond to the absorption peaks of the C-down species and the integrated absorbance is extracted from the spectrum in Fig. 5.4a. The frequency of 2036.7 cm^{-1} corresponds to the maximum of the O-down peak and the integrated absorbance is extracted from the spectrum in Fig. 5.4b. The statistical errors (1σ) associated with the integrated absorbance values are estimated as 10^{-5} cm^{-1} using a similar procedure as desribed in the caption of Fig. 7.1.

Species	Peak frequency (cm^{-1})	$A^{(s)}$ (10^{-4} cm^{-1})	$A^{(p)}$ (10^{-4} cm^{-1})	$A^{(s)}/A^{(p)}$
O-down	2036.7	5.2	4.8	1.07 ± 0.03
C-down	2048.3	0.7	0.9	0.80 ± 0.14
C-down	2053.5	6.0	16.9	0.36 ± 0.01

the spectra in Fig. 5.4 were acquired. Note, however that α only corresponds to the molecular tilt angle in the case of uncoupled molecules or totally symmetric exciton modes where the coupled molecules are oriented in the same direction, as for example in a (1×1) structure.

For the C-down species, the dynamic frequency splitting into two peaks implies that at least two molecules per unit cells exist. When the small intensity peak at 2048.3 cm^{-1} is neglected and only the absorbance ratio of the high intensity peak at 2053.5 cm^{-1} (0.36 ± 0.01) is considered, the C-down structure can be approximately described as a (1×1) structure with a tilt angle of $(35 \pm 1)°$, which is in perfect agreement with an earlier estimate by Heidberg *et al.* [44] The presence of the peak at 2048.3 cm^{-1} does, however, imply that the C-down molecules have slightly different azimuthal orientations. Therefore, the effective tilt angle of 35° obtained for the symmetric vibration at 2053.5 cm^{-1} probably slightly underestimates the molecular tilt angle. In principle, a quantitative determination of the buried monolayer structure through spectra simulation based on the exciton model and the electronic and vibrational polarizability values from Chapter 7 should be possible but is beyond the scope of this work.

For the O-down species, a molecular tilt angle of $(69 \pm 2)°$ can be obtained from the $A^{(s)}/A^{(p)}$ ratio. In terms of the electrostatic model in Chapter 5, where $\theta = 0°$ is defined as a perpendicular C-down orientation, this angle would correspond to $\theta = (111 \pm 2)°$. Note, however, that the O-down absorption peak shows clear signs of heterogeneous broadening and that the absorbance ratio slightly differs for different absorption frequencies. Therefore, the estimated tilt angle of the O-down species represents an average tilt angle.
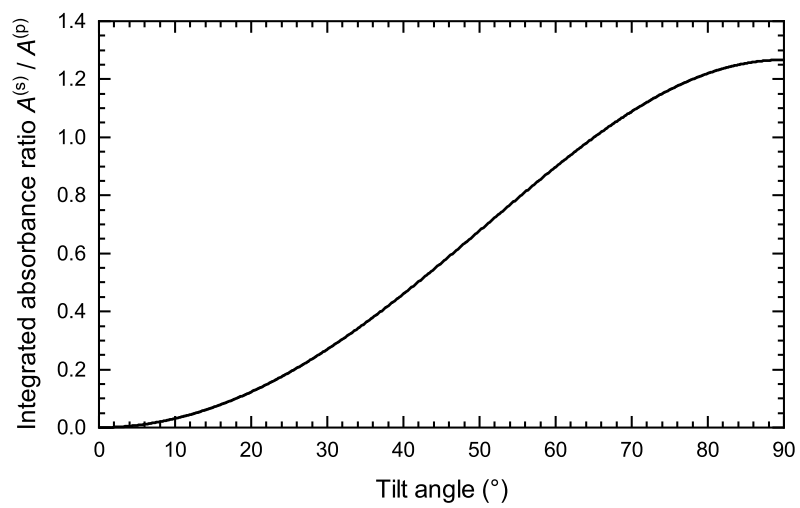
Figure C.1: Theoretical integrated absorbance ratio, $A^{(s)}/A^{(p)}$, as a function of α according to Eq. C.1. The presented $A^{(s)}/A^{(p)}$ curve is valid for the vacuum-NaCl interface ($n_1 = 1$ and $n_3 = 1.52$) under an incidence angle of 34°.

Electrostatic model of the orientation-dependent frequency shift

In the following, the equations used to describe the individual contributions to the electrostatic potential energy surface (PES) (Eq. 5.4) of the CO/NaCl(100) monolayer and thus the vibrational frequency shift relative to gas phase CO (Eq. 5.5). Note that the subscripts v and the arguments $\mathbf{r}$, θ and ϕ will be generally omitted in the following for clarity. However, keep in mind that all multipole moments and electrostatic interaction energies are functions of v and the molecular coordinates.

CO-CO interactions

The electrostatic interaction energy between two CO molecules consists of individual contributions from the interactions between multipole moments centered in the center of mass positions of the two molecules, which are labeled by indices i and j:

$$V^{\text{CO}\leftrightarrow\text{CO}} = \sum_{i=1}^{N} \sum_{j>i}^{N} V^{\mu_i \leftrightarrow \mu_j} + V^{\mu_i \leftrightarrow \Theta_j} + V^{\Theta_i \leftrightarrow \mu_j} + \cdots + V^{\Omega_i \leftrightarrow \Omega_j} \qquad \text{(D.1)}$$

Here, all combinations of multipole-multipole interactions up to the octopole-octopole interaction are considered and the summation runs over all CO pairs. In Eq. D.2, the individual multipole-multipole interactions are expressed in terms of the multipole moments on molecule i (μ_i, Θ_i or Ω_i) and molecule j (μ_j, Θ_j or Ω_j), where T_{tu}^{ij} describes the orientation and distance-dependent interaction term for an interaction

Table D.1: Interaction terms T_{tu}^{ij} for all multipole-multipole interactions relevant to this work. From Ref. [126]. Adapted with permission from AAAS.

t	u	$4\pi\varepsilon_0 T_{tu}^{ij}$
μ	μ	$R_{ij}^{-3}\left[3r_z^i r_z^j + c_{zz}\right]$
Θ	μ	$\frac{3}{2}R_{ij}^{-4}\left[5(r_z^i)^2 r_z^j - r_z^j + 2r_z^i c_{zz}\right]$
Ω	μ	$\frac{1}{2}R_{ij}^{-5}\left[5\left(7(r_z^i)^3 - 3r_z^i\right)r_z^j + 3\left(5(r_z^i)^2 - 1\right)c_{zz}\right]$
Θ	Θ	$\frac{3}{4}R_{ij}^{-5}\left[35(r_z^i)^2(r_z^j)^2 - 5(r_z^i)^2 - 5(r_z^j)^2 + 20r_z^i r_z^j c_{zz} + 2c_{zz}^2 + 1\right]$
Ω	Θ	$\frac{5}{4}R_{ij}^{-6}\left[21\left(3(r_z^i)^3 - r_z^i\right)(r_z^j)^2 + 6\left(7(r_z^i)^2 - 1\right)r_z^j c_{zz} - 7(r_z^i)^3 + 3r_z^i + 6r_z^i c_{zz}^2\right]$
Ω	Ω	$\frac{5}{4}R_{ij}^{-7}\left[21\left(11(r_z^i)^3 - 3r_z^i\right)(r_z^j)^3 - 21\left(3(r_z^i)^3 - r_z^i\right)r_z^j \right.$ $\left. + \left(189(r_z^i)^2(r_z^j)^2 - 21(r_z^i)^2 - 21(r_z^j)^2 + 3\right)c_{zz} + 42r_z^i r_z^j c_{zz}^2 + 2c_{zz}^3\right]$

involving multipole moments t and u (see also Section 2.5.2).

$$V^{\text{CO}\leftrightarrow\text{CO}} = \sum_{i=1}^{N}\sum_{j>i}^{N}\mu_i\mu_j T_{\mu\mu}^{ij} + \mu_i\Theta_j T_{\mu\Theta}^{ij} + \Theta_i\mu_j T_{\Theta\mu}^{ij} + \cdots + \Omega_i\Omega_j T_{\Omega\Omega}^{ij} \qquad \text{(D.2)}$$

The interaction terms relevant to this work are taken from the table in Ref. [124] and summarized in Table D.1. Only the octopole-octopole interactions was not tabulated in Ref. [124] and was derived according to Eq. 24 of that same reference The interaction terms are written using the direction cosines (or projections) $r_z^i = \mathbf{e}_i \cdot \mathbf{e}_{ij}$, $r_z^j = -\mathbf{e}_j \cdot \mathbf{e}_{ij}$ and $c_{zz} = \mathbf{e}_i \cdot \mathbf{e}_j$. $R_{ij}\mathbf{e}_{ij} = \mathbf{R}_{ij}$ is the intermolecular separation vector with magnitude R_{ij} and direction $\mathbf{e}_{ij}$, pointing from molecule i to molecule j. The corresponding orientation unit vectors, which are parallel to the CO bond axis and point from the carbon to the oxygen atom, are $\mathbf{e}_i$ and $\mathbf{e}_j$, respectively, which can easily calculated from the corresponding tilt angles (θ_i and θ_j) and azimuthal angles (ϕ_i and ϕ_j), as defined in Section 5.1.3:

$$\mathbf{e}_i = \begin{pmatrix} \sin\theta_i\cos\phi_i \\ \sin\theta_i\sin\phi_i \\ \cos\theta_i \end{pmatrix} \qquad \text{(D.3)}$$

CO-NaCl interactions

The electrostatic interaction energy between a single CO molecule i and the NaCl(100) surface can be written as a sum of individual contributions:

$$V^{\text{CO}\leftrightarrow\text{NaCl}} = \sum_{i=1}^{N} V^{\mu_i \leftrightarrow F_z^i} + V^{\Theta_i \leftrightarrow \partial F_z^i/\partial z} + V^{\Omega_i \leftrightarrow \partial^2 F_z^i/\partial z^2} \tag{D.4}$$

The first term inside the sum describes the interaction of the dipole moment, μ_i, with the electric field component along the z-axis (perpendicular to the NaCl surface) at the position of molecule i, F_z^i. The second term describes the interaction of the quadrupole moment, Θ_i with the gradient of the electric field along the z-direction, $\partial F_z^i/\partial z$. The third term describes the interaction of the octopole moment, Ω_i with the second gradient of the electric field along the z-direction, $\partial^2 F_z^i/\partial z^2$. The sum runs over all CO molecules in the simulation box. I will prove below that Eq. D.4 can be written in the following simple form, assuming the CO molecules adsorbed directly on top of the Na$^+$ ion:

$$\begin{aligned} V^{\text{CO}\leftrightarrow\text{NaCl}} = \sum_{i=1}^{N} &- \cos\theta_i \mu_i F_z^i - \frac{1}{4}\left(3\cos^2\theta_i - 1\right)\Theta_i \frac{\partial F_z^i}{\partial z} \\ &- \frac{1}{12}\left(5\cos^3\theta_i - 3\cos\theta_i\right)\Omega_i \frac{\partial^2 F_z^i}{\partial z^2} \end{aligned} \tag{D.5}$$

Here, θ_i is the tilt angle of molecule i with respect to the surface normal, as defined in Section 5.1.3. By describing the NaCl(100) surface as a lattice of point charges, a simple analytical expression can be derived for the position-dependent electric field of the surface along the z-direction: [188]

$$F_z^i = \frac{8\pi n e}{4\pi\varepsilon_0 a^2} \sum_{l,m} \frac{(-1)^{(l+m)/2}}{1 + e^{-\pi\sqrt{l^2+m^2}}} e^{-\frac{2\pi z}{a}\sqrt{l^2+m^2}} \cos\left(2\pi\left(\frac{lx}{a} + \frac{my}{a} - \frac{l+m}{4}\right)\right) \tag{D.6}$$

Here, $n = 1$ is the valency of the Na$^+$ and Cl$^-$ ions. e is the elementary charge and ε is the vacuum permittivity. $a = 5.64\,\text{Å}$ is the bulk lattice constant of NaCl. [189] l and m are odd integers and the summation runs over all combinations (l, m). It is however convenient to think about the summation in groups of (l, m) constrained by the value $\sqrt{l^2 + m^2}$. The sum converges rapidly [188] and the largest contribution comes from the sum for $\sqrt{l^2 + m^2} = \sqrt{2}$: $(l, m) = (1, 1), (1, -1), (-1, 1)$ and $(-1, -1)$. In the calculation, contributions up to $\sqrt{5^2 + 5^2}$ were included. The first and second gradients of

the electric field along the z-axis are found analytically as the first and second derivative of F_z^i with respect to z ($\partial F_z^i / \partial z$ and $\partial^2 F_z^i / \partial z^2$, respectively)

CO-NaCl interaction for arbitrary CO positions

In this section, a more general expression for the CO-NaCl interaction, $V^{\text{CO}\leftrightarrow\text{NaCl}}$, will be presented, which is valid for any position of CO at the surface. In addition, the derivation of Eq. D.5, which is valid only if CO adsorbs directly on top of a Na$^+$ ion ($x = y = 0$), is provided. Following Refs. [190] and [123], the interaction between a single molecule and an external electric potential Φ is generally given by Eq. D.7, where the Einstein summation convention is used (see also Section 2.5.1).

$$V = q\Phi - \mu_\alpha F_\alpha - \frac{1}{3}\Theta_{\alpha\beta}F_{\alpha\beta} - \frac{1}{15}\Omega_{\alpha\beta\gamma}F_{\alpha\beta\gamma} - \cdots \tag{D.7}$$

q describes the charge of the molecule and is zero for CO. μ_α, $\Theta_{\alpha\beta}$ and $\Omega_{\alpha\beta\gamma}$ are cartesian components of the traceless dipole, quadrupole and octopole tensors, respectively. F_α, $F_{\alpha\beta}$ and $F_{\alpha\beta\gamma}$ are cartesian components of the tensors describing the electric field, the field gradient and the second field gradient, respectively. For linear molecules, the tensor components are defined by a single scalar value for each multipole moment and the orientation of the molecule by the following set of equations (equation 17 in Ref [190]):

$$\mu_\alpha = \mu l_\alpha,$$
$$\Theta_{\alpha\beta} = \frac{1}{2}\Theta\left(3l_\alpha l_\beta - \delta_{\alpha\beta}\right), \tag{D.8}$$
$$\Omega_{\alpha\beta\gamma} = \frac{1}{2}\Omega\left(5l_\alpha l_\beta l_\gamma - l_\alpha\delta_{\beta\gamma} - l_\beta\delta_{\gamma\alpha} - l_\gamma\delta_{\alpha\beta}\right).$$

The components l_α are components of the unit vector that describes the orientation of the high-symmetry axis (bond axis) of the linear molecule in a given coordinate system. If the internal coordinate system of CO is chosen, in which the bond axis (C-to-O direction) is aligned with the z-axis, then the components $\mu_z = \mu$, $\Theta_{zz} = \Theta$ and $\Omega_{zzz} = \Omega$ would correspond to the characteristic scalar values of the multipole moments. To describe the rotation of the molecule within the fixed electric potential of the NaCl(100) surface, it is more convenient to describe the molecular multipole components in the coordinate system of the surface electric potential, where the cartesian coordinates are aligned with the lattice vectors of the bulk unit cell (x and y are in the surface plane; z is perpendicular and pointing away from the surface). [188] In the surface coordinate system, the vector **l**

is identical to the orientation unit vector in Eq. D.3:

$$\mathbf{l} = \begin{pmatrix} \sin\theta\cos\phi \\ \sin\theta\sin\phi \\ \cos\theta \end{pmatrix} \tag{D.9}$$

According to Ref. [188], the electric potential of the NaCl(100) surface is given by the following analytical expression:

$$\Phi(x, y, z) = \frac{4ne}{4\pi\varepsilon_0 a} \sum_{l,m} \frac{(-1)^{(l+m)/2}}{\sqrt{l^2 + m^2}} \cos\left(2\pi\left(\frac{lx}{a} + \frac{my}{a} - \frac{l+m}{4}\right)\right) \frac{e^{-\frac{2\pi z}{a}\sqrt{l^2+m^2}}}{1 + e^{-\pi\sqrt{l^2+m^2}}} \tag{D.10}$$

Here, the definitions of all quantities is the same as in Eq. D.6. The corresponding components of the electric field and its gradients at a given position $\mathbf{r}$ can be calculated as the partial derivatives of the electric potential $\Phi(x, z, y)$:

$$F_\alpha = -\left(\frac{\partial\Phi}{\partial\alpha}\right)_{\mathbf{r}}, \quad F_{\alpha\beta} = -\left(\frac{\partial^2\Phi}{\partial\alpha\partial\beta}\right)_{\mathbf{r}}, \quad F_{\alpha\beta\gamma} = -\left(\frac{\partial^3\Phi}{\partial\alpha\partial\beta\partial\gamma}\right)_{\mathbf{r}} \tag{D.11}$$

With Eqs. D.7 to D.11 at hand, the CO-NaCl interaction energy for a single molecule can be evaluated for any position ($\mathbf{r}$) and orientation (θ and ϕ) of the CO molecule on the NaCl surface.

Now consider the simplified case where CO adsorbs on top of the Na$^+$ ion ($x = y = 0$). Careful inspection of Eq. D.10 and its derivatives shows that the only non-zero components are:

$$F_z,$$
$$F_{xx} = F_{yy} = -\frac{1}{2}F_{zz}, \tag{D.12}$$
$$F_{zxx} = F_{xzx} = F_{xxz} = F_{zyy} = F_{yzy} = F_{yyz} = -\frac{1}{2}F_{zzz}.$$

Considering Eqs. D.8 and D.12 as well as the relations $l_z = \cos\theta$ and $l_x^2 + l_y^2 + l_z^2 = 1$,

Eq. D.7 becomes:

$$
\begin{aligned}
V =& q\Phi - l_z \mu F_z - \frac{1}{4}\left(3l_z^2 - 1\right)\Theta F_{zz} - \frac{1}{12}\left(5l_z^3 - 3l_z\right)\Omega F_{zzz} - \cdots \\
=& q\Phi - \cos\theta\mu F_z - \frac{1}{4}\left(3\cos^2\theta - 1\right)\Theta\frac{\partial F_z}{\partial z} \\
& - \frac{1}{12}\left(5\cos^3\theta - 3\cos\theta\right)\Omega\frac{\partial^2 F_z}{\partial z^2} - \cdots .
\end{aligned}
\tag{D.13}
$$

Considering that the charge of CO is zero, Eq. D.13 gives the individual terms used for the summation in Eq. D.5.

Assignment of impurity spectra

Fe(CO)$_5$ absorption peaks in the ^{12}C^{16}O overlayer

The peaks at 1995, 2003, 2029 and 2039 cm^{-1} in Fig. 6.1 are in reasonable agreement with peaks observed for Fe(CO)$_5$ in an Ar matrix. [191] Peaks in a similar frequency range are also expected for iron diluted in a CO matrix. [192] Since Fe(CO)$_5$ should show only two IR-active peaks corresponding to vibrations of e' and a_2'' symmetry, I suspect that four peaks either result from strong distortion of the D_{3h} symmetry or that it consists of two doublets from Fe(CO)$_5$ in two different matrix sites. For the latter case, the concentration of Fe(CO)$_5$ can be estimated from the absorbance ratio ($\tilde{A}(\text{Fe(CO)}_5)/\tilde{A}(\text{CO}) \approx 1:68$). The molar decadic absorption coefficient of Fe(CO)$_5$, based on density functional theory (DFT) calculations for the gas phase molecule, [193] is the sum of the contributions from e' (1910 km mol^{-1}) and a_2'' (1129 km mol^{-1}) vibrations. The decadic absorption coefficient of solid ^{12}C^{16}O is 25.2 km mol^{-1}. [167] Thus, the concentration of Fe(CO)$_5$ is estimated as only 0.01 %.

Evidence for ^{13}C^{16}O^{18}O emission in the m26o38 emission spectrum

After the laser experiments with the m26o38 sample, an asymmetric absorption line that shows no polarization dependence appeared near 2263 cm^{-1} (Fig. E.1a). The frequency agrees well with the gas phase vibrational frequency of the antisymmetric stretch mode of ^{13}C^{16}O^{18}O (2266 cm^{-1} [194]) considering a plausible matrix shift of -3 cm^{-1}. The lack of polarization dependence suggests random orientation of the CO$_2$ molecules and

that it is present in the $^{13}C^{18}O$ multilayer. Fig. E.1b shows the corresponding emission spectrum after **m26**o38 excitation where mainly fluorescence from the overlayer is observed. However, another vibrational progression is observed which is indicated by the dashed line. In addition, two arrows denote the most intense combination band $v_1 + v_3$ found for gas phase $^{13}C^{16}O^{18}O$: a transition from the ground state, (00^00), to the higher $(10^01)_1$ level and the lower $(10^01)_2$ levels, which result from a Fermi resonance between the symmetric mode and the bending overtone, and have an intensity ration of $\sim 2:1$ in the gas phase. [194] Due to the Fermi resonance, hot bands of these transitions are expected to shift towards both positive and negative frequencies. Thus, the observed vibrational progression is possibly related to emission of vibrationally excited $^{13}C^{16}O^{18}O$ emission after accepting vibrational energy from CO. However, more controlled experiments would be necessary to test whether that energy transfer from CO to $^{13}C^{16}O^{18}O$ is possible and results in the observed spectral progression.
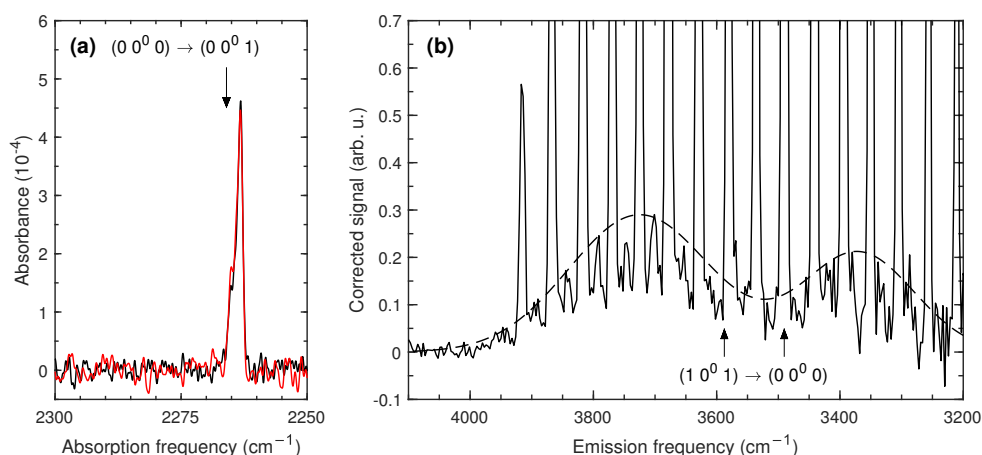
Figure E.1: (a) Shows the FTIR absorption spectrum after the LIF experiments in the antisymmetric stretch region of $^{13}C^{16}O^{18}O$. Black and red curves correspond to p- and s-polarization. The arrow denotes the fundamental frequency of the antisymmetric stretch of $^{13}C^{16}O^{18}O$ in the gas phase. The nomenclature for vibrational states of CO_2 vibrational states is $(v_1 v_2^{l_2} v_3)$ where v_1, v_2 and v_3 are quantum numbers of the symmetric, bending and antisymmetric mode, respectively. l_2 denotes the angular momentum due to the bending mode. (b) shows the part of the **m26**o38 emission spectrum where an additional vibrational progression is observed that cannot be assigned to CO isotopologues. The dashed line is drawn as a guide for the eye. Arrows denote the combination bands that correspond to transitions from the ground state to the $(10^01)_1$ and $(10^01)_2$ states.

List of Figures

List of Tables

Acronyms

APA average polarizability approximation

CPS Chance-Prock-Silbey

cw continuous-wave

DFG difference frequency generation

DFT density functional theory

DOF degree of freedom

DOS density of states

EDMF electric dipole moment function

FRET Förster resonance energy transfer

FTIR Fourier-transform infrared

FWHM full width at half maximum

IR-LIF infrared laser-induced fluorescence

IVR intramolecular vibrational energy redistribution

KMC kinetic Monte Carlo

LEED low-energy electron diffraction

LIF laser-induced fluorescence

MCS multi-channel scaler

MIR mid-infrared

Nd:YAG Neodymium-doped yttrium aluminum garnet

PES potential energy surface

RDE relative detection efficiency

RF radio frequency

RGA residual gas analyzer

SNR signal-to-noise ratio

SNSPD superconducting nanowire single-photon detector

ST Skinner-Tully

TPD temperature-programmed desorption

UHV ultra-high vacuum

UV-Vis ultraviolet-visible

V-E vibration-to-electronic

V-T vibration-to-translation

V-V vibration-to-vibration

VEP vibrational energy pooling

VET vibrational energy transport

ZPE zero-point energy

Jascha Alexander Lau

Born on October 31st, 1992

Place of birth: Gronau (Leine)   Nationality: German

Hermann-Rein-Str. 2b, 37075 Göttingen, Germany

Education

01/2017 – present	**Doctoral Studies in Chemistry** *University of Göttingen, Germany*
10/2014 – 10/2016	**M.Sc. Chemistry, with distinction** (final grade: 1.0) *University of Göttingen, Germany*
10/2011 – 08/2014	**B.Sc. Chemistry, with distinction** (final grade: 1.0) *University of Göttingen, Germany*
08/2004 – 06/2011	**Abitur** (final grade: 1.0) *Gymnasium Alfeld, Germany*

Research Experience

01/2017 – present	**Doctoral thesis** *Supervisor: Alec M. Wodtke, University of Göttingen, Germany* Thesis title: Vibrational Energy Transfer Between CO Molecules on a NaCl(100) Surface Studied by Infrared Fluorescence Spectroscopy
04/2016 – 10/2016	**Master thesis** *Supervisors: John Ellis and William Allison, University of Cambridge, UK* Thesis title: Structure and Dynamics of Cyclooctatetraene on the Cu(111) Surface Studied with Helium Atom Scattering
08/2014 – 09/2015	**Research assistant** *Supervisor: J. Peter Toennies, Max Planck Institute for Dynamics and Self-Organization, Göttingen, Germany*
05/2014 – 08/2014	**Bachelor thesis** *Supervisor: Alec M. Wodtke, University of Göttingen, Germany* Thesis title: Translational inelasticity in collisions of NO with Au(111) and Ag(111) surfaces

Publications

1. **J. A. Lau**, L. Chen, L., A. Choudhury, D. Schwarzer, V. B. Verma, A. M. Wodtke, Transporting and concentrating vibrational energy to promote isomerization, *Nature* **589,** 391-395 (2021).

2. **J. A. Lau,** A.-M. Schönemann, D. Schwarzer, A. M. Wodtke, The coverage dependence of the infrared absorption of CO adsorbed to NaCl(100), *J. Chem. Phys.* **153**, 154703 (2020).

3. **J. A. Lau**, A. Choudhury, L. Chen, D. Schwarzer, V. B. Verma, A. M. Wodtke, Observation of an isomerizing double-well quantum system in the condensed phase, *Science* **367**, 175-178 (2020).

4. L. Chen*, **J. A. Lau***, D. Schwarzer, J. Meyer, V. B. Verma, A. M. Wodtke, The Sommerfeld ground-wave limit for a molecule adsorbed at a surface, *Science* **363**, 158-161 (2019). * Both authors contributed equally to this work.

5. Ch. Steinsiek, P. R. Shirhatti, J. Geweke, **J. A. Lau**, J. Altschäffel, A. Kandratsenka, Ch. Bartels, A. M. Wodtke, Translational Inelasticity of NO and CO in Scattering from Ultrathin Metallic Films of Ag/Au(111), *J. Phys. Chem. C* **122**, 18942-18948 (2018).

6. L. Chen, D. Schwarzer, **J. A. Lau**, V. B. Verma, M. J. Stevens, F. Marsili, R. P. Mirin, S. W. Nam, A. M. Wodtke, Ultra-sensitive mid-infrared emission spectrometer with sub-ns temporal resolution, *Opt. Express* **26**, 14859-14868 (2018).

7. **J. A. Lau**, I. Calvo-Almazán, P. S. M. Townsend, D. J. Ward, A. P. Jardine, W. Allison, J. Ellis, B. J. Hinch, N. Avidor, Structural Evolution of a Cyclooctatetraene Adlayer on Cu(111) during Isothermal Desorption, *J. Phys. Chem. C* **122**, 8941-8945 (2018).

8. **J. A. Lau**, J. P. Toennies, K. T. Tang, An accurate potential model for the $a^3\Sigma_u^+$ state of the alkali dimers Na_2, K_2, Rb_2, and Cs_2, *J. Chem. Phys.* **145**, 194308 (2016).

Awards and Scholarships

2019	First poster prize, Gordon Research Conference on Dynamics at Surfaces 2019
2016	Boomerang scholarship, International Center for Advanced Studies of Energy Conversion, awarded for a research visit at the University of Cambridge
2014	Otto Wallach Award, University of Göttingen, awarded for the best Bachelor degree in Chemistry